Three-Dimensional Inversion of Multi-Component Loop-Source Transient Electromagnetic Data: Investigating the Roter Kamm Impact Crater, Namibia

Inaugural-Dissertation

zur Erlangung des Doktorgrades
der Mathematisch-Naturwissenschaftlichen Fakultät
der Universität zu Köln

vorgelegt von

Hannah Nienhaus

aus Coesfeld

Köln, 2025

1. Gutachter: Prof. Dr. B. Tezkan
2. Gutachter: Prof. Dr. A. Hördt

Tag der mündlichen Prüfung: 10.03.2025

Abstract

The Roter Kamm impact crater, estimated to be between 4 and 5 million years of age, is located within a national park in the southern Namib Desert. This location has been restricted from public access for over a century, significantly limiting research activities. This thesis determines the multi-dimensional shape of the sediment cover of the impact structure by applying 1D and 3D inversion schemes to loop-source transient electromagnetic (TEM) data, while simultaneously comparing the single-loop and multi-component fixed-loop set-ups in terms of model resolution.

The Roter Kamm impact crater, which belongs to one of multiple survey areas in the Namib and Atacama Deserts of the Collaborative Research Center CRC 1211 "Earth Evolution at the Dry Limit", is of particular interest in this study. The CRC 1211 investigates the evolution of the areas in hyper-arid deserts by applying various methods from disciplines such as geosciences, physics and biology. Several geophysical methods, such as TEM, Audiomagnetotellurics, Magnetics and Seismics, were carried out in the Namib Desert to analyse two suitable drilling locations for palaeoclimatological research. In the framework of this thesis the fixed- and single-loop TEM set-ups were employed at the Roter Kamm impact crater. The two methods can be used complementary to achieve a maximum resolution in shallow and large depths depending on their transmitter size. The single-loop configuration, which uses one loop as both a transmitter and receiver, employs loop sizes smaller than those used for the fixed-loop configuration. The fixed-loop configuration uses one stationary large transmitter and several multi-component receivers at various locations, both inside and outside the transmitter. This configuration, especially the horizontal components, is sensitive to lateral conductivity boundaries.

A variety of synthetic 3D TEM studies present the effects of a multi-dimensional subsurface and topography on transient data, and additionally highlight the superior performance of fixed-loop data-sets in multi-dimensional inversion schemes. The 1D inversion paints an highly distorted image of the resistivity distribution inside the Roter Kamm impact crater. However, the comprehensive 3D inversion results, corroborated by a 2D AMT resistivity model, reveal a large, lens-shaped conductor inside the impact structure. This conductor likely represents water-saturated sediments overlying brecciated bedrock.

This work marks the first independent geophysical model of the Roter Kamm impact crater.

Contents

List of Figures

List of Tables

CHAPTER 1

Introduction

The focus of this thesis is the exploration of the Roter Kamm impact crater using the transient electromagnetic (TEM) method. A three-dimensional (3D) inversion of multi-component fixed-loop and single-loop TEM data was performed. Not only the vertical but also the horizontal components of the induced voltages were used.

The TEM survey was carried out as part of the Collaborative Research Centre CRC 1211 "Earth Evolution at the Dry Limit". CRC 1211 is an interdisciplinary project dedicated to palaeoclimatology (Dunai et al., 2020). Sedimentary basins play an important role in understanding past climate. The CRC 1211 studies sedimentary basins to determine the role of water in their formation. Deep climate archives are obtained by studying the stratigraphy of these basins through the study of drill cores (Cohen, 2012). A typical way to determine the location of the deepest and oldest sediments is to use geophysical methods. The most commonly used is the seismic method (e.g. Diederich et al., 2020; Melles et al., 2011). However, electromagnetic (EM) methods have also been successfully used for exploration (e.g., Blanco-Arrué et al., 2022; Yogeshwar, 2014). The CRC 1211 focuses on the evolution of the hyper-arid Atacama Desert in Chile and the Namib Desert in Namibia to study surface processes and biological activity in the near absence of water. Here, two potential targets for scientific drilling in the southern Namib Desert were investigated using seismic and EM methods. The results from the Aurus clay pan have already been published in Nienhaus et al. (2023c) and are only presented here to give an overview of the tasks involved in this work. However, the focus of this thesis is solely on the field survey carried out at the Roter Kamm impact crater.

The Roter Kamm impact crater is located in a remote area of the southern Namib Desert. Its location in a former diamond mining area has provided the unique conditions of an undisturbed natural habitat for flora and fauna over the past century. Although the impact crater has been studied in the past, very few geophysical surveys have been conducted (e.g., Brandt et al., 1998; Fudali, 1973; Grant et al., 1997; Reimold et al., 1992). However, only forward modelling studies of magnetic and gravity data have been carried out, based on diameter to depth ratios found at similar impact structures and assumptions

of material properties (Brandt et al., 1998; Fudali, 1973). To my knowledge, no inversion of field data has ever been published. Therefore, the EM data presented in this thesis can provide valuable information, not only for palaeoclimatological research, but also for a better understanding of impact craters. The Roter Kamm impact crater is only one of the few impact craters that is well enough preserved to allow further in-depth studies of the morphology of simple impact structures (Grieve, 1993).

During the field survey at the Roter Kamm impact crater, TEM and Audiomagnetotelluric (AMT) soundings were carried out along two profiles. The profiles have lengths of 3,800 m and 2,400 m and cross each other perpendicularly in the centre of the impact structure. Both methods chosen for the investigation are electromagnetic (EM) methods. These methods use either natural or artificial sources to induce EM fields into the subsurface and measure the response of the Earth. The TEM method is often used for sedimentary basins or valleys (e.g., Blanco-Arrué et al., 2022; Danielsen et al., 2003; Jørgensen et al., 2003; Yogeshwar, 2014) but is equally successful in investigating groundwater (e.g., Fitterman, 2014; Goldman et al., 1991). In the most common TEM setup, a receiver in the form of a vertical induction coil or horizontal loop is placed at the centre of a loop-source transmitter (central-loop). During the field survey at the impact crater, the transmitter loop was also the receiver loop. Such a setup is called single-loop. However, more advanced source-receiver configurations can also be used. For this thesis, the fixed-loop configuration with large transmitter loops was used to obtain a deep image of the Roter Kamm impact crater. General descriptions of the TEM method can be found in various textbooks, such as Spies and Frischknecht (1988), Nabighian and Macnae (1988) and Christiansen et al. (2006). The AMT soundings complement the TEM measurements in terms of depth resolution and ensure that the vertical dimensions of any large scale conductive structure are well resolved. However, the focus of this thesis is on the TEM method.

The thickness of the sedimentary cover is expected to be at least 300 m (Fudali, 1973). Typical central-loop surveys using small-source transmitters cannot reach such depths, especially in conductive areas (e.g., Blanco-Arrué, 2024; Yogeshwar, 2014). Therefore, a fixed-loop TEM survey was carried out using larger transmitters. Typically, TEM surveys only measure the vertical field component (e.g., Auken et al., 2019; Maurya et al., 2022; Xiao et al., 2023). However, several authors have noted the importance of the horizontal components in identifying the lateral boundaries of conductive bodies (Christensen, 2014; Newman et al., 1987; SanFilipo et al., 1985). They are routinely measured in airborne time domain electromagnetic methods (Kirkegaard et al., 2012; Smith and Keating, 1996), but still not in ground-based TEM. A major reason for this may be that the one-dimensional inversion of horizontal components can be challenging and is only possible under near 1D conditions (Ley-Cooper et al., 2010). In addition, many studies have demonstrated that one-dimensional inversion of transient electromagnetic data is generally insufficient to explain complex subsurface structures (e.g., Hördt et al., 1992; Newman et al., 1987; Xiao et al., 2023; Yogeshwar and Tezkan, 2017). This is particularly true for the fixed-loop TEM configuration, where one or more receivers can be placed inside and outside the transmitter loop (Rochlitz et al., 2019; Zhang et al., 2021). In the past 3D time-domain inversions have been considered time-consuming and impractical for large TEM datasets (Vignoli et al., 2015). However, 1D approaches are only applicable

in cases where resistivity contrasts are moderate or lateral transitions are smooth, and spatially and laterally constrained inversions lead to reasonable two-dimensional sections (e.g. Auken et al., 2008; Vignoli et al., 2015).

A 2D AMT inversion revealed a large conductive anomaly inside the crater rims, which shows a strong conductivity contrast to its surroundings, indicating that the conditions for a 1D TEM inversion are unlikely to be met. Nevertheless, 1D TEM inversions were performed using only the vertical components of the TEM data. Several observations were made. Firstly, the treatment of single-loop data as central-loop data leads to an underestimation of the induced voltages in early times, and it is strongly recommended to use extended receivers for modelling. Secondly, the single-loop dataset lacks depth resolution in the central part of the Roter Kamm impact crater and fails to resolve the lower boundary of the large conductive anomaly. As expected, the fixed-loop data provide better depth resolution, which is also deep enough to resolve the lower boundary. Thirdly, the multi-dimensional effects appear to be too strong for a 1D inversion to give reasonable results in both single and fixed-loop data.
To motivate 3D TEM inversion, the 3D CSEM modelling python toolbox custEM (Rochlitz et al., 2023, 2021, 2019) was used to investigate multi-dimensional and topographic effects using realistic subsurface and topographic models. The effects on the horizontal and vertical components of fixed-loop TEM data and the vertical component of central-loop data are investigated. Central and fixed-loop setups show strong multi-dimensional effects, but only the fixed-loop setup experiences strong topographic effects due to the offset between transmitter and receiver (cf. Goldman et al., 1994). Nevertheless, topographic effects are found in the inversion results of both TEM setups. Since the first 3D TEM inversion algorithms in the early 2000s (e.g., Commer and Newman, 2004; Haber et al., 2007), the development has accelerated in recent years (e.g., Heagy et al., 2017; Liu et al., 2024; Oldenburg et al., 2013; Xiao et al., 2022).This opens up new possibilities for the application of the transient electromagnetic method. Setups such as the fixed-loop configuration, which are more influenced by multi-dimensional effects, can now be explored and additional components can be measured and interpreted. TEM3Dinv (Liu et al., 2024) was used to perform the 3D inversion of synthetic and field data to fully exploit both TEM data sets and obtain a single comprehensive model describing the interior of the Roter Kamm impact crater.

1.1. Structure of this Thesis

Chapters 2 and 3 present the theoretical background of the transient electromagnetic method and geophysical inversion techniques. The following chapter gives a brief introduction to the CRC 1211 with a focus on its geophysical work and explains in more detail the current knowledge about meteoritic impact craters and the Roter Kamm in particular. The chapter concludes with a description of the field survey and the equipment used in the Namib Desert at both survey sites. It includes a detailed description of the survey setups and the motivations for their design. Chapter 5 is entirely devoted to the AMT survey. It not only presents the data and the 2D inversion results, performed using MARE2DEM (Key, 2016), but also provides a brief introduction to the method and data processing. Chapter 6, introduces the TEM data processing and discusses systematic

errors caused by the system response and the incorrect approximation of an extended receiver loop by a point receiver. Based on these evaluations and the measured noise level, error models have been proposed for the 1D inversion of the single-loop and fixed-loop data. Chapter 7 describes the 1D inversions using EMUPLUS (e.g., Scholl, 2005) and first observations are made that a 1D inversion is not feasible for the TEM data sets of the Roter Kamm impact crater. Furthermore, the resolution of the lower boundary of a large conductive anomaly is compared for each EM method applied. Chapter 8 presents extensive synthetic 3D modelling and inversion studies. The studies discuss and compare the effects of topography and multi-dimensionality on central and fixed-loop TEM data. The feasibility of 3D inversion using only profile data is evaluated, the optimal parameters for reasonable inversion results are determined, and areas that may be distorted by topographic effects are identified. The specific advantages of central and fixed-loop TEM setups are compared, as well as their multi-component inversion. The thesis concludes with the 3D TEM inversions of the field data and a final evaluation of the quality of each inversion model. A final comparison of the TEM and AMT inversion models is made and the conductivity structures are fully described. Finally, the geophysical models are placed in the geological context of an impact crater and compared with studies of the Roter Kamm impact crater. The final chapter summarises the main findings of this thesis and presents perspectives for future work.

CHAPTER 2

The Transient Electromagnetic Method

Geology is the study of the solid Earth. Its aim is to understand the structure of the Earth's crust and surface. But it needs tools to map everything below the surface. Geophysical methods can be used to obtain information about this internal structure of the Earth by studying the physical parameters of rocks. The main focus of this work is the transient electromagnetic method. TEM is sensitive to conductive zones in the subsurface, which may be caused by metal ores or water. Therefore, it is often used in connection with groundwater studies, such as the detection of water-bearing aquifers and salt-water intrusions in coastal areas (e.g., Danielsen et al., 2003; Fitterman, 2014; Goldman et al., 1991; Ruiz-Aguilar et al., 2018) or mineral exploration (e.g., Cox et al., 2012; Lu et al., 2021; Yang et al., 2019; Zeng et al., 2019). However, it can also be used to map the surface of the solid rock beneath a sedimentary overburden (e.g., Blanco-Arrué et al., 2022; Jørgensen et al., 2003; Yogeshwar, 2014).

This chapter introduces the basics of electromagnetism and the TEM method. Detailed descriptions can be found in Ward and Hohmann (1988), Nabighian and Macnae (1988) and Spies and Frischknecht (1988). In addition, the audiomagnetotelluric method has been used to obtain complementary data. Both methods have the same physical background, and additional information about the AMT method can be found in Vozoff (1988) and Simpson and Bahr (2005). Table 2.1 lists the physical quantities and their units used in this thesis.

Table 2.1.: Physical variables and their symbols and units. Underlined characters represent vectors.

Variable	Symbol	Unit
Magnetic Field Intensity	$\underline{H}$	A/m
Magnetic Flux Density	$\underline{\mathrm{B}}$	$\mathrm{T} = \mathrm{Vs/m^2}$
Electric Field Intensity	$\underline{E}$	V/m
Electric Displacement Field	$\underline{D}$	$\mathrm{As/m^2}$
Electrical Charge Density	q	$\mathrm{As/m^3}$
Electric Current Density	$\underline{j}$	$\mathrm{A/m^2}$
Electric Current	I	A
Voltage	U	V
Electrical Conductivity	σ	S/m
Electrical Resistivity	$\rho = \frac{1}{\sigma}$	Ωm
Magnetic Permeability	$\mu = \mu_0\mu_r$	Vs/(Am)
Vacuum Permeability	μ_0	Vs/(Am)
Relative Magnetic Permeability	μ_r	dimensionless
Electrical Permittivity	$\epsilon = \epsilon_0\epsilon_r$	As/(Vm)
Vacuum Permittivity	ϵ_0	As/(Vm)
Relative Electrical Permittivity	ϵ_r	dimensionless
Frequency	f	Hz
Angular Frequency	ω	1/s
Wave Number	k	1/m
Time	t	s
Noise Level	η_ν	$\mathrm{V/m^2}$

2.1. Electrical Conduction

EM methods are sensitive to electrical conductivity, the inverse of electrical resistivity. Conductivity is a measure of how well a material conducts electrical currents, so it is important to understand the conduction mechanisms within the Earth. Currents can be transported by three different conduction mechanisms; electronic, dielectric and electrolytic conduction (Telford et al., 1990).

Electronic conduction is characterised by the free movement of electrons within a material, such as a metal, generating a current. However, typical rock-forming materials do not have enough free charges and this mechanism is negligible in most cases (Knödel et al., 2005). Dielectric conduction can also be neglected in the case of TEM and MT as it only occurs in very resistive or insulating materials in the presence of an external electric field (Telford et al., 1990).
The dominant conduction mechanism in EM methods is electrolytic conduction in semiconductors. Here, the charge is transported by ions in the pore fluid within the rock matrix. The pore fluid consists of water with dissolved salts. The conductivity of the pore fluid dominates the conductivity of porous rocks and sediments (e.g., Dentith and Mudge, 2014; Knödel et al., 2005). Even small amounts of water, e.g. thin layers of

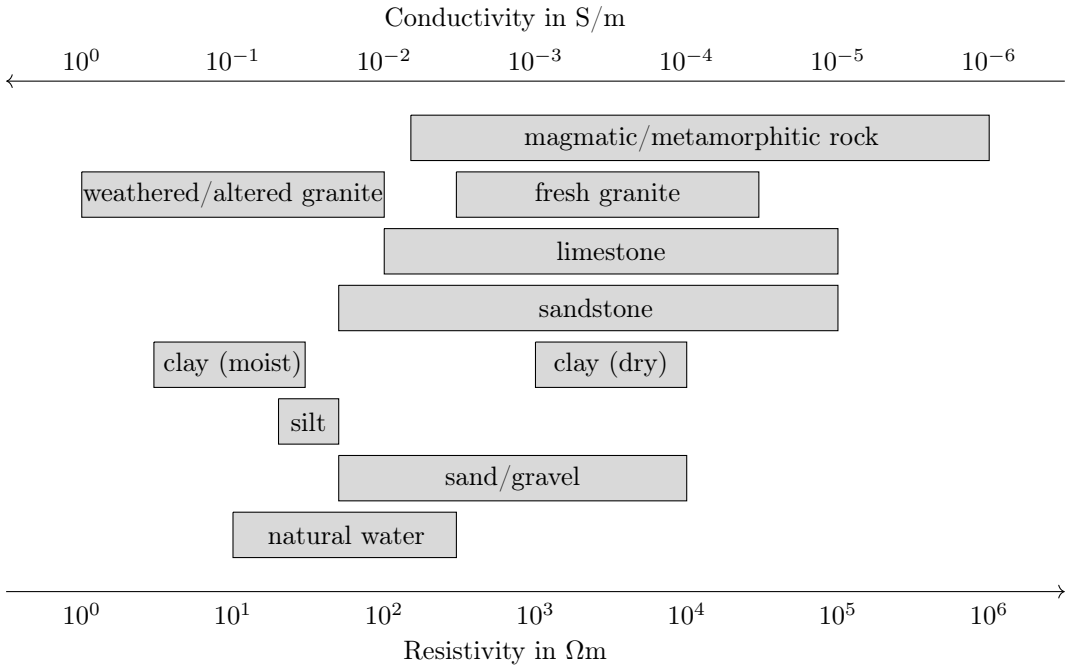

Figure 2.1.: Resistivity ranges of typical rocks in the southern Namib desert. Values taken form Ward (1997) and Knödel et al. (2005)

moisture around the rock matrix, can increase the conductivity by 4-5 decades (Knödel et al., 2005). Electrolytic conductivity is influenced by several factors such as porosity, degree of saturation and tortuosity. This is described for clay-free porous rocks by Archie (1942):

$$\rho_e = a\phi^{-m}S^{-n}\rho_W \tag{2.1}$$

The empirical law defines the resistivity of a saturated rock (ρ_e) as a function of the resistivity of the pore fluid (ρ_W), the effective porosity (ϕ), the degree of saturation (S), the saturation and cementation exponents ($n \approx 2$ and $1.3 \leq m \leq 2.4$) and a constant factor ($0.5 \leq a \leq 1$). In the presence of clay, the bulk resistivity decreases significantly and Archie's law no longer applies. Because clay has a high ion exchange rate, a bilayer is formed, resulting in an increased density of charge carriers near the surface of the clay minerals (Ward, 1997).

This paragraph shows that the conductivity of rock is highly dependent on its composition, pore space and water content. Therefore, only ranges of conductivity can be estimated for materials, not definitive values. As these ranges overlap, it is impossible to identify materials by their conductivity alone. A selection of conductivities of materials found in the Tsau //Khaeb (Sperrgebiet) National Park is shown in Figure 2.1.

2.2. The Maxwell Equations

The Maxwell equations are a set of uncoupled differential equations that describe electromagnetic fields. Their differential formulations are the following:

$$\nabla \cdot \underline{D} = q \tag{2.2}$$

$$\nabla \cdot \underline{B} = 0 \tag{2.3}$$

$$\nabla \times \underline{H} = \underline{j} + \frac{\partial \underline{D}}{\partial t} \tag{2.4}$$

$$\nabla \times \underline{E} = -\frac{\partial \underline{B}}{\partial t} \tag{2.5}$$

Gauss's law (Equation 2.2) states that the electric displacement field $\underline{D}$ has sources and sinks in the form of the electric charge density q, while the magnetic flux density $\underline{B}$ is source free (Equation 2.3). Ampere's and Faraday's laws (Equations 2.4 and 2.5) link the properties of magnetic and electric fields. Ampère's law describes how electric currents $\underline{j}$ and time-varying displacement currents induce a perpendicular magnetic field $\underline{H}$, and Faraday's law describes how a time-varying magnetic flux induces a perpendicular electric field $\underline{E}$. Maxwell's equation are coupled by the following three relations:

$$\underline{j} = \sigma \underline{E} \tag{2.6}$$

$$\underline{D} = \epsilon \underline{E} \tag{2.7}$$

$$\underline{B} = \mu \underline{H} \tag{2.8}$$

The first one is a formulation of Ohm's law (Equation 2.6), that expresses that the electric field intensity is linearly linked to the electric current density via the electric conductivity σ. The material equations (Equation 2.7 and 2.8) relate the electric and magnetic field intensities to the electrical displacement field and the magnetic flux densities by the electric permittivity $\epsilon = \epsilon_r \epsilon_0$ and magnetic permeability $\mu = \mu_r \mu_0$, respectively. In geophysical applications we assume linear, isotropic and homogeneous media and thus σ, ϵ and μ are independent of time, temperature and pressure. Furthermore, the relative magnetic permeability μ_r is assumed to be close to 1 and μ equals the magnetic permeability of free space μ_0. Additionally, no free charges exist in homogeneous media and Equations 2.2 and 2.6 yield to:

$$\nabla \cdot \underline{j} = 0 \tag{2.9}$$

Stating that the subsurface is source free.

2.2.1. Telegrapher's and Helmholtz Equations

Assuming $\underline{H}$ and $\underline{E}$ are piecewise continuous, a few transformations can yield to two differential equations, one for the magnetic and one for the electric field. Following steps are necessary:

- taking the curl of Equations 2.4 and 2.5
- substituting the mentioned conditions for μ, ϵ and σ valid for electromagnetic methods
- utilizing the vector identity $\nabla \times \nabla \times \underline{f} = \nabla \nabla \cdot \underline{f} - \nabla^2 \underline{f}$ together with Equations 2.3 and 2.9

The two gained equations are called the Telegrapher's equations:

$$\nabla^2 \underline{H}(t) = \mu\sigma \frac{\partial}{\partial t} \underline{H}(t) + \mu\epsilon \frac{\partial^2}{\partial t^2} \underline{H}(t) \tag{2.10}$$

$$\nabla^2 \underline{E}(t) = \mu\sigma \frac{\partial}{\partial t} \underline{E}(t) + \mu\epsilon \frac{\partial^2}{\partial t^2} \underline{E}(t) \tag{2.11}$$

Both equations have the same structure and henceforth $\underline{F}$ is used to denote either the electric or magnetic field intensity; $\underline{E}$ or $\underline{H}$. The Telegrapher's equations are stated in time domain and their Fourier transforms with respect to time are called the Helmholtz equations:

$$\nabla^2 \underline{F}(\omega) = \underbrace{(\imath\mu\sigma\omega - \mu\epsilon\omega^2)}_{\kappa^2} \underline{F}(\omega) \tag{2.12}$$

using $\partial \underline{F}(t)/\partial t = \imath\omega \underline{F}(\omega)$ for the time derivative with ω as the angular frequency. κ^2, the squared wave number, is consisting of two part; one is representing the conduction currents ($\imath\mu\sigma\omega$) and one the displacement currents ($\mu\epsilon\omega^2$). Considering the typical frequency range of EM methods ($f < 10^5$ Hz) and conductivities common in the Earth, the displacement currents are much smaller than the conduction currents:

$$\epsilon\omega << \sigma \tag{2.13}$$

Therefore, the displacement currents can be neglected and Equations 2.10, 2.11 and 2.12 simplify to:

$$\nabla^2 \underline{F}(t) = \mu\sigma \frac{\partial}{\partial t} \underline{F}(t) \tag{2.14}$$

$$\nabla^2 \underline{F}(\omega) = \imath\mu\sigma\omega \underline{F}(\omega) \tag{2.15}$$

This approximation is called the quasi-static or MT-approximation. The simplified Equation 2.14 and 2.15 are diffusion equations.

2.2.2. 1D Solutions for a Uniform Conductor

As mentioned earlier, EM methods are distinguished in frequency and time domain methods. Solutions to 2.14 and 2.15 are presented here for a 1D subsurface. One solution is for a harmonic time dependency $\exp(\imath\omega t)$ and for the impulsive electric and magnetic field at $z = 0$.

Plane Wave Solution

The harmonic Ansatz to solve a diffusion equation for a wave propagating in positive z-direction is (Ward and Hohmann, 1988):

$$\underline{F}(t) = \underline{F}_0 \exp\left[\imath\left(\omega t - kz\right)\right] \tag{2.16}$$

$\underline{F}_0$ is the amplitude and k is the wave number:

$$k = \alpha - \imath\beta = \sqrt{-\imath\omega\mu\sigma} \tag{2.17}$$

and

$$\alpha = \beta = \sqrt{\frac{\omega\mu\sigma}{2}} \tag{2.18}$$

Inserting Equation 2.17 into 2.16 the solution can be written in the following form:

$$\underline{F}(t) = \underline{F}_0 \exp\left[\imath\left(\omega t - \alpha z\right)\right] \exp\left(-\beta z\right) \tag{2.19}$$

The term including β represents the attenuation of the EM fields. The depth at which the EM wave is attenuated by a factor of $1/e$ is called skin depth. The skin depth is described by:

$$\delta_{FD} = \sqrt{\frac{2}{\omega\mu\sigma}} \tag{2.20}$$

The skin depth increases for lower conductivities and frequencies.

Step-Excitation Solution

To describe a sudden change in the electromagnetic fields, a Fourier transform to Equation 2.16 (Ward and Hohmann, 1988) can be calculated:

$$\underline{F}(t) = \underline{F}_0 \frac{(\mu\omega)^{1/2} z}{2\pi^{1/1} t^{3/2}} \exp\left(-\frac{\mu\sigma z^2}{4t}\right) \tag{2.21}$$

The maximum amplitude of the field occurs at a depth of:

$$\delta_{TD} = \sqrt{\frac{2t}{\mu\sigma}} \tag{2.22}$$

This depth is called the diffusion depth. Note that the diffusion depth decreases with increasing conductivity and earlier times. The form of the diffusion depth is very similar to the skin depth (Eq. 2.20), only the dependencies on frequency and time are different. The velocity of the maximum is given by the time derivative of the diffusion depth:

$$v = \sqrt{\frac{1}{2\mu\sigma t}} \tag{2.23}$$

The velocity also shows that the EM fields travel slower in conductive media.

2.3. Transient Electromagnetics (TEM)

Step excitation of EM fields is the integral characteristic of time domain methods. The pulse generated by an abrupt switch-off or switch-on of an electric current in the transmitter causes the primary magnetic field to collapse, inducing eddy currents in a conductor according to Faraday's law (Equation 2.5). The orientation of these eddy currents depends on the shape of the conductor. In a sheet-like conductor, eddy currents can only flow in the plane of the sheet, whereas in a spherical conductor the direction of the primary field is decisive. The temporal behaviour of the eddy currents is identical for all conductor shapes (Figure 2.2). Initially, eddy currents are induced only at the surface, producing a magnetic field identical to the primary field (early time). However, ohmic losses (e.g. heat) cause a decrease in current strength and hence a change in the secondary magnetic field. This change in time leads to an inward diffusion of eddy currents (intermediate time). Eventually, an almost stable current distribution is reached (late stage) and only the amplitude of the magnetic field decreases. This diffusion process depends

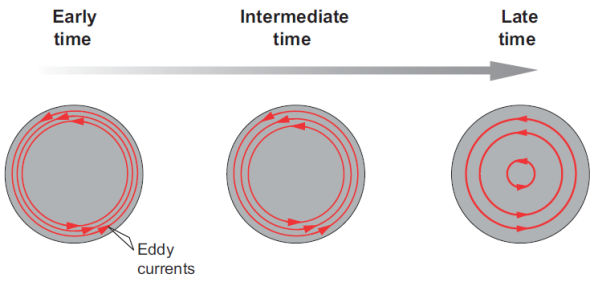

Figure 2.2: Eddy current distribution with time in a spherical conductor. Taken from (Dentith and Mudge, 2014).

on the conductivity of the conductor. A high resistivity leads to a fast diffusion process due to high ohmic losses, whereas a low resistivity leads to a slow decay of the secondary magnetic field. Therefore, observing the magnetic field can provide information about the conductivity distribution in the subsurface.

Time domain methods differ in their transmitter-receiver geometry. Systems where the receiver is inside or close to the transmitter are called short-offset TEM (SHOTEM). If the transmitter-receiver offset is greater than the diffusion depth (Eq. 2.22), the method is called long-offset TEM (LOTEM). In this thesis, TEM refers only to the short-offset variant of transient electromagnetic methods.

2.3.1. Diffusion of Electromagnetic Fields

Typically, TEM uses a horizontal loop as a transmitter. A current is injected into the transmitter and abruptly switched off, triggering an induction process in the subsurface. The resulting diffusion of EM fields is well described by the smoke ring concept of Nabighian (1979) in homogeneous half-spaces.

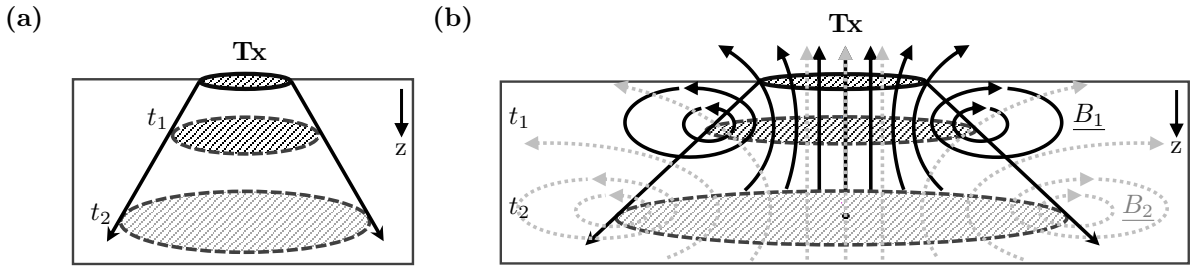

Figure 2.3.: Diffusion of the electric and magnetic field into the earth for a circular loop transmitter Tx. t_1 and t_2 ($t_1 < t_2$) indicate different diffusion times after the transmitter is switched off. B_1 and B_2 are the corresponding magnetic fields. **(a)** Smoke ring concept describing the current sheets moving downwards with time. Modified from Nabighian (1979). **(b)** Equivalent current sheets at two different diffusion times and the resulting magnetic fields. Modified from Nabighian and Macnae (1988).

The concept describes that at t = 0, when the transmitter current is switched off, eddy currents are induced in the surface of the homogeneous Earth in the exact shape of the transmitter loop (Nabighian and Macnae, 1988). Due to the high resistivity contrast between air and the Earth's materials, these eddy currents must be horizontal (Ward and Hohmann, 1988; Weidelt, 1986). The eddy currents move outwards and downwards at a 30° angle with time (Figure 2.3a). To describe the time derivative of the magnetic field, which is often measured in field surveys, all induced eddy currents can be approximated by an equivalent current filament that moves outward and downward like the smoke rings,

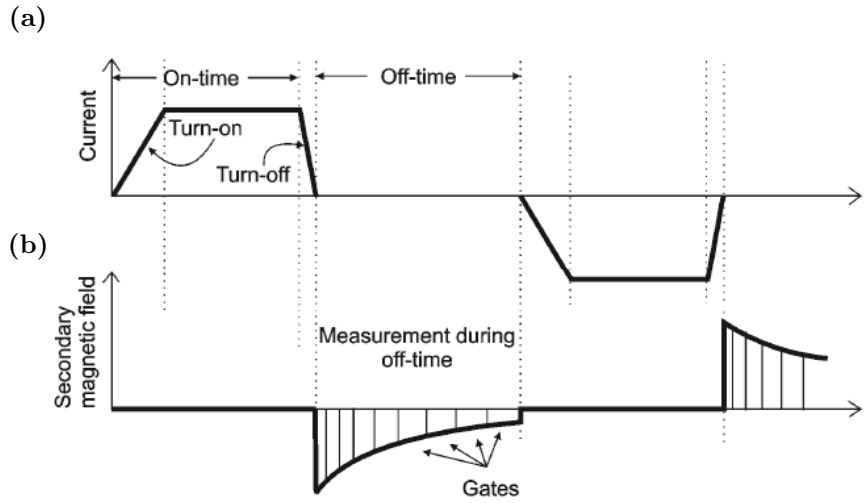

Figure 2.4: **(a)** Time-dependent transmitted current signal and **(b)** induced voltage behaviour measured at the receiver. Modified from Christiansen et al. (2006).

but at a 47 ° angle (Figure 2.3b). The velocity and depth of the downward motion are given by the equations 2.23 and 2.22. At all times, these eddy currents generate secondary magnetic fields that can be measured at the surface (Figure 2.3b).

2.3.2. TEM Surveys

In the field TEM measurements are often realised using a square loop as a transmitter and conductor loops or induction coils as receiver. These receiver types measure the induced voltage. The induced voltage U_{ind} is connected to the time derivative of the magnetic field $\frac{\partial \underline{B}}{\partial t}$ in the following way for a coil:

$$U_{ind} = -\frac{\partial}{\partial t} \int_{\underline{A}} N \underline{B} d\underline{A} \tag{2.24}$$

A voltage is only induced, if the magnetic flux ($\Phi = \underline{BA}$) passing through the area of the coil $\underline{A}$ with turns N is changing with time, by either a time varying magnetic field or coil area. In case of TEM, the magnetic field is decaying with time and the induced voltage can be measured after the collapse of the primary magnetic field (Figure 2.4).

This process is repeated multiple time by using a transmitter current with a rectangular wave form. A common rectangular wave form is a 50 % duty cycle, where the current is switched on and off with a selected base frequency and alternating polarity (Figure 2.4a). Exemplary, a 50 %-duty-cycle using a base frequency of 0.5 Hz and alternating polarity is shown in Figure 2.5.

Source-Receiver-Geometries and Survey Modes

Different transmitter-receiver geometries can be realised; single-loop, coincident-loop, central-loop and separate-loop (Figure 2.6a to d).

The simplest geometry is the single-loop configuration, where a single loop of wire is used as both transmitter and receiver. Coincident loops differ in that there are two cables, one for the transmitter and one for the receiver. The central-loop setup is similar to these setups, but the receiver is much smaller in size and can also be an induction coil, placed in the centre of the transmitter loop. A receiver unit can also be placed anywhere

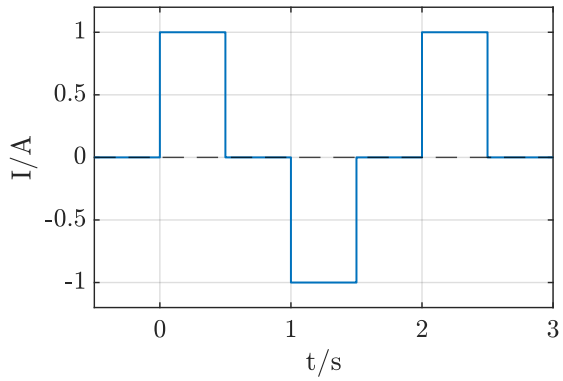

Figure 2.5: 50 %-duty-cycle using a base frequency of 0.5 Hz and a transmitted current strength of 1 A.

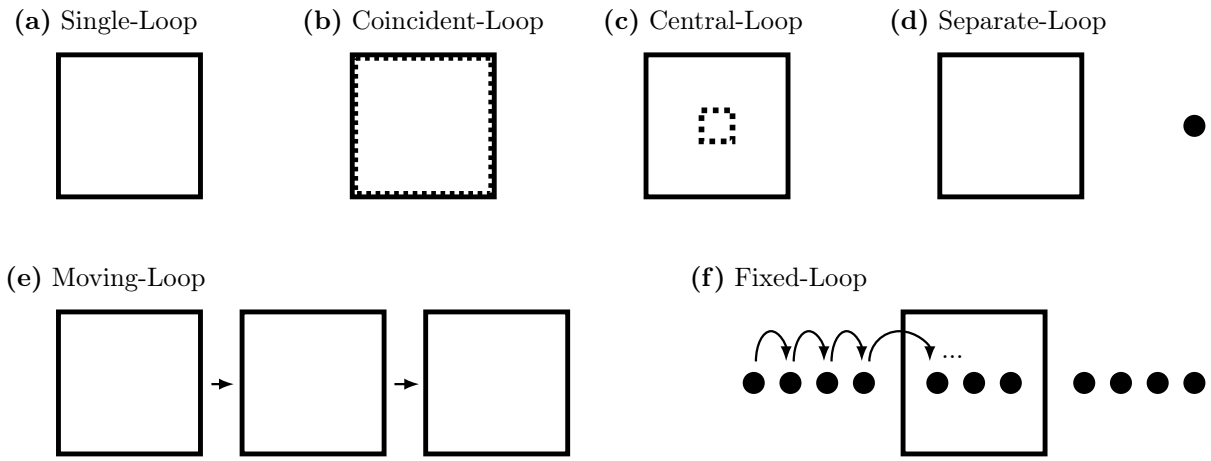

Figure 2.6.: TEM configurations (a) to (d) and measuring modes (e) and (f).

inside or outside the transmitter loop. This geometry is called separate-loop. The data from this setup is not as easy to interpret as the single, coincident or central-loop data. While the vertical component of those always has one polarity for a 1D subsurface, the vertical components of separate-loop data with receivers outside the transmitter loop have a change in polarity. This can be explained by the figure 2.3b. As the equivalent current filaments move outwards and downwards, they pass below the receiver location at a point in time. Therefore the sign of the magnetic field and its derivative change at this time point. Figure 2.7 shows the induced voltage U_{ind} decay with time t at different transmitter-receiver offsets. The time of sign reversal becomes later as the offset increases because the locus of the electric field has to travel farther. In addition, the magnetic field has horizontal components outside the loop (see Figure 2.3b) which are not present in the centre of the loop.

Depending on the chosen transmitter-receiver geometry, TEM data of a whole area can be collected in two modes: the moving loop mode and the fixed-loop mode. The former is used for single, coincident and central-loop measurements, the latter for separate-loop measurements with multiple receiver locations and offsets, but one stationary transmitter. Both modes have advantages and disadvantages (Dentith and Mudge, 2014): The moving loop layout has good vertical resolution, but a fixed-loop survey can better resolve the shapes of the conductors due to multiple strong magnetic field components. Fixed-loop

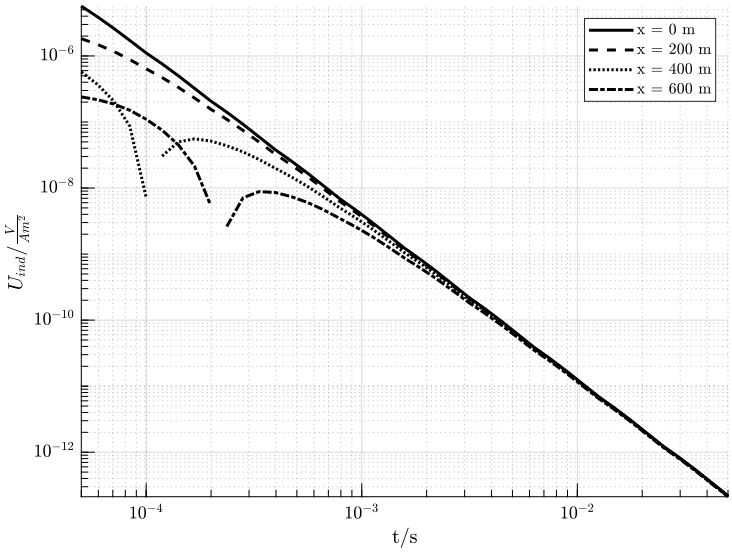

Figure 2.7: Induced voltage at different transmitter-receiver offsets for a 100 Ωm homogeneous halfspace for a transmitter loop size of 200 m x 200 m and its center located at x = 0 m.

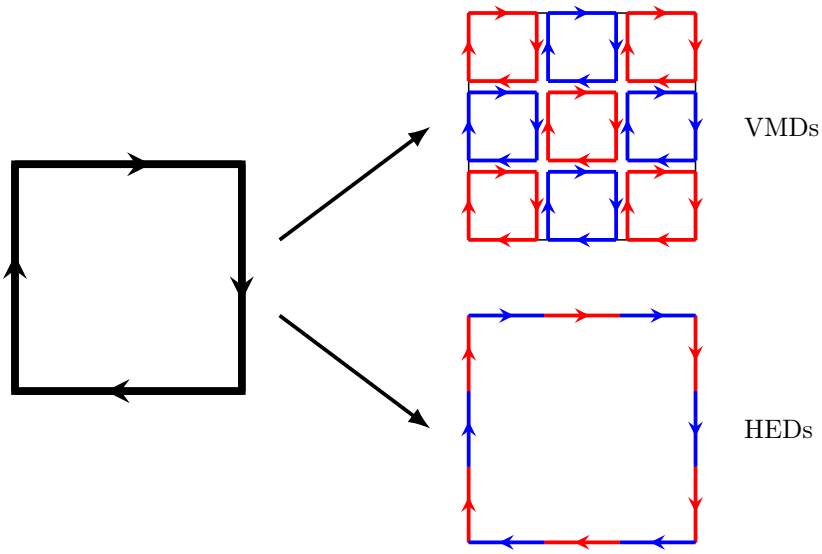

Figure 2.8: Square loop source transmitter as a superposition of VMDs and HEDs. The current direction is indicated by the arrow heads. The different colors only aim to distinguish between neighbouring dipoles.

surveys are better for areas with a known strike direction, and moving-loop surveys are good for any area with unknown geometry.

2.3.3. Solving One-Dimensional Problems in TEM

The source geometry is a crucial factor for the shape of the EM fields. In TEM the transmitter is an inductively coupled loop transmitter. The EM fields of a loop transmitter can be calculated by superposing elementary dipoles, either vertical magnetic dipoles (VMD) or horizontal electric dipoles (HED) (e.g., Kaufman and Keller, 1983; Ward and Hohmann, 1988; Weidelt, 1986).

Figure 2.8 presents the superposition of elementary coils or dipoles to adapt a loop. The VMDs are integrated over the whole loop area with the internal currents cancelling each other, so that only a current along the edge of the loop remains (Weidelt, 1986). The VMDs are arranged along the edge directly. Both ways lead to the same result, as the solution for the vertical magnetic field at the broadside of a HED has the same form as for the VMD, as the galvanic terms become irrelevant (Ward and Hohmann, 1988). However,

solutions cannot be calculated analytically, but only approximated numerically for a one- or multi-dimensional case.

Homogeneous Halfspace

Nevertheless, the uniform conducting halfspace solution for a circular loop can be found analytically. It is a good approximation for a square loop with an identical area coverage, if the receiver is placed in the center or in a large enough distance from the transmitter cable (Ward and Hohmann, 1988). An analytical solution only exists in the center of the said loop. The vertical magnetic field component can be described by the following equation (Spies and Eggers, 1986; Spies and Frischknecht, 1988):

$$H_z = \frac{I}{a^3 \sigma \mu_0} \left[\frac{6}{\sqrt{\pi}} \Theta a \exp(-\Theta^2 a^2) + \left(2\Theta^2 a^2 - 3\right) \operatorname{erf}(\Theta a) \right] \tag{2.25}$$

a is the radius of the loop and

$$\Theta a = \frac{a}{\sqrt{2}\delta_{TD}} \tag{2.26}$$

the induction number. $\operatorname{erf}(\Theta a)$ denotes the *gaussian error function*

$$\operatorname{erf}(\Theta a) = \frac{2}{\sqrt{\pi}} \int_0^{\Theta a} e^{-x} dx \tag{2.27}$$

To use this solution for a square loop transmitter the radius can be replaced by the radius a square loop would have, if it would be a circular loop with the identical size A. The voltage response can be found in Spies and Eggers (1986):

$$U_z = -\frac{N A_{Rx} I}{\sigma a^3} \left[3\operatorname{erf}(\Theta a) - \frac{2}{\sqrt{\pi}} \Theta a (3 + 2\Theta^2 a^2) \exp(-\Theta^2 a^2) \right] \tag{2.28}$$

N is the number of turns of the receiver coil and A_{Rx} its area. This solution can be approximated (Spies and Eggers, 1986) for early ($t \to 0$ and $\Theta a \gg 1$)

$$U_z^e = -\frac{3INA_{Rx}}{\sigma a^3} \tag{2.29}$$

and late times ($t \to \infty$ and $\Theta a \ll 1$):

$$U_z^l = -\frac{I\sigma^{3/2}\mu_0^{5/2} a^2 N A_{Rx}}{20\pi^{1/2} t^{5/2}} \tag{2.30}$$

The early-time approximation is directly linear to the inverse of the electrical conductivity, the resistivity. The late-time approximation, however, is proportional to $\sigma^{3/2}$ and $\mathrm{t}^{-5/2}$. From these equations the solutions for the early and late-time apparent resistivities can be obtained by rearranging them:

$$\rho_a^e = -\frac{a^3}{3INA_{Rx}} U_z^e \tag{2.31}$$

$$\rho_a^l = -\frac{I^{2/3}\mu_0^{5/3} a^{4/3}}{20^{2/3}\pi^{1/3} t^{5/3}} \left(\frac{U_z^l}{NA_{Rx}} \right)^{-2/3} \tag{2.32}$$

The apparent resistivities represent a mean resistivity value at each time step. This mean value represents the resistivity that a homogeneous halfspace would have at that time and induced voltage amplitude. It is equal to the true resistivity of the subsurface if the subsurface is homogeneous. This transformation reduces the dynamic range of the data and normalises it in a way that makes it comparable to measurements made with other loop or receiver sizes (Spies and Frischknecht, 1988). However, although it can be useful for a first impression of the subsurface, it must be used with care to avoid misinterpretation.

Layered Conducting Halfspace

Unlike the uniformly conducting halfspace, there is no analytical solution for the layered conducting halfspace and it cannot be approximated by a simpler source geometry. However, various approaches can be used to find numerical solutions to this problem. In the following section I will concentrate on the approach based on the HED solutions (Weidelt, 1986). It is used in the one-dimensional forward and inversion algorithm EMUPLUS developed at the University of Cologne, which is used in this thesis.
To find solutions for the EM field of a HED, Weidelt (1986) uses Debye potentials. Debye potentials describe divergence-free vector fields by scalar potentials corresponding to their toroidal and poloidal parts. It is possible to determine Debye potentials that obey Maxwell's equations (Equations 2.2 - 2.5) and can be used to derive the magnetic and electric fields. Each Debye potential is related to either the tangential electric (TE) or tangential magnetic (TM) polarisation in a horizontally layered halfspace. In the TE mode of EM fields there is no vertical electric field component and in the TM mode there is no vertical magnetic field component. Only the TE mode is required to calculate the fields of the TEM loop source transmitter as it is derived from the poloidal Debye potential.

The solution of the vertical magnetic field for a point HED looks the following at the surface ($z = 0$) in frequency domain (Weidelt, 1986):

$$H_z(\underline{r}, t) = \frac{D_0}{4\pi}\left[\frac{1}{r^2} - \int_0^\infty \frac{B_E(k) - k}{B_E(k) + k} k J_1(k\underline{r}) dk\right] \sin(\phi) \tag{2.33}$$

$\underline{r}$ is the distance between transmitter and receiver, D_0 the dipole moment, B_E the admittance, J_1 a Bessel function of first order and ϕ the angle between the dipole axis and $\underline{r}$.
By applying the inverse fourier transform and using Eq. 2.8 and 2.24 a time domain solution for the induced voltage can be found (Petry, 1987):

$$U_z(\underline{r}, t) = -\frac{1}{2\pi}\int_{-\infty}^{\infty} \mu_0 A_{Rx} e^{i\omega t} \frac{D_0 \sin(\phi)}{4\pi} \int_0^\infty \frac{B_E(k) - k}{B_E(k) + k} k J_1(k\underline{r}) dk d\omega \tag{2.34}$$

A square or rectangular loop source transmitter can be constructed using either VMDs or HEDs. If the horizontal electric dipole is used, the magnetic field components can be calculated by integrating HEDs along the path of the transmitter edge (Figure 2.8). In the case of a one-dimensional subsurface, the calculation of one HED is sufficient, the remaining HEDs can be calculated by coordinate transformations (Rätz, 2000).
The integral over the Besselfunction cannot be solved analytically, but can be solved numerically using a fast Hankel transform. Details can be found in Weidelt (1986).

2.3.4. Depth of Investigation

A crucial point in interpretation is the estimation of the maximum reliable depth that contains usable information, called the depth of investigation (DOI). Estimates based on diffusion depth can be made (Meju, 1994), but these neglect aspects such as noise level and transmitter power. (Spies, 1989) defines the DOI as the depth at which the measured signal decays into the noise level:

$$d_{doi} = 0.55 \cdot \left(\frac{IA}{\bar{\sigma}\eta_\nu} \right)^{1/5} \tag{2.35}$$

with:

$$\bar{\sigma} = \frac{1}{d_{doi}} \int_0^{d_{doi}} \sigma(z) dz \tag{2.36}$$

The DOI is a function of the transmitter area A, the transmitted current I, the noise level η_ν and the average electrical conductivity $\bar{\sigma}$. Two of these parameters can be selected depending on the target depth. For a deep investigation a large loop with a high current is needed, but for a shallow investigation a small loop is likely to be sufficient and more practical. These aspects should be considered when planning a field survey and can influence not only the size of the transmitter but also the chosen transmitter-receiver geometry and survey mode.
To avoid overestimation, Yogeshwar (2014) suggested that the true survey depth may be only 70 % of this value. For this thesis an even lower value of only 50 % of the definition of Spies (1989) is used, as otherwise the DOI would be clearly overestimated.

2.3.5. Multidimensional Problems for TEM

Multidimensional problems cannot be solved analytically and require numerical methods. However, these require significant time and computational resources. Therefore, it is important to assess the dimensionality of the data set in the early stages of data interpretation and evaluation.
An easy way to do this for magnetotelluric datasets is to use the knowledge of field distributions in a homogeneous or layered conductive subsurface. In MT it is assumed that only horizontal magnetic field components exist in such a case, so a vertical magnetic field would be a direct indicator of a lateral conductivity variation in the Earth. A vertical magnetic field occurs only in the vicinity of a lateral conductivity contrast, is strongest immediately adjacent to the contrast. It changes polarity depending on whether it is in the more or less resistive medium. The Tipper, also known as the magnetic field transfer function, describes the relationship between the vertical and the two horizontal magnetic field components (Simpson and Bahr, 2005). It can be plotted as induction arrows on a 2D map to locate zones of higher conductivity. Two conventions are used for such representation; the Wiese convention, where the induction arrows point away from good conductors, and the Parkinson convention, which points towards good conductors.

This concept can also be applied to central-loop TEM measurements. In the case of TEM, the magnetic field at the centre of the transmitter loop is purely vertical over a one-dimensional subsurface. Horizontal components occur only in the presence of lateral conductivity changes. MT and central-loop TEM are similar in this respect, although the

field components are different. In the case of TEM, the Tipper defines the relationship between the horizontal and vertical field components and is defined as follows for magnetic fields (Spies and Frischknecht, 1988):

$$T_H(t) = \frac{H_r(t)}{H_z(t)} \tag{2.37}$$

and induced voltages (Spies and Frischknecht, 1988):

$$T_U(t) = \frac{U_r(t)}{U_z(t)} \tag{2.38}$$

Spies and Frischknecht (1988) suggest a value of 0.1 as the limit to distinguish between a one and a multidimensional subsurface; higher values indicate a multi- and lower value a one-dimensional subsurface.

Any lateral conductivity variation causes a distortion of the horizontally induced current systems, therefore it is easy to observe 2D/3D effects in a fixed-loop TEM setup as an asymmetry of transient responses can be observed at a fixed distance on each side of the transmitter loop.

CHAPTER 3

Inversion Theory

Geophysical methods aim to map the physical parameters of the subsurface in order to better understand the structure and evolution of the Earth. Therefore, it is necessary to find models of the subsurface based on measured geophysical data. Section 2.3.3 briefly described how to calculate electromagnetic fields or induced voltages from a given one-dimensional model for the desired transmitter. The prediction of data is called forward calculation, while the calculation of a model from given data is called inversion. Inversions are much more time-consuming than solving the forward problem, because inversions consist of a large number of forward calculations. The geophysical inverse problem is non-linear and a solution can only be approximated by numerical iteration schemes.

This chapter introduces the inverse problem and several methods used in this thesis, such as Gauss-Newton based algorithms. For this thesis, 1D Marquardt-Levenberg and Occam inversions were performed using the EMUPLUS inversion algorithm (e.g., Scholl, 2005). The 3D inversions were performed with the regularised Gauss-Newton based TEM3DInv (Liu et al., 2024).

3.1. The Inverse Problem

The prediction of data of a given model is expressed in the following way:

$$\underline{d} = \mathbf{g}(\underline{m}) \tag{3.1}$$

$\underline{d}$ is a vector including all N data points:

$$\underline{d} = (d_1, d_2, ..., d_N) \tag{3.2}$$

and $\underline{m}$ contains all M model parameter such as resistivities or layer thicknesses:

$$\underline{m} = (m_1, m_2, ..., m_M) \tag{3.3}$$

$\mathbf{g}$ are the forward functions, also called forward operators. Solving this problem for m is not trivial as it is often not well-posed and the solution is non-unique. The inverse

problem can be overdetermined ($N > M$) and one set of model parameters leads to multiple data predictions, or underdetermined ($M > N$) and multiple models can represent a single data prediction. However, most geophysical problems are mixed-determined, so that some model parameters are overdetermined and others underdetermined. This group of problems is called ill-posed because unique and stable solutions cannot be found (Zhdanov, 2002).

3.2. The Weighted Least-Square Method

One way to find a suitable model describing the measured data, is by minimizing the predicted data error $\underline{e}$ (Menke, 2018):

$$\underline{e} = \underline{d}_{obs} - \underline{d}_{pred} \tag{3.4}$$

Here $\underline{d}_{pred}$ is the predicted data and $\underline{d}_{obs}$ the observed data in the field. The best fitting model can be found by minimizing the length of the predicted error. Commonly used measures are the L-norms, which are characterised by different exponents n of the individual elements during the summation (Menke, 2018):

$$||f||_{L_n} = \left(\sum_{i=1}^{N} |\underline{e}|^n \right)^{(1/n)} \tag{3.5}$$

The results of the L-norms are affected differently by outliers. The higher the exponent n of the L-norm, the greater the influence of each individual outlier on the result. The L_1-norm is considered the most robust, as outliers have the same weight as any other observed data point. Typically, the L_2-norm is chosen because it is assumed that the data points are normally distributed and the L_2-norm follows the Gaussian statistic (Menke, 2018). This method is then called the *least-squares method*.
Further, it is useful to consider the error in the minimizing problem in form of weights. In this thesis, the data fit is evaluated by using the error-weighted root-mean-square (wRMS) or χ-value (e.g., Chave and Jones, 2012; Constable et al., 1987):

$$\chi = \sqrt{\frac{1}{N} \sum_{i=1}^{N} \frac{\left(d_i^{pred} - d_i^{obs} \right)^2}{\delta d_i^2}} \tag{3.6}$$

A predicted model is well-fitted once the χ-value reaches a value of 1, indicating that the difference between the predicted and the observed data, $\underline{d}^{pred}$ and $\underline{d}^{obs}$, has the same size as the observed data error $\delta \underline{d}$.
The problem that has to be minimized is called the cost-function (Meju, 1994):

$$\Phi_d = (\underline{d}_{obs} - \mathbf{g}(\underline{m}))^T \, \underline{\underline{W}}_d^2 \, (\underline{d}_{obs} - \mathbf{g}(\underline{m})) \tag{3.7}$$

The weighting of the cost-function is realized by a matrix $\underline{\underline{W}}_d$ containing the inverses of the data errors:

$$W_{d,ii} = \frac{1}{\delta d_i}; \qquad i = 1, 2, .., N \tag{3.8}$$

The values along the main diagonal of the weighting matrix are the inverse of the observed data errors $\delta \underline{d}$. In general the geophysical inverse problems are not linear and solving the minimization problem is not straight forward.

3.3. Non-Linear Inversion Approaches

This section describes two different approaches to overcome the non-linearity of the forward operator $\mathbf{g}$. Both methods are iterative and require several iteration steps to approximate a well-fitted solution. The steepest decent method uses knowledge of the gradient, while the Gauss-Newton method approximates the forward operator to minimise the cost function.

3.3.1. The Gauss-Newton Method

Linearisation of the cost function can be achieved using either Newton's method (Menke, 2018; Zhdanov, 2002) or the Gauss-Newton method (Chave and Jones, 2012; Meju, 1994). Both use the Taylor theorem, which states that a function can be approximated by its derivatives around a trial solution. In the case of the Newton method the Taylor theorem is applied to the cost function up to the third derivative, in the case of the Gauss-Newton method it is applied directly to the non-linear forward operator $\mathbf{g}$.
The forward operator is approximated by the first order Taylor series expansion:

$$\mathbf{g}(\underline{m}) \approx \mathbf{g}(\underline{m}_0) + \left.\frac{\partial \mathbf{g}}{\partial \underline{m}}\right|_{\underline{m}=\underline{m}_0} \underbrace{(\underline{m} - \underline{m}_0)}_{\Delta \underline{m}} + \ldots \tag{3.9}$$

This approximation includes only the first Fréchet derivative of $\mathbf{g}$:

$$[\underline{\underline{J}}](\underline{m}_0)_{ij} = \left.\frac{\partial g_i(\underline{m})}{\partial m_j}\right|_{\underline{m}=\underline{m}_0} \tag{3.10}$$

This $(N \times M)$ matrix $\underline{\underline{J}}$ is called Jacobi-Matrix and contains the derivatives of $\mathbf{g}$ with respect to each model parameter. It is also called the sensitivity matrix in geophysics, as it its value are a measure how sensitive the forward operator is against small perturbations of the model parameter. For well resolved parameters the values are high, for poorly resolved values small.
The linearised cost-function (Equation 3.7) has following shape:

$$\Phi_d(\underline{m}) \approx \left(\underline{d}_{obs} - \mathbf{g}(\underline{m}_0) - \underline{\underline{J}}\Delta\underline{m}\right)^T \underline{\underline{W}}_d^2 \left(\underline{d}_{obs} - \mathbf{g}(\underline{m}_0) - \underline{\underline{J}}\Delta\underline{m}\right) \tag{3.11}$$

$$= \left(\underline{e} - \underline{\underline{J}}\Delta\underline{m}\right)^T \underline{\underline{W}}_d^2 \left(\underline{e} - \underline{\underline{J}}\Delta\underline{m}\right) \tag{3.12}$$

This approximation is parabolic, hence, a unique minimum exists. However, it is necessary to repeatedly apply this approximation to get a model satisfying the termination criterion (Figure 3.1a). The minimum of this function can be calculated by finding $\frac{\partial \Phi_d}{\partial \Delta \underline{m}} \stackrel{!}{=} 0$:

$$\frac{\partial \Phi_d}{\partial \Delta \underline{m}} = -2\underline{\underline{J}}^T \underline{\underline{W}}_d^2 \underline{e} + 2\underline{\underline{J}}^T \underline{\underline{W}}_d^2 \underline{\underline{J}}\Delta\underline{m} = 0 \tag{3.13}$$

Each time a model update is calculated:

$$\Delta\underline{m}_k = \underline{m}_{k+1} - \underline{m}_k = \left[\underline{\underline{J}}^T \underline{\underline{W}}_d^2 \underline{\underline{J}}\right]^{-1} \underline{\underline{J}}^T \underline{\underline{W}}_d^2 \left(\underline{d} - \mathbf{g}(\underline{m}_k)\right) \tag{3.14}$$

However, choosing an appropriate starting model is crucial to avoid getting trapped in a local instead of the global minimum. Figure 3.1a illustrates the Gauss-Newton method

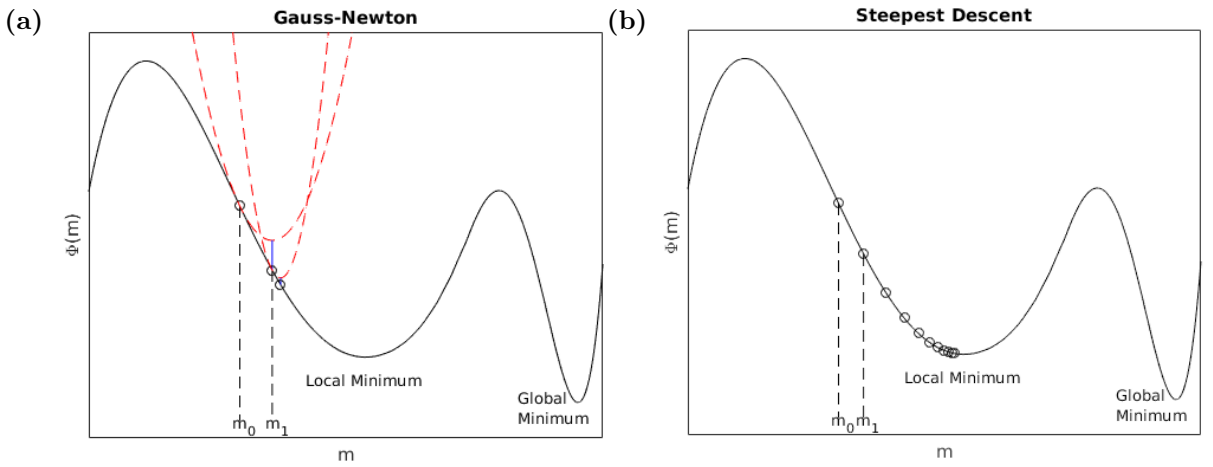

Figure 3.1.: Iterative search for the best-fit model at the global minimum of the cost function $\Phi(m)$. This shows an unfortunate choice of initial model, as the closest minimum in the right direction of the cost function is a local one. Both sketches are 2D projections of 3D space. **(a)** The Gauss-Newton method approximates the cost function at each position with a parabolic function and determines the model at the minimum. This model is the location of the next parabolic approximation. **(b)** The steepest decent method searches for the minimum of the cost function in the direction of the gradient until it finds a minimum. Taken from Mörbe (2020)

and how parabolic approximations at each iteration yield to a new approximation closer to the minimum than the previous one. However, it also shows how it can easily get trapped in a local instead of the global minima by the unlucky choice of starting model.

The Gauss-Newton method cannot be solved when the inverse of the matrix product $\underline{\underline{J}}^T \underline{\underline{W}}_d^2 \underline{\underline{J}}$ is ill-conditioned or singular. Regularisation is a way to condition the cost-function in a way to ensure that a model can be found, that solves the inverse problem (Tikhonov and Arsenin, 1977). In the sections 3.4 and 3.5 two different approaches based on the Gauss-Newton method are describe: the Marquardt-Levenberg and the Occam inversions.

3.3.2. The Steepest Decent Method

The method of the steepest decent is another iterative method that searches for the optimal model by moving in the direction of the strongest decrease of the cost function, the gradient. The gradient of the cost-function is (Sen and Stoffa, 2013):

$$\underline{r}_k = \frac{\partial \Phi_d}{\partial \underline{m}_k} = -2\underline{\underline{J}}^T \underline{\underline{W}}_d^2 \left(\underline{d} - \mathbf{g}(\underline{m}_k)\right) \tag{3.15}$$

Therefore, the predicted model after each step is defined as (e. g., Sen and Stoffa, 2013; Zhdanov, 2002):

$$\underline{m}_{k+1} = \underline{m}_k + \alpha_k \underline{r}_k \tag{3.16}$$

with α_k being the step size. Therefore, the model update is:

$$\Delta \underline{m}_k = -2\alpha_k \underline{\underline{J}}^T \underline{\underline{W}}_d^2 \left(\underline{d} - \mathbf{g}(\underline{m}_k)\right) \tag{3.17}$$

The step size is crucial for convergence. A large step size results in fast convergence, but may miss the minimum. A small step size, on the other hand, has a very slow convergence

rate. So it is optimal to start with a large step size, which decreases as the number of iterations increases. A step size can be determined by a line search. At each iteration step, the updated cost functions can be minimised with respect to the step size (Sen and Stoffa, 2013):

$$\frac{\delta\Phi_d}{\delta\underline{\alpha}_k} = \frac{\delta\Phi_d}{\delta\underline{m}_k}^T \frac{\partial}{\partial\alpha_k}\underline{m}_k = \underline{r}_k^T\underline{r}_{k-1} \stackrel{!}{=} 0 \tag{3.18}$$

This shows that each new step is perpendicular to the previous one. Figure 3.1b shows how the steepest decent method approaches the minimum by following the direction of the gradient to the next better solution depending on the step length. It is obvious how a smaller step size contributes to a more accurate solution. However, the steepest decent still has a low convergence rate for higher iterations. To overcome this weakness, the Conjugate Gradient (CG) method can be used (Rodi and Mackie, 2001).

3.4. Marquardt-Levenberg Inversion

The Marquardt-Levenberg method is a modification of the Gauss-Newton method (Section 3.3.1). As only the first two terms of the Taylor series are considered, the approximated cost function has the shape of a parabola. However, that is not true for Φ_d of non-linear problems, especially when not in the vicinity of the minimum (Marquardt, 1963). Levenberg (1944) proposed a damping factor to minimize the effect of the inaccurate approximation of the cost function by the Taylor series. Marquardt (1963) formulated an algorithm based on this suggestion. The modified cost function has the following form (Meju, 1994):

$$\Phi = \Phi_d + \lambda^2\Phi_m = \left(\underline{e} - \underline{\underline{J}}\Delta\underline{m}\right)^T \underline{\underline{W}}_d^2 \left(\underline{e} - \underline{\underline{J}}\Delta\underline{m}\right) + \lambda^2\underline{m}^T\underline{m} \tag{3.19}$$

and the new model update is:

$$\Delta\underline{m} = \left(\underline{\underline{J}}^T\underline{\underline{W}}_d^2\underline{\underline{J}} + \lambda^2\underline{\underline{I}}\right)^{-1} \underline{\underline{J}}^T\underline{\underline{W}}_d^T\underline{\underline{W}}_d\underline{e} \tag{3.20}$$

For optimal damping, the Lagrangian multiplier λ must be small when the Taylor series is a suitable approximation, especially when close to the real minimum (Marquardt, 1963). However, large λ can be used for fast convergence in early iterations. This behaviour is close to that of the steepest decent method (Marquardt, 1963). Thus, the Maquardt-Levenberg method combines the advantages of the steepest decent gradient method and the Gauss-Newton method.
Typically only a limited number of layers are used for this inversion scheme, as both layer thickness and resistivity are included in the model parameters. It is crucial to use an appropriate initial model as it will strongly influence the result. Therefore, prior knowledge of the subsurface, e.g. from other geophysical surveys or other inversion methods such as the Occam inversion (Section 3.5), is advantageous.

3.4.1. Singular Value Decomposition

To calculate the inverse of matrices the *sigular value decomposition (SVD)* can be used. Any $(N \times M)$ matrix, such as $\underline{\underline{J}}_W = \underline{\underline{W}}_d\underline{\underline{J}}$, can be written as a product of three matrices (Sen and Stoffa, 2013):

$$\underline{\underline{J}}_W = \underline{\underline{U\Lambda V}}^T \tag{3.21}$$

The matrices have following characteristics:

- $\underline{\underline{U}}$ and $\underline{\underline{V}}$ are orthogonal matrices ($\underline{\underline{U}}^{-1} = \underline{\underline{U}}^{T}$ and $\underline{\underline{V}}^{-1} = \underline{\underline{V}}^{T}$) that span the data and model space, respectively.
- $\underline{\underline{U}}^{T}\underline{\underline{U}} = \underline{\underline{I}}_{N\times N}$ and $\underline{\underline{V}}^{T}\underline{\underline{V}} = \underline{\underline{I}}_{M\times M}$
- $\underline{\underline{U}}$ contains the eigenvectors of $\underline{\underline{J}}_{W}^{T}\underline{\underline{J}}_{W}$ and $\underline{\underline{V}}$ of $\underline{\underline{J}}_{W}\underline{\underline{J}}_{W}^{T}$
- $\underline{\underline{\Lambda}}$ is a matrix with the size $(N \times M)$ and contains the non-zero eigenvalues of $\underline{\underline{J}}_{W}^{T}\underline{\underline{J}}_{W}$ and $\underline{\underline{J}}_{W}\underline{\underline{J}}_{W}^{T}$, which are the square-roots of the eigenvalues $\lambda_1, \lambda_1, ..., \lambda_{min(N,M)}$ of $\underline{\underline{J}}_{W}$, on its main diagonal in decreasing order.

The inverse of $\underline{\underline{J}}_{W}$ can be calculated using the described factorization:

$$\underline{\underline{J}}_{W}^{-1} = \underline{\underline{V}}\,\underline{\underline{\Lambda}}^{-1}\underline{\underline{U}}^{T} \tag{3.22}$$

The transformed model update is achieved, when the factorization of the weighted Jacobian is inserted in Equation 3.20 (Jupp and Vozoff, 1975):

$$\Delta\underline{m} = \underline{\underline{V}}\left(\underline{\underline{\Lambda}}^{2} + \beta\underline{\underline{I}}\right)\underline{\underline{V}}^{T}\underline{\underline{V}}\,\underline{\underline{\Lambda}}^{T}\underline{\underline{U}}^{T}\underline{e} \tag{3.23}$$

and inserting the identity matrix $\underline{\underline{I}} = \underline{\underline{\Lambda}}\,\underline{\underline{\Lambda}}^{-1}$:

$$\Delta\underline{m} = \underline{\underline{V}}\underbrace{\left(\underline{\underline{\Lambda}}^{2} + \beta\underline{\underline{I}}\right)\underline{\underline{\Lambda}}^{T}\underline{\underline{\Lambda}}}_{\underline{\underline{T}}}\underline{\underline{\Lambda}}^{-1}\underline{\underline{U}}^{T}\underline{e} \tag{3.24}$$

leads to the model update in a form similar to Equation 3.22, when a new matrix $\underline{\underline{T}}$, the damping matrix, is introduced. It contains non-zero entries along the main diagonal (Jupp and Vozoff, 1975):

$$T_{ii} = \left(\frac{\lambda_i^2}{\lambda_i^2 + \beta^2}\right) \tag{3.25}$$

The damping factor β prevents the instability of the method, by avoiding divisions by very small values (Petry, 1987). For large eigenvalues ($\lambda_i >> \beta$) the damping becomes irrelevant, and, therefore, only affects smaller eigenvalues. For $\beta = \lambda_i$ the damping is $T_{ii} = 0.5$. Typically the values of λ and β of the matrix are normed by the maximum singular value λ_1 ($\hat{\lambda} = \lambda/\lambda_1$ and $\hat{\beta} = \beta/\lambda_1$)

$$T_{ii} = \frac{\hat{\lambda}_i^2}{\hat{\lambda}_i^2 + \hat{\beta}^2} \tag{3.26}$$

Jupp and Vozoff (1975) suggested to use a higher order of exponents for the parameters in the damping matrix:

$$T_{ii} = \frac{\hat{\lambda}_i^{2C}}{\hat{\lambda}_i^{2C} + \hat{\beta}^{2C}} \tag{3.27}$$

with $\hat{\beta}$ being the damping value threshold. The exponent C can be chosen by the user, and equals 2 for the TEM method. In EMUPLUS a default threshold of 10% is applied. Only parameters with values higher than the threshold are changed during the inversion process, others remain untouched.

3.4.2. Equivalent Models

Geophysical problems are ill-posed and there is no unique solution to the inverse problem. All models that predict the data within the data error bounds are called equivalent models because they describe the subsurface equally well. A mixed Marquardt-Levenberg Monte-Carlo approach is used to compute equivalent models by systematically perturbing each model parameter by a predefined percentage (Scholl, 2005). Large scatter within a model parameter indicates the inability of the inversion to resolve the parameter. On the other hand, if the deviation of the model parameters is minimal for all equivalent models, the model parameter is well recovered by the data.

3.5. Occam Inversion

Another popular approach to regularize the solution of the inverse problem is the Occam method (Constable et al., 1987). The Occam method tries to find the smoothest model fitting the data, by not allowing a high contrast between adjacent layers. The cost-function has a similar shape as the one used in the Marquardt-Levenberg method (Equation 3.19):

$$\Phi(\underline{m}) = \left(\underline{e} - \underline{\underline{J}}\Delta\underline{m}\right)^T \underline{\underline{W}}_d^2 \left(\underline{e} - \underline{\underline{J}}\Delta\underline{m}\right) + \mu \underline{m}^T \underline{\underline{R}}^T \underline{\underline{R}}\underline{m} \tag{3.28}$$

μ is the regularization parameter and $\underline{\underline{R}}$ the roughness. That is defined by the discreet first or second derivatives of the resistivity with respect to the depth z (Constable et al., 1987):

$$\underline{\underline{R}}_1 = \sum_{i=2}^{N} (\rho_i - \rho_{i-1})^2 \qquad \text{and} \qquad \underline{\underline{R}}_2 = \sum_{i=2}^{N} (\rho_{i+1} - 2\rho_i + \rho_{i-1})^2 \tag{3.29}$$

The roughnesses can be written as a matrix vector product $\underline{\underline{R}}\underline{m}$, with the model vector only including the electrical resistivities. The roughness matrices then have a very simple shape:

$$\underline{\underline{R}}_1 = \begin{bmatrix} 0 & 0 & \dots & 0 & 0 \\ -1 & 1 & 0 & \dots & 0 \\ 0 & -1 & 1 & 0 & \vdots \\ \vdots & \ddots & \ddots & \ddots & \vdots \\ 0 & \dots & 0 & -1 & 1 \end{bmatrix} \qquad \text{and} \qquad \underline{\underline{R}}_2 = \underline{\underline{R}}_1^T \underline{\underline{R}}_1 \tag{3.30}$$

The first derivative represents the differences of the resistivity and enforces smooth models with minimal gradients. The second order derivative is the curvature of the resistivity with depth and it penalizes the gradient. This forces the gradient to change smoothly with depth.

The model update of the Occam inversion is defined as

$$\begin{aligned} \Delta\underline{m} &= \left(\underline{\underline{J}}^T \underline{\underline{W}}_d^2 \underline{\underline{J}} - \mu \underline{\underline{R}}_{1,2}^T \underline{\underline{R}}_{1,2}\right)^{-1} \left(\underline{\underline{J}}^T \underline{\underline{W}}_d^2 \underline{e} - \mu \underline{\underline{R}}_{1,2}^T \underline{\underline{R}}_{1,2} \underline{m}\right) \\ &= -\underline{\underline{H}}^{-1} \underline{g} \end{aligned} \tag{3.31}$$

with $\underline{\underline{H}}$ being the Hesse matrix and $\underline{g}$ being the gradient of the cost-function (Equation 3.28). The Hesse matrix is the second Fréchet derivative of the cost-function.

The Occam inversion algorithm is usually combined with initial models with a high number of layers (≥ 30) to explain the subsurface reasonably well, and a homogeneous resistivity distribution. The algorithm allows the resistivity to be updated only when necessary to explain the measured data, but suppresses complex structures (Constable et al., 1987). The predicted model of the Occam-R_1 algorithm does not experience updates to layers with no data coverage or influence of regularisation. The second derivative roughness forces the underdetermined layers to a constant resistivity gradient. Therefore, the depth of divergence of the models of each roughness is an additional indication of the DOI (Yogeshwar, 2014).

3.5.1. Regularization Parameter

The principle of Occam's inversion is to find the simplest model possible that describes the measured data by suppressing complexity. The regularisation parameter μ marks the trade-off between the focus on the data and the regularisation term. A large μ puts the emphasis on the regularisation term, leading to smooth models. For $\mu = 0$ the algorithm switches to the Gauss-Newton algorithm without constraints. The goal of the algorithm is to introduce only necessary structure into the model, so it is convenient to start with a high value of μ that decreases as the data misfit increases. Various ways of finding an optimal μ have been proposed, e.g. a line search (Constable et al., 1987) or the L-curve criteria (Hansen and O'Leary, 1993), where an optimal trade-off between data fit and model smoothness is sought.

3.5.2. Pre-Conditioned Conjugate Gradient

The computation of the Jacobi matrix is very expensive. It is possible to avoid its explicit calculation by using the Pre-conditioned Conjugate Gradient (PCG) method to compute the model update (e.g., Chave and Jones, 2012). Therefore, the PCG approach is implemented in the multi-dimensional inversion algorithm TEM3Dinv (Liu et al., 2024). The PCG method is used to calculate the model update (Equation 3.31), which is a linear system and can be solved for each iteration of the Gauss-Newton system.
For simplicity the indices for the Gauss-Newton inversion iteration are not included and only a new index l for the PCG iteration number is introduced. At each Gauss-Newton iteration a new string of L models is generated with $\underline{m}_1 = \underline{m}_k$ and $\underline{m}_L = \underline{m}_{k+1}$. The PCG model update can be calculated using

$$\underline{m}_{l+1} = \underline{m}_l + \alpha_l \underline{p}_l \tag{3.32}$$

with α_l being the step size and $\underline{p}_l$ being the search direction. It is similar to the steepest decent method (Section 3.3.2), however not only the step size is adapted, but also the search direction is modified. The step size is determined in the same way as for the steepest decent method by minimizing the cost function at $\underline{m}_{l+1}$ with respect to α, yielding to:

$$\alpha_l = -\frac{\underline{g}(\underline{m}_l)^T \underline{p}_l}{\underline{p}_l^T \underline{\underline{H}}_k \underline{p}_l} \tag{3.33}$$

In the next step the new search direction is determined. In the pre-conditioned conjugate gradient method a matrix $\underline{\underline{C}}$, a so called pre-conditioner, is used in this process. The

initial search direction is $\underline{p}_0 = \underline{\underline{C}}\underline{g}_l$. The update in the search direction is defined as

$$\underline{p}_{l+1} = -\underline{\underline{C}}\underline{g}_l + \beta_l \underline{p}_l; \qquad l = 1, 2, ..., L-2 \tag{3.34}$$

Here $\underline{g}_l$ denotes the gradient or steepest decent direction at $\underline{m}_{k,l}$. β can be calculated from the gradients of the cost-functions:

$$\beta_k = \frac{\underline{g}_{l+1}^T \underline{\underline{C}}\underline{g}_{l+1}}{\underline{g}_l^T \underline{\underline{C}}\underline{g}_l} \tag{3.35}$$

The search direction is always perpendicular to the previous gradient $\hat{\underline{g}}_l$.

3.6. Summary

There are several different inversion approaches. In this chapter only those used in this thesis are presented. All are based on the least-squares approach to formulate the cost function and assume that geophysical data are always Gaussian distributed. The cost function considered is non-linear and two ways of dealing with the non-linearity are presented. Both are iterative methods. The first is to approximate the forward operator using the Gauss-Newton method, the second is to use a gradient based method and more specifically the steepest descent. This method searches for the minimum by following the gradient to the next minimum. Modifications of these methods lead to better convergence behaviour, such as the conjugate gradient method, which also optimises the search direction in each iteration. The introduction of regularisation terms in the Gauss-Newton method also avoids singularity problems of the Jacobian.
The Marquardt-Levenberg and Occam inversion algorithms are both regularised Gauss-Newton methods and are used in the 1D inversion algorithm EMUPLUS. The Marquardt-Levenberg method introduces damping into the cost function to avoid unstable solutions. Alternatively, the Occam inversion searches for the smoothest models in terms of resistivity depth gradient or curvature. The 3D TEM algorithm TEM3Dinv is also based on a regularised Gauss-Newton approach, which uses a roughness constraint similar to the Occam method. To avoid high memory requirements, model updates are estimated using the pre-conditioned conjugate gradient method instead of explicitly computing the Jacobi matrix.

CHAPTER 4

Roter Kamm and Field Survey

In the context of this thesis, a field survey was carried out in the southern part of the Namib Desert, the Tsau //Khaeb (Sperrgebiet) National Park. It was motivated by similar field campaigns in the Atacama Desert in recent years as part of CRC 1211, in particular those presented by Blanco-Arrué et al. (2022). Here, the authors also used the TEM method. These studies were carried out on clay pans with depths < 200 m. This time the focus is on a meteoritic impact crater. The formation of meteoritic impact craters is independent of local geology such as tectonic fault systems, which is in stark contrast to the evolution of clay pans. Information on the geology of the impact crater and its sedimentary cover is sparse, and only a minimum thickness of 300 m is estimated for the sedimentary cover. Investigating such depths with the TEM method is challenging and requires a large transmitter size. The single-loop or central-loop TEM setup is inconvenient for surveys with large transmitter sizes and high lateral density. Therefore, fixed-loop TEM measurements were also carried out. To ensure adequate depth resolution for the Roter Kamm impact crater, AMT data were collected sparsely along a transect. All these methods and setups required a large number of different receiver units. Depending on the type of data output, the data must then be processed before it can be further evaluated.

This chapter introduces the geological background of the Roter Kamm impact crater and the motivation for its investigation, and gives an overview of the field campaign in the Namib Desert. It also includes a brief description of the geophysical equipment used for each applied method and setup.

4.1. CRC 1211

The research for this thesis is part of the Collaborative Research Centre CRC 1211 "Earth - Evolution at the dry limit". The project aims to characterise Earth surface processes, biological activity and their interactions in water-limited environments (Dunai et al., 2020). The areas of interest are the Atacama and Namib Deserts in Chile and Namibia

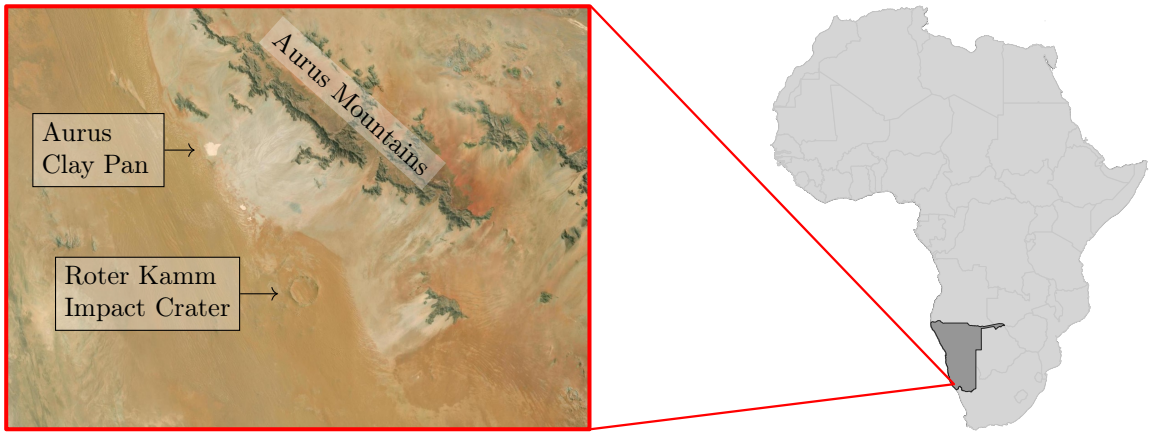

Figure 4.1.: The location of the study area on the African continent and Namibia is shown on the right. On the left are the Aurus Clay Pan and the Roter Kamm impact crater and their surroundings. Map data for the satellite image: ESRI (2022) and African continent: QGIS Development Team (2022).

respectively. While the primary focus of the research is on the evolution of the Atacama Desert, there has been a shift in interest towards the Namib Desert as a comparative study area during the course of the project.
Traces of wetter climates can be found buried in the sediments in places where sediments could have accumulated over periods of thousands or millions of years. Drill cores in these sedimentary basins can serve as long-term climate records (e.g., Diederich et al., 2020; Melles et al., 2011; Ritter et al., 2019; Wennrich et al., 2024). However, drilling is invasive and expensive. Therefore, it is necessary to study promising sedimentary basins in advance and determine the location with the thickest sediment cover. Within CRC 1211, geophysical methods have been successfully applied by Diederich et al. (2020) and Ritter et al. (2019), but most notably by Blanco-Arrué et al. (2022). With the growing interest in the Namib Desert, plans were made to recover climate records, and the Aurus clay pan and the Roter Kamm impact crater were selected as potential targets (Figure 4.1). Therefore, the motivation for the geophysical field survey in the Namib Desert in the context of CRC 1211 was to determine the thickness and internal structure of the sedimentary cover in both basins. This thesis focuses only on the Roter Kamm impact crater as the geophysical field survey and methods were more sophisticated. In addition, the results of the geophysical and geological field survey of the Aurus clay pan have been published in Nienhaus et al. (2023c).

4.2. Roter Kamm Impact Crater

The Roter Kamm crater (diameter 2.5 km) is located in southern Namibia in the Namib Desert (Figure 4.1). It was formed by a meteoritic impact 4-5 million years ago (Hecht et al., 2008). Its rim is 40 to 90 m elevated above the surface, however its surface inside is around 50 m lower than the surrounding plain.
There are currently 190 confirmed impact structures on Earth (Earth Impact Database, 2011). The morphological form of impact structures can either be simple or complex. While a simple crater is bowl-shaped with an elevated, fractured rim, a complex crater has a smaller depth to diameter ratio and is more altered (Pilkington and Grieve, 1992).

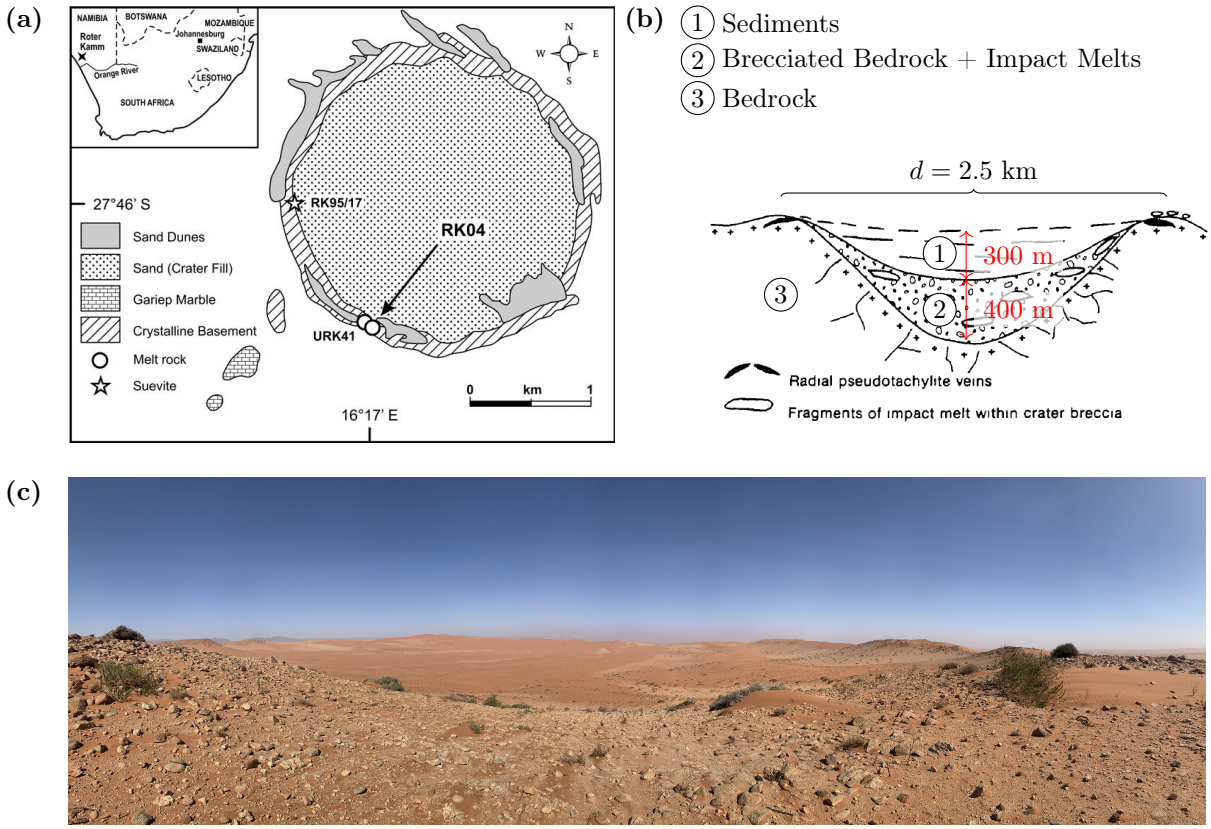

Figure 4.2.: Roter Kamm impact crater. **(a)** Geological map of the Roter Kamm showing materials at the surface of the Roter Kamm impact crater, such as sand and active sand dunes, and the crystalline basement at the crater rim. Samples of melt rock and suevite are also shown. Taken from Hecht et al. (2008). **(b)** Schematic representation of a cross section through the present crater. The maximum thickness of the sediments (300 m) and the brecciated bedrock including impact melts (400 m) is indicated. Modified from Reimold and Miller (1989). **(c)** Photo taken during the field survey from the top of the rim of the Roter Kamm impact crater in a south-easterly direction (Photo by H. Nienhaus).

Simple craters typically have a diameter smaller than 4 km or 2 km in crystalline or sedimentary target rock, respectively (Dence, 1972). According to this size range, around 30 % of the confirmed impact structures are simple craters, with the Roter Kamm impact crater being among the largest (Earth Impact Database, 2011). The Roter Kamm impact crater has been described as one of only a few simple craters that are sufficiently well preserved for morphometric studies about the structure of simple craters (Grieve, 1993). Nevertheless, the Roter Kamm impact crater shows signs of degradation in form of incisions in to the crater rim and a low wall slope (Grant, 1999). Furthermore, it is extensively covered by post impact sediments and only the rim remains exposed (cf. Figure 4.2c, Dietz, 1965; Fudali, 1973; Reimold and Miller, 1989). This circumstance makes a surface study difficult (Koeberl, 1994)

Geophysical studies can provide information on the sedimentary cover and structure of impact craters. Only a limited number of geophysical studies have been carried out at the Roter Kamm impact crater (e.g., Brandt et al., 1998; Fudali, 1973; Grant et al., 1997; Reimold et al., 1992). Modelling studies based on gravimetric data suggest a sediment thickness of about 300 m in the centre of the Roter Kamm crater (Brandt et al., 1998; Fudali, 1973). In addition, the best fit model to the magnetic data places a magnetic

anomaly at a depth of 700 - 800 m (Brandt et al., 1998), which is consistent with the assumptions made by Fudali (1973) regarding the lower boundary of the brecciated zone above the basement. Grant et al. (1997) concludes that alluvial activity was dominant in the 1.0 - 2.7 million years after the formation of the Roter Kamm during a wetter climate, but since the Late Pleistocene and Holocene aeolian processes have modified the landscape and accumulated the extensive sand cover. However, Miller (2010) contradicts this hypothesis of fluvial transport, as the typical rainfall in the area has been rather low over the last 15 ma. Although, there is evidence for periods of higher rainfall during the Pleistocene (Miller, 2010). Furthermore, transport distances are too short to justify abrasion by fluvial transport. In their opinion, aeolian transport and abrasion by strong winds were the driving forces in the modification of surface sediments and rocks.

4.3. Survey Design

The survey included various geophysical techniques (TEM, AMT, magnetics and active seismics). An international team of geophysicists and geologists from Namibia (Geological Survey of Namibia and University of Namibia) and Germany (TU Bergakademie Freiberg and University of Cologne) participated in the field work. A team led by the Technical University Bergakademie Freiberg focused its efforts on the Aurus Clay Pan, carrying out extensive seismic measurements along two profiles (Figure 4.3), complemented by TEM measurements and geological surface sampling, and a 4 m hand-drilled sediment core. Although the survey plan of the Aurus Clay Pan is shown here (Figure 4.3), it is beyond the scope of this thesis to present the results of this survey. Therefore I refer to Appendix C and Nienhaus et al. (2023c) for detailed information.

The focus of this thesis is solely on the EM measurements at the Roter Kamm impact crater. During the fieldwork, the research permit restricted the use of cars in the National Park to limit human impact on the flora and fauna. Therefore, it was not possible to use them extensively and only one route was allowed to approach the rim. This limited the field survey to two perpendicular profiles at the Roter Kamm impact crater and a regional profile from the crater to the Aurus Mountains (Figure 4.4). The direction of faulting in the Aurus Mountains generally follows a northwest to southeast trend (Thomas et al., 2016). Therefore, the direction of Profile 1 was roughly oriented at a 90° degree angle to this ridge. The regional profile follows the path designated by the National Park officials. Profile 1 crosses the crater from south-west to north-east and extends into the plain surrounding the crater (length: 3,800m), while Profile 2 extends only from the south-eastern part of the rim to the north-west (2,400m, Figure 4.4 a and b). A regional profile extends from the plain surrounding the Roter Kamm impact crater to the Aurus Mountains (length: 8,000 km). Along the regional profile only single-loop TEM (transmitter size: 50×50 m^2) and AMT soundings were carried out. The spacing between the TEM soundings is 500 m in the southwest and 1,000 m in the northeast, while the spacing between the AMT stations is 2,000 m in the southwest and 1,000 m in the northeast.
Along Profile 1, single loop and fixed-loop TEM were used in a moving mode, complemented by sparse AMT soundings. Along Profile 2 only single-loop measurements were carried out. The TEM transmitter size varied between 50×50 m^2 and 100×100 m^2.

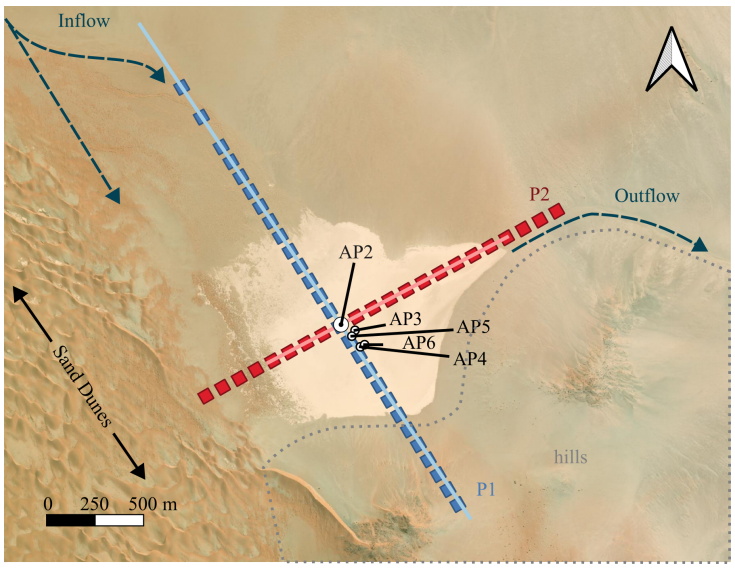

Figure 4.3: ESRI Satellite Image with the transects P1 and P2 of the TEM (blue and red squares) and seismic (light blue and light red lines) measurements and location of sediment core AP2 (large white circle) and surface samples AP3 to AP6 (small white circles). Fluvial transport directions are indicated by dark blue-green arrows labelled "inflow" and "outflow", topographic elevations "hills" are outlined by gray dashed lines. In the western part of the image active sand dunes are visible. Taken from Nienhaus et al. (2023c).

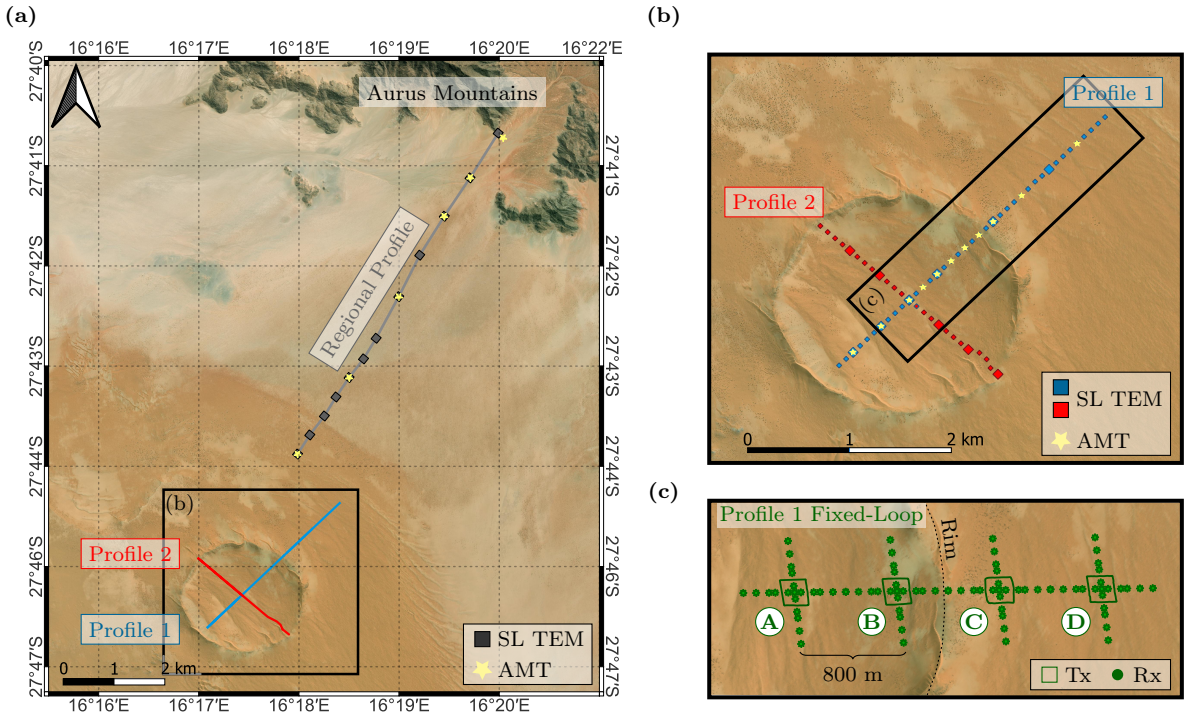

Figure 4.4.: Satellite Images of the Roter Kamm impact crater and its environment including the the two local profiles Profile 1 (blue) and Profile 2 (red) and the regional Profile (gray). **(a)** Overview of all three profile locations. The individual TEM (dark gray squares) and AMT stations (yellow stars) are marked along the regional profile. The TEM transmitter all have a size of 50×50 m^2. **(b)** Magnification of the area highlighted in (a). All locations of TEM transmitters are indicated by blue and red squares. The TEM transmitter loop sizes are either 50×50 m^2 or 100×100 m^2. Additionally, AMT sounding locations along Profile 1 are marked by yellow stars. **(c)** Fixed-loop TEM survey location with dimensions as presented in (b). The green lines follow the tracks of the transmitter loops (200×200 m^2) and the green circles indicate the receiver locations. The three receiver locations in the middle between two transmitters were covered with measurements related to both of the nearest transmitters. Map Data for satellite image: ESRI (2022)

The spacing between locations is consistently 100 m, with one exception on Profile 1 near the northeast rim, where the spacing is 200 m. The larger TEM loops are located every 400 m in the crater up to the north-eastern and south-eastern parts of the crater rim. Both transmitter sizes were used along this section of Profile 1. At all other locations one transmitter size was preferred. Outside the crater, only one TEM measurement was made with the larger loop size, halfway between the north-eastern end of Profile 1 and the crater rim. The AMT soundings are mainly located inside the Roter Kamm impact crater. The station spacing is 400m in the south-west section of Profile 1 and 200m in the north-east. Outside the crater, the spacing is greater and is at the same locations as Transmitters C and D of the fixed-loop transect. The fixed-loop transect follows the course of Profile 1. The middle point is at the top of the crater rim. The transmitters (size: 200×200 m^2) are placed symmetrically around the crater rim. The distance between them is 800 m. At each transmitter location, the receiver arrays are spread 400 m in each direction of Profile 1 and also perpendicular to it, forming a cross at each transmitter. At transmitter A, the off-profile array coincides with Profile 2. The receivers are located at distances of 0 m, 50 m, 150 m, 200 m, 300 m and 400 m from the centre of the transmitter loop (Figure 4.4c).

The parameter of each profile and the corresponding method can be found in Table 4.1.

Table 4.1.: Acquisition parameters of the TEM and AMT surveys at the Roter Kamm impact crater for the local profiles 1 and 2 and the regional profile. The TEM station at the crossing point of Profiles 1 and 2 is counted as a position of a receiver at both profiles. The table shows the TEM transmitter size, the number of TEM receivers and AMT sounding location, the coordinates of the starting and ending points of the profile corresponding to each method applied, the distance between receiver stations and the length of the profile covered with each method. The total length of each profile corresponds with the single-loop TEM profile lengths.

Profile 1

	Tx	Rx	Start	End	Rx Spacing in m	Length in m
single-loop TEM	50×50 m^2 100×100 m^2	35 6	-27.7723 N 16.2816 E	-27.7473 N 16.3081 E	100	3,800
fixed-loop TEM	200×200 m^2	84 (44 Rx/Tx)	-27.7683 N 16.2856 E	-27.7473 N 16.3083 E	50/100	3,200
AMT	x	11	-27.7709 N 16.2830 E	-27.7500 N 16.3053 E	200/400/800	3,200

Profile 2

	Tx	Rx	Start	End	Rx Spacing	
single-loop TEM	50×50 m^2 100×100 m^2	20 6	-27.7607 N 16.2974 E	-27.7583 S 16.2798 E	100	2,400

Regional Profile

	Tx	Rx	Start	End	Rx Spacing	
single-loop TEM	50×50 m^2	12	-27.7376 N 16.2997 E	-27.6735 N 16.3397 E	500/1000	8,000
AMT	x	6	-27.7376 N 16.2997 E	-27.6745 N 16.3408 E	1,000/2,000	8,000

The equipment, settings and processing routines for both, TEM and AMT, method are explained in the next section.

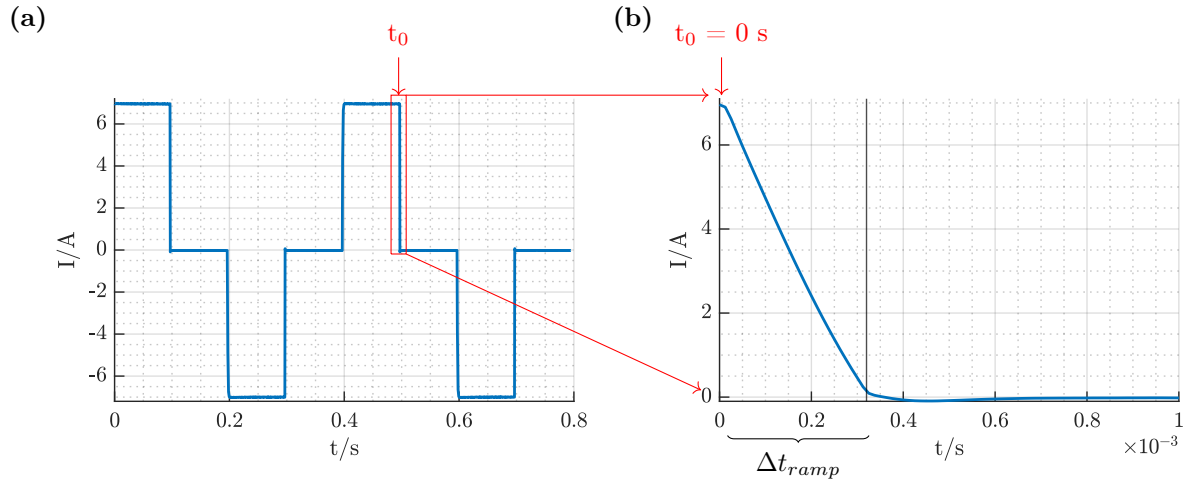

Figure 4.5.: (a) Recording of the transmitted current with a current strength of 7 A at fixed-loop transmitter 3. A 50 %-duty-cycle was used with a base frequency of 2.5 Hz. (b) Magnification of the turn-off flank. The approximated length of the ramp is 320 μs.

4.4. Equipment and Settings

The survey with two different TEM setups and additional AMT soundings requires a range of different transmitter (only TEM) and receiver units. For the single-loop TEM measurements the TEM-FAST 48 (AEMR, 2007) was selected. A device including a transmitter and receiver unit in one single case. It is especially user-friendly in harsh terrain, such the Namib Desert due to its compact built and light weight. However, its transmitter unit is not designed to transmit high electric currents ($>$ 4 A) and therefore not strong enough for the fixed-loop measurement. For those a dedicated transmitter, Zonge ZT-30 ZeroTEM (Zonge, 2000), was used in combination with two different receiver units. Along the main profile the SMARTem24 (EMIT, 2018) and along the perpendicular transects the KMS-820 (KMS Technologies, 2019). The AMT soundings were carried out with the S.P.A.M Mk IV system (Klose et al., 2011).

4.4.1. Fixed-Loop TEM

The fixed-loop survey was designed to reach large penetration depths, therefore devices and sensors designed for this purpose were chosen. The Zonge ZT-30 ZeroTEM transmitter (Zonge, 2000) was powered by two 12 V car batteries and transmitted an electrical current with around 7 A current strength (6.7 A - 7.2 A). The transmitter was operated in a 50 %-duty-cycle and base frequencies of 0.5 Hz and 2.5 Hz (Figure 4.5a) and synchronised using a GPS-clock. The turn-off process of the current took around 320 μs and showed an almost linear behaviour (Figure 4.5b).

Two different types of receivers were used with each connected to a different sensor. Along Profile 1, we used the EMIT SMARTem24 (EMIT, 2018) with the 3D-3LF induction coil triple of Geonics Limited (Geonics, 02.11.2024). Along the perpendicular segments, the KMS-820 Data Acquisition Unit of KMS Technologies (KMS Technologies, 2019) in combination with two Zonge TEM/3 induction coils (Zonge, 2013).
Both receiver units are suitable for a variety of different methods (SMARTem24: TEM, In-

duced Polarisation, Controlled-Source AMT and MT; KMS-820: MT and microseismics). The KMS-820 has also been used for time domain methods such as LOTEM (Haroon et al., 2015; Mörbe, 2020). Both are GPS synchronised and use a 24-bit analogue-to-digital converter (ADC). However, the SMARTem24 has a slightly higher sampling rate of 120 kHz, while the KMS-820 has a maximum sampling frequency of 80 kHz. They have comparable minimum voltage inputs of 10 V (SMARTem24) and 9 V (KMS-820). Both devices also offer different gain settings. The SMARTem24 offers three different gain settings (1, 10, 100), which can be selected manually or automatically in different modes (auto and auto noisy), successfully avoiding saturation in the early time gates. While automatic gain selection was not available on the KMS-820, it does offer a wider range of gain factors from 1 to 2560 in twelve steps. During the survey, the SMARTem24 typically used the highest gain setting of 100, and only in windy conditions at Transmitter D did it use a lower gain setting of 10. The KMS-820 recorded with a more variable gain between 1 and 152. One noise recording was even made with a gain factor of 2432. With the selected parameter it is possible to estimate the lowest voltage value that can be recorded.:

$$V_{res} = V_{min}/f_{\text{Gain}}/2^{\text{ADC}-1} \tag{4.1}$$

with V_{min} being the minimum voltage input, f_{Gain} the gain factor and ADC the resolution of the analogue-to-digital converter. This yields to a lowest measurable voltage of 1.2×10^{-8} V for a gain of 100 for the SMARTem24 and 7.1×10^{-9} V with a gain of 152 for the KMS-820. Therefore, the resolution limit of the KMS-820 was at times lower than that of the SMARTem24. However, as the gain setting was variable, this is not true for all recordings.
Not only two different receiver units were used, but also different sensors. In case of the SMARTem24 along Profile 1, the Geonics 3D-3FL coil triple was used. These coils had the advantage of being perfectly positioned to each other to measure all three components of the induced voltage in a solid box. They have an effective area of 200 m^2. The Zonge TEM/3 coils come separately and must be arranged in a 90° angle by the user. The effective area is 40,000 m^2. In this survey only the vertical and the strong horizontal component were measured along the perpendicular transect of the fixed-loop profile.

4.4.2. Single-Loop TEM

Single-loop data was collected with the TEM-FAST 48 (AEMR, AEMR, 2007). It combines a transmitter and receiver unit in one small, lightweight device. In contrast to the ZT-30 ZeroTEM transmitter, it only transmits a uni-polar rectangular pulse and the on and off times of the transmitter are not equally long. Two current settings are available (1 A and 4 A) and only the high current setting was used during this field survey due to the expected high target depth. The turn-off current behaviour was distinctly non-linear, however rather short in length (< 4 μs for a 50×50 m^2 transmitter loop, Figure 4.6a). The TEM-FAST 48 is very user-friendly and easy to use. Apart from the current strength, the transient length and the amount of stacks can be selected. We opted to set both to a maximum after testing in the crater center. So the transient length was 1.6384×10^{-2} s consisting of 48 time gates. The data is automatically processed by the TEM-FAST 48 inside the Data Acquisition System (DAS, Figure 4.7).
The DAS is a multi-channel system with 48 channels and each time gate is assigned to one channel. Within each channel, the incoming signal is integrated in the assigned time

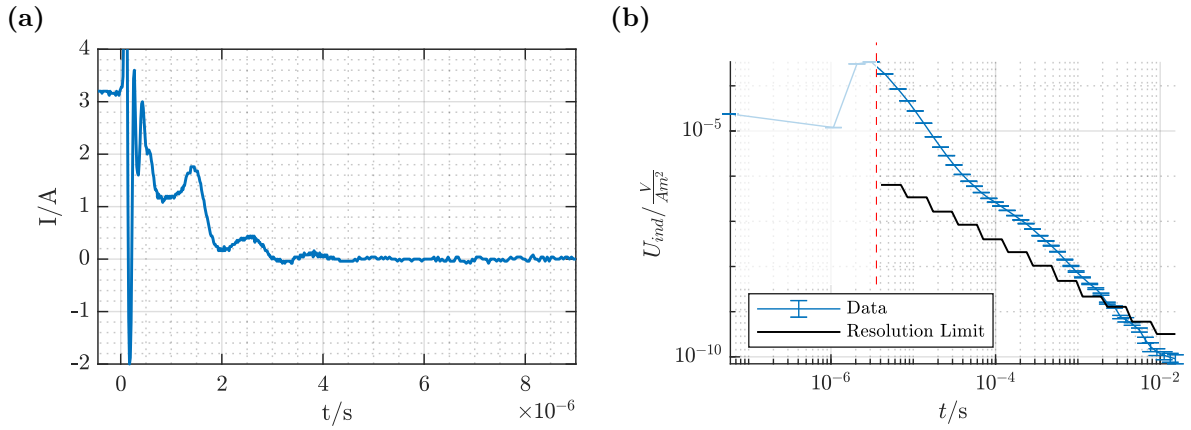

Figure 4.6.: **(a)** Ramp of the TEM-FAST 48 for a single-loop with dimensions 50×50 m^2. **(b)** Transient in the centre of the Roter Kamm impact crater from a single-loop measurement with a loop size of 50×50 m^2. For the early times the voltage protection is active as this time period overlaps with the transmitter ramp. The TEM-FAST 48 displays the dynamic range of the instrument normalised to the current measurement settings. In this example, the last 11 time gates record data below the resolution limit and are therefore not trustworthy.

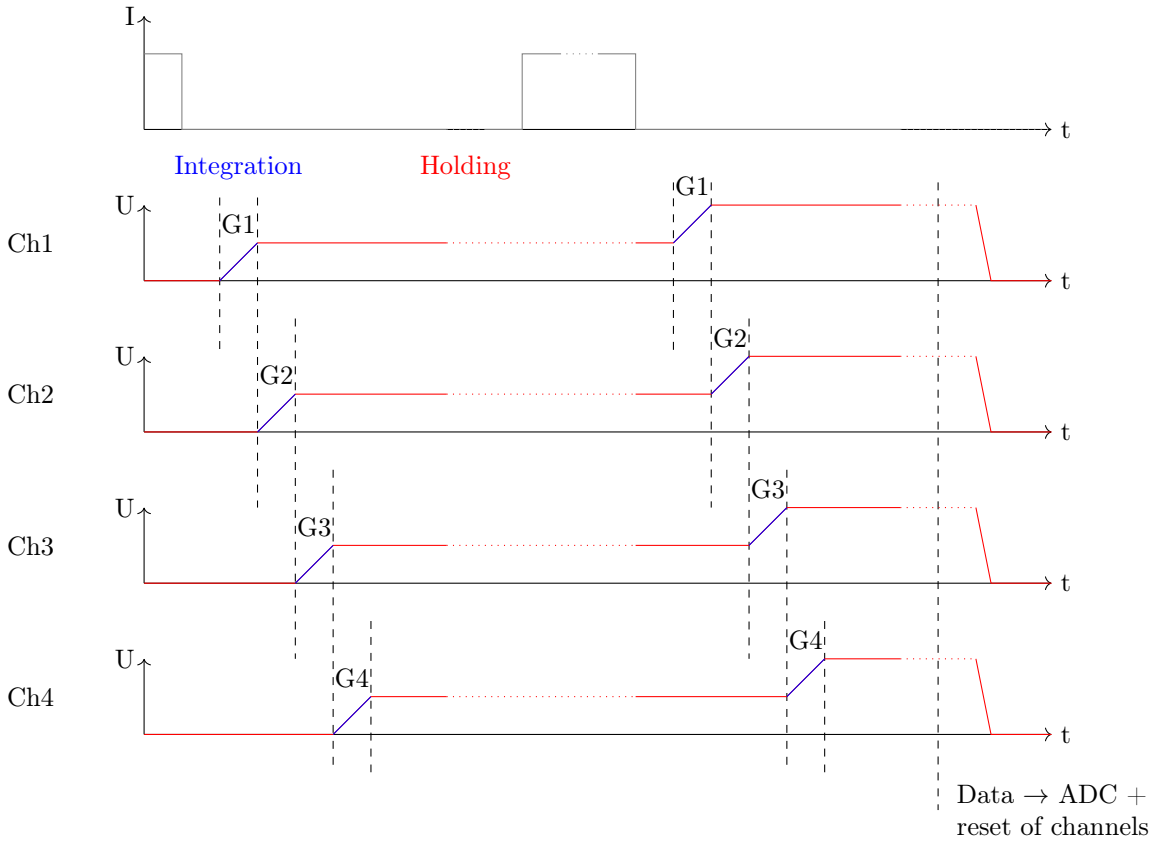

Figure 4.7.: Multi-Channel system of the TEM-FAST 48. Sketch of integration and holding patterns of data in each channel, here only the first four channels are presented (Ch 1, Ch 2, Ch 3 and Ch 4). Each channel is used for one time gate (t1, t2, t3 and t4). The integration inside each time gate is repeated for the maximum time period reserved for analogue stacking.

interval ("strobe"). Outside the integration time interval, the channel is put on hold until the same time interval is repeated in the next transmitter cycle. This process is repeated in the pre-set constant time period. Therefore, the number of analogue stacks is reduced for longer transients. As the highest time setting was chosen, only four integration cycles could be completed. A multiplexer then passes the integrated data to the ADC, which has a resolution of 16 bits and a minimum unit of 1 μV. The total dynamic range extends from this unit to 10 V. For error estimation the TEM-FAST 48 allows to set a number of digital stacks N, which is a multiple of 13 with a maximum of 260. The error is estimated by the standard error of the mean (SEM):

$$\mu = \frac{1}{N}\sum_{i=1}^{N} d_i; \qquad \text{SEM} = \sqrt{\frac{1}{(N-1)N}\sum_{i=1}^{N}(d_i - \mu)^2} \tag{4.2}$$

N is the number of data points and d_i are the data points.
The TEM-FAST 48 presents the user with processed ready-to-go transients (Figure 4.6b) and displays the resolution limits for the current survey settings. For further settings and details I refer to the manual of the TEM-FAST 48 (AEMR, 2007).

4.4.3. AMT

For the AMT measurements we used the S.P.A.M. Mk IV system of the Geophysical Instrument Pool Potsdam (GIPP, grant no: 202127, Klose et al., 2011), which was powered by a 12 V car battery during recording. The system is capable of a maximum sampling frequency of 25 kHz. Therefore, it allows measurements of up to 10 kHz. The sensors used were the Metronix MFS07 induction coil magnetometer for the magnetic field and 60 m long grounded dipoles for the electric field measurements. The two horizontal field components of the electric and magnetic field were measured. As the non-polarizable Ag/AgCl electrodes had high contact resistances, soundings 0001 to 0003 and 0010 to 0016 were carried using copper tubes as electrodes (Figure 4.8). This lowered the contact resistance significantly. The tubes were approximately 70 cm long and had a diameter of 2 cm.

The data was recorded using two sampling frequencies; 500 Hz and 25,000 Hz. During the 500 Hz measurements, a low pass filter at 200 Hz was used, as this sampling frequency is unsuitable for any higher frequency signals. The typical recording time was 20 minutes for a sampling frequency of 500 Hz otherwise it was 10 minutes (Figure 5.3a). There were a few exception of this recording time, namely sounding 0009, where a longer sounding was conducted. At this location time series with a length of 180 min and 170 min were recorded for sampling frequencies of 500 Hz and 25,000 Hz, respectively. Soundings 0008, 0014 and 0016 have a bit shorter recording time which ranges between 5 and 8 min for the higher sampling frequency and sounding 0001 has a longer recording time of 30 min for the lower one.

Figure 4.8: Installed copper pipe electrode used for the grounded dipoles for the AMT soundings. The electrodes were approximately 70 cm long and had a diameter of 2 cm. The walls of the pipe were 2 - 3 mm thick.

4.5. Summary

The Roter Kamm impact crater in the southern Namib Desert was investigated in the framework of the CRC1211. It has a simple crater structure and is well preserved for geological investigations, however extensively covered by post-impact sediments. Several objectives for investigating the Roter Kamm using geophysics, and more specifically electromagnetic methods, arise. For palaeoclimate research the sediment cover plays an important role, as it was accumulated in a time period of up to 4-5 ma. The important parameter to determine are

(a) the thickness and

(b) the internal structure

of the sediment cover inside the impact crater. However, also the impact structure itself can be investigated. Additional motivations for a geophysical survey are the determination of

(c) the surface of the brecciated bedrock and

(d) the true impact crater, which is marked by the surface of the undisturbed bedrock

However, the last motivation might not be possible to achieve with the data collected, as the transition is expected in a large depth ($\geq$ 700 m) and both applied methods are sensitive to conductors rather then resistors.
Different methods and setups were applied during the field survey, namely TEM and AMT. The AMT soundings were carried out to validate the TEM data in larger target depths. Furthermore, the survey was used as a chance to apply two different TEM setups in the field, the fixed- and the single-loop setups. Which are comparable in terms of depth scales. The different data-sets require specified equipment. The TEM-FAST48 provides processed transient data for each sounding. However, the other receiver units only record time series. Therefore, an additional data processing is necessary to interpret the fixed-loop TEM and AMT data.

CHAPTER 5

Complementary Audiomagnetotelluric Study

The Audiomagnetotelluric method is a passive, frequency domain method. It uses a frequency range from 1 Hz to 10 kHz. The natural source fields are generated in the atmosphere during lightning storms. It is sensitive to conductive bodies at depths of up to several kilometres. Therefore, it has a higher depth of penetration than the TEM method. The sedimentary cover is expected to have at least a thickness of 300 m inside the Roter Kamm impact crater (Fudali, 1973). Thus, the comparative AMT data-set is concentrated inside the crater, with only sporadic soundings outside. In total 16 AMT soundings were carried out on Profile 1 and the regional profile and the horizontal magnetic and electrical fields were measured.
For the processing the EMERALD processing tool (Ritter et al., 1998) was used. A commonly used transfer function is the impedance tensor, that connects the horizontal magnetic field with the horizontal electric field. The impedance tensor can indicate the dimensionality of the subsurface. However, in a two dimensional region it is important to align the coordinate system of measurement with the regional strike direction. To confirm the dimensionality and a possible geological strike direction the impedance tensor can be analysed and rotated if a strike is found. In the case of the Roter Kamm impact crater, a strike direction was found to be consistent with the confirmed fault direction in the Aurus Mountains (Thomas et al., 2016). Thus, the data was inverted using the 2D algorithm MARE2DEM (Key, 2016). For the sounding in the center of the Roter Kamm impact crater, a 1D inversion using EMUPLUS is executed to determine the vertical resistivity structure.
All coordinates and data fits of the 2D inversion can be found in the Appendix A.3.

5.1. The Impedance Tensor

The impedance tensor is a transfer function between the horizontal electric and magnetic fields:

$$\begin{bmatrix} E_x \\ E_y \end{bmatrix} = \begin{bmatrix} Z_{xx} & Z_{xy} \\ Z_{yx} & Z_{yy} \end{bmatrix} \begin{bmatrix} H_x \\ H_y \end{bmatrix} \tag{5.1}$$

Depending on the dimensionality of the subsurface, the impedance tensor follows different patterns. For one- and two-dimensional resistivity distributions the main diagonal elements equal Zero ($Z_{xx} = Z_{yy} = 0$). Additionally, in a 1D case the off-diagonal elements have the same absolute value but opposing signs ($Z_{xy} = -Z_{yx}$). In three-dimensional cases all elements can be non-zero.
From the Impedance tensor apparent resistivity (ρ_a) and phase (ϕ) can be calculated for $i = \{x, y\}$ and $j = \{x, y\}$:

$$\rho_{a,ij} = \frac{1}{\omega\mu_0}|Z_{ij}|^2 \tag{5.2}$$

$$\Phi_{ij} = \tan^{-1}\left(\frac{\mathrm{Im}(Z_{ij})}{\mathrm{Re}(Z_{ij})}\right) \tag{5.3}$$

These two quantities allow first conclusions about the resistivity structure in the subsurface, similar to the late-time apparent resistivity transform for TEM data. The apparent resistivity is directly indicating the resistivity structure of the subsurface. The phase has a constant value of 45° in a homogeneous halfspace. The phase angle increases ($> 45°$), when the underlying layer is less resistive and decreases ($< 45°$), when the resistivity increases. Therefore, both, apparent resistivity and phase, give a first impression of the subsurface.

5.2. 2D Earth and the E- and B-Polarisation

In a simple two-dimensional Earth, the electrical and magnetic field components can be measured parallel or perpendicular to a lateral discontinuity (Figure 5.1). Let the direction of the lateral discontinuity, the strike direction, be parallel to the x-axis of the coordinate system, then the y-axis is perpendicular to the discontinuity. The electric current density (j_y) must be conserved at the vertical boundary. Therefore, the electrical field is discontinuous:

$$j_y = \sigma_1 E_y^1 = \sigma_2 E_y^2 \tag{5.4}$$

σ_1 and σ_2 are the conductivities of the two zones on either side of the discontinuity. In this case Ampère's and Faraday's laws (Equation 2.4 and 2.5) can be decoupled into two modes, referred to as the B- and E-polarizations.
The B-polarisation consists of B_x, E_y and E_z and the E-polarisation of E_x, B_y and B_z. They are named after the field component parallel to the strike direction (x-direction). The B-polarisation is also referred to as the transverse magnetic (TM) mode and the E-polarisation as the transverse electric (TE) mode.

5.2.1. Static Shift

In case a lateral conductivity discontinuity is only present in depths lower than the diffusion depth of the EM-fields, the apparent resistivity curve shifts towards a higher or lower magnitude (Simpson and Bahr, 2005). This behaviour is called static shift and does not occur for the phases, as the effect is time-independent. The static shift is a result of the conservation of currents across the lateral boundary. Along the boundary electric charges build up and cause the shift in apparent resistivity. In a 2D case with the lateral conductivity parallel to the x-axis, this only affects the B-polarisation, which contains E_y

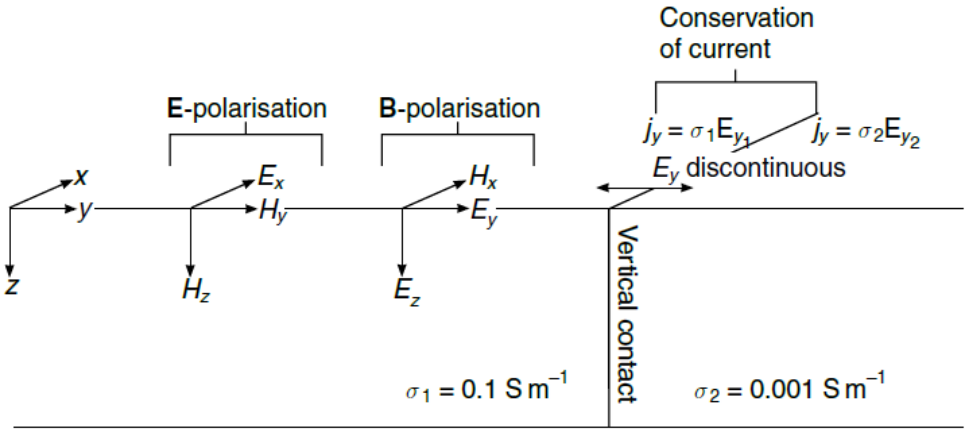

Figure 5.1.: Two-dimensional Earth and E- and B-polarisations. In case of a lateral discontinuity, the Maxwell Equations can be decoupled into the E- and B-polarisations, when electrical and magnetic fields are measured in the same coordinate system as the regional strike direction. The E_y components is not continuous at the vertical contact of two conductivities (σ_1 and σ_2), due to the conservation of currents across the boundary. Taken from Simpson and Bahr (2005)

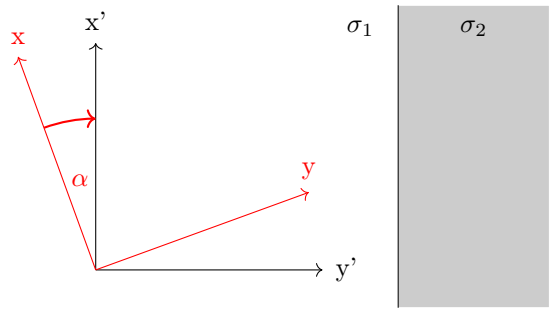

Figure 5.2: Regional strike direction and rotation of the coordinate system. The boundary between two conductive media (σ_1 and σ_2) is parallel to the x'-direction (black) and defines the regional strike direction. The data was measured in a different coordinate system (red). The data can be rotated around angle α to align both coordinate systems.

(Figure 5.1).
The static shift can be corrected by comparing the apparent resistivities with the late-time apparent resistivities of TEM soundings (e. g., Meju, 1994; Sternberg et al., 1988). For that the AMT frequencies must be connected to the transient times. This is achieved by setting the skin depth (Equation 2.20) and diffusion depth (Equation 2.22) equal (Sternberg et al., 1988):

$$t = \frac{194}{f} \tag{5.5}$$

The AMT apparent resistivity curves can multiplied by a factor to be on the same magnitude level as the TEM late-time apparent resistivity transforms.

5.2.2. Strike Angle Analysis

Data measured in a two-dimensional area can appear 3D, i.e. the main diagonals of the impedance tensor differ from 0, when the coordinate system of the measurement setup is not correctly aligned with the regional strike direction (Figure 5.2, red coordinate system). The coordinate system can be rotated in such a way that it coincides with a coordinate system where one axis is parallel to the regional strike and one perpendicular (Figure 5.2, black coordinates system).

Neither dimensionality of the subsurface nor the regional strike direction were known during this survey and the AMT field setup was oriented into North (x), East (y) and downwards (z). To analyse the dimensionality, different skews can be calculates, e.g. by Swift (1967) and Bahr (1988). However, the Swift model does not yield to satisfactory results if small scale 3D heterogeneities are presents. Therefore, the phase-sensitive skew proposed by Bahr (1988) is used here:

$$\eta = \frac{(|[D_1, S_2] - [S_1, D_2]|)^{1/2}}{|D_2|}. \tag{5.6}$$

The following definitions are used:

$$\begin{aligned} S_1 &= Z_{xx} + Z_{yy} \qquad & S_2 &= Z_{xy} + Z_{yx} \\ D_1 &= Z_{xx} - Z_{yy} \qquad & D_2 &= Z_{xy} - Z_{yx} \end{aligned} \tag{5.7}$$

$[A, B]$ is the commutator and defined as:

$$[A, B] = \mathrm{Im}(A \cdot B^*) = \mathrm{Re}(A)\mathrm{Im}(B) - \mathrm{Re}(B)\mathrm{Im}(A) \tag{5.8}$$

When the skew η is below 0.1, Bahr (1991) suggests the so-called phase-sensitive model to calculate the regional strike direction (Bahr, 1988):

$$\tan(\alpha) = \pm\sqrt{\frac{B+C}{B-C} + \left(\frac{A}{B-C}\right)^2} - \frac{A}{B-C} \tag{5.9}$$

with following definitions:

$$\begin{aligned} A &= [S_1, D_1] + [S_2, D_2] \\ B &= [S_1, S_2] + [D_1, D_2] \\ C &= [D_1, S_2] + [S_1, D_2] \end{aligned} \tag{5.10}$$

The impedance tensor can be rotated into the coordinate system of the geological strike by applying the rotation matrix $\underline{\underline{R}}_\alpha$ to the electrical and magnetic field components:

$$\left.\begin{aligned} \underline{E}' &= \underline{\underline{R}}_\alpha \underline{E} \\ \underline{H}' &= \underline{\underline{R}}_\alpha \underline{H} \end{aligned}\right\} \underline{\underline{Z}}' = \underline{\underline{R}}_\alpha \underline{\underline{Z}} \underline{\underline{R}}_\alpha^T \tag{5.11}$$

After this rotation the impedance tensor shows the typical characteristics of a two-dimensional subsurface conductivity distribution.

5.3. Data

At the Roter Kamm impact crater 16 AMT soundings were carried out, being in a North-East-Down coordinate system. All data was measured as a time-series. As an example the time series of the station in the center of the Roter Kamm impact crater is shown in Figure 5.3a. It shows the recording time of 20 min and both electric field components show a shift in the voltage level after 10 min. However, any long period contamination does not affect the transfer function due to the band pass filtering applied in the processing stage. The power density spectra of the magnetic field components appears to be uncontaminated

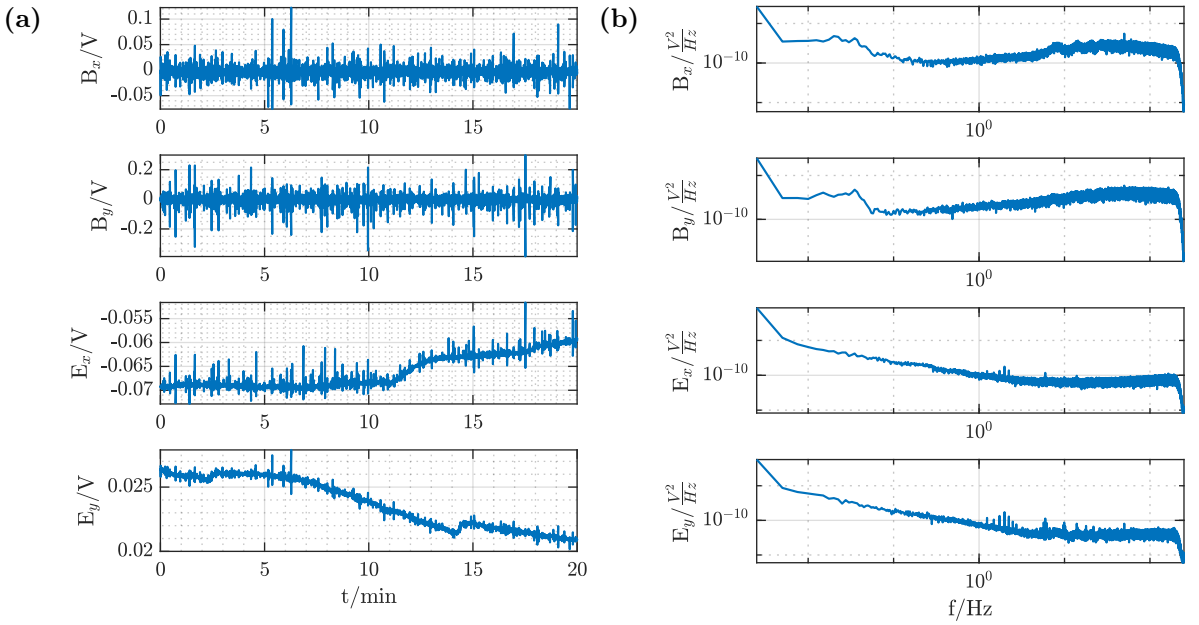

Figure 5.3.: Time series displayed in measured voltages (a) and power spectra (b) of the AMT sounding 0003 with a sampling frequency of 500 Hz in the center of the Roter Kamm impact Crater. In (a) and (b) the components are shown in the following way from top to bottom: the magnetic field components B_x and B_y and the electric field components E_x and E_y.

by noise, except for a peak at 50 Hz related to the power grid in Namibia. It is only visible in the B_x component as well as the E_y component. In the electric fields signals with frequencies around 2 Hz and their harmonics are visible, which cannot be correlated to the natural EM spectra (e.g., Constable and Constable, 2023)

The time-series were processed using the EMERALD processing tool (Ritter et al., 1998). The first step is to calculate the Fourier transforms and calibrate the magnetic fields with the sensor calibration functions for each used induction coil. Measured electric field time-series are normalized to the receiver length. Now linear systems in the form of

$$Z = aX + bY + \delta Z, \qquad Z = \{E_x, E_y\}, \qquad X = B_x, \qquad Y = B_y \tag{5.12}$$

must be solved. It is assumed that only the electrical field has an error δZ. Using the Least-Squares approach to minimize δZ, the impedance tensor elements ($a = \{Z_{xx}, Z_{xy}\}$, $b = \{Z_{yx}, Z_{yy}\}$) can be calculated using the auto- and cross-spectra of the magnetic and electrical field components (Ritter et al., 1998):

$$\begin{aligned} a &= \frac{\langle ZX^* \rangle \langle YY^* \rangle - \langle ZY^* \rangle \langle ZX^* \rangle}{\langle XX^* \rangle \langle YY^* \rangle - \langle XY^* \rangle \langle YX^* \rangle} \\ b &= \frac{\langle ZY^* \rangle \langle XX^* \rangle - \langle ZX^* \rangle \langle ZY^* \rangle}{\langle XX^* \rangle \langle YY^* \rangle - \langle XY^* \rangle \langle YX^* \rangle} \end{aligned} \tag{5.13}$$

The auto- and cross spectra are calculated and stacked from several time segments and afterwards averaged over a certain frequency band (Ritter et al., 1998). Particularly noisy frequencies can be rejected by applying a coherency threshold. The coherency Ψ is a level of random noise and can be calculated as a ratio between cross- and auto-spectra between the electric and magnetic fields (Simpson and Bahr, 2005):

$$\Psi = \frac{\langle E_i^* B_j \rangle}{\langle \langle E_i^* E_i \rangle \langle B_j^* B_i \rangle \rangle^{1/2}} \tag{5.14}$$

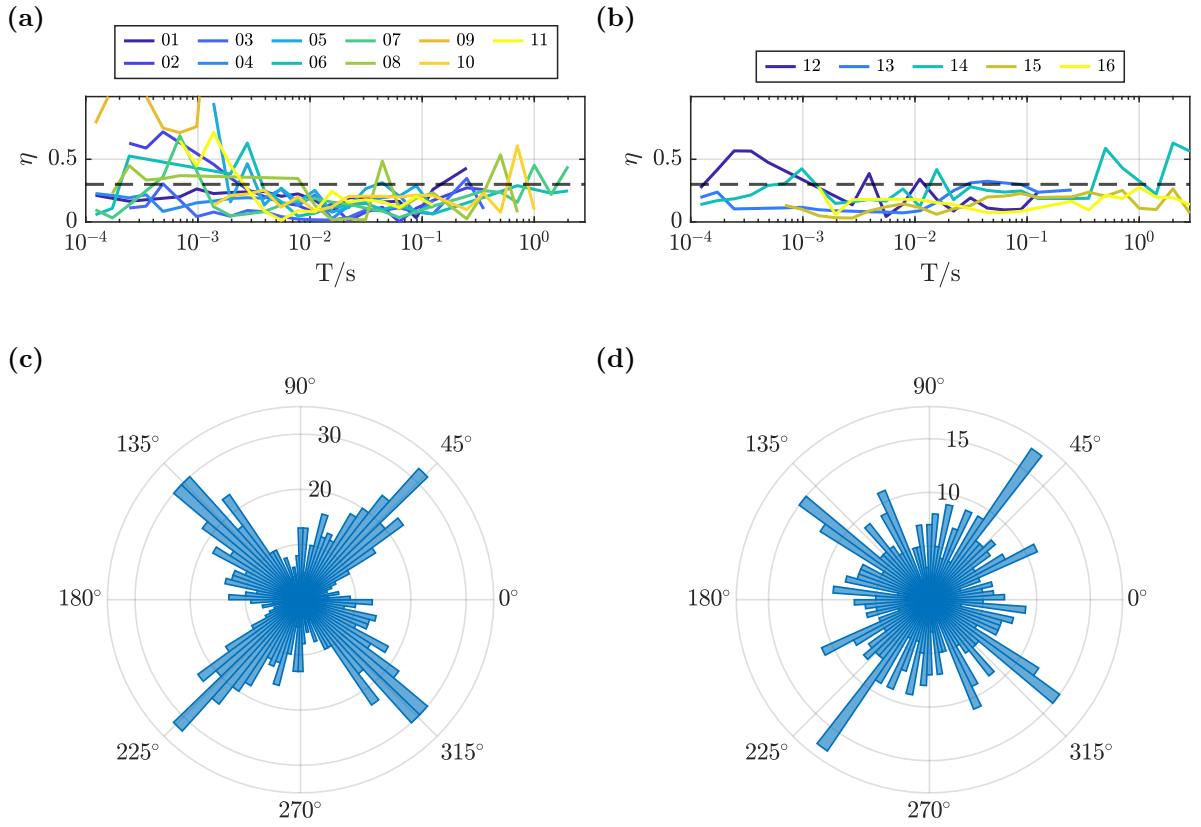

Figure 5.4.: Dimensionality analysis. **(a)** and **(b)** Phase-sensitive skew of the AMT transfer functions. The dimensionality threshold are indicated in a black dashed line. Below this value the data is assumed to be two-dimensional. The data is presented in a gradient from dark blue to yellow. **(a)** Soundings 01 to 11 along Profile 1. **(b)** Soundings 12 to 16 along the regional profile. **(c)** and **(d)** Rose diagrams of the strike angles. **(c)** Soundings 01 to 11 along Profile 1. **(d)** Soundings 12 to 16 along the regional profile.

The coherency level can have values between 0 and 1, with 1 being fully coherent signals containing less random noise. Different coherency levels were tested to find the one which leads to the smoothest transfer function, but includes a reasonable number of data points. This process was also an indicator of the data quality. The frequency range covers frequencies from 0.3536 to 8192 Hz. However, not all transfer functions contain data within the entire range, as the data quality varies throughout the survey.

Dimensionality and Strike Angle Analysis

As no strike angle was known prior to the survey, the coordinate system of the data is unlikely to coincide with any strike direction if even present. Therefore, the skew (Equation 5.6) was calculated for all transfer functions (Figure 5.4). η is exceeding the proposed threshold value of 0.1 for many periods and soundings at Profile 1 and the regional profile (Figure 5.4). However, it stays below a value of 0.3 for periods shorter than 3×10^{-3} s. According to Bahr (1991), the model can still be used, when strike angles can be calculated. As both models lead to the same result in this case, the strike angles were calculated using the phase-sensitive model.
For the strike angle analysis periods shorter than $T = 3 \times 10^{-3}$ s were generally excluded, as the shallow subsurface seems to include small local anomalies (Figure 5.4a and b).

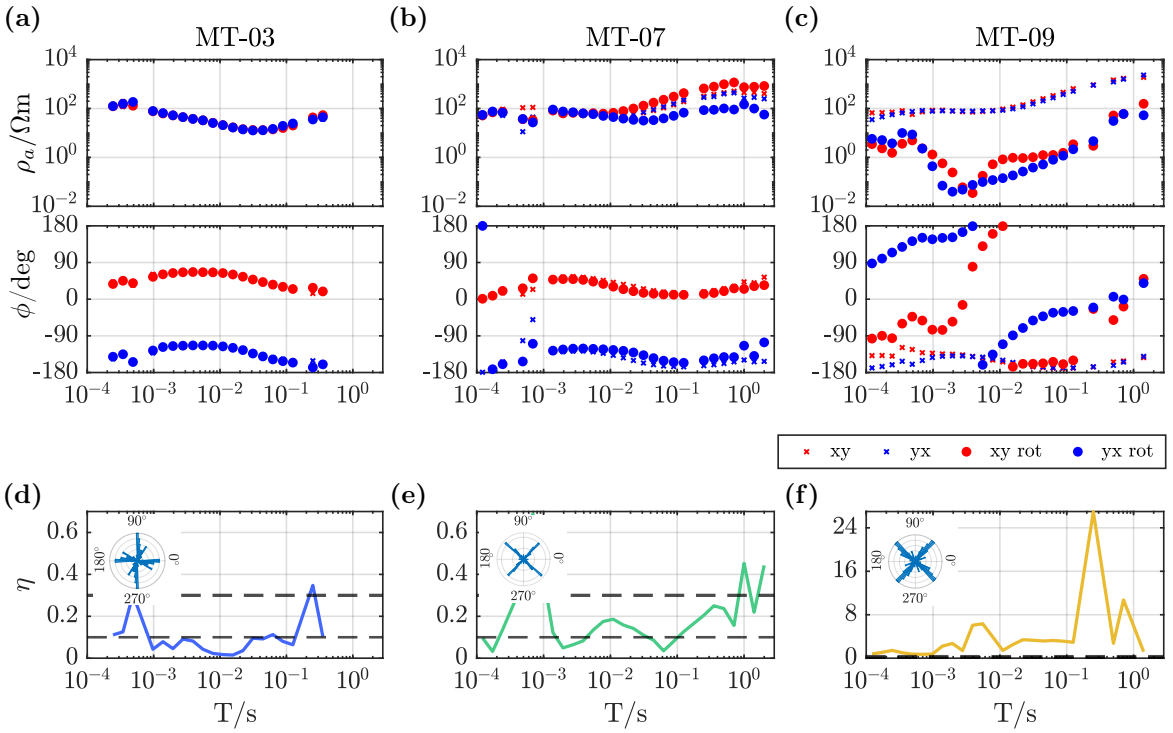

Figure 5.5.: Dimensionality analysis and transfer functions of selected soundings. The upper two panels show apparent resistivity and phase for the original coordinate system (crosses) and the one rotated onto the regional strike direction (circles). The xy-polarisation or TE-mode is indicated in red, the yx-polarisation or TM-mode in blue. The lower shows the phase-sensitive show (η). Rose diagrams for each sounding are shown in the upper right corner of each skew plot. **(a)** and **(d)** MT-03 in the center of the Roter Kamm impact crater. **(b)** and **(e)** MT-07 on the inside slope of the crater. **(c)** and **(f)** MT-09 on top of the crater rim.

The Rose diagrams show a local strike. However, due to the ambiguities knowledge of the region is necessary to determine the appropriate options. Profile 1 has a 43° heading and is perpendicular to the rim of the Roter Kamm impact crater and the faulting in the Aurus Mountains. Therefore, a regional strike direction of 46° for Profile 1 and 54° for the regional profile seem the most likely. However, not all transfer functions indicate a two-dimensional subsurface. In fact, all three dimensions can be found in the survey area. For illustration Figure 5.5 presents three soundings along Profile 1. In the center of the Roter Kamm impact crater (MT-03) the phase-sensitive skew is very low and the strike angle seems to be 0°, 90° or their ambiguities. Nevertheless, both polarisations show the same magnitude indicating a one-dimensional subsurface. Closer to the rim (MT-07) the situation is different and the skew is higher and the strike angle matches the determined. The rotated transfer functions show a typical behaviour of a 2D subsurface structure. Here, both polarisations show the same apparent resistivity for small periods, but for longer periods the curves diverge, although they were similar before rotation. The last example is on top of the rim (MT-09). The transfer function is clearly not 1D or 2D (Figure 5.5f), even though the strike angle analysis shows the determined strike angle of 46°. The apparent resistivity and phase of the unrotated impedance tensors are smooth. However, the expected 180° between both polarisations is not present like in the transfer functions of the other two soundings. The apparent resistivities of the rotated tensor are significantly smaller and the phases show high gradients and discontinuities. Therefore, I

conclude that a 3D resistivity structure is present at the rim.
Furthermore, it can be seen that the presence of one or more outliers in the impedance tensor at a frequency can lead the rotated transfer function to appear noisier than the original data.

5.4. 2D Inversion

The AMT data was inverted with the freely available, 2D inversion algorithm MARE2DEM, suitable for MT, Controlled-Source and surface-borehole EM data both on- and offshore (Key, 2016). MARE2DEM uses unstructured grids with arbitrarily shaped polygons, such as triangles or quads. This provides a high flexibility to image different shapes of bodies. Furthermore, it possible to incorporate topography by aligning the electric fields with the topography at the measurement location. MARE2DEM uses a dual-grid approach, where the grid for the forward calculation is automatically refined if necessary and not identical with the inversion grid. This is very efficient as the fine grid for the forward calculation does not effect the memory requirements. For the inversion MARE2DEM is using a fast parallel implementation of the Occam inversion method. MARE2DEM contains a large number of MATLAB interface tools to design meshes, create input files and plot models and data. MARE2DEM is very well documented and has an extensive manual with description of all necessary files and parameters al well as about the functions of the algorithm[1].

In MAR2DEM the forward response can be rotated to the survey coordinate system. Therefore it was not necessary to rotate the data. Rotating the data would result in loss of data due to noisy impedance tensor elements. In addition, the static shift correction factors derived from the rotated data proved inadequate for MT-02. Therefore, the process was repeated using the original apparent resistivities. This procedure was more successful as the curves were less noisy and the visible shift between MT-02 and the other curves could be eliminated.

5.4.1. Inversion Results

A 2D inversion was performed on Profile 1 and the regional profile. Figure 5.6 shows the data fit of three soundings. The data shows a high noise content. Hence, a relatively high error of 15 % on apparent resistivity and a constant 6.5° error on phase was assumed. A possible cause for the high noise content are the high electrode contact resistance during the field survey and the short recording time. A high electrode contact resistance affects the comparably high frequencies used in AMT more than methods such as MT, where lower frequencies are measured (Zonge and Hughes, 1985). According to tests, the electric fields measured for ungrounded electrodes appear to be shifted to a lower magnitude compared to perfectly grounded electrodes. For decreasing electrode contact resistances, the shift to a lower magnitude happens at increasing frequencies (Zonge and Hughes, 1985). This effect could let the shallow subsurface appear less resistive than it

[1] `https://mare2dem.bitbucket.io/master/index.html`

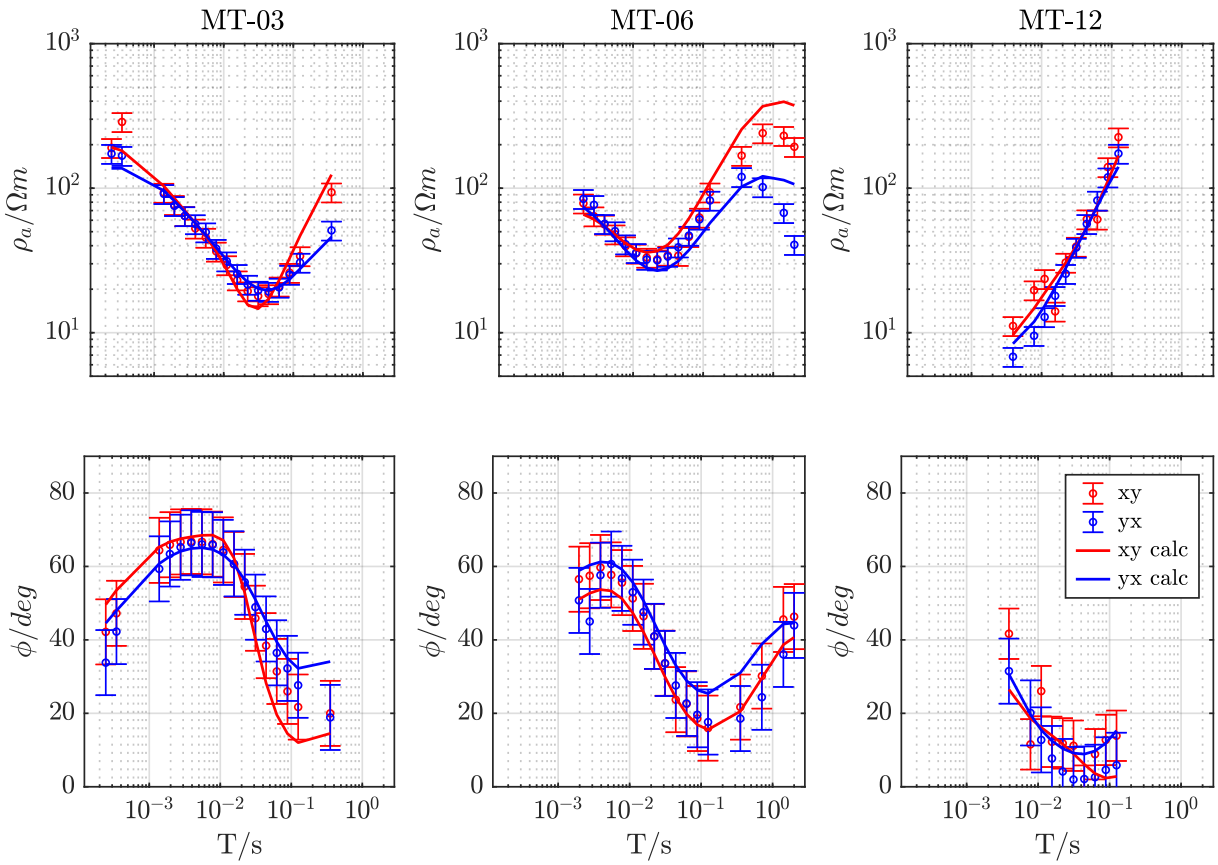

Figure 5.6.: Data fit of apparent resistivity and phase curves of three AMT soundings. The xy-mode is indicated in red, the yx-mode in blue. Measured data is shown circles with errorbars and the modelled response with the solid lines. The sounding locations were in the center of the Roter Kamm impact crater (MT-03), on the inner North-Eastern slope of the crater (MT-06) and on the plain outside of the crater (MT-12).

is in reality. Therefore, the TEM measurements are more reliable for the shallow subsurface, as they are inductively coupled and measure only the magnetic field. In particular, the phases show erratic behaviour. The yx-mode of MT-12 shows high noise content. Here, the yx-mode does not equal the TM-mode, as the data coordinates are not in the geological strike coordinate system. Overall the apparent resistivities could be fitted well. However, there are exceptions, such as MT-06, where at long periods the calculated and measured apparent resistivities diverge.

The inversion models of Profile 1 and the regional profile show very simple models (Figure 5.7. The data fits are shown in the Appendix (Figures A.13 and A.14). The inversion was performed with roughnesses of $\theta_x = 30$ (default) and $\theta_z = 0.1$, which is smaller than the default to allow for higher contrasts. A triangular mesh was chosen for the inversion, as the curved boundaries were expected within the Roter Kamm impact crater. Along Profile 1 the most dominant feature is a large conductive anomaly ($\rho < 30$ Ωm) within the Roter Kamm impact crater. It is about 1300 m to 1400 m wide and has a maximum thickness of 200 m. Otherwise, there is only one notable conductive anomaly along the surface outside the crater with slightly lower conductivities than inside the crater. It is less than 50m thick and appears to start somewhere between MT-09 and MT-10 and extends to the north-east end of the profile. The surrounding material appears to be highly

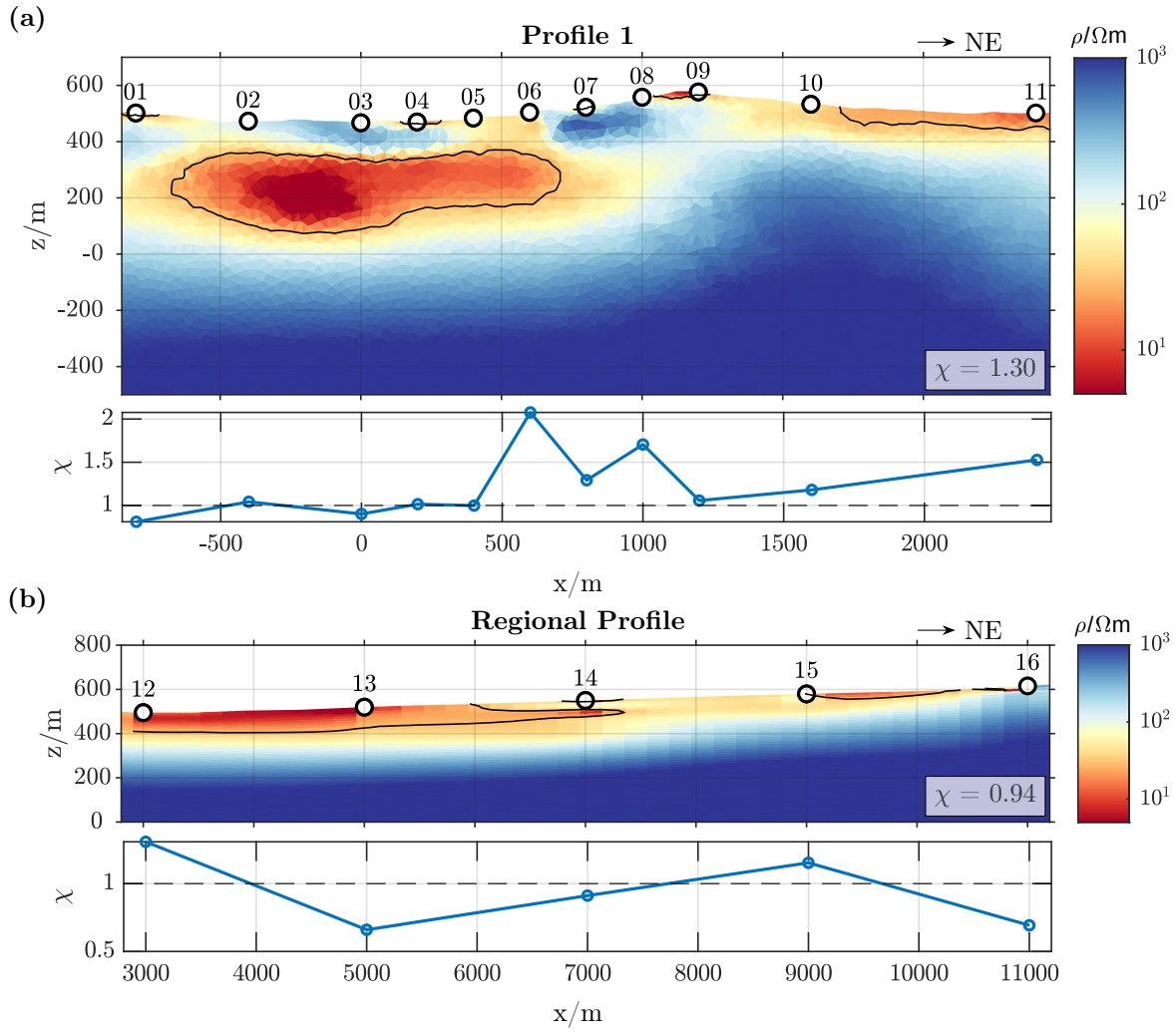

Figure 5.7.: 2D inversion models of the AMT data. The upper panels show the models with the sounding location along the surface. The lower panels show the data misfit χ of each sounding. **(a)** Inversion model of Profile 1 with a χ-value of 1.30. The data misfit is highest on the inner North-Eastern slope of the Roter Kamm impact crater. **(b)** Inversion model of the regional profile with a χ-value of 0.94. Topography data: NASA JPL (2022).

resistive with resistivities greater than 500 Ωm.
The data misfit is highest for stations on the inner, North-Eastern slope. This coincides with the data measured with the non-polarizable electrodes (MT-04 to MT-09). The modelled phases do not agree well with the measured data, the apparent resistivities show deviations for long periods for MT-06, MT-07 and MT-08, especially in the xy-mode.

The regional profile contains only five soundings with quite large distances in between ($\Delta x = 2000$ m). Due to the sparseness of the data, the model roughness is a factor of 10 higher ($\theta_x = 300$ and $\theta_z = 1$) than for the other model. Furthermore, a quadrilateral grid was used, as the conductive structure extents along the whole profile. Quads are more efficient, as they can be elongated in one direction (x), where no high spatial resolution is existing and thin where the data provides higher vertical resolution. The conductive anomaly along this profile appears to have high conductivities in the South-west, which coincides with the lowest topographic elevation of the profile. Conductivities decrease

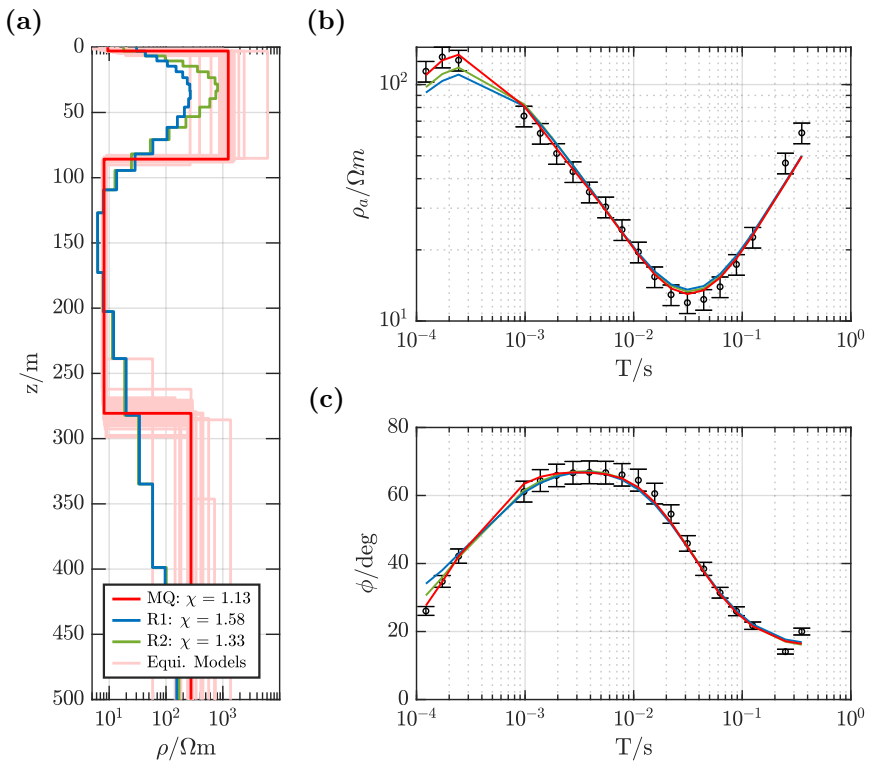

Figure 5.8: 1D Inversion Models of the AMT sounding in the center of the Roter Kamm impact crater. **(a)** The Marquardt-Levenberg model (red) and its equivalents (light red), and the Occam R1 (Blue) and R2 (green) inversion models are presented. The χ-values are shown in the legend. The DOI is deeper than the provided depth range. **(b)** and **(c)** Measured apparent resistivity and phase data is indicated in black, the modelled curves are indicated in red (Marquardt-Levenberg), blue (Occam R1) and green (Occam R2).

towards the Aurus mountains, which seem to consist of resistive material (MT-16). The data-fit is good along the entire profile.

5.4.2. Thickness of Conductive Anomaly

To achieve a better estimate for the vertical layering, a 1D inversion using EMUPLUS is performed. The sounding in the center of the Roter Kamm impact crater shows 1D characteristics and is located on top of the thickest part of the conductive anomaly. An error of 5 % on the impedance tensor elements is chosen, as the apparent resistivities and phase curves are smooth. A homogeneous starting model with a resistivity of 100 Ωm was chosen for the Occam inversions, while the starting model for the Marquardt-Levenberg inversion was based on the Occam R1 inversion model. The 1D inversion of the xy-polarization shows a four layered subsurface in the presented depth section (Figure 5.8). The upper boundary of the conductive anomaly is in a depth of approximately 85 m and is covered by a resistive layer ($\rho = 1000$ Ωm) with a thin more conductive surface layer. The resistivity of the layer is not well resolved, which is expected for the AMT method. The conductive layer has a thickness of 195 m and a conductivity of 8 Ωm. While the upper boundary is well resolved, the lower boundary has a lower resolution. A study of the resolution is presented in Section 7.3.

5.5. Summary

The AMT method is a passive, frequency domain method and is well suited to detecting conductive bodies at depths of up to several kilometres. During the measurement,

the electrode contact resistance proved to be a challenge and reduced the data quality. Strike angle analysis showed that the electrical conductivity in the subsurface has a two-dimensional structure, except at the crater rim. A strike angle of 46° was determined for Profile 1 and 54° for the regional profile, consistent with the direction of the crater rim and the direction of faulting in the Aurus Mountains. Due to the high noise in the data, a high data error was assumed for the 2D inversions with MARE2DEM (Key, 2016). The 2D models show consistent simple structures consisting of a large conductive anomaly inside the Roter Kamm impact crater and a layered subsurface outside the crater. The anomaly inside the crater extends horizontally for 1300 m to 1400 m and vertically to 195 m with the upper limit at a depth of about 85 m to 100 m. The data mismatch is greatest in the area where the non-polarisable electrodes were used and increased surface conductivities are visible. A thick conductive layer is visible at the surface outside the crater. The layer along the regional profile appears to be thicker than immediately outside the crater and appears to become thinner towards the Aurus Mountains.

CHAPTER 6

TEM Data Processing and Data Overview

The TEM survey was conducted using the single-loop and the fixed-loop setups. Therefore, different receiver units were necessary. The TEM-FAST 48 provides the user with processed data including error estimates. However, it is necessary to prepare the measured time series data of the fixed-loop TEM survey for the interpretation and inversion stage. The induced voltage time series must be transformed into a single induced voltage decay curve for each sounding and component. During the field survey at the Roter Kamm impact crater, 216 transients were recorded with the fixed-loop TEM setup and 79 with the single-loop setup. The data require a thorough investigation of the data quality, consistency and comparability of each data set. Appropriate post-processing is also required as factors such as the shape and length of the ramp are taken into account by the TEM inversion. A further test must be carried out to check the difference in response between the point and an extended receiver.
All data not shown in this Chapter can be found in the Appendix A. All processed TEM data is archived in the CRC 1211 Database:

- Aurus clay pan: Nienhaus et al. (2023a)
- Roter Kamm impact crater: Nienhaus et al. (2023b)

6.1. The Single-Loop Data-Set

A dense single-loop data set was acquired along three profiles at the Roter Kamm impact crater. The data is very consistent and shows smooth transitions along the profiles. However, there are several factors affecting the data that need to be discussed prior to inversion. One of these effects is the influence of the non-linear ramp. Another is the different response of a point receiver and an extended receiver. This effect is particularly interesting as only point receivers are implemented in the inversion algorithms used. It is important to understand these effects and try to quantify systematic problems that cannot otherwise be considered. In addition, two different loop sizes were used to achieve high spatial density with small loops and greater penetration depth with larger loops. It is necessary to compare the data carefully and investigate the differences.

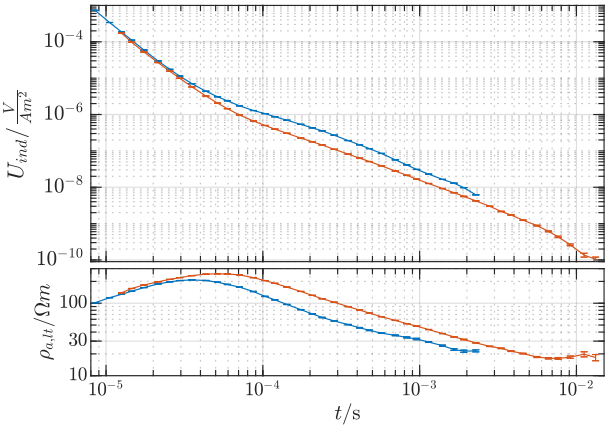

Figure 6.1: Comparison of the two different loop sizes at the centre of the Roter Kamm impact crater. Data from the large single loop (100×100 m^2) are shown in orange and the small (50×50 m^2) in blue. t = 0 s is defined at the start of the ramp. The top panel shows the induced voltages normalised to a transmitter loop area of 100×100 m^2 and the bottom panel shows the late time apparent resistivity transformations.

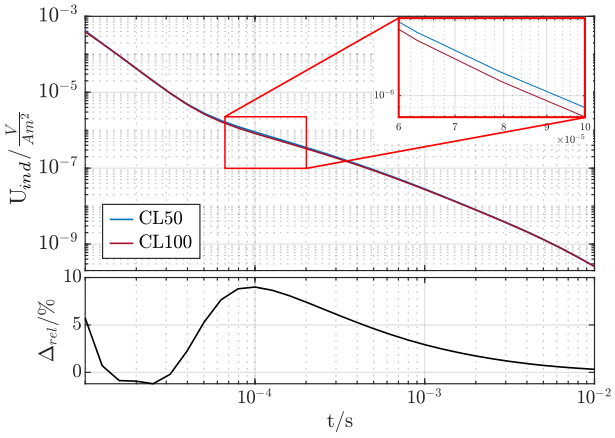

Figure 6.2: Comparison of synthetic data of two different loop sizes with a model similar to the one found in the centre of the Roter Kamm impact crater. Data from the large single-loop (100×100 m^2) are shown in orange and the small (50×50 m^2) in blue. t = 0 s is defined at the start of the ramp. The top panel shows the induced voltages normalised to a transmitter loop area of 100×100 m^2 with a magnified section of the transients and the bottom panel the relative difference between the two transients.

6.1.1. The Different Loop Sizes

Two different loop sizes were used during the field survey at the Roter Kamm impact crater. The larger one had the size of 100×100 m^2 and the smaller of 50×50 m^2.

Figure 6.1 illustrates the induced voltage decays measured during both soundings. A divergence between the transients is very prominent in the times between 5×10^{-5} s and the last time point of the smaller loop. This expresses itself in a shift of the late-time apparent resistivities towards larger depths and higher resistivities for the transient of the larger loop. In general, this can partly be explained by the different loop sizes, as seen in Figure 6.2. Synthetic data was modelled for different loop sizes based on the 1D model at the center of the Roter Kamm impact crater. However, the simulated difference is much smaller (< 10 %) and cannot explain the gap on its own and it is possible multi-dimensional effects are present.
Another important observation is that the larger loop produced a longer transient (Figure 6.1), which results in a higher penetration depth. This can also be seen in the late-time apparent resistivities. The late-time apparent resistivties show a possible four-layered subsurface. The most prominent features are a resistive and conductive layer as second and third layer. However, it seems that a low resistive layer can only barely be detected underneath the conductor, even for the larger loop. Therefore, it is unlikely to resolve the boundary to the lower resistor well.

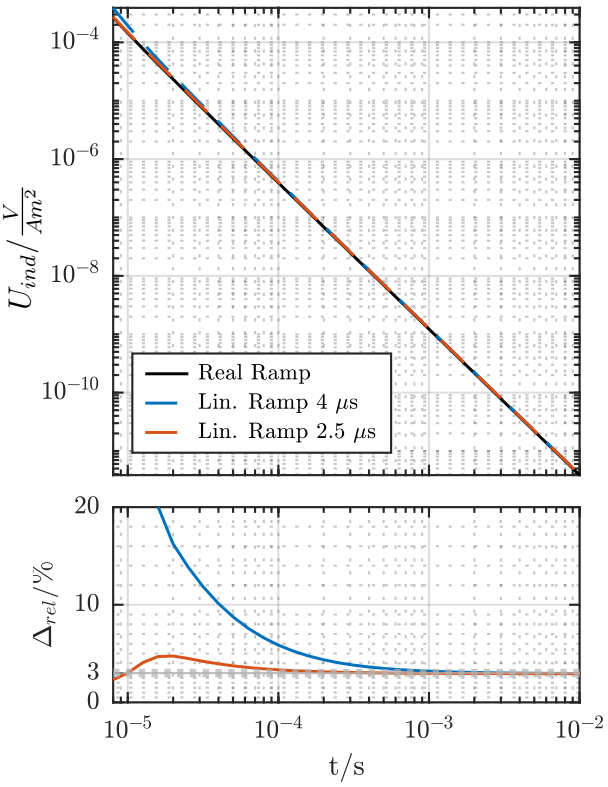

Figure 6.3: Synthetic data of a homogeneous halfspace of 100 Ωm with different ramps. The real ramp (4 μs, black) and two linear ramps with lengths of 4 μs (blue) and 2.5 μs (orange). The upper panel shows the synthetic transients and the lower the relative different of the transients including the real ramp and each linear ramp.

6.1.2. The Non-Linear Ramp

During the field survey the transmitted current signal was observed and one ramp recorded with an oscilloscope (Figure 4.6a). The ramp appears to be approximately 4 μs long, but continuous to fluctuate for at least 5 μs longer. Figure 6.3 shows the comparison of the real ramp (first 4 μs) and linear ramps with two the lengths 4 μs and 2.5 μs. At late times a deviation of 3 % is visible. Using the linear ramp of 2.5 μs, this deviation increases slightly at early times to a maximum of 4.75 % at 2×10^{-5} s . However, using the linear ramp of 4 μs, a strong relative difference is visible in the early times.
Different lengths for the real ramp were tested up the maximum recorded length of 10 μs. However, the stable deviation of the linear ramps at late times is highly dependent on the exact position were the ramp is cut due to the small scale fluctuations at late times (3 % to 7 %). While the ramp of the Zonge ZT-30 zeroTEM transmitter, used for fixed loop measurements, has been recorded for a longer period of time, this current signal has not. All approximations are based on two recordings. Therefore, the usage of the real ramp is considered unreliable due to low data quality and short recording time. Hence, the 2.5 μs linear ramp is used in all subsequent inversions. A minimum error of 3 % must be considered for the data during inversion.

Unfortunately, no transmitter current recording was performed during a measurement with the large 100×100 m^2 loops. However, at five locations measurements with both transmitters were conducted. A series of Occam R1 inversions were run using different

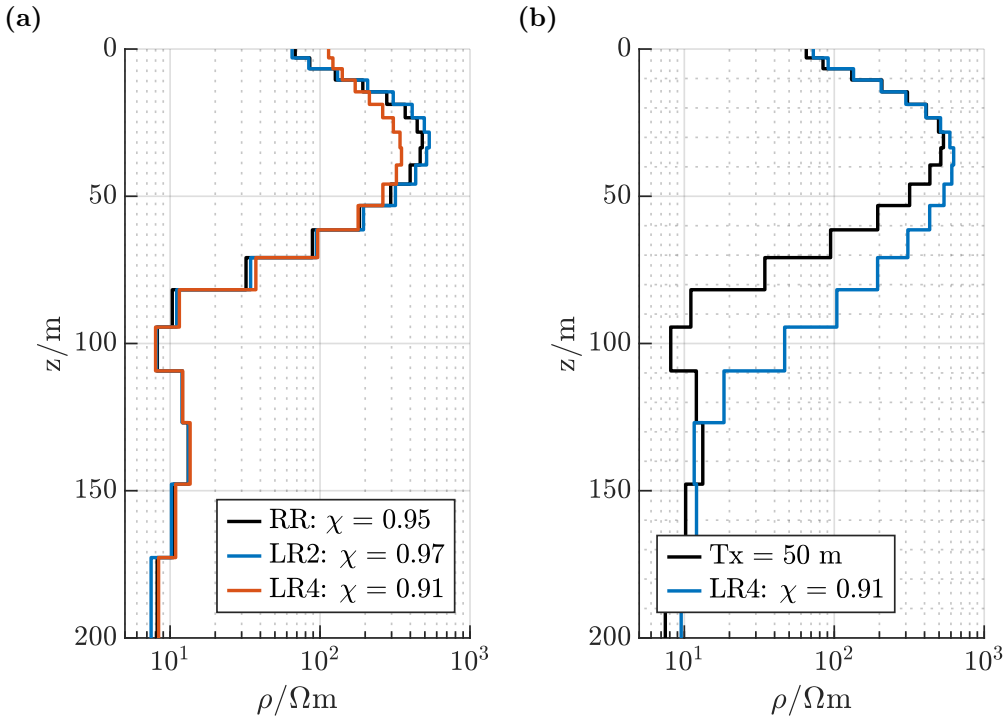

Figure 6.4.: Inversions of the single-loop data using different ramps at the location in the center of the crater (P1-11). **(a)** Comparison of the real ramp (RR), a linear ramp with the length of 4 μs (LR4) and a linear ramp of 2.5 μs (LR2). The loop size is 50×50 m^2. **(b)** Comparison of the inversion models of the small loop (Tx = 50 m) and the larger 100×100 m^2. A linear ramp of 4 μs (LR4) is used.

linear ramps. The Occam R1 model of the small loop was used as a reference model to determine an approximate ramp length. Figure 6.4a shows the inversion models of the small loop with the real ramp and linear ramps of 4 μs and 2.5 μs. Figure 6.4b compares the inversion model including the real ramp with the inversion model of the large transmitter loop with the linear ramp that matches the early times best. However, the transition to lower resistivities happens at later times. This discrepancy is visible in the field data. This test shows, that the gap cannot be totally explained by the different loop sizes. Therefore, another factor affects the data.

6.1.3. Comparison of Synthetic Single- and Central-Loop Data

The 1D inversion algorithm EMUPLUS has only point receivers implemented. Therefore, it is necessary to quantify differences between a single- and a central-loop sounding. To achieve this a large number of forward calculations were performed inside a transmitter loop. The minimum distance to the transmitter is 0.5 m, as no solution can be calculated on the transmitter location. Only solutions in one quadrant of the transmitter are needed due to the symmetry of the magnetic field. Transients were calculated on a 41×41 regular grid. All transients are then discreetly integrated over the loop quadrant and multiplied by four and normalized to the integration area. Figure 6.5 shows a comparison of synthetic single- and central-loop data and the single-loop inversion results for a 100 Ωm homogeneous halfspace. For both loop sizes strong deviations between the single- and central loop transients are visible in the first time decade. The larger loop is more

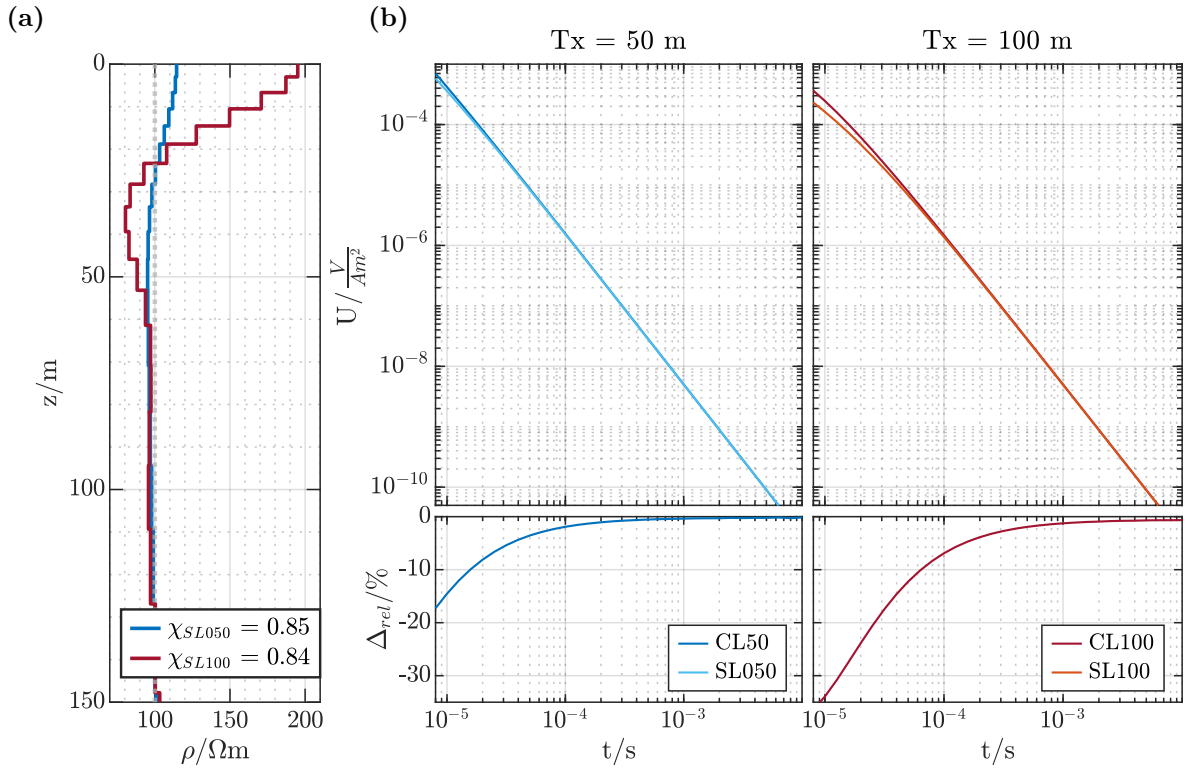

Figure 6.5.: Comparison of single- and central-loop data of a homogeneous halfspace of 100 Ωm using two different transmitter sizes. Data of the large loop (100×100 m^2) is presented in reds, data of the small loop (50×50 m^2) in blues. **(a)** Occam R1 inversion models of the single-loop transients. The 100 Ωm are marked with a light gray line. The data fit is presented in the legend. **(b)** Synthetic transients of two transmitter loop sizes of both central- and single-loop setup. The lower panel shows the relative differences between the central- and single-loop transient for each loop size.

affected by the different receiver areas than the smaller loop. This can be explained by the downward and outward movement of the equivalent current filaments (Figure 2.3a). For early times the flux density of the secondary magnetic field is maximal in the center of the loop, but lower closer to the transmitter. For later time stages the current filaments increase in size and the flux density becomes homogeneous inside the larger single-loop receiver area. Therefore, no deviation is visible for the later times of the transient. For a large loop the magnetic field is more inhomogeneous inside the single-loop area, and thus, more distinct than for smaller transmitters. The deviation between the central- and single-loop transient also influences the inversion results for shallow depths (Figure 6.5a). For depths larger 80 m the differences seem negligible, but for smaller depth both inversion models show deviations. However, the differences of the inversion model of the smaller transmitter loop are quite small and have a maximum at the most shallow depth of 20 % on a linear scale. On a logarithmic scale the deviation is barely 4 %. However, the deviation of the inversion model of the large transmitter is quite significant on both scales, on a linear scale almost 100 % and on a logarithmic one still 15 %. The effect increases for increasing conductivities as well. Therefore, this difference between a single-loop and central-loop receiver area must be considered, if the area cannot be accustomed for during the inversion process.

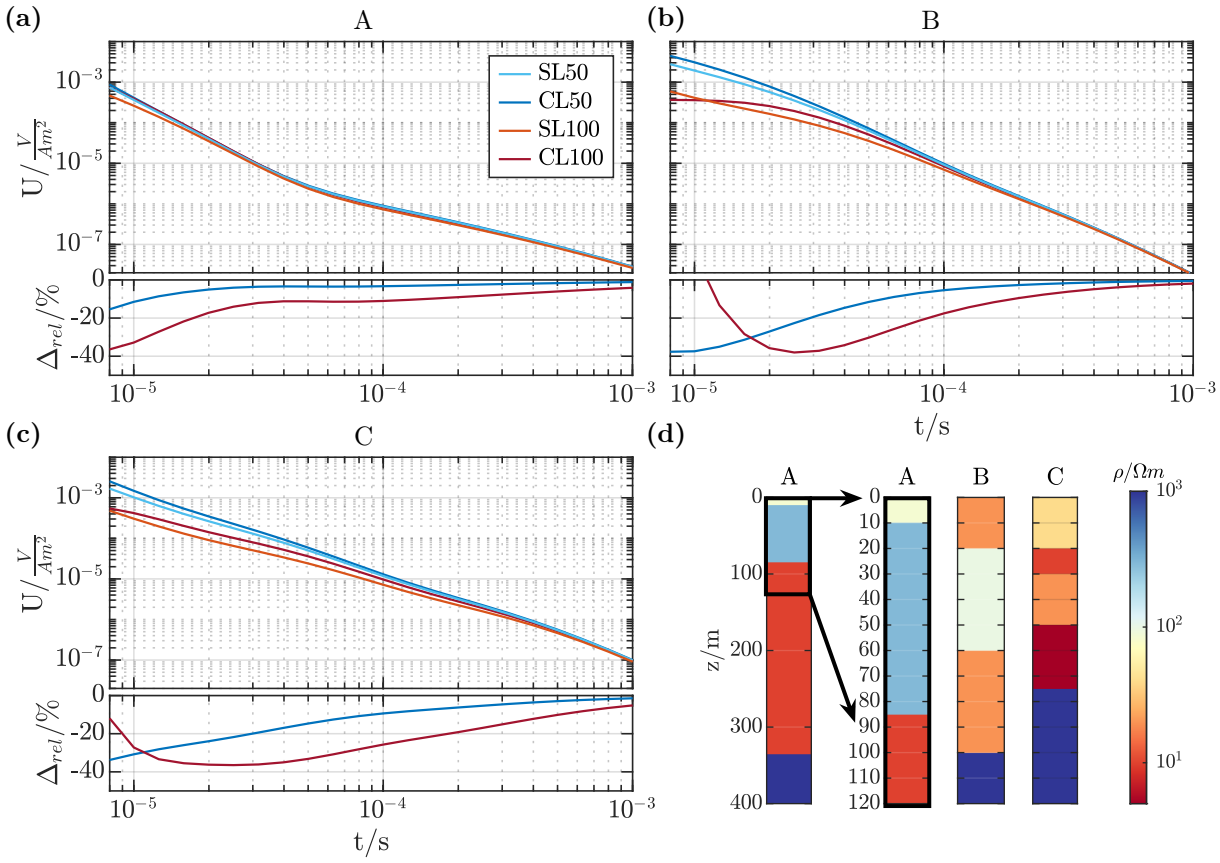

Figure 6.6.: Comparison of synthetic induced voltages of single- and central-loop TEM setups for different realistic layered cases. The blue colours indicate transmitter loops with an area of 50×50 m^2 and the red of 100×100 m^2. The lighter colors are indicative of the single- and the darker of the central-loops. The lower panels show the relative difference in percent between the single- and central-loop transients. **(a)**, **(b)** and **(c)** show synthetic data of models "A", "B" and "C". **(d)** Models "A", "B" and "C" as columns.

For a realistic assessment of the deviations on the field data, transients for three models based on three different locations were calculated for both loop sizes and setups. The locations chosen were in the center of the Roter Kamm impact crater (Model A), on the plain next to the crater (Model B) and one location explanatory for the regional profile (Model C). Inside the crater the central- and single-loop setups of the small loop (50×50 m^2) only have small deviation of maximal 3.5 % and only the first few time points deviate more strongly. The other two models show a much stronger difference between the two setups at early times up to 35 % to 40 %. Both of them are more conductive in shallower depths then Model A, with Model C being the most conductive. The behaviour of both curves is slightly different, as Model C causes a more linear course of the relative difference than Model B. The large loops show a similar trend as the small loops, but are more affected. The first decade shows deviations up to 40 % percent. This shows that all data is affected, especially those measured outside the crater due to the high conductivities in shallow depths. As the conductive layer inside the crater is buried, the effects are minimal. Nevertheless, it is necessary to account for the deviations of the single-loop data compared to the central-loop data as EMUPLUS only has a solution

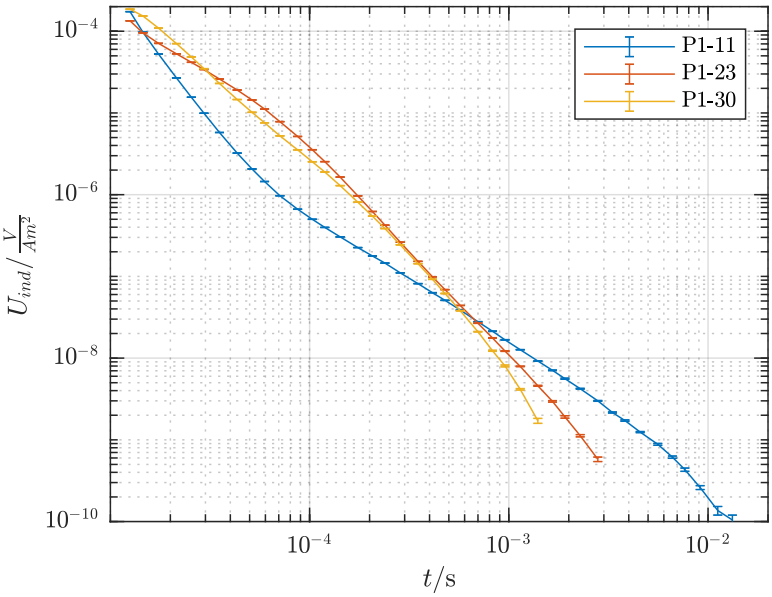

Figure 6.7.: Comparison of transients at different locations along Profile 1 measured with the loop area of 100×100 m^2. The locations are in the center of the Roter Kamm impact crater (P1-11, blue), on top of the crater rim (P1-23, orange) and on the plain next to the crater (P1-30, yellow).

for a point receiver implemented. Therefore, a minimum error level of 3.5 % is set for all 1D inversions. Additionally, the first decade of the transients is down-weighted for the small loops outside the crater with a linear increase to an error level of 10 % at the first time gate on a logarithmic time axis. The large loops are much more severely affected and the first two decades are down-weighted. It seems reasonable to remove the first decade of data due to the high deviations and the unknown ramp. At the locations of half of the measurements, soundings with a small loop were carried out as well. At those locations a combined inversion of both transients without the first decade of data of the large transmitter is the best option to get the most trustworthy model. Under the assumption that the layering in shallow depths is constant, it would be possible to combine the informations of neighbouring stations with each other to achieve a model that also has resolution in the shallow depths.

6.1.4. Overview of Data-Set

The data-set at the Roter Kamm impact crater consists of 79 single-loop transients measured with two different loop sizes. Exemplary, transients of three locations are presented in Figure 6.7, measured with the large single-loop. P1-11 is in the center of the crater, P1-23 on top of the crater rim and P1-30 on the plain next to the crater. The data from the crater center has a totally different behaviour than the other two transients. It indicates a much more resistive shallow subsurface due to its steep voltage decay. At the other two locations the data has a slower decay at early times and a faster at intermediate and late times. Comparing the two transients on top of the rim and on the plain, it becomes clear that the subsurface differs significantly in and outside of the Roter Kamm impact crater.

To get an overview of all data and their gradual behaviour along the profiles sections along those are presented in Figure 6.8. Overall, the induced voltages are very consistent

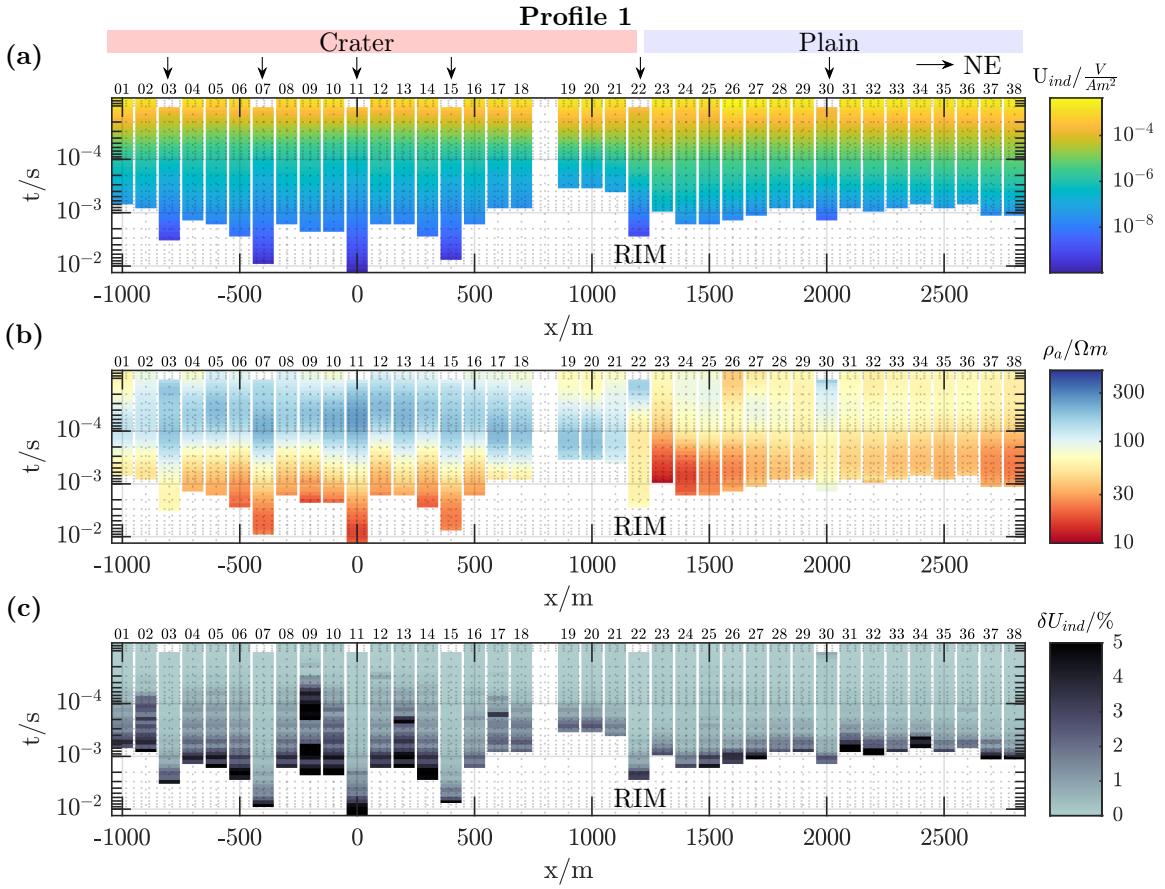

Figure 6.8.: Single-loop TEM data along Profile 1. All data is normalized to a transmitter area of 100×100 m^2 for comparison. The x-axis denotes the position along Profile 1 with the center of the crater being the reference (x = 0 m). The y-axis indicates the time after initiating the current turn-off. (a) Induced voltage, (b) late-time apparent resistivity and (c) relative error of the induced voltage. As the late-time apparent resistivity is a transformation of the data, it only differs from the induced voltage error by a factor of 2/3. The location of the large loops are indicated by the downward pointing arrows at the top.

along the whole Profile 1, as well as the other profiles (Figure A.4). The large loops are easily identifiable by the longer transient length at the marked locations. The slight difference between the neighbouring transients is also visible in this presentation. The transient are shortest south-east of the crater rim and longest inside the crater. Furthermore, the voltage amplitude is higher outside of the crater. The late-time apparent resistivity transforms reveal a resistive shallow subsurface inside the crater with a conductive layer underneath. On the outside the subsurface seems to be less resistive in shallow depths. The small single-loop TEM data shows higher data errors inside the crater, with especially high errors at location P1-09 of Profile 1 (Figure 6.8). Data of the larger single-loop TEM (locations marked by arrows) and data outside of the crater exhibit generally smaller errors.

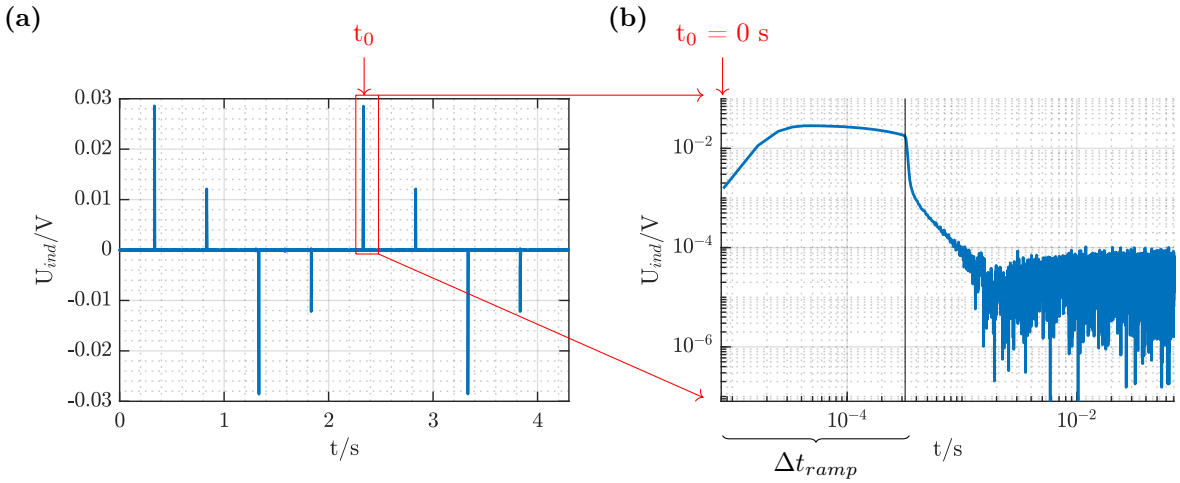

Figure 6.9.: (a) Filtered time series of the central-loop sounding at fixed-loop transmitter A with a transmitted base frequency of 0.5 Hz. (b) Magnification of transient behaviour of the induced voltage. It is visible that the input voltage of the SMARTem24 receiver unit was exceeded during turn-off of the current signal (time period Δt_{ramp}).

6.2. The Fixed-Loop Data-Set

A fixed-loop data-set was collected along Profile 1 at the Roter Kamm impact crater. In total four transmitter loops with a loop area of 200 × 200 m^2 were used. At each transmitter 21 soundings were made with a maximum offset of 400 m at each side of the transmitter loop. The distance between the receiver position was 50 m to 100 m. The ramp effecting the data has a length of 320 μs and is approximately linear. It must be considered due to its sheer length alone. However, the data must be transformed from the raw time-series to a transient with error estimates by applying a log-gating and selective gate-stacking algorithm. In the following the vertical component is denoted with "z", the excited horizontal component along the Profile 1 with "x" and "y" along the perpendicular transects, the weak component at the Profile 1 is denoted with "y".

6.2.1. TEM Data Processing

Both the SMARTem24 and KMS-820 recorders measure continuous time series. Therefore, the processing of their data is identical. In this thesis, I apply a log-gating approach based on Munkholm and Auken (1996) and Larsen et al. (2021) and a selective gate-stacking (Hanstein et al., 1986).
The first step is to apply digital filtering to the time series. Here a three-point filter is used, which is described in Mörbe (2020). It averages each point with the time points half a period earlier and then later (forward and backward movement). This filter removes correlated noise, e.g. by power lines (f = 50 Hz in Namibia). It removes the DC level by averaging two different polarities and linear drift. After filtering, the time series is cut into individual sections with a length of half a period starting at the time points of the transmitter turn-off. Only those time periods are kept, during which the transmitter was switched off. Due to the alternating polarity of the transmitter current, every second segment is multiplied by a factor of −1 (Figure 6.9). The ramp of the transmitter is

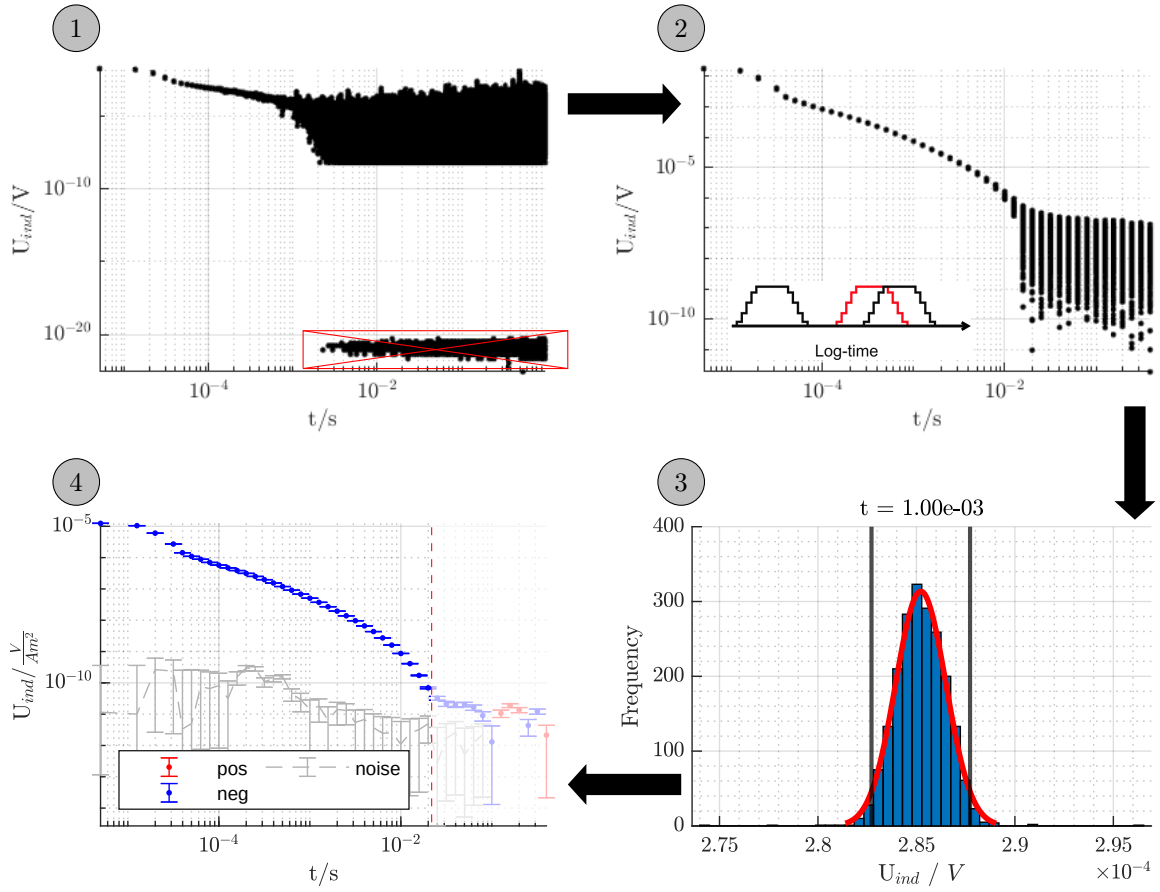

Figure 6.10.: TEM data processing steps at the example of the central-loop sounding of fixed-loop transmitter A. (1) All data points with the reference time point $t_0 = \Delta t_{ramp}$. The data point with no physical meaning (below the resolution threshold of the receiver device) are removed. Here the resolution limit is 4.9×10^{-9} V, which is lower than the theoretical value estimated. (2) Log-Gating of the transients with 10 time gates per decade with overlapping windows (50 %). The used semi-tapered window function is show in the bottom left corner (Taken from Larsen et al., 2021). All measured transients are presented. (3) Gaussian statistics at the time gate of 1×10^{-3} s. Symmetric rejection of data points (5 %). (4) Final transient after selective stacking and normalisation to receiver area and transmitter current. The transient shows a behaviour indicating that the voltage is below the resolution limit at late times. This part is therefore manually cut off. The noise level is shown in grey.

considered and the earliest time recording for each transient is set to be at the end of the ramp. At this point, N single transients are prepared for the log-gating and gate-stacking procedure and N is the total number of stacks recorded. The steps of the TEM data processing, which are illustrated by an example in Figure 6.10, are:

1. Removal of all data points below the resolution threshold. The origin of those points is unclear, but they occur in all time series. The resolution limit of the device is clearly visible by the smooth lower limit of the data points (Figure 6.10). It is slightly lower than the estimated limit of 1.2×10^{-8} V with 4.9×10^{-9} V. This observation could be made for many soundings, but was especially prominent for the z-components inside and close to the transmitter.

2. Log-gating of each time gate. For TEM data Munkholm and Auken (1996) proposed to use a log-gating approach to reduce the influence of noise, especially at later times. I chose ten logarithmic equidistant time gates per decade. The time gates contain an increasing number of sample point with increasing time. In this thesis an overlapping semi-tapered window function proposed by Larsen et al. (2021) is used for weighting of the data point at each center time point. This can suppress noise in the later time gates more strongly than a box car window (Larsen et al., 2021). The increasingly large scattering of data points at late times ($> 1 \times 10^{-2}$) indicates the decreasing resolution, rather than the local noise (Figure 6.10).

3. Evaluating the statistics in each time gate. The stacking algorithm is assuming a Gaussian distribution of the population. However, while most of the time gates exhibit a normal distribution, the early time gates deviate from any Gaussian distribution. It is likely that this behaviour is caused by the long ramp of the transmitter device. Therefore, the early time gates are strongly affected by the turn-off current behaviour of the transmitter. Here a symmetric, selective stacking is applied (Hanstein et al., 1986). Which cuts the same percentage of the smallest and largest data off. For this thesis 95 % of the data points are kept. After that the mean μ and the standard error of the mean SEM are calculated (Equation 4.2).

4. Stacked transient. At each time gate the mean is used as the estimation of the true data point and the error is estimated by the 99 % confidence interval of the SEM to prevent underestimation of the data error. The transient was further normalized to the current strength and the effective receiver area.

Two different behaviours of transients reaching the noise level can be observed. A levelling of the transient for later times and a sign reversal at late times followed by a almost constant induced voltage level (Yogeshwar, 2014). Therefore, I manually discarded the late times when the described patterns were recognizable.

6.2.2. Overview of Data-Set

The fixed-loop data was recorded with different receiver units along two transects. However, a comparison shows an identical behaviour at each comparative measurement (Figure 6.11a). The data recorded with the KMS-820 has signs of saturation at early times, therefore, spans less time periods at several locations. The data exhibits the expected changes in polarity of the vertical (z) component at increasingly later times outside of the transmitter (Figure 6.11c and e) and also has sign reversals in the horizontal components (Figure 6.11f).
Figure 6.11 shows the behaviour of the transients with increasing offset between receiver and transmitter of Transmitter C. Transmitter C is located at the outside flank of the Roter Kamm impact crater. Sector "a" starts on top of the crater rim and the distance is maximal at the end of sector "c". Sectors "b" and "d" cover the segments parallel to the rim direction 400 m down the flank. It illustrates the progression in each direction of the transmitter loop (sectors "a", "b", "c" and "d"). Additionally, it presents the noise level in each plot. It is visible that with increasing distance from the transmitter the transients in each sector deviate more. Especially, sector "a" exhibits a different behaviour than the other three directions (Figure 6.11e), the later sign reversal indicates a more conductive

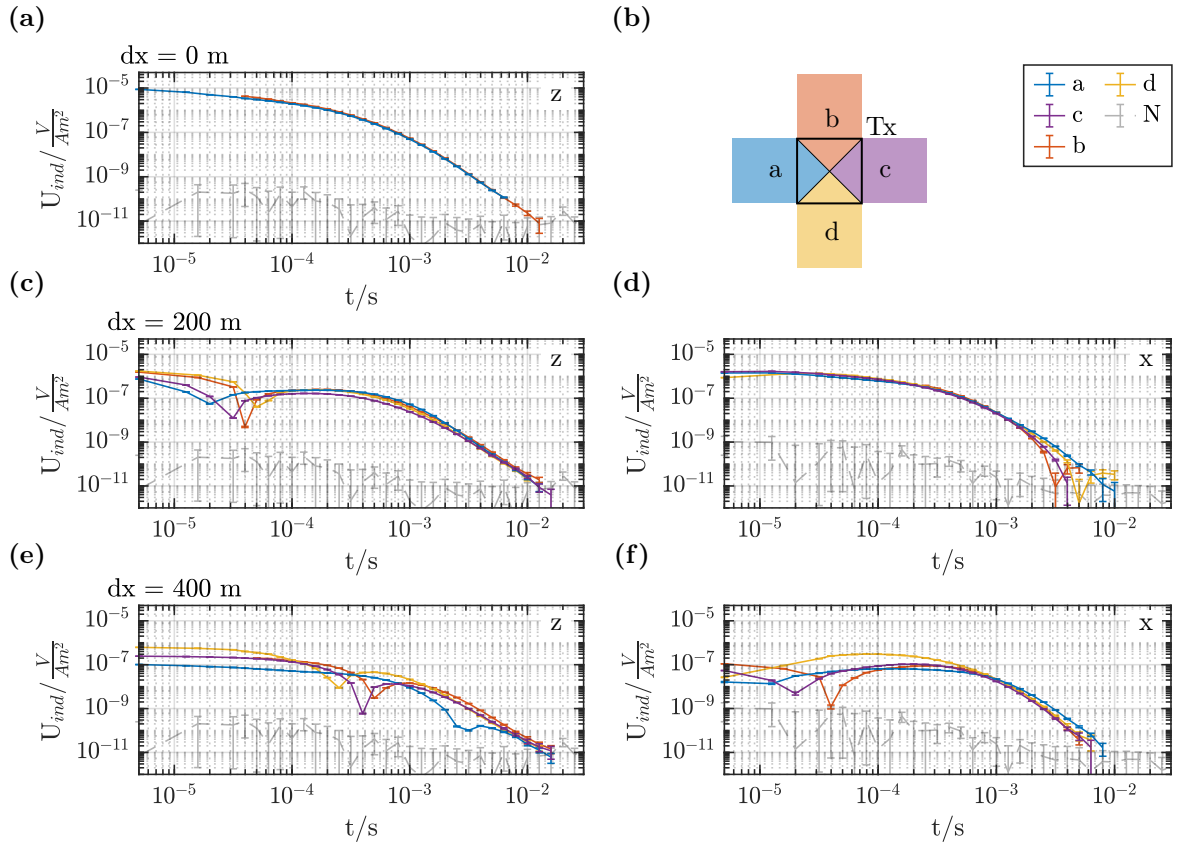

Figure 6.11.: z- and x-components of the induced voltage decays at fixed-loop transmitter C at different offsets dx from the center of the transmitter loop. Each color represents one direction of the offset of the transmitter. The sectors of each direction are indicated in **(b)**. Each sub-figure includes the noise level (gray).

subsurface in that direction than in the others.

Figure 6.12 shows all recorded induced voltage decays along Profile 1, as a section plot as well as the relative data error in percentage. The z-component is the strongest measured component with a maximum underneath the center of the transmitter. The x-component is weaker and shows maxima underneath the transmitter cables. A different geometry of the induced voltage distribution can be observed at the transmitter locations indicating different subsurface structures. If Transmitter A acts as a reference, then the z-component of the induced voltages appear weaker and decays faster at Transmitter B. The induced voltages are decaying slower at early and intermediate times at Transmitters C and D. At all transmitters the sign reversals are visible as locations with lower amplitude left and right of the transmitter. The temporal and spatial distribution of the x-component also changes at each transmitter. The distribution patterns seem to mirror the ones of the z-component. The existence of the y-component is depending on the subsurface dimensionality. The variations at each transmitter indicate a multidimensional subsurface structure. Especially, Transmitter B and C exhibit visible asymmetries along Profile 1. Transmitters A shows the lowest y-components.

The relative data errors show low errors for the strong z-component with higher errors at the location of the sign-reversals and increasingly higher errors outside of the Roter Kamm impact crater. Inside the crater, the transient length often was depending on the

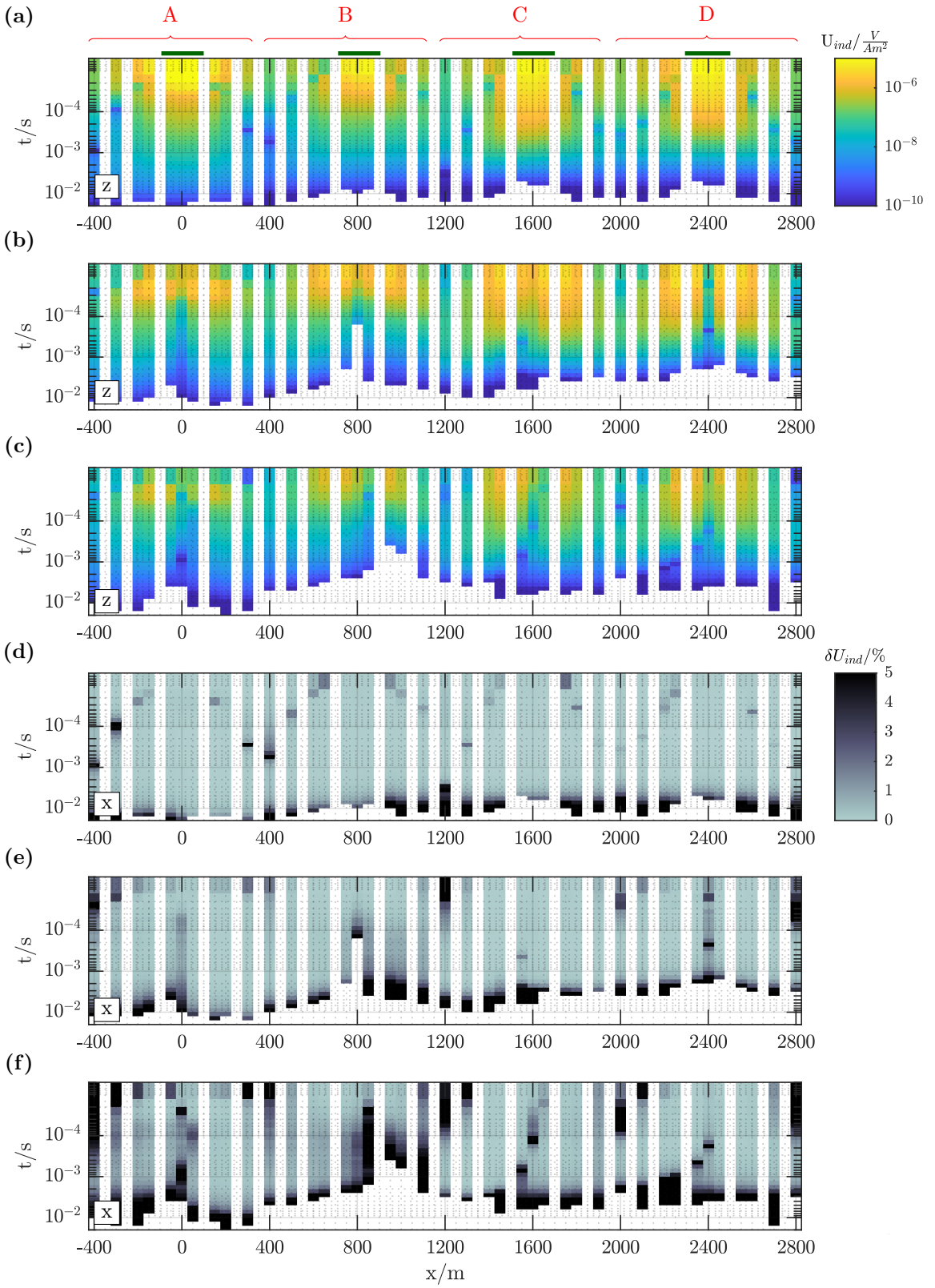

Figure 6.12.: Fixed-loop TEM data along Profile 1. The center of the crater acts as a reference on the x-axis (x = 0 m). The y-axis is the time after the end of the transmitter turn-off process. (a), (b) and (c) absolute induced voltages and (d), (e) and (f) relative induced voltage error. The receiver are grouped in red and the transmitters are indicated by green lines in panel (a).

resolution threshold, while outside the noise level seemed to be the limiting factor. The x- and y- component are lower than the z-component, and are stronger influenced by noise. Especially the weak y-component shows large errors at late times and around the crater rim (x = 1200 m).

6.3. Error Estimates for the TEM Data

The distribution of the measured induced voltages and their absolute stacking error is not normal, neither for the fixed loop nor for the single-loop TEM data (Figure 6.13). In both cases the maximum of the stacking error is smaller than that of the induced voltages. However, the distributions overlap. The distributions of the fixed-loop and single-loop data have different shapes. The fixed-loop data is asymmetrically distributed with the maximum shifted towards higher voltages. The maximum of the single-loop data is shifted towards lower voltages. The stacking error underestimates the true data error, because errors not explained by statistical processes can affect the data, such as errors caused by instrumentation, geometry, geology and electromagnetic noise (Spies and Frischknecht, 1988). The underestimation of data errors can lead to a biased interpretation of the inversion model. Modelling errors have already been discussed in section 6.1.3, other errors are not considered here. The data error can be divided into two parts: a relative δU and an absolute error η:

$$\Delta U_{ind} = \delta U \cdot U_{ind} + \eta \tag{6.1}$$

They can be determined by studying the relationship between the measured induced voltage and its absolute error (Figure 6.13). It is decided that a relative error of 3 % is sufficient to explain all the data, except the y-component of the fixed-loop data set, which is better described by a relative error of 5 %. To determine the absolute error of the fixed-loop data, an average noise level of 1.7×10^{-11} V/(Am^2) was calculated from the measured noise (Figure 6.11). As no noise was measured for the single-loop setup, this value is scaled to the transmitter sizes used.

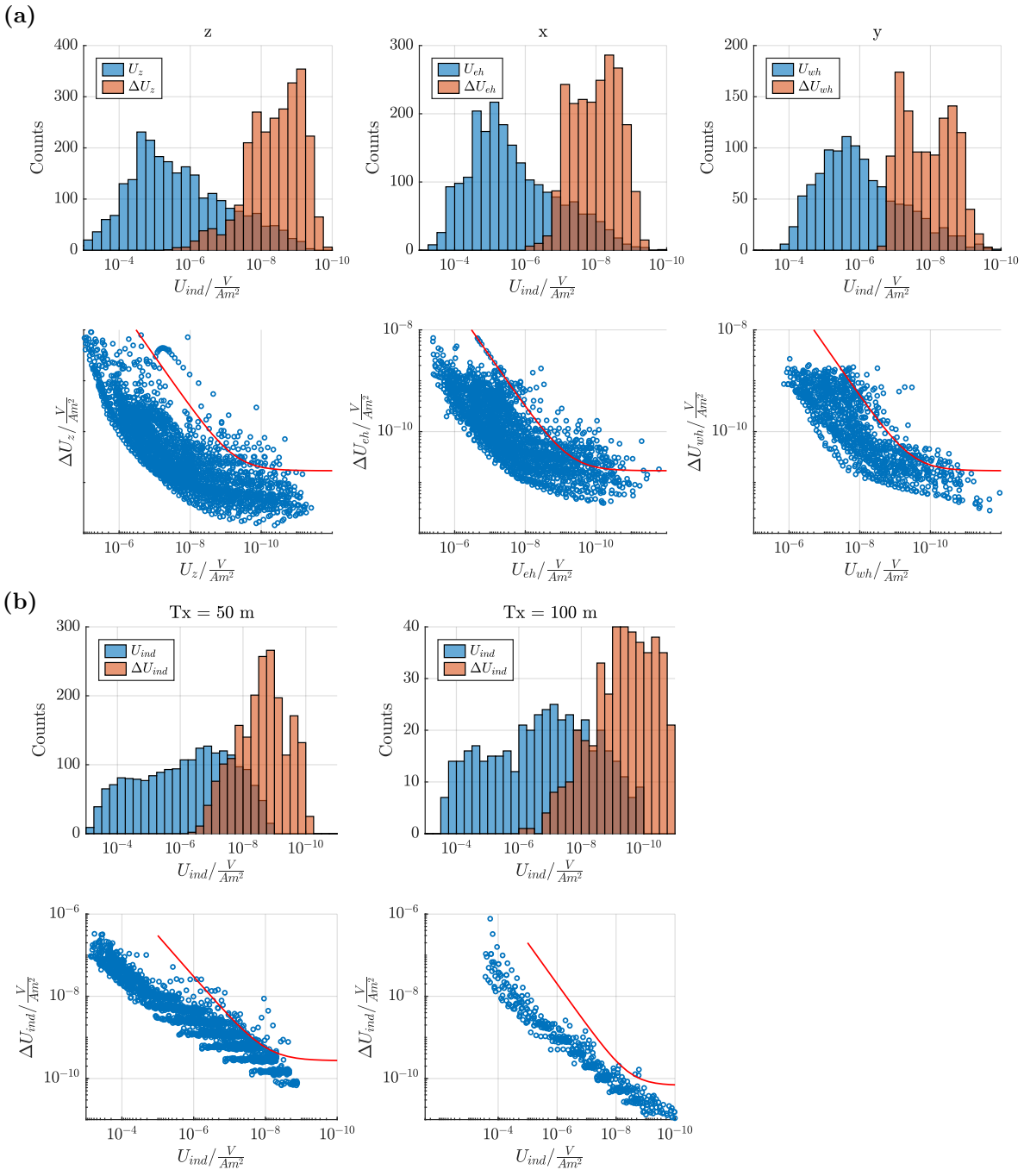

Figure 6.13.: Distribution of processed TEM data (absolute values) and stacking errors (upper panel) and stacking error for each induced voltage (lower panel). **(a)** Fixed-loop data and **(b)** single-loop data.

6.4. Summary

The single-loop data are very consistent for each loop size. However, the comparison of different loop sizes shows systematic inconsistencies that vary with the subsurface structure. While some of the differences between the transients can be explained by the different transmitter areas, others could not be explained. The influence of the TEM setup on the transient behaviour was observed. It was shown that for the conductivities present in the study area, differences of up to 40 % can be expected between the single and central-loop setups. The modelled single-loop response is smaller than the central-loop response due to the weaker magnetic flux density closer to the transmitter cable compared to the transmitter centre. This deviation has to be taken into account in the error estimation when inverting the data in the expectation of a central-loop setup by adjusting the error levels and data weighting. Furthermore, the turn-off current behaviour of the TEM-FAST 48 is non-linear and fluctuates over a long period of time. Due to the lack of a sufficiently long current recording, a linear approximation was made with minimal deviation from the real ramp. For the large loop, no recording was available and an estimate was made by comparing the inversion results between the two loop sizes. As the early times of the large loops were already down-weighted by the TEM setup, no further action was taken. For future surveys with the TEM-FAST 48 it may be useful to systematically test different loop sizes on a known multi-dimensional test site to study the transient behaviour. It is recommended that the transmitted current signal be recorded for longer periods of time. An additional TEM dataset was collected using the fixed-loop setup with a larger transmitter size (200×200 m^2) with small coil receivers to overcome potential resolution problems at greater depths while still maintaining high horizontal resolution. Data processing revealed minor resolution problems with the SMARTem24 and Geonics LF coil combination, and induction coils with larger effective areas may have been a better choice for this measurement. In addition, the use of a dual mode consisting of a low and high current mode to avoid saturation of the early time gates would have improved the resolution at shallower depths, particularly along the KMS-820 transect. Overall, the fixed-loop data show a consistent behaviour along the profile. However, it shows signs of a multi-dimensional subsurface in all components, as the induced voltages are not symmetrically distributed in both profile directions. This may prove difficult to invert using a 1D algorithm and already indicates that at least a 2D inversion is required to adequately interpret the data.

CHAPTER 7

Conventional 1D TEM Inversion

It is still common to invert the vertical components of the induced voltages of the TEM method using 1D inversion schemes, as especially small central-loop measurements have a small footprint and a good vertical resolution. However, the vertical magnetic fields of central-loop soundings are less sensitive to multi-dimensional conductivity structures than single- and fixed-loop setups (Ward and Hohmann, 1988). Since the vertical field component is less affected by the multi-dimensionality in the center of the transmitter loop. However, the data can still be inverted assuming a one-dimensional surface if the structures are large and contrasts low. This chapter presents the 1D inversion results of the single-loop data and some fixed-loop data using the EMUPLUS algorithm, developed at the University of Cologne (e.g., Scholl, 2005; Yogeshwar, 2014). Two inversion algorithms were applied to the data, the Occam and Marquardt-Levenberg methods. The Occam inversion determines a smooth model, that only introduces variations in resistivity if the data requires it. Two roughnesses are used for the regularization, the first one demands a smooth resistivity gradient and the second a smooth resistivity curvature. It only changes resistivities of the starting model, which had 30 logarithmically spaced layers with a resistivity of 100 Ωm. On the other hand, the Marquardt-Levenberg inversion changes the thickness and resistivity of each layer. However, the model is heavily depending on the starting model. Therefore, the starting model is based on the Occam model. Furthermore, this dependency was used to enforce a consistent appearance of the 1D inversion models along the profile.
All 1D inversion not shown in this Chapter, can be found in Appendix B.

7.1. Inversion of the Single-Loop Data

At all locations 1D inversions using the Marquardt-Levenberg and Occam R1 and R2 inversion methods were performed for each loop size. The Occam R1 and R2 inversions were conducted using a homogeneous halfspace of 100 Ωm is as a starting model. The starting model consists of 30 logarithmically spaced layers up to a depth of 1000 m. The first and thinnest layer has a thickness of 3 m. The starting models of the Marquardt-

Levenberg inversion are derived from the final Occam R1 inversion models. As a first approximation a starting model with a predefined amount of layers is calculated with layer boundaries at the depths with the strongest resistivity gradients. However, the large loops resolve a resistive bottom layers inside the Roter Kamm impact crater and the small loops do not. Therefore, for the locations inside the crater, where data of both loop sizes was available, the identical starting model was chosen for the Marquardt-Levenberg inversion. For all stations in between those reference points the thickness of the conductive layer was adjusted to achieve a smooth transition in between. Furthermore, as the resistivity of the lowest layer cannot be resolved by the TEM method, the last layer was set to 1000 Ωm to match the resistive subsurface outside the crater on Profile 1 and 2.
The error threshold of all inversions was set to 3.5 %. Early times were downweighted for the large loop size and all transients outside of the crater in accordance to the deviation between single- and central-loops and the difficulties with the ramp recording.

7.1.1. Inversion of Different Loop Sizes

At five locations along Profile 1 measurements with both loop sizes were carried out, with separate inversions of both transients and additional combined inversions. Exemplary, two locations are shown in Figure 7.1. The Figure shows the Marquardt-Levenberg, its equivalents and the Occam R1 inversion models of each single and the combined inversion. On the right hand side, the data fit of the Marquardt-Levenberg inversion is presented for each loop size. The weighted RMS is presented in the legends. Figure 7.1a presents the data from the center of the Roter Kamm impact crater, which is representative of profile numbers P1-03 and P1-07. The first decade of data of the large loop were removed and the second decade were down-weighted with 5 %. Furthermore, the calibration factor was not fixed for the large loop's data, as it appeared to be stronger affected by external factors such as the setup. All Marquardt-Levenberg inversion were performed using the same starting model. A significant shift in induced voltages in the intermediate times was visible (Figure 6.1). This shift can be observed in the inversion models, while the overall structure is similar and all weighted RMSs show optimal data fitting. The overall structure seems to be a 70-m-thick resistive layer (ρ = 310 Ωm) covered by a thin less resistive surface layer. Underneath an almost 200-m-thick conductive layer can be found (ρ = 2 Ωm - 20 Ωm), subdivided into two sections. Underneath a resistive layer is indicated. The model of the large loop's data has the layer boundaries in a larger depth and the conductive layer appears to be more resistive. The DOI indicates that the model of the small loop's data does not resolve the lower boundary of the conductor. However, the larger loop appears to have resolution of the lower boundary according to the DOI, but the Occam R1 does not indicate any high resistivity contrast. Therefore, the resolution of the boundary needs to be investigated further. The combined inversion shows a model similar to the inversion result of the small loop, which is a result of the free calibration factor of the large loop's transient (CF = 0.4856). However, otherwise a higher uncertainty to the upper layer boundaries would have been introduced and up until now there is no indication for strong systematic errors to this data. The depth resolution is improved compared to the models of the small loop and the DOI is comparable to the the DOI of the models belonging to the large loop.

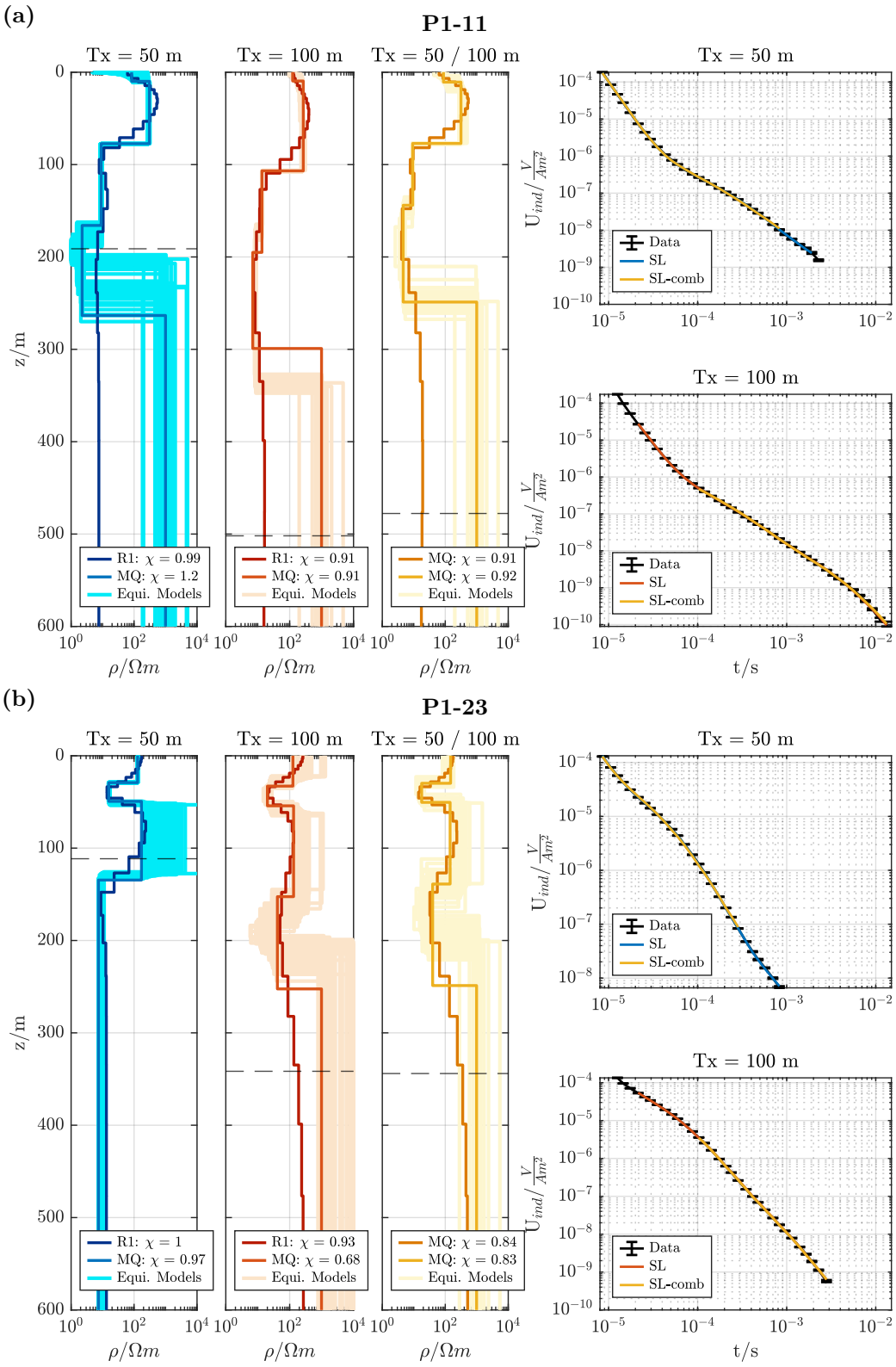

Figure 7.1.: 1D Marquardt-Levenberg and Occam R1 inversion models of different loop sizes at two locations. The left models are models resulting from the small transmitter, the middle from the large and the right from a joint inversion of both loop sizes. The DOI is indicated as a black dashed line. The right columns shows the data fits of the Marquardt-Levenberg inversion. **(a)** Inversion models of data in the center of the Roter Kamm impact crater. The calibration factor of the joint inversion for the data of the large loop is 0.4856. **(b)** Inversion models of data ontop of the crater rim. The calibration factor of the joint inversion for the data of the large loop is 0.8464.

The second example shows an ideal case, where no significant shift between both transients occurs (Figure 7.1b). This happened at locations P1-15 and P1-23. P1-23 is chosen to illustrate a vastly different subsurface than presented before. This time the data measured with the large loop was not down weighted and only the processing errors were included. The models of the small and large loops are an excellent example of the different depth resolution capabilities of both loops sizes. Both models agree well in shallow depths ($<$ 120 m) and the small loop's data exhibits a better resolution for the layer boundaries. It shows a conductive layer with a resistivity of 10 Ωm in a depth of approximately 30 m and a thickness of 20 m. In a depth of 135 m another, thicker conductive layer (ρ = 40 Ωm) can be found. However, the lower boundary of the conductive structure can only be resolved by the larger loop ($\approx$ 250 m), albeit with high equivalence. No significant shift occurs between both models and the calibration factor of the transient belonging to the large loop is 0.8464 and therefore by a factor of 1.7 larger than for the other example.

Both examples show, that combined inversions need to be handled with care and strongly depend on the inversion parameters and the data weighting. Therefore, it is still questionable which inversion leads to the optimal results as the true subsurface is unknown. For further interpretations no combined inversion models are presented, as it is still unclear what is causing the shift in the transients between data of the two loop sizes.

7.1.2. Quasi-2D Section of 1D Models

A quasi-2D section of all 1D models along each profile can be helpful for getting an overview of the subsurface structures. For this presentation all 1D models are presented next to each other at the position of the profile meter. The reference point (x = y = 0 m) for all following quasi-2D sections is the center of the crater, which is also the crossing point of Profiles 1 and 2. The models itself are presented color coded and the true elevation above mean sea level is used to represent the topography. The direction of the profiles is given in the top right corner above the section. The DOI is indicated by a dashed black line at locations of large loops and at both ends of the profile regardless of its size. For the Occam inversions the models are shaded below the DOI at each locations. For the DOI a 50 % estimation of Spies' DOI definition (Equation 2.35) is applied. The lowest panel presents the weighted RMS at each location of the section for all three inversion models.

Figure 7.2 presents all three inversion models at each presented location. The inversion models of the large loops were favoured above the smaller ones at locations were data of both loops was available. Those locations are marked by a pink square at the profile number. The north-eastern part of the profile (1800 m $<$ x $<$ 2800 m), which is located outside of the Roter Kamm impact crater, shows a very consistent conductive layer of approximately 20 Ωm with a thickness of 40 m to 60 m in a depth of 50 m to 60 m. The layer or layers above have a higher resistivity of up to 100 Ωm. At most locations both Occam inversion models reveal a very resistive lower layer. Along the outside slope of the crater (1300 m $<$ x $<$ 1700 m) the conductive layer seems to have a higher conductivity, and the layer is not as consistent any more. Furthermore, the surface layer has a higher conductivity. On top of the crater rim (x = 1200 m), a thin, shallow conductive layer is still visible, but another conductive layer appears (cf. Figure 7.1b). This conductive layer

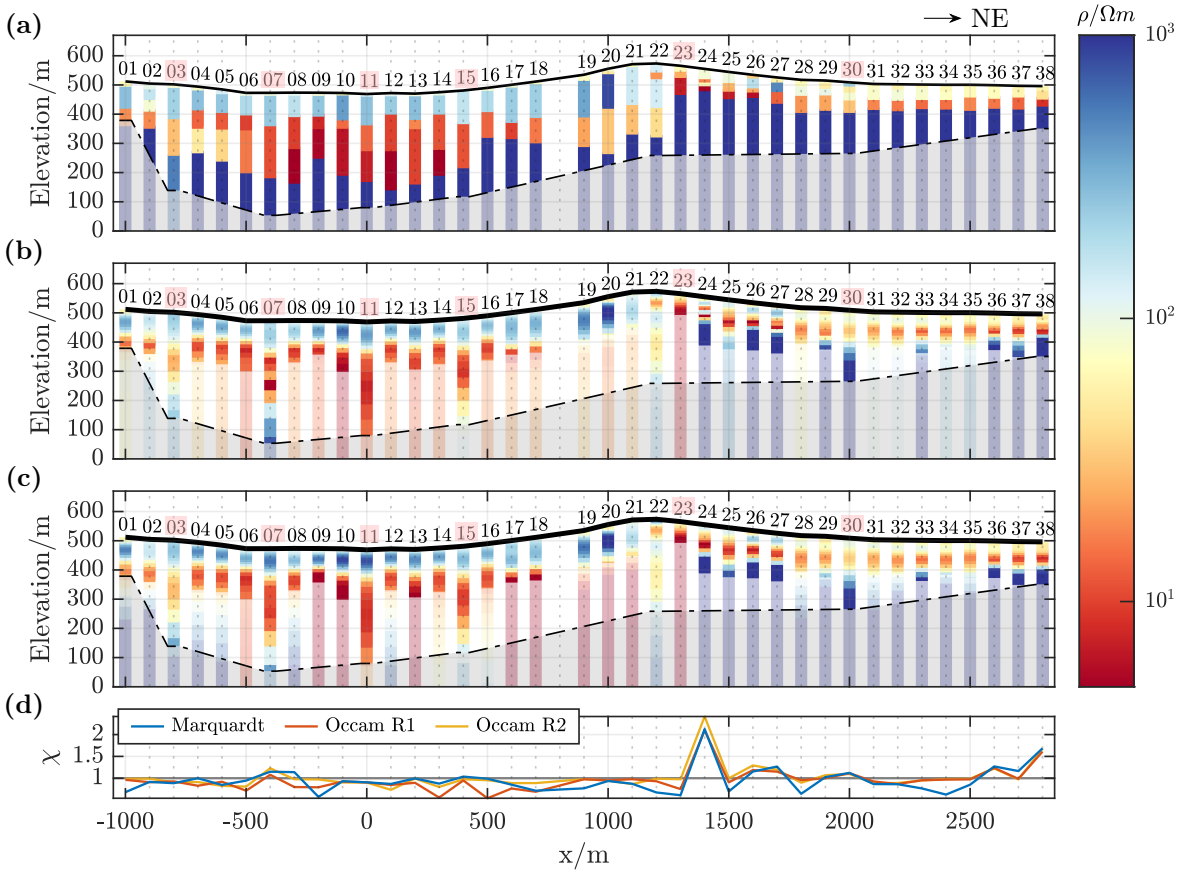

Figure 7.2.: 1D Maquardt-Levenberg and Occam inversion models along Profile 1. All 1D models are presented with color coded resistivities. The DOI is 50 % of Spiess' definition and only indicated for large loops (locations indicated in pink) and the start and end of the profile in black. The Occam models are shaded white below each models DOI. **(a)** Marquardt-Levenberg models, **(b)** Occam R1 models and **(c)** Occam R2 models. **(d)** Weighted RMS χ along the profile. The optimal value of 1 is indicated in gray. Topography data: NASA JPL (2022).

continues into the Roter Kamm impact crater, however, the lower boundary cannot be resolved with the data measured with the small loops. While the shallow conductor seems to disappear, the strength of the deeper conductor increases based on the models derived from the data of the large loop. The upper boundary, however, seems stable (cf. Figure 7.1a). No smooth transition of the lower boundary of the conductor could be achieve by using adapted starting models. The conductivity of the conductor ranges from 3 Ωm to 20 Ωm. Often times only a two layered conductor lead to a good data fit.
Figure 7.3a present the quasi-2D section along Profile 2 and indicates very similar overall shape compared to Profile 1. Although, no large loop was used in the north-west of Profile 2, the lower boundary of the conductive layer is detected. Otherwise, the behaviour of the 1D models along the section is very consistent and seems similar to Profile 1 in dimensions and depth. Figure 7.3c and d shows the 1D Marquardt-Levenberg along the regional profile shows an overall very conductive subsurface, especially in the south-west. Two conductive layers are visible in the shallow subsurface ($<$ 100 m depth). One conductive layer in a depth of 30 m in the south-west and 100 m in the north-east with increasing thickness. The conductivity of the layer seems to be highest in the south-west ($<$ 5 Ωm) and lowest in the north-east (40 Ωm). Both trends coincide with

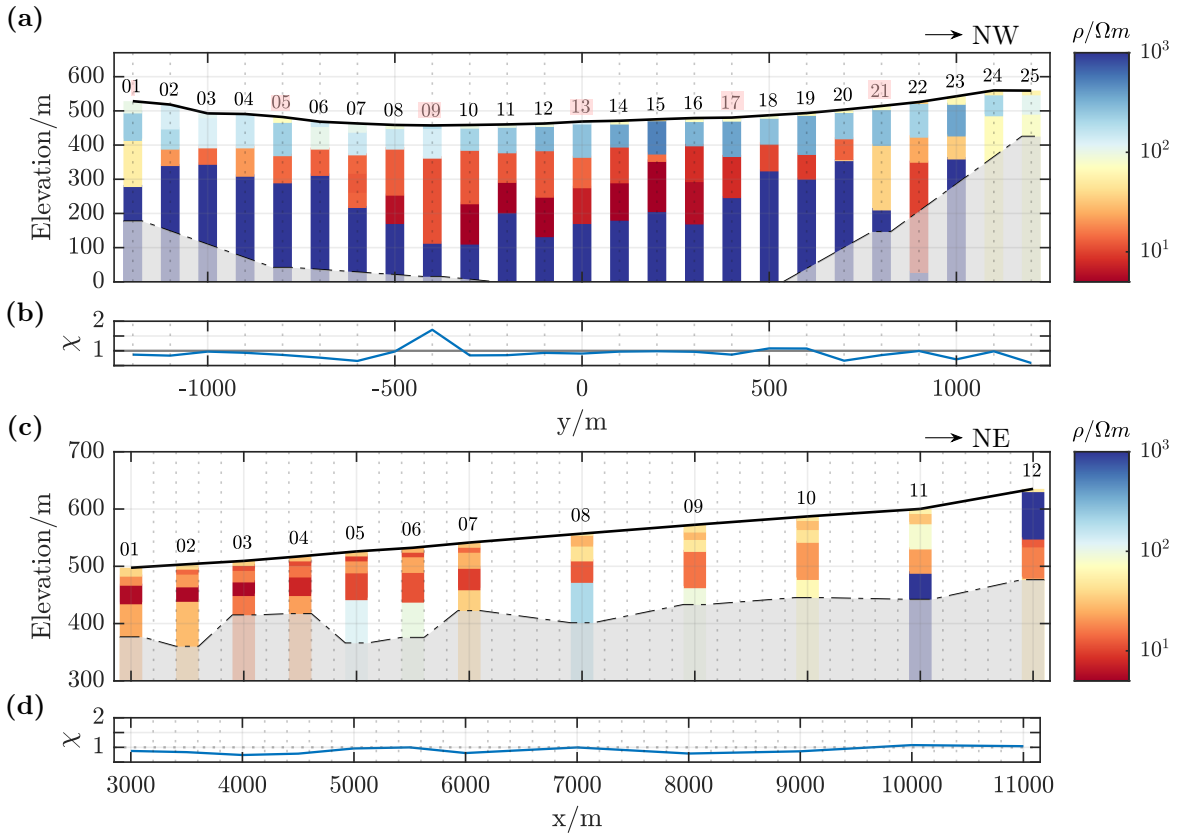

Figure 7.3.: 1D Maquardt-Levenberg and Occam inversion models along Profile 2 and the regional profile. All 1D models are presented with color coded resistivities. The DOI is 50 % of Spiess' definition and only indicated for large loops (locations indicated in pink) and the start and end of the profile in black. The Occam models are shaded white below each models DOI. **(a)** Marquardt-Levenberg models along Profile 2. **(b)** Weighted RMS χ along Profile 2. The optimal value of 1 is indicated in gray. **(c)** Marquardt-Levenberg models along the regional profile. **(d)** Weighted RMS χ along the regional profile. The optimal value of 1 is indicated in gray. Topography data: NASA JPL (2022).

the topographic elevation, which is lowest in the south-west. Along the majority of the profile a thin shallow conductor is visible with a similar resistivity as the deep. The lowest layer seems to be more resistive, but the resistivity is not resolved. The north-western station exhibits a different subsurface behaviour, as it is located directly on solid rock of the Aurus Mountains.

7.2. Fixed-Loop Data

A fixed-loop data-set was collected along Profile 1 at the Roter Kamm impact crater. At each of the four transmitters 21 soundings were made with a maximum offset of 400 m. The distance between the receiver position was 50 m to 100 m. The ramp effecting the data has a length of 320 μs and is approximately linear. 1D inversions using EMUPLUS were attempted for all vertical components along Profile 1 using a similar approach as with the single-loop data. The same starting model as described before was used for the Occam R1 and R2 inversions. For the Marquardt-Levenberg inversion one starting model was used, that was based on the Occam R1 inversion model in the center of the transmitter loop.

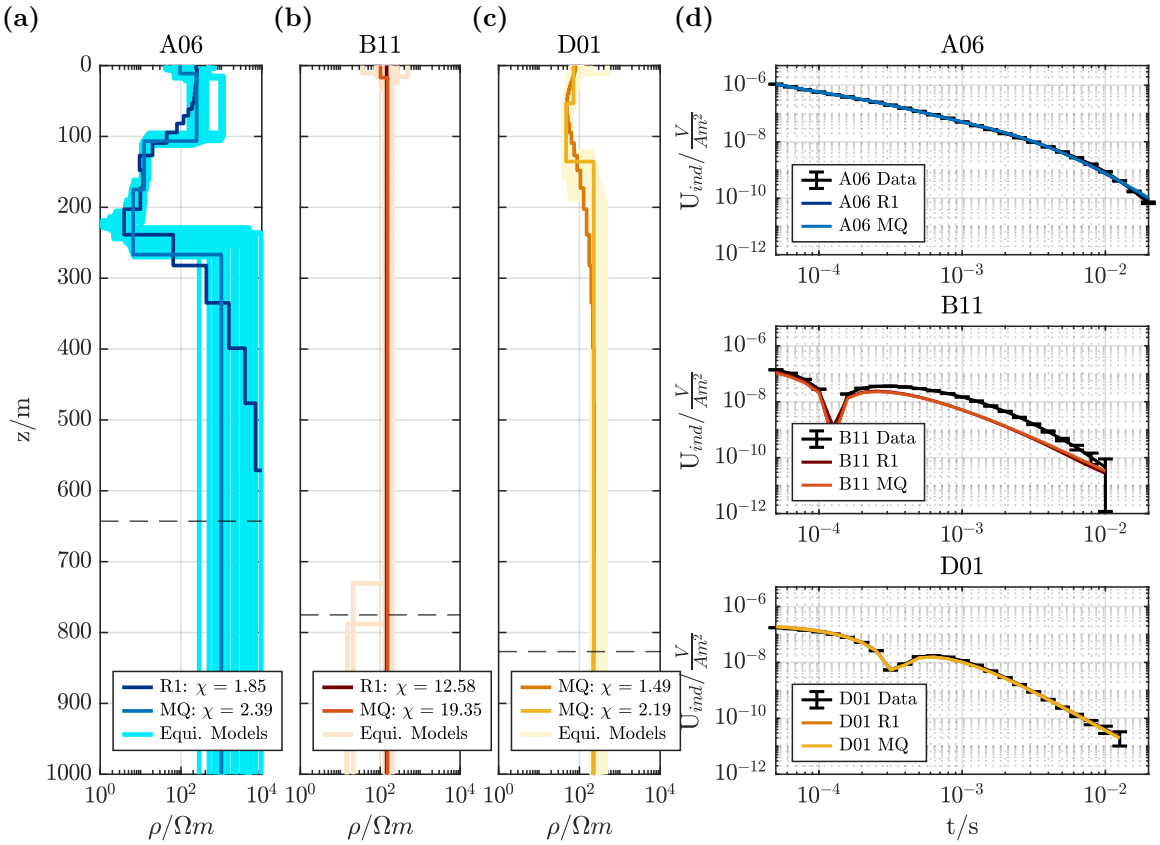

Figure 7.4.: **(a)**, **(b)** and **(c)** Marquardt-Levenberg and Occam R1 inversion models of fixed-loop data along Profile 1 (A06, B11 and D01). **(a)** Central-loop position of Transmitter A in the center of the Roter Kamm impact crater (A06), **(b)** on top of the crater rim (B11, 400 m offset to Transmitter B) and **(c)** data from the plain outside the crater (D01, 400 m offset to Transmitter D). The DOI is indicated as a black dashed line. **(d)** Data fit of the Marquardt-Levenberg and Occam R1 inversion models. The measured data is indicated in black, the calculated in colors.

Furthermore, instead of a logarithmic transformation of the data during the inversion, an *asinh*-transformation was applied as it is suitable for data with sign reversal. This transformation is necessary to accommodate for the logarithmic behaviour of the data.

7.2.1. 1D Inversion

1D Marquardt-Levenberg and Occam R1 and R2 inversions of the z-components were conducted for a part of the fixed-loop data-set. Only the transients along Profile 1 were used for this process. The same starting model for the Occam R1 and R2 inversion was used, namely a homogeneous halfspace with a resistivity of 100 Ωm with 30 logarithmically spaced layer boundaries. The thinnest layer has a thickness of 3 m, the maximum depth of the layers in 1000 m. For the central-loop position the starting model for the Marquardt-Levenberg inversion was derived from the final Occam R1 inversion model. For all offsets this starting model was used.

Figure 7.4 presents 1D inversion models from the fixed-loop measurement. The inversions of the z-components of Transmitter A and D were successful. Exemplary, the central-loop sounding and a sounding of Transmitter D with the maximal offset of 400 m are presented (Figure 7.4a and c). Both show a good agreement in both inversion. Both models are

very similar to all models of their corresponding transmitter. Only a minimal difference between the models is visible. However, the data of Transmitters B and C could not been inverted successfully. Only a few inversions converged. Figure 7.4b shows that the Occam R1 inversion did not converge and remained close to the starting model of 100 Ωm. The 1D inversions of the single-loop data (Figure 7.2) showed the biggest variations. Therefore, it can be assumed that the multi-dimensionality of the subsurface distorts the data at fixed-loop B and C. Fixed-loop data is more sensitive to the subsurface geometry than single-loop data due to the source-receiver offset. If the subsurface is close to a one-dimensional conductivity distribution, a 1D inversion is possible.

7.3. Comparison of Depth Resolution

The collected data-sets have different depth resolution capabilities. Therefore, a 1D resolution study was carried out to proof that the expectations were met. Marquardt-Levenberg models of each data-set (single- and fixed-loop TEM and AMT) were used to perform a series of forward calculations in which only the thickness of the conductor and the resistivity of the halfspace below were varied systematically. As not all 1D Marquardt-Levenberg inversion converged to an ideal data fit of $\chi = 1$. All models were considered equivalent that had a data fit below 150 % of the original data fit. The results are presented as equivalent models to the original Marquardt-Levenberg models in different shades of gray, with darker colors denoting χ-values closer to the original data fit (Figure 7.5a-c). Additionally, they are displayed in heatmaps (Figure 7.5d). Those heatmaps show the results as clusters of resistivity-depth combinations. This presentation helps evaluating the distribution pattern and range of the resolution study.
As expected does the single-loop TEM data (large transmitter) show the lowest resolution of the lower boundary of the conductive anomaly (Figure 7.5a and d). While the depth resolution of the large fixed-loop transmitter is better, both cannot resolve the resistivity of the resistive halfspace. However, the TEM method is not sensitive to resistors an this behaviour was expected as well. The heatmap of the AMT sounding has a notably different shape than the ones of the TEM measurements. While its depth resolution is not as good as the one of the fixed-loop TEM data, it seems that the AMT method is capable to determine the resistivity of the lower layer.
Considering the systematic problems with the single-loop data related with the used 1D inversion algorithm and the ramp, the fixed-loop TEM and AMT data are considered the more reliable data-sets. Therefore, a combined 1D inversion of the fixed-loop TEM transient and the AMT transfer functions in the center of the Roter Kamm impact crater is performed to combine the unique resolution capabilities in a all depth scales. The Marquardt-Levenberg inversion of both the fixed-loop TEM and the AMT data has a quite high χ-value of 2.77. Especially, in the short periods the data fit is low. However, the data fit for periods between 10^{-2} s and 10^{-1} s have a better data fit and the resistivity of the conductor is better fitted. The TEM data is fitted with a similar datafit as in an individual inversion. The upper and lower boundaries are well resolved, while the shallow part down to 100 m depth is not (Figure 7.6). The upper and lower boundaries, however, are. The thickness of the conductor is 213 m, and therefore a bit thicker than estimated otherwise. The conductivity is similar, as well as the depth of the conductor in about 110 m, which is closer to the estimations of the TEM inversions.

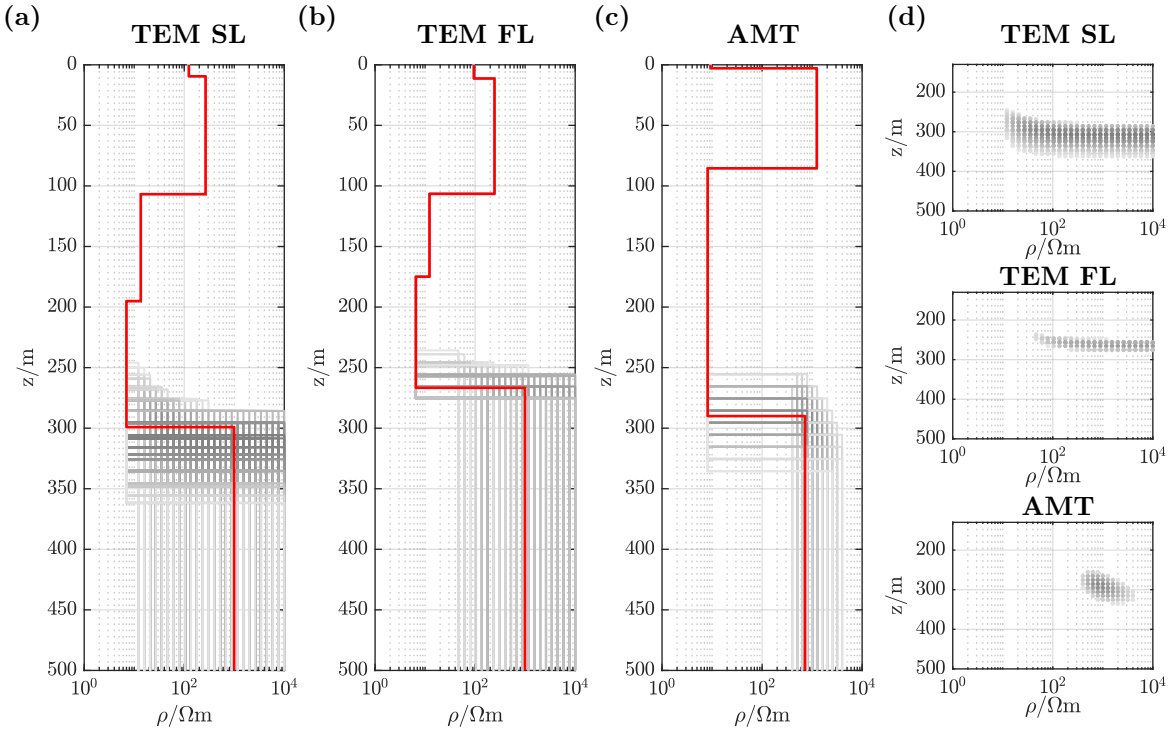

Figure 7.5.: 1D resolution studies of the TEM and AMT data in the center or the Roter Kamm impact crater. **(a)**, **(b)** and **(c)** Marquardt-Levenberg models in red and the equivalent models in gray, **(d)** heatmaps for each method. The y-axis denotes the resistivity of the resistive halfspace and the x-axis the lower boundary of the conductor.

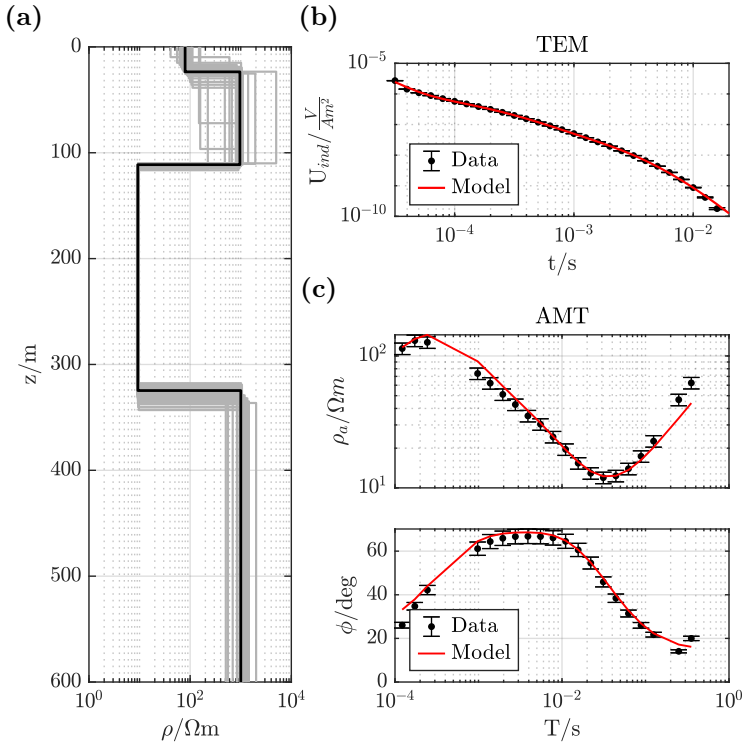

Figure 7.6: 1D combined inversion of fixed-loop TEM and AMT data in the center of the Roter Kamm impact crater. **(a)** Marquardt-Levenberg model with a χ-value of 2.77 in black and the equivalent models in gray. **(b)** Data-fit of the TEM data. The data is indicated in black, the modelled response in red. **(c)** Data-fit of the AMT data. The data is indicated in black, the modelled response in red.

7.4. Summary

The 1D inversion models along the three profiles at the Roter Kamm impact crater and its vicinity are very consistent except the inconsistency between the loop sizes. Along Profile 1 and 2, a conductor can be seen inside the crater that has its maximum in the center (200 m) and is thinning towards the rims. The upper boundary seems to be levelled in a depth of 80 m to 100 m relative to the elevation in the center, and only its lower boundary is changing. At the rim the conductor appears to have a lower conductivity, but higher thickness. The small transmitter loops cannot resolve the lower boundaries of the conductor, therefore it can only be estimated by the large loops. Outside of the crater a thin conductive layer with an approximate thickness of 50 m is present in a depth of 40 m to 60 m. This is not consistent with the models along the regional profile, which also shows thin conductive layers, but with higher resistivity and an additional layer in shallower depths. A deep resistive layer seems to be present in the whole area.
For a better resolution of the subsurface structures a larger loop size is necessary a different TEM setup is necessary, which is compatible with available inversion algorithms. An lateral constraint 1D inversion might lead to an improved overall impression of the models, however, the horizontal and vertical resolution will still be lacking. Therefore, an additional TEM data-set was collected using the fixed-loop setup with larger transmitter size (200×200 m^2) with small coil receivers. This should allow for a better depth resolution due to the loop size and a higher horizontal resolution due to the lateral offsets between receiver and transmitter.

The fixed-loop data exhibits a consistent behaviour along the profile. However, its induced voltages are not identical at a constant offset. This indicates, that the subsurface is not one-dimensional. The 1D inversion confirms this, as only the z-components of the induced voltages of Transmitters A and D can be inverted. Arrays of those transmitters are located in areas where the single-loop data suggests only small variations in the subsurface. The other two transmitters, which are located on the slopes on either side of the crater rim, could not be inverted successfully and the models either did not converge to a low data misfit or the inversion was aborted after a few iterations. Therefore, it is determined that a multi-dimensional inversion is necessary.

Furthermore, the depth resolution of single-loop and fixed-loop TEM and AMT has been investigated. Fortunately, the fixed-loop TEM setup proved capable of resolving the lower boundary of the prominent conductive anomaly inside the crater. The single-loop data could not do so. The AMT can provide a better estimation of the resistivity distribution underneath the conductive anomaly. Overall, does the TEM data agree with the AMT results. However, to really understand the structure of the Roter Kamm impact crater, a multi-dimensional inversion of the horizontally dense TEM data-set is required.

CHAPTER 8

3D Synthetic Forward and Inverse Modelling Studies

The previous chapter showed difficulties inverting the fixed-loop data using a 1D algorithm. Zhang et al. (2021) observed that in the presence of a 3D conductivity structure the distortion of the electric field is too strong to use a 1D approximation on the receiver data outside of the transmitter loop. Furthermore, the comparison of the 1D single-loop TEM inversion models and the 2D AMT inversion model shows significant differences in the area around the rim of the Roter Kamm impact crater. To achieve a conclusive TEM model, it is necessary to invert both TEM data-sets using a 3D algorithm. However, it needs to be kept in mind, that the single-loop data lacks depth resolution and cannot describe the Roter Kamm impact crater on its own.

To confirm the multi-dimensionality of the study area and its strong effects on the TEM data synthetic studies were carried out. All forward modelling studies were calculated using the python toolbox custEM (Rochlitz et al., 2023, 2021, 2019). This is a 3D forward and inversion algorithm for passive and active EM methods. custEM is a finite element algorithm using a tetrahedral mesh. This provides ideal conditions for modelling a circular impact crater, as it is capable of modelling arbitrarily shaped bodies. Furthermore, the topography can be incorporated, which influences TEM data, especially at the elevated crater rims. Even though forward modelling is possible, no inversion for time-domain data is provided at the time of this thesis. Therefore, TEM3Dinv (Liu et al., 2024) was chosen, which has been extensively tested and validated for central-loop data by Blanco-Arrué (2024). Therefore, the main focus of this chapter is the fixed-loop TEM data. TEM3Dinv is a 3D TEM inversion algorithm using the finite volume method and a quadrilateral Yee-staggered grid (Yee, 1966). As no topography is included within TEM3DInv, the influence of topography must be investigated to identify areas of distortion in the inversion model.

The TEM data of both setups was mainly located along two transects, although, the inversion algorithm models in three spatial dimensions. Therefore, the studies focus on the best way to invert the 2D profile data using a 3D algorithm. Fixed-loop TEM data proved to be more sensitive to multi-dimensional conductivity distributions and topography, especially for the transient data outside the transmitter loops making it even more

important to pay special attention to this data-set.
To estimate the DOI of the 3D models, a cumulative sensitivity approach is used (Christiansen and Auken, 2012). This approach can give a better estimate than the previously introduced method of Spies (1989), which does not take into account the transmitter-receiver geometry.

8.1. 3D Time-Domain Forward and Inversion Algorithms

Two TEM modelling algorithms were used in the framework of this thesis, custEM and TEM3Dinv. Both have unique advantages and disadvantages based on their implementation. The most significant difference is their use of different spatial discretization methods. Three prominent methods are used for the spatial discretization of the Maxwell equations: the finite difference, finite volume and finite element methods. The finite difference is the simplest of those three methods as it is relatively easy to implement, and, thus, has been used extensively (e. g., Avdeev, 2005; Börner, 2010). The most commonly used grid is the staggered grid introduced by Yee (1966). It is implemented in many frequency and time domain approaches for the finite difference method (e. g., Commer and Newman, 2004; Druskin and Knizhnerman, 1988). The finite volume and element methods are superior in the representation of arbitrarily shaped bodies, as they can use an unstructured grid (Börner, 2010; Jahandari et al., 2017). However, both methods have different advantages. The finite volume method is physically more meaningful, as it preserves the divergence free magnetic field and Gauss' law (e. g., Hermeline et al., 2008). The finite element method, on the other hand, is more accurate and convenient to implement for unstructured meshes, but also slightly more expensive to solve (Jahandari et al., 2017).
For time domain methods additional measures must be taken to also integrate the time. One of three approaches can be used: Explicit and Implicit Time-Stepping (e. g., Commer and Newman, 2004; Heagy et al., 2017; Liu et al., 2024; Lu and Farquharson, 2020), Fourier transform based (e. g., Mulder et al., 2008) or Krylov subspace schemes (e. g., Börner et al., 2015; Druskin and Knizhnerman, 1988). A comparison between those approaches can be found in Rochlitz et al. (2021). In this thesis only implementations with an explicit time stepping are used, even though custEM provides solutions of all three approaches.

8.1.1. TEM3Dinv

TEM3Dinv is a 3D time-domain inversion algorithm developed by Liu et al. (2024). It uses a finite volume discretisation with a Yee staggered-grid (Yee, 1966) and an implicit Time Stepping approach to discretize time. To solve the inverse problem a regularized Gauss-Newton approach is implemented (Section 3.3.1), which uses the direct solver MUMPS (Amestoy et al., 2001) and a pre-conditioned conjugate gradient to calculate the model updates in order to increase performance and efficiency (Section 3.5.2). The methodology is described in detail in Liu et al. (2020) and Haber et al. (2007).

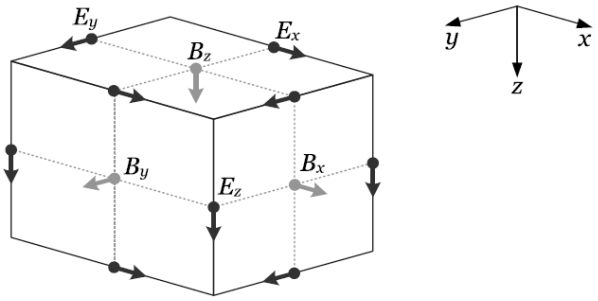

Figure 8.1: Yee grid cell with electric fields averaged onto the edges and magnetic fields onto the faces of the cell. Taken from Han et al. (2018).

3D TEM Forward Modelling

The forward solution is based on the time-dependent Maxwell Equations including the source current density $\underline{S}_r$:

$$\nabla \times \underline{E} = -\frac{\partial \underline{B}}{\partial t} \tag{8.1}$$

$$\nabla \times \mu^{-1} \underline{B} = \sigma \underline{E} + \epsilon \frac{\partial \underline{E}}{\partial t} + \underline{S}_r \tag{8.2}$$

These equations are discretized in time using the backward Euler method, as it is stable regardless of the step size (e. g., Haber et al., 2007; Um et al., 2010). The semi-discretized equations are:

$$\nabla \times \underline{E}^{i+1} = -\frac{\underline{B}^{i+1} - \underline{B}^{i}}{\delta t} \tag{8.3}$$

$$\nabla \times \mu^{-1} \underline{B}^{i+1} = \sigma \underline{E}^{i+1} + \epsilon \frac{\underline{E}^{i+1} + \underline{E}^{i}}{\delta t} + \underline{S}_r^{i+1} \tag{8.4}$$

$\underline{E}_i$ and $\underline{B}_i$ denote the electric and magnetic fields at each time step i. In order to discretize the Maxwell equations in space, the finite volume method is applied using a Yee staggered grid (Yee, 1966). The electric fields are placed on the edges of the grid cells and the magnetic fields on the faces of each cuboidal grid cell (Figure 8.1). This yields to the fully discretized formulations (Han et al., 2018):

$$\underline{Curl}\underline{E}^{i+1} = -\alpha \left(\underline{B}^{i+1} - \underline{B}^{i} \right) \tag{8.5}$$

$$\underline{Curl}^T \underline{\underline{M}}_{f\mu} \underline{B}^{i+1} = \underline{\underline{M}}_{e\sigma} \underline{E}^{i+1} + \alpha \underline{\underline{M}}_{e\epsilon} \left(\underline{E}^{i+1} + \underline{E}^{i} \right) + \underline{S}_r^{i+1} \tag{8.6}$$

Here $\underline{Curl}$ is the discreet curl operator and $\alpha = 1/\delta t$ defines the time step. $\underline{B}^i$ and $\underline{E}^i$ are the magnetic and electric fields on the faces and edges of the grid cells. The matrices $\underline{\underline{M}}_{f\mu}$, $\underline{\underline{M}}_{e\epsilon}$ and $\underline{\underline{M}}_{e\sigma}$ map the magnetic permeability, electric permittivity and conductivity by averaging neighbouring cells. If $\underline{B}^{i+1}$ is eliminated in Equations 8.5 and 8.6, $\underline{E}^{i+1}$ can be calculated by:

$$\begin{aligned} \left(\underline{Curl}^T \underline{\underline{M}}_{f\mu} \underline{Curl} + \alpha_{i+1} \underline{\underline{M}}_{e\sigma} + \alpha_{i+1}^2 \underline{\underline{M}}_{e\epsilon} \right) \underline{E}^{i+1} - \alpha_{i+1}^2 \underline{\underline{M}}_{e\epsilon} \underline{E}^{i} \\ = \alpha_{i+1} \underline{Curl}^T \underline{\underline{M}}_{f\mu} \underline{B}^{i} - \alpha_{i+1} \underline{S}_r^{i+1} \end{aligned} \tag{8.7}$$

To solve this equation, the initial conditions must be understood. For the transient electromagnetic method two different kind of signals can be used, the step-on and the

step-off signal. If the initial fields are Zero and a transmitter is turned on to generate an impulse, the signal is called step-on. If the initial field is a constant magnetic field, which decays to Zero within a certain time span, the signal is called step-off. In this thesis, only the step-off signal is used.
The initial field can be found by eliminating $\underline{E}^{i+1}$ from Equations 8.5 and 8.6 and the step length α is set to Zero. Furthermore, the magnetic field is divergence free (Oldenburg et al., 2013). This yields to the initial field condition:

$$\underline{Curl}\underline{\underline{M}}_{e\sigma}^{-1}\underline{Curl}^T\underline{\underline{M}}_{\mu f}\underline{B}^0 + \underline{Grad}\underline{\underline{M}}_{e\sigma}\underline{Grad}^T\underline{B}^0 = \underline{Curl}\underline{\underline{M}}_{e\sigma}\underline{S}_r \tag{8.8}$$

The discreet source current density $\underline{S}_r$ describes the transmitter, which must be placed along the edges of the grid cells.

The final system that needs can be expressed by following linear partial differential equation system:

$$\begin{pmatrix} \underline{\underline{A}}^1(\alpha^1) & \dots & & 0 \\ \underline{\underline{P}}^2(\alpha^2) & \underline{\underline{A}}^2(\alpha^2) & \dots & \\ & \dots & \dots & \\ 0 & & \underline{\underline{P}}^n(\alpha^n) & \underline{\underline{A}}^n(\alpha^n) \end{pmatrix} \begin{pmatrix} \underline{E}^1 \\ \underline{E}^2 \\ \vdots \\ \underline{E}^n \end{pmatrix} = \begin{pmatrix} \underline{\underline{C}}^1(\alpha^1)\underline{B}^0 - \alpha_1\underline{S}_r^1 \\ \underline{\underline{C}}^2(\alpha^2)\underline{B}^1 - \alpha_2\underline{S}_r^2 \\ \vdots \\ \underline{\underline{C}}^n(\alpha^n)\underline{B}^{n-1} - \alpha_n\underline{S}_r^n \end{pmatrix} \tag{8.9}$$

Following simplifications are used:

$$\begin{aligned} \underline{\underline{A}}^i(\alpha_i) &= \underline{Curl}^T\underline{\underline{M}}_{f\mu}\underline{Curl} + \alpha_i\underline{\underline{M}}_{e\sigma} + \alpha_i^2\underline{\underline{M}}_{e\epsilon} \\ \underline{\underline{P}}^i(\alpha_i) &= -\alpha_i^2\underline{\underline{M}}_{e\epsilon} \\ \underline{\underline{C}}^i(\alpha_i) &= \alpha_i\underline{Curl}^T\underline{\underline{M}}_{f\mu} \end{aligned} \tag{8.10}$$

At each time step a linear equation system must be solved:

$$\underline{\underline{A}}^i(\alpha_i)\underline{E}^{i+1} + \underline{\underline{P}}^i\underline{E}^i = \underline{\underline{C}}^i(\alpha_i)\underline{B}^{i-1} - \alpha_i\underline{S}_r^i \tag{8.11}$$

For any given model grid and parameter the matrix $\underline{\underline{A}}^i$ only depends on the time step length α_i. For accuracy and efficiency a time stepping method with increasing step lengths is chosen. For early times, small time steps are necessary to resolve the broad frequency spectrum of the TEM source field. However, the late times do not contain high frequencies and small time steps are not required (Um et al., 2010). Therefore, the step length is multiplied by a factor F after N_{step} steps. A small factor is useful for resistive models, while larger factors are acceptable for conductive models (Um et al., 2010). The right-hand-side of the system contains the source terms (Equation 8.11), which include the information about the ramp. Currently only a linear ramp is implemented.
The equation system is solved recursively using the direct solver MUMPS. The typical quantity measured in TEM is the induced voltage or time derivative of the magnetic field, which can be calculated using Equation 8.5:

$$\underline{B}^{i+1} = \underline{B}^i - \frac{1}{\alpha_i}\underline{Curl}\underline{E}^{i+1} \tag{8.12}$$

3D Time-Domain Inversion

A regularized Gauss-Newton approach is used for the inversion (Section 3.3.1). The cost function is defined as:

$$\phi(\underline{m}) = \phi_d(\underline{m}) + \beta\phi_m(\underline{m}) \tag{8.13}$$

β is the global regularization parameter. A starting value of β is reduced by a user defined factor in each iteration (Liu et al., 2024). The model parameter is consisting of the conductivities. Those are transformed into a logarithmic space ($\underline{m} = \ln(\underline{\sigma})$) to avoid negative values.
The data functional $\phi_d(\underline{m})$ is defined as:

$$\phi_d(\underline{m}) = \frac{1}{2}\left[\underline{F}(\underline{m}) - \underline{d}^{obs}\right]^T \underline{\underline{C}}_d^{-1}\left[\underline{F}(\underline{m}) - \underline{d}^{obs}\right] \tag{8.14}$$

$\underline{F}(\underline{m})$ is the forward response, $\underline{d}^{obs}$ the observed data and $\underline{\underline{C}}_d^{-1}$ is a weighting matrix which contains the observed data error:

$$\underline{\underline{C}}_d^{-1} = Diag\left(\frac{1}{\delta|\underline{d}^{obs}| + \eta}\right) \tag{8.15}$$

The observed data error can be described by a relative error δ and an absolute error η. The model functional $\phi_m(\underline{m})$, which is the Tikhonov regularization, is defined as:

$$\begin{aligned} \phi_m(\underline{m}) &= \frac{1}{2}\left[\underline{m} - \underline{m}_{ref}\right]^T \underline{\underline{C}}_m^{-1}\left[\underline{m} - \underline{m}_{ref}\right] \\ \underline{\underline{C}}_m^{-1} &= \gamma_x \underline{\underline{D}}_x^T \underline{\underline{D}}_x + \gamma_y \underline{\underline{D}}_y^T \underline{\underline{D}}_y + \gamma_z \underline{\underline{D}}_z^T \underline{\underline{D}}_z \end{aligned} \tag{8.16}$$

$\underline{\underline{C}}_m^{-1}$ is the modelling covariance matrix, which consists of scaled first order differences in all three modelling directions ($\underline{\underline{D}}_x$, $\underline{\underline{D}}_y$ and $\underline{\underline{D}}_z$) and the smoothness weighting parameter (γ_x, γ_y and γ_z). The smoothness weighting parameter can be used to enforce smoothness in either of the three modelling direction.
To calculate the model update, the Jacobian matrix is necessary. However, it is more efficient to only implicitly calculate the Jacobian. To achieve this the PCG method is used (Section 3.5.2). The following linear system has to be solved in each Gauss-Newton iteration k:

$$\underline{\underline{H}}_k \delta\underline{m}_k = -\underline{g}_k \tag{8.17}$$

$\underline{\underline{H}}$ is the Hesse matrix, $\delta\underline{m}$ the model update and $\underline{g}$ the gradient of the cost function (Equation 8.13). The Hesse matrix can be approximated by:

$$\underline{\underline{H}}_k = \underline{\underline{J}}_k^T \underline{\underline{C}}_d^{-1} \underline{\underline{J}}_k + \beta\underline{\underline{C}}_m^{-1} \tag{8.18}$$

To determine the step length for the PCG method, the Armijo line search method, also called weak Wolfe condiction, is used (Nocedal and Wright, 1999). The Armijo line search method states that during each iteration the objective function must be sufficiently decreased. The used inequality to measure a sufficient decrease is defined as:

$$\phi(\underline{m} + \alpha\delta\underline{m}_k) \leq \phi(\underline{m}_k) + c\alpha\nabla\underline{g}(\underline{m}_k)^T\delta\underline{m}_k \tag{8.19}$$

c is a constant and must be between 0 and 1.
Matrix-vector multiplications of the Jacobi matrix can be calculated and used to iteratively find a model update. For more details of this procedure please read the Appendix of Liu et al. (2024).

Framework of 3D TEM Inversion Algorithm

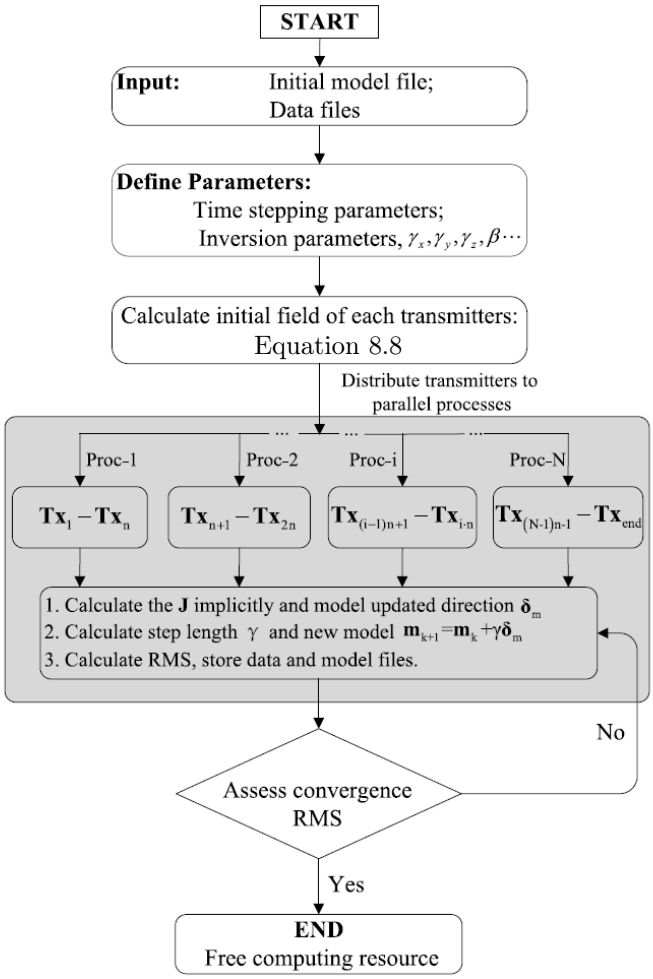

Figure 8.2.: Flowchart of the 3D TEM inversion algorithm. Taken from Liu et al. (2024).

The 3D TEM inversion algorithm is implemented in the Julia programming language. Julia is a high-level programming language with a focus on high performance, which is easy to read, maintain and extend (Peng et al., 2021). The user has to commit the data and starting model to the algorithm and set multiple parameter, such as smoothness weight, global regularization and time stepping parameter. The algorithm starts by calculating the initial field conditions for each transmitter in serial. Only after this step the algorithm is parallelised and calculates the forward responses of the model using MUMPS for each transmitter group. The transmitter groups can contain one or multiple transmitters, whose responses are calculated in serial. The system matrix $A^i(\alpha_i)$ only needs to calculated once per transmitter group. From each forward response the model update can be found by the PCG. These steps are repeated until the targeted χ value is met and the final inversion model is determined. The 3D TEM algorithm is summarized in Figure 8.2.

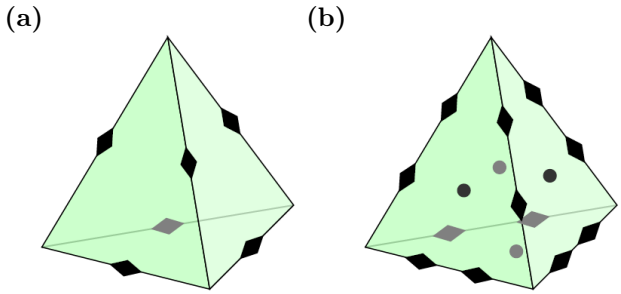

Figure 8.3: First **(a)** and second **(b)** order edge-based Nédélec elements. The electric fields are discretized on the diamond symbols along the edges. Taken from (Seidel, 2019).

Coverage

A measure of resolution of a inversion model is the sensitivity, also called coverage, which is defined as (Martin, 2009)

$$\underline{C}_j = \frac{1}{C_{max}} \sum_{i=1}^{N} |\underline{\underline{W}}_{d,ii} \underline{\underline{J}}_{ij}| \tag{8.20}$$

$\underline{\underline{W}}_{d,ii} = \underline{\underline{C}}_{d,ii}^{-1}$ is the error weighting matrix. The coverage can be calculated by summing up each column of the Jacobian matrix and apply a weighting depending on the observed data error. The resulting matrix is subsequently normalized by the cell volume and the maximum sensitivity value C_{max}. Large values indicate a well resolved model parameter, while low values indicate not well resolved conductivities. No well defined threshold exists, however other authors found that 10^{-2} is suitable for central-loop setups (Martin, 2009). Smaller coverages might be more suitable for a fixed-loop setup (Liu et al., 2024; Martin, 2009).

8.1.2. custEM

The python toolbox custEM is a 3D forward and inversion algorithm of controlled source, transient and natural source electromagnetic data (Rochlitz et al., 2023, 2021, 2019). It is based on the finite element library FEniCS (Logg et al., 2012) and uses TetGen (Si, 2015) and pyGIMLI (Rücker et al., 2017) for the generation of tetrahedral meshes. The inversion is only implemented for frequency domain methods. Here, I only briefly describe the implicit Euler approach for the calculation of the time domain EM forward response, although also the Fourier based and Rational Arnoldi approaches are implemented (Rochlitz et al., 2021).
Such as TEM3Dinv, custEM uses an electric field approach for solving the Maxwell equations and is neglecting the displacement currents. The electric field in the modelling domain Ω is defined as (Rochlitz et al., 2019):

$$\nabla \times \mu^{-1} \nabla \times \underline{E} + \sigma \frac{\partial \underline{E}}{\partial t} = -\frac{\partial \underline{j}_e^t}{\partial t} \qquad \underline{r} \in \Omega,\ t \in [t_0, t_{end}] \tag{8.21}$$

Here $\underline{j}_e^t = \underline{q}(\underline{r}) s(t)$ is the source current density function and can be split into the spatial distribution pattern $\underline{q}(\underline{r})$ and a temporal wave form $s(t)$.
The custEM toolbox uses the finite element discretization using first and second order Nédélec elements (Nedelec, 1980) on an unstructured tetrahedral mesh. The electric field

are discretized onto the edges of each tetrahedron (Figure 8.3). Using the variational formulation of the Maxwell equations and solving them with the Galerkin method, following ordinary partial differential equation must be solved:

$$\underline{\underline{C}}\underline{u} + \underline{\underline{M}}\frac{\partial \underline{u}}{\partial t} = 0 \tag{8.22}$$

with the initial condition ($t = 0$):

$$\underline{\underline{M}}\underline{u} = \underline{s} \tag{8.23}$$

$\underline{\underline{C}}$ is the discreet curl-curl matrix, $\underline{\underline{M}}$ is the mass matrix of the conductivity, $\underline{s}(t)$ is the source term vector and u is the discretized electric field vector. This ODE describes each of the N cells in the Nédélec basis.

This ODE can be fully discretized using the implicit Euler method (e. g., Um et al., 2010). The second order implicit Euler scheme yields to a fully discretized electric field (Rochlitz et al., 2021):

$$(3\underline{\underline{C}} + 2\Delta t\underline{\underline{M}})\underline{u}^{i+2} = 4\underline{\underline{C}}\underline{u}^{i+1} - \underline{\underline{C}}\underline{u}^{i} - 2\Delta t\underline{s}^{i+2} \tag{8.24}$$

$\underline{u}^i$ is the fully discretized electric field and Δt is the time step. A second order implicit Euler scheme can yield to improved results for non-linear source currents compared to a first order one (Um et al., 2010). A different method for the time step length is applied in custEM than in TEM3Dinv. In custEM the whole time vector is divided into n_{log} logarithmic time segments, which are subdivided into n_{lin} time steps. Therefore, only n_{log} matrix factorizations have to be calculated and $n_{log} \cdot n_{lin}$ solutions with the direct solver MUMPS (Rochlitz et al., 2021).

8.2. Validation of 3D Time-Domain Forward Algorithms

In this thesis two 3D time-domain algorithms are used to achieve optimal modelling results to study different effects on the data. custEM is significantly more suitable to model realistic crater-like models as it can incorporate topography and the tetrahedral mesh allows an accurate representation of round shapes. However, no inversion has been implemented yet and TEM3Dinv is used to invert the data. To validate that the algorithms responses are comparable, a homogeneous and a layered halfspace are used to compare the modelled transient data of both algorithms to the 1D algorithms EMUPLUS. In a next step a simple 3D model is used where a conductive block is embedded into a resistive background. The block has similar dimensions than the Roter Kamm impact crater. All resistivities are based on the observations from the 1D TEM and 2D AMT inversion models.
Both, custEM and TEM3Dinv, have been successfully validate using EMUPLUS and SLDMem3t (Druskin and Knizhnerman, 1988, 1994) in the past (Blanco-Arrué, 2024; Seidel, 2019). Therefore, the focus of this validation study is on the fixed-loop setup with the large transmitters.

8.2.1. One-Dimensional Halfspaces

The focus of the geophysical study at the Roter Kamm impact crater is in the inside of the crater. Therefore, the models chosen are representative of this area in terms of resistivities and layering. For the modelling with custEM the automatic mesh generation was used and standard values were taken, as finer grids did not improve the modelled data. The same observation was made with the time stepping parameter. For TEM3Dinv more tests were made using different grid and time stepping parameters. In this section only the final results are presented. The proper grid design and the optimal choice of time stepping parameter is essential for the performance of forward and more so inverse calculations. However, due to the small modelling domain and reduced transmitter number it is sufficient the choose parameters above the necessary thresholds. Furthermore, the aims of the validation study are different to those of inversions and finer grid and time stepping can increase the accuracy and better comparability.

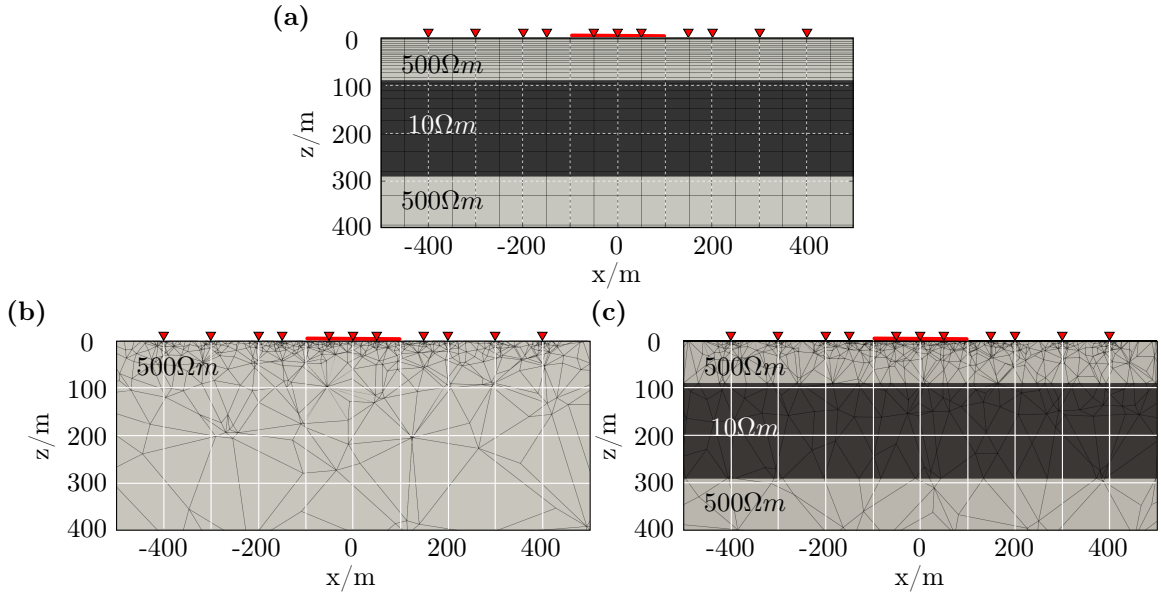

Figure 8.4.: One-dimensional validation models with the model meshes. The transmitter is indicated by the red line on the surface and the receiver by the red triangles. **(a)** Grid used for the 1D validations. The grid has been used for both the layered and the homogeneous models. The grid lines in the upper 50 m have a distance of 3 m, below that depth the distance increases with a factor of 1.2 until 400 m. **(b)** and **(c)** Automatically generated grids of custEM for both 1D validation models.

The 1D models presented here are a 500 Ωm homogeneous halfspace and a layered model which includes a conductive layer with a resistivity of 10 Ωm and a thickness of 200 m in a depth of 90 m. Figure 8.4 presents the used models and model meshes. The grid used for TEM3Dinv was identical for both models. It consists of grid lines with a 3 m spacing in the upper 50 m. Between 50 m and 400 m the grid line distance increases with a factor of 1.2. Below that depth 10 grid lines with an logarithmic distance are included up to the maximum diffusion depth in a 500 Ωm homogeneous halfspace. The horizontal grid lines have a distance of 50 m in x and y-direction in the immediate vicinity of the receiver and transmitter locations. The same logarithmic approach like for the vertical direction was used for the outer grid lines. Grid lines at the exact layer boundaries were inserted as a

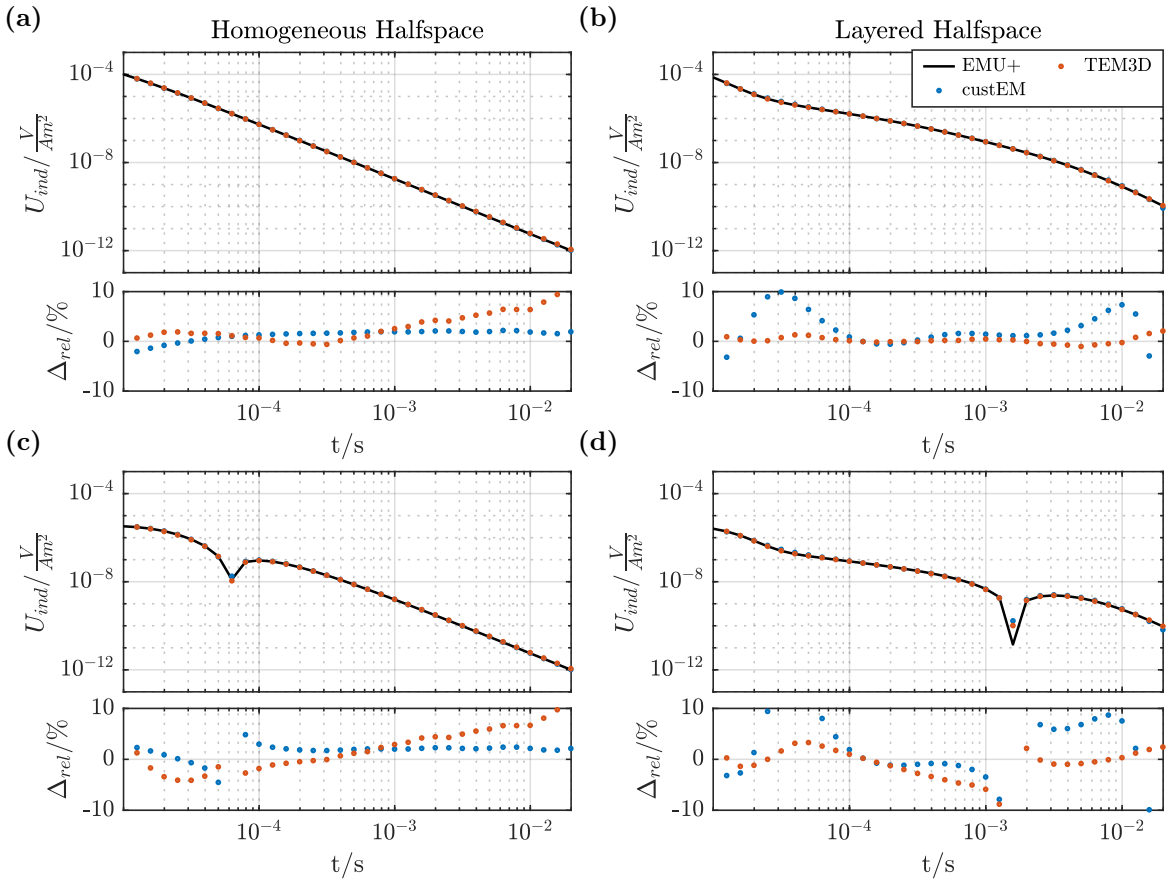

Figure 8.5.: Comparison of the modelled transients for EMUPLUS, TEM3Dinv and custEM for the 1D validation models. The 1D responses calculated by EMUPLUS are indicated as a black line, the responses of TEM3Dinv and custEM are indicated by orange and blue dots, respectively. The upper panels show the transient responses and the lower the relative differences between EMUPLUS and either of the 3D algorithms. **(a)** and **(c)** responses of the 500 Ωm homogeneous halfspace model for offsets of 0 m and 400 m. **(b)** and **(d)** responses of the layered halfspace model (500 Ωm, 90 m; 10 Ωm, 200 m and 500 Ωm halfspace) for offsets of 0 m and 400 m.

last step. The custEM grids generated by TetGen show smaller cells around the transmitter and receiver locations. The transmitter was separated into 300 segments at each edge and each receiver was at the corner of 10 tetrahedra. The tetrahedra size increases with distance from the surface and the survey setup (Figure 8.4b). Due to the included layer the cell size is smaller in the layered model mesh (Figure 8.4c). For simulations with custEM the second order Nédélec elements were used.

In Figure 8.5 the transient responses of both 3D forward algorithms are compared to the 1D EMUPLUS. The agreement is measured using the relative difference in percentage. Due to the symmetry of the problem, it is unnecessary to study data on both sides of the transmitter. The modelled transient of TEM3Dinv show a good agreement with the 1D solution of EMUPLUS for both selected offsets (dx = 0 m and dx =400 m, Figure 8.5). The only significant deviations can be observed around the sign reversals and in the location of the upper boundary of the conductive layer. This deviation from the 1D response of EMUPLUS is even stronger for the transients modelled with custEM and could not be minimized with a finer discretization of the conductive layer (Figure 8.5b

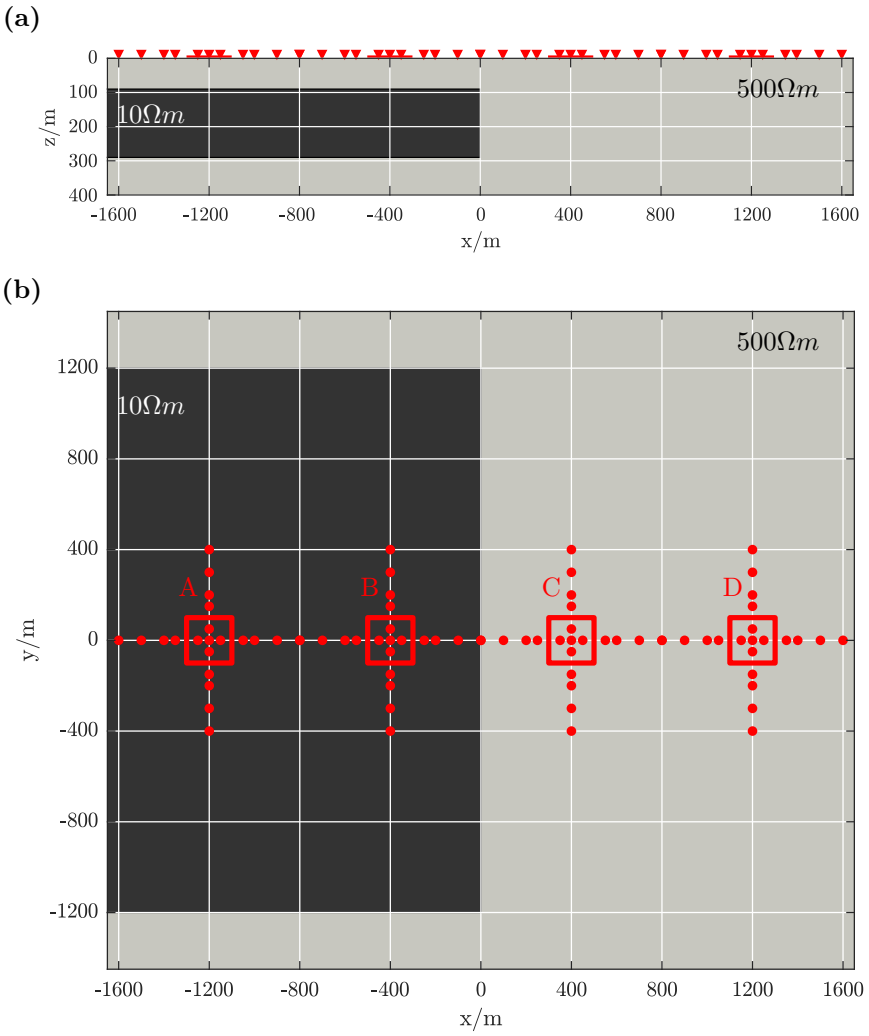

Figure 8.6: Three-dimensional validation models and survey setup. The transmitter is indicated by the red line or square and the receiver by the red triangles or circles. **(a)** xz-slice of the model (y = 0 m). **(b)** xy-slice at 100 m depth.

and d). Additionally, the late-time solutions show higher differences. However, this seems acceptable, with regards to the typically higher error for late-time data.

8.2.2. Simple Three-Dimensional Model

The 3D model consists of conductive block (ρ = 10 Ωm) embedded into a 500 Ωm background (Figure 8.6). The dimensions of the block are roughly based on the dimensions of the Roter Kamm impact crater. The horizontal dimensions are 1200 × 1200 m^2, the thickness and depth are identical to the conductive layer discussed in the last section. The modelled survey setup is identical with the field setup (Figure 8.6). The modelled data of Transmitter A and D shows an almost 1D dimensional behaviour, therefore, it is not presented here. However, this observation matches the conclusions drawn from the 1D inversions of the single- and fixed-loops previously. The modelled data of both Transmitter B and C, show multi-dimensional effects. In this study the transients modelled using custEM and TEM3Dinv are compared directly (Figure 8.7). Nevertheless, the 1D response of EMUPLUS is shown for the model directly underneath the receiver to observe the dimensionality. Overall, the 3D TEM algorithms show are good agreement for both the excited horizontal and vertical components. Larger deviations occur at the

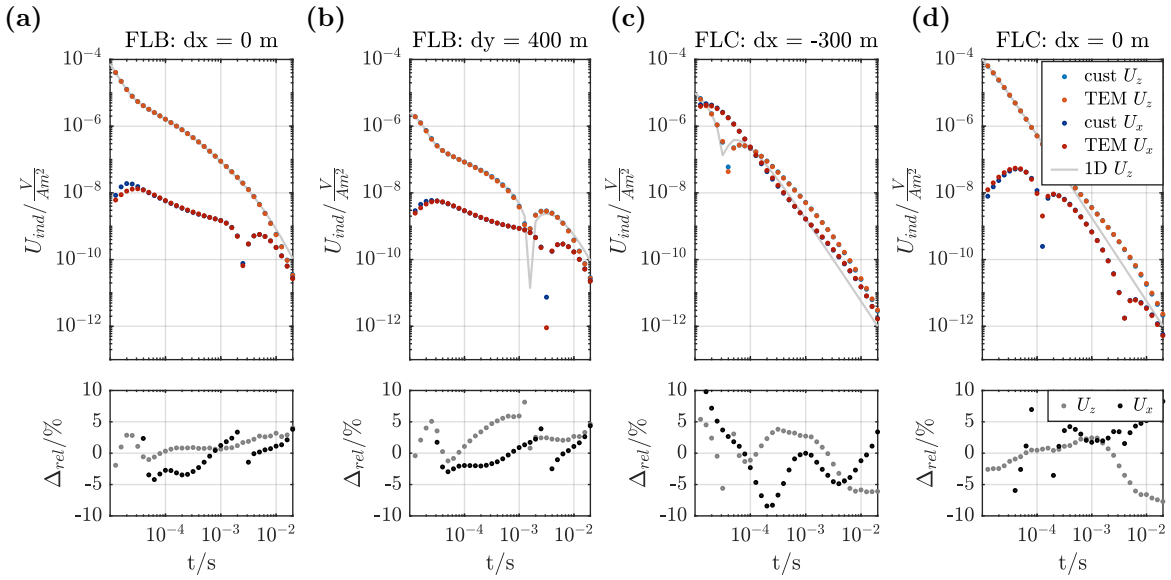

Figure 8.7.: Comparison of the modelled transients for EMUPLUS, TEM3Dinv and custEM for the 3D validation model. The 1D responses calculated by EMUPLUS are indicated as a gray line in the background as a comparison only, the responses of TEM3Dinv and custEM are indicated by orange and blue dots, respectively. The darker shades indicate the x-component and the lighter the z-component. The upper panels show the transient responses of both components and the lower the relative differences between the 3D algorithms. **(a)** Transient of the receiver in the centre of Transmitter B. **(b)** Transient of the receiver with an offset of 400 m in y-direction to Transmitter B. **(c)** Transient of the receiver with an offset of -300 m in x-direction to Transmitter C. **(d)** Transient of the receiver in the centre of Transmitter C.

layer boundary and in the late-times, but all are reasonably small. For Transmitter B the early times of the horizontal induced voltage component show large deviations, probably due to the coarse grid.

This study proved that both 3D algorithms yield to comparable modelled data. However, it also highlighted the importance of the model mesh. While TEM3Dinv showed superior results in the validation of the 1D models, it was very time consuming to design a suitable grid. The presented grid (Figure 8.4a) is very fine in shallow depths and includes a large number of grid cells. This is not desirable for inversion studies. Therefore, an optimized grid has to be found to perform efficient inversions in the field data.

8.3. Topographic Effects

The Roter Kamm impact crater has an elevated rim compared to the surface level in and outside of the crater. It is not possible to incorporate topography into the inversion using TEM3Dinv. However, custEM is capable to do so and is better suited to model round shapes. Therefore, I investigated possible topographic effects using custEM by modelling a homogeneous halfspace with different topographies and compare it to a flat surface model. To understand the influences of resistivity and slope angles, a synthetic topography was performed first. For this study a simplified rim-like topography was chosen, consisting of

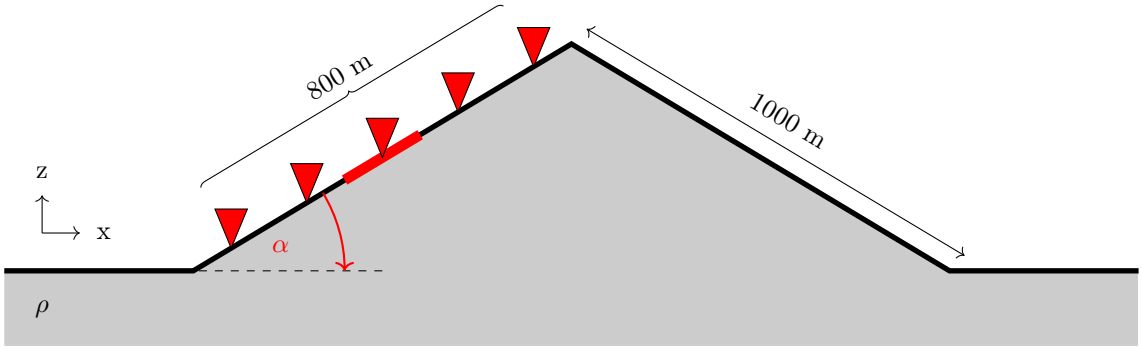

Figure 8.8.: Symmetric isosceles triangle rim-like topography model. The transmitter is indicated as a red line and some exemplary receivers as downward pointing triangles along the upward slope of the rim-like topography. The maximum receiver offset is 400 m to either side in x-direction. The slope angle α was changed during the study (3°, 7°, 11°, and 15°) as well as the resistivity ρ (10 Ωm, 100 Ωm and 1000 Ωm). The slope has a fixed length of 1000 m.

an isosceles triangle. This study yields to a valuable understanding of the real topography and its possible effects on the field data.

8.3.1. A Symmetric Triangular Rim Model

For this study the crater rim is simulated using an isosceles triangle with a leg length of 1000 m, to represent the real slope length of the rim of the Roter Kamm impact crater. Therefore, the height is depending on the chosen slope angle (Figure 8.8). A fixed-loop setup resembling the field setup is used and its dimensions are indicated in Figure 8.8. Three different resistivities (10 Ωm, 100 Ωm, 1000 Ωm) and four different slope angles (3°, 7°, 11°, 15°) were modelled. Figure 8.9a shows the influence of the resistivity on the modelled data and the relative difference to a flat surface for a fixed-slope angle of 11°. The vertical component of the central-loop receiver seems to be totally unaffected of the topography and shows only minimal deviations. The effect seems to be stronger on the receivers having an offset. While the geometry is not symmetric in this case, only an offset of 400 m is shown here, as the differences were minimal and do not change the conclusions. The deviations between a flat and elevated surface seem to be confined to the early times. All three transients show a slight upward trend for the early times, which does not correspond to a homogeneous halfspace. The relative differences show, that this effect is the strongest for conductive halfspaces rather than resistive ones. This is the exact opposite observation than the one that can be made for the horizontal component with increasing off-sets (Figure 8.9a). Here, the largest deviation can be seen at the late-time stages for the most resistive model. Furthermore, a notable difference in the geometry of the induced voltage distribution occurs inside the transmitter loop for the horizontal component. In 1D no horizontal component exists for the TEM method. However, if the measurement is carried out on a tilted surface a horizontal component occurs. No relative difference is shown for this case, as it is significantly larger than any other relative difference observed.

The slope angle study shows the expected results. The deviations are larger with increasing slope angle. All results are shown for a 100 Ωm homogeneous halfspace. The observations are similar as for the resistivity. The topography does not seem to affect the

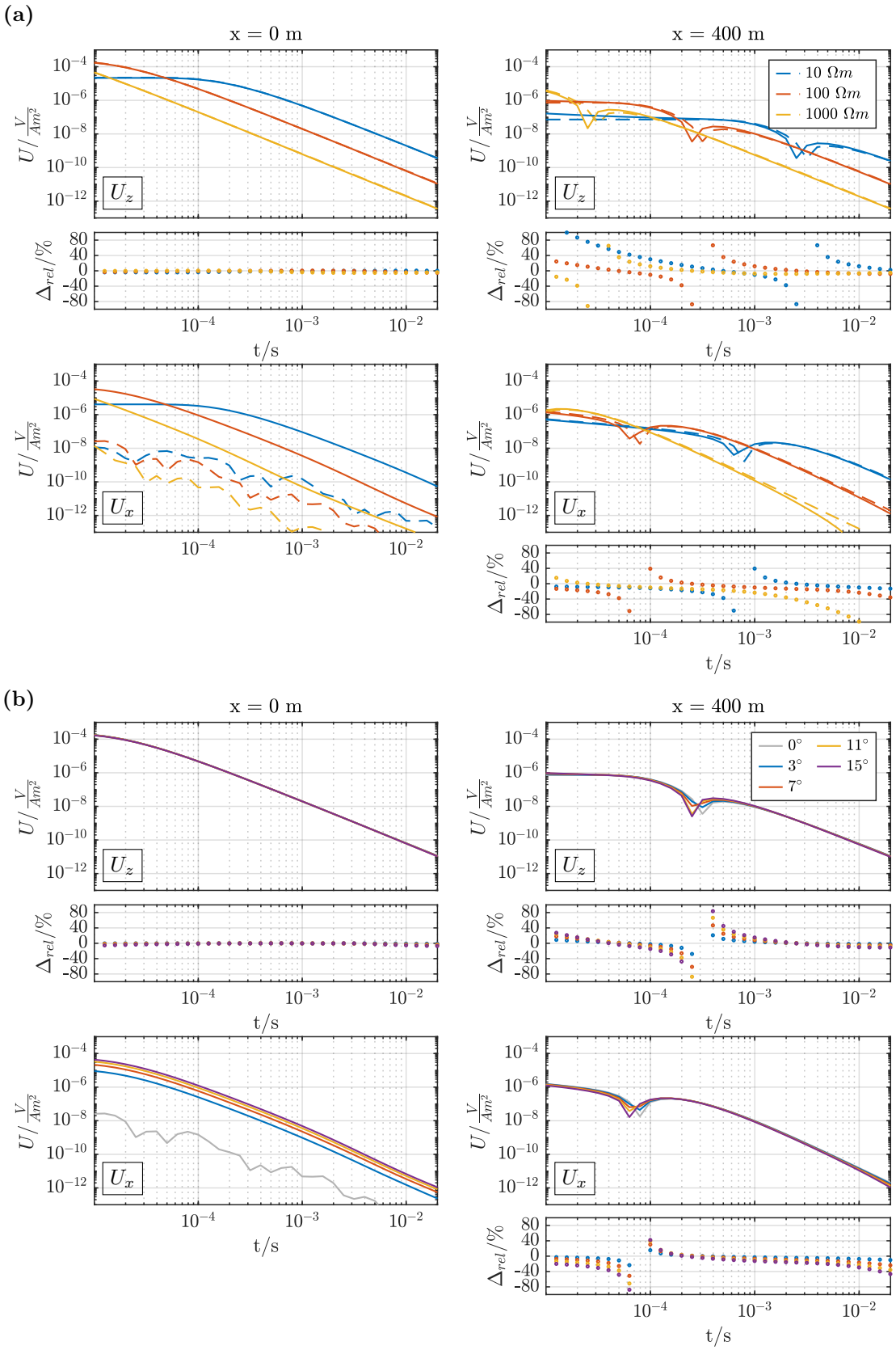

Figure 8.9.: Topographic effect of a isosceles triangular rim-like structure. Comparison of the model responses including topography with responses of a flat model. The large panels show the modelled transients, the smaller the relative differences to the flat model. The upper two panels show the vertical and the lower the horizontal component in x-direction in both subfigures. **(a)** Effects on responses on different resistivities of the homogeneous halfspace (10 Ωm, 100 Ωm, 1000 Ωm). **(b)** Effects on responses of different slope angles (3°, 7°, 11°, 15°).

vertical component of the induced voltage in the centre of the transmitter loop, but only at an location with an offset. However, also outside are the effects below 40 % for the vertical component. The most notable deviations occur at sign reversals and early and late times, which seem to increase with the slope angle. The horizontal component is most affected at late times and the observed effect is stronger than for the vertical component. In the centre of the transmitter loop horizontal components appear and increase with the slope angle.

This section shows, that the topography can play a significant role for the inversion on a homogeneous halfspace. The same observation has been made by Börner et al. (2015) and Hördt and Müller (2000). The effect is stronger on the horizontal component of the induced voltage than the vertical component. Especially, inside the transmitter loop, the vertical component does not show any significant distortion caused by the topography. It can be observed that the resistivity causes opposing effects on the vertical and horizontal component of the induced voltages. Lower resistivities affect the z-component more strongly than higher. However, high resistivities yield to stronger topographic effects in the horizontal component.
The topographic effects can be explained by the tilted source field. The transmitter follows the slope of topography, while the receiver are always levelled. Hördt and Müller (2000) identified the same effect for a horizontal transmitter and tilted receiver. Therefore, is the coordinate system of primary field rotated compared to the orientation of the receivers. If the whole survey setup is located along a slope, a simple rotation of the field data could minimize the topographic effects. However, the topography of the rim consists of two finite slopes, which are barely longer than each transmitter-receiver array.

8.3.2. Modelling the Real Topography

The real rim structure is not symmetric and does not have a linear slope. Therefore, it is important to investigate the effects of the real topography on the data. The resistivity of the subsurface is set to 500 Ωm for this modelling study. The full TEM fixed-loop setup was modelled. However, only the data along Profile 1 is discussed here, as the effects on the perpendicular sections are of similar strength or smaller. Here, only the relative differences between the model including topography and with a flat surface in percentage are presented to achieve a spacial overview to locate areas with possible strong topographic effects (Figure 8.10). Relative differences higher than 10 % are masked in black to easily identify zones with strong distortions. Transmitters A and D and the corresponding receivers are on almost plane ground (Figure 8.10a). However, the vertical induced voltage component inside the Roter Kamm impact crater is more strongly influenced than the data outside and similar distorted than below the crater rim at later times. Overall, the vertical components are most strongly affected at early times for receiver data outside of the transmitter loop at elevated locations. The horizontal induced voltage component shows significantly stronger topographic effects than the vertical component (Figure 8.10). The x-component shows, that topographic effects are indeed strongest on the rim. Generally, it can be said, that the topography influences the horizontal magnetic fields most notable inside and close to the transmitter and less further away, as the horizontal components inside the transmitter are small. Furthermore, the late times of the data are more affected than the early times.

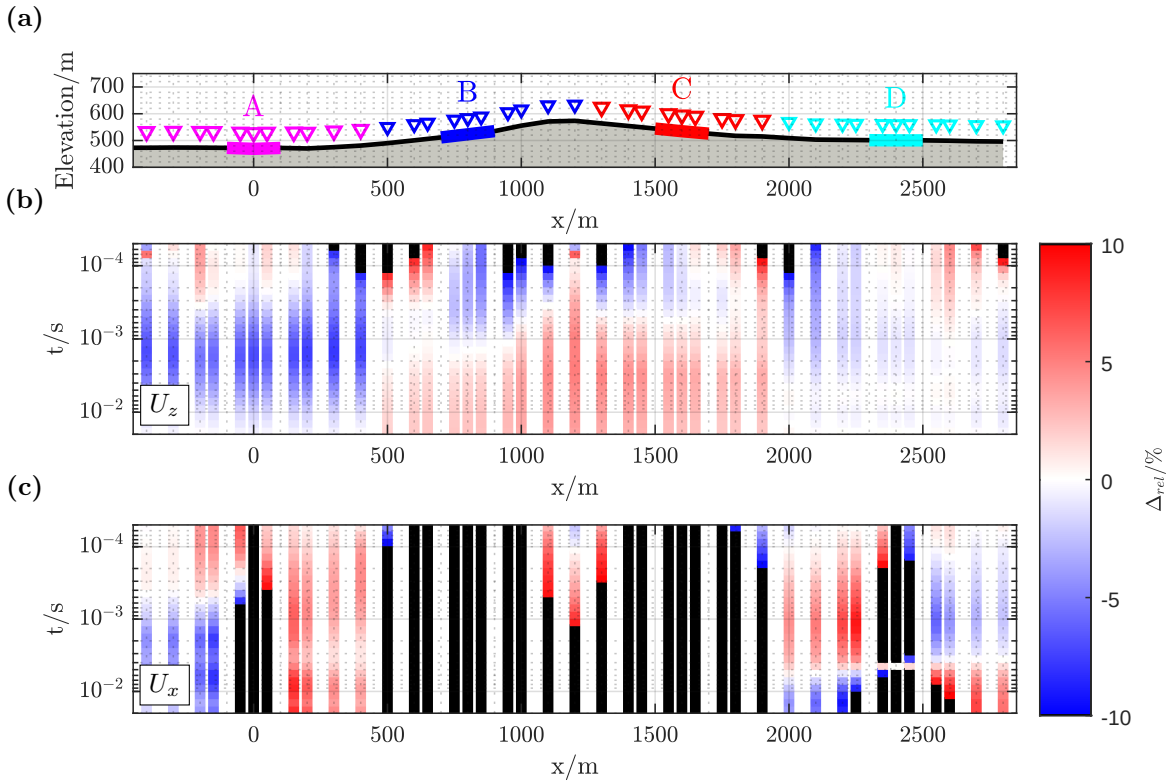

Figure 8.10.: Topographic effect of the real topography modelled using a 500 Ωm homogeneous halfspace. **(a)** The real topography of along Profile 1. The transmitters are indicated in thick lines and the receivers as downward pointing triangles. **(b)** Relative differences between the modelled response with and without topography of the vertical component. **(c)** Relative differences between the modelled response with and without topography of the horizontal component in x-direction. All relative differences larger equal 10 % are masked in black. Topography data: NASA JPL (2022).

I conclude, that the topography could be relevant for inversions including the horizontal component, but less for the vertical components alone. Central-loop data appears to be fairly unaffected by topography. This study did not include the additional effects of conductive bodies in the subsurface, but merely the topography on its own. To get a even more realistic impression more studies are necessary to truly understand the complexity of all effects.

8.4. Realistic Impact Crater Model

After understanding the general impacts of topography on central- and fixed-loop TEM data, several aspects regarding inverting profile data using a 3D inversion algorithm must be studied. Furthermore, must be understood in what way the data is affected by multi-dimensional effects. A balanced approach must be chosen to find an appropriate way to invert the measured data-set. Inversion studies were conducted using synthetic data modelled using custEM. To study the general procedure to invert profile data on a 3D subsurface model, the topography is excluded. The model contains of two conductive anomalies ($\rho = 10$ Ωm) in a 500 Ωm background (Figure 8.11). The anomaly representing the conductive body inside the Roter Kamm impact crater is a tapered cylinder with a maximum diameter of 2,400 m and a minimum diameter of 400 m. It has a thickness of

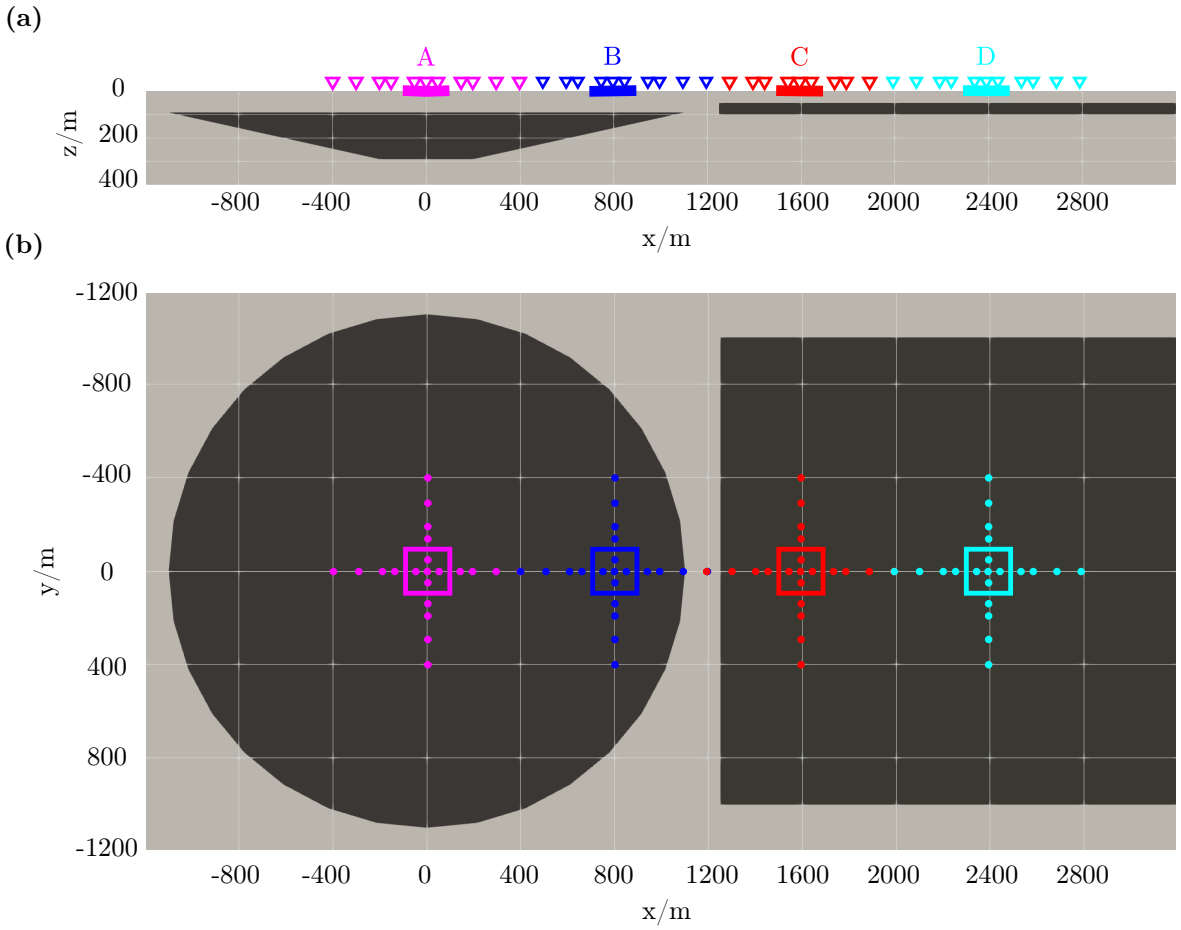

Figure 8.11.: 3D model of a simple impact crater with a flat surface. The background has a resistivity of 500 Ωm and the anomalies 10 Ωm. **(a)** xz-slice of the model (y = 0 m). The fixed-loop survey setup is shown at the surface. The thick lines indicate the transmitters, the downward pointing triangles the receivers. **(b)** Top view of the dimensions of the anomalies. The circular anomaly represents the crater interior. The conductive layer outside is represented as a plate to minimize calculation effort. The transmitters are indicated by squares and the receivers by small circles.

200 m. The anomaly is located 90 m below the surface. The second anomaly is a 50-m-thick sheet-like body. It is 2000 m wide in y-direction and 2,950 m in x-direction. The anomaly represents the observed layer in the 1D TEM inversion models and is located in a depth of 50 m. The transmitter-receiver setup is identical with the one used during the field survey.
This model is used to select the optimal grid, time stepping and inversion parameters for the field data. Additionally, it will give a first impression on the strength of the multi-dimensionality of the survey area and how this can affect the inversion of a 2D profile of a 3D model.

8.4.1. Multi-Dimensional Effects on Central- and Fixed-Loop Data

A multi-dimensional inversion is only necessary if the conductivity structure in the sub-surface changes significantly along the profile or close vicinity. A comparison between the

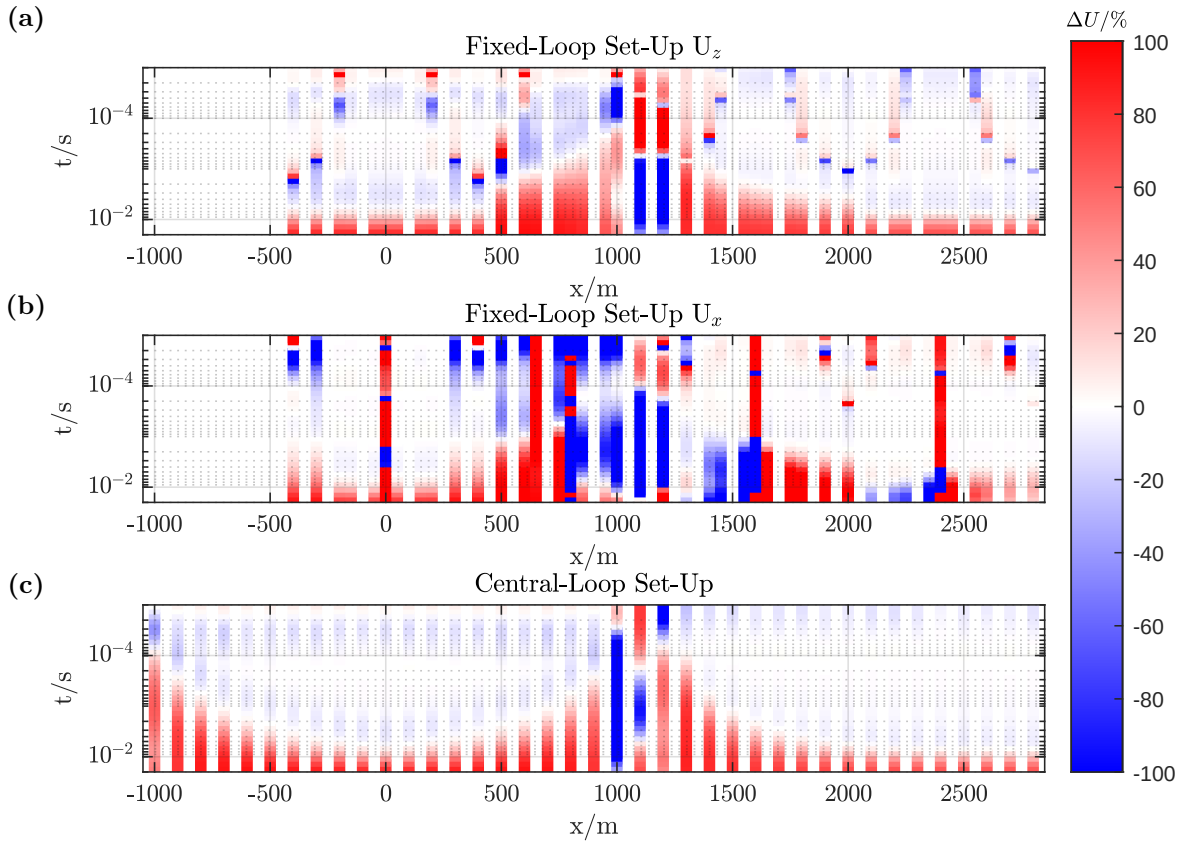

Figure 8.12.: Multi-dimensional effects on the TEM data. Relative differences in percentage between the z- and x-component of the induced voltages of the 3D crater model and the 1D responses of the models directly underneath each receiver location. Relative differences in the TEM data of **(a)** and **(b)** vertical and horizontal component using the fixed-loop setup **(c)** the vertical component of using the central-loop setup.

modelled responses of the simple crater model in Figure 8.11 and 1D responses modelled with EMUPLUS using the model directly underneath the receiver location was made. If the differences are small, a one-dimensional inversion can be suitable. However, in the case presented here, large relative differences can be observed (Figure 8.12). The relative differences of both setups show similar large scale patterns. Significant multi-dimensional effects can be observed around the edges of the anomalies (500 m $\leq x \leq$ 2000 m). The fixed-loop TEM data-set clearly shows the shape of the anomalous body, the central-loop deviations transition more smoothly. For the fixed-loop setup Transmitter B and C are strongly affected by multi-dimensionality, as the conductivity structure changes drastically beneath the receiver arrays (Figure 8.12a). In the centre of the Roter Kamm impact crater (-400 m $\leq x \leq$ 400 m) the subsurface is almost one-dimensional as is the subsurface on the plain ($x >$ 2000 m). In general, the vertical induced voltages are weaker in the 3D model at late times than for a true 1D subsurface with the identical vertical resistivity distribution. The responses are stronger inside the anomalous body and in the area of the rim for the horizontal component (Figure 8.12).
Another indicator for multi-dimensionality is the TEM-Tipper (Figure 8.13). An absolute Tipper value larger than 0.1 indicates multi-dimensionality and can be observed for Transmitters B and C at late times. The vectors point in opposite directions and indi-

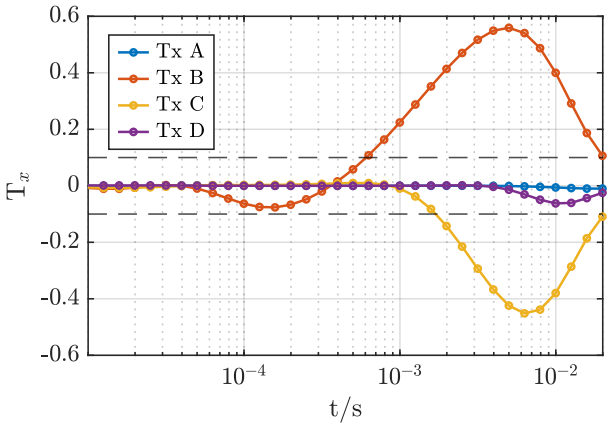

Figure 8.13: TEM-Tipper in x-direction at the locations of the fixed-loop transmitters in the Wiese convention.

cate different conductors, as they point towards each other. Therefore, they both detect the anomaly closets to them, so the sounding at Transmitter B is sensitive to the large anomaly within the Roter Kamm impact crater and the sounding at Transmitter C to the conductive layer outside of the impact crater. The data of Transmitters A and D appears to be 1D.
The observations from this study confirms the assumptions made in Section 3.6, that the data on the rim and nearby is affected by multi-dimensional effects. This proves that a multi-dimensional inversion of this data is essential.

8.4.2. Error Model for Synthetic Inversion Studies

For an inversion study a realistic error model has to be chosen. Auken et al. (2008) presented an error model for sedimentary basins based on the standard deviation of the data and the noise level for log-gated transient data (Munkholm and Auken, 1996). The noisy data and the noise level are defined as:

$$\begin{aligned} V_{resp} &= V + G(0,1) \cdot \left[STD + \frac{V_{noise}}{V} \right]^{1/2} \cdot V \\ V_{noise} &= b \cdot \left(\frac{t}{t_{ref}} \right)^{1/2} \end{aligned} \tag{8.25}$$

V is the simulated induced voltage, V_{resp} the noisy simulated induced voltage, V_{noise} the noise level, $G(0,1)$ are Gaussian distributed values between 0 and 1, STD is the standard deviation of induced voltage and b is the noise at reference time t_{ref}. Auken et al. (2008) suggested a value of 2 % for the standard deviation, however, I chose a higher value of 3 % to better accommodate modelling errors. The reference time and noise level was chosen based on the measured noise in the fixed-loop field data; $t_{ref} = 1.6 \times 10^{-2}$ s and $b = 1.7 \times 10^{-11}$ V/(Am^2), which is based on the field data (Section 6.3)

The sign reversals in the fixed-loop data are down-weighted by an error model presented by Seidel and Tezkan (2017). The authors suggested to put high relative errors at the data points closest to the sign reversal and to reduce this relative error by half at each data point next to it and continue with this procedure until the relative error is zero.

$$e_{SR} = \frac{1}{2^{j-1}} \times STD \tag{8.26}$$

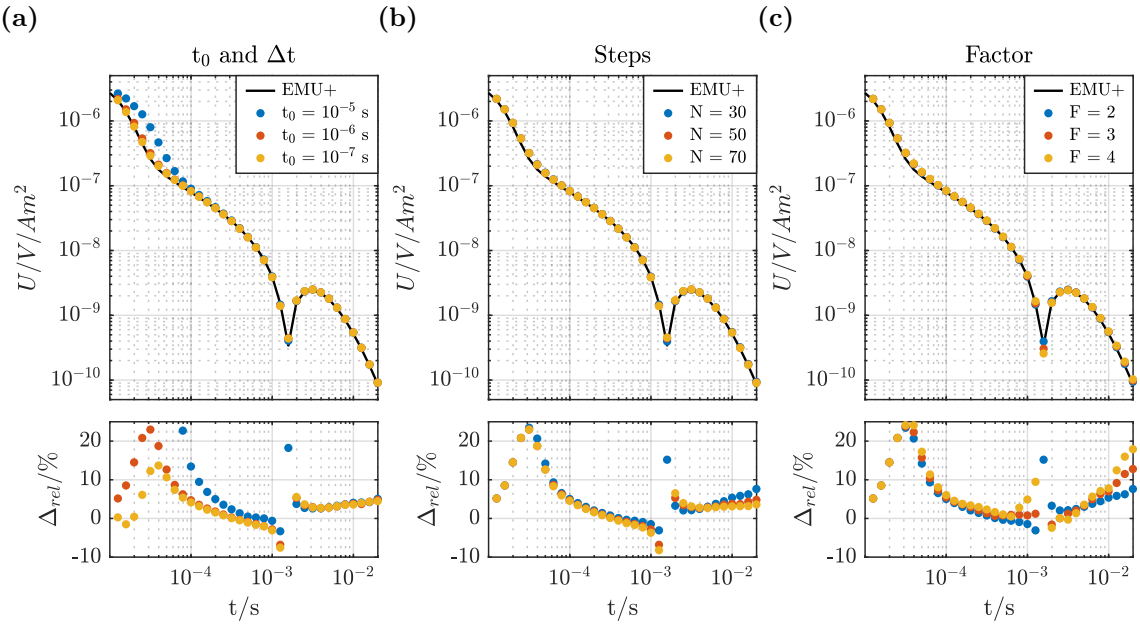

Figure 8.14.: Comparison of different Time Stepping parameter: First time point t_0, minimal time increment Δt, number of linear steps N and enlargement factor F. **(a)** Variation of $t_0 = \Delta t$ (N = 50, F = 2). **(b)** Variation of N ($t_0 = \Delta t = 10^{-6}$ s, F = 2). **(c)** Variation of F ($t_0 = \Delta t = 10^{-6}$ s, N = 30).

e_{SR} is the error model with the reference point at the sign reversal ($j = 0$). The sign reversals in this work originate from transmitter receiver geometry and not from Induced Polarization. Hence, the sign reversal can be modelled quite well. I chose a relatively low value of 50 %. An increase of the relative error floor around the sign reversal is still necessary due to influences from the grid accuracy and topography.

8.4.3. Grid Design and Time Stepping

The final inversion grid needs to have the minimum amount of grid cells necessary to ensure numerical efficiency. A large number of grids have been tested. A grid can be regarded as most suitable if the trade-off between calculation resources and modelling accuracy is adequate. Close to receivers and transmitter the horizontal grid lines were 50 m apart in both horizontal directions. In the end a grid with minimum grid line distance of 5 m in z-direction for the upper 50 m was chosen. To be able to model a reasonable depth of structures the boundary between linear and logarithmic increasing of grid line distance, was set to 600 m. The number of grid lines in z direction is 37, in y-direction 25 and in x-direction 103. The chosen grid is suitable for the central-/single- and fixed-loop setup. For the inversion of the full fixed-loop setup including the perpendicular transects, it can be extended to 39 grid lines in y direction.
The upper layer boundary cannot be modelled well with a coarser grid (Figure 8.14). However, the number of grid line influences the calculation time and needed memory the most. Therefore, this compromise was made to ensure a fast and cheap computation of inversions.
Modelling studies with different Time Stepping parameter are able to support the choice of parameters. Various combinations of the Time Stepping parameters have been tested (Figure 8.14). For early times, the starting time point t_0 and the starting time increment

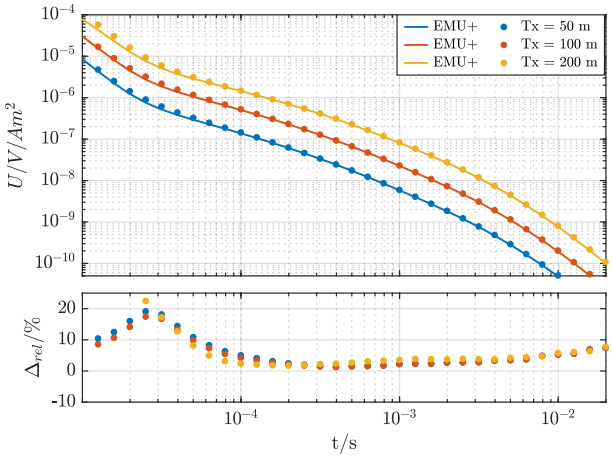

Figure 8.15: Transients modelled using EMU-PLUS and TEM3Dinv using the final inversion grid and time stepping parameter. The upper panel shows the modelled transients for three different loop sizes (yellow: 200 × 200 m^2, orange: 100 × 100 m^2, blue: 50 × 50 m^2). The lower relative difference in percentage is displayed in the lower panel.

Δt can lead to significant differences. The earliest time gate of the field data, that was measured with a reference time at the beginning of the ramp, is 3.2×10^{-4}. However, for this study earlier times were include as well, as they are present in the single-loop data. An adequate choice seems to be to select them a decade smaller than the first measured time point (e.g., Blanco-Arrué, 2024; Liu et al., 2024). For the number of linear steps 30 steps seem to be sufficient, while the factor should be chosen quite small (F = 2). The grid and Time Stepping parameters have been tested for both single-loop transmitter inversion and single grid inversion of both TEM data-sets together. The relative difference between the 1D and 3D modelled transients for different time stepping parameters is comparable to the ones for the large fixed-loop transmitter (Figure 8.15). The fit is even better for the smaller transmitter at earlier times. The early time still show a relative difference of 10 % at the approximate time of the uppermost layer boundary. However, the single-loop data has high modelling errors from inaccuracies resulting from the neglected extended transmitter size in this time range and are down-weighted any way.

8.4.4. Smoothing Parameters

During the field survey, it was only possible to measure TEM central-loop and fixed-loop data along two profiles. Therefore, smoothness weighting parameters must be chosen in a way to represent only a 2D section of the Roter Kamm impact crater. This can be best controlled by the smoothness parameters. In previous studies it has been found that this can be achieved by a high smoothness weighting parameter in the off-profile direction, to constrain the underdetermined 3D problem (Blanco-Arrué, 2024; Liu et al., 2024). Both of this studies used models that have a perpendicular conductivity boundary at the location of the profile. However, an impact crater is circular and the anomalies detected have a curvature, which might influence the inversion. The intention is to invert the whole fixed-loop data set. Hence, the smoothness weighting shall be the same in both horizontal directions. For this study, the forward simulated data of the model presented in Figure 8.11 were taken and the error model described in Section 8.4.2 was used. Subsequently, inversions with different smoothness weighting parameters were carried out.

The regularization strongly influences the inversion result. For a smoothing that is lower than what is appropriate for the chosen setup and grid ($\gamma_{xy} = 1$), each transmitter location

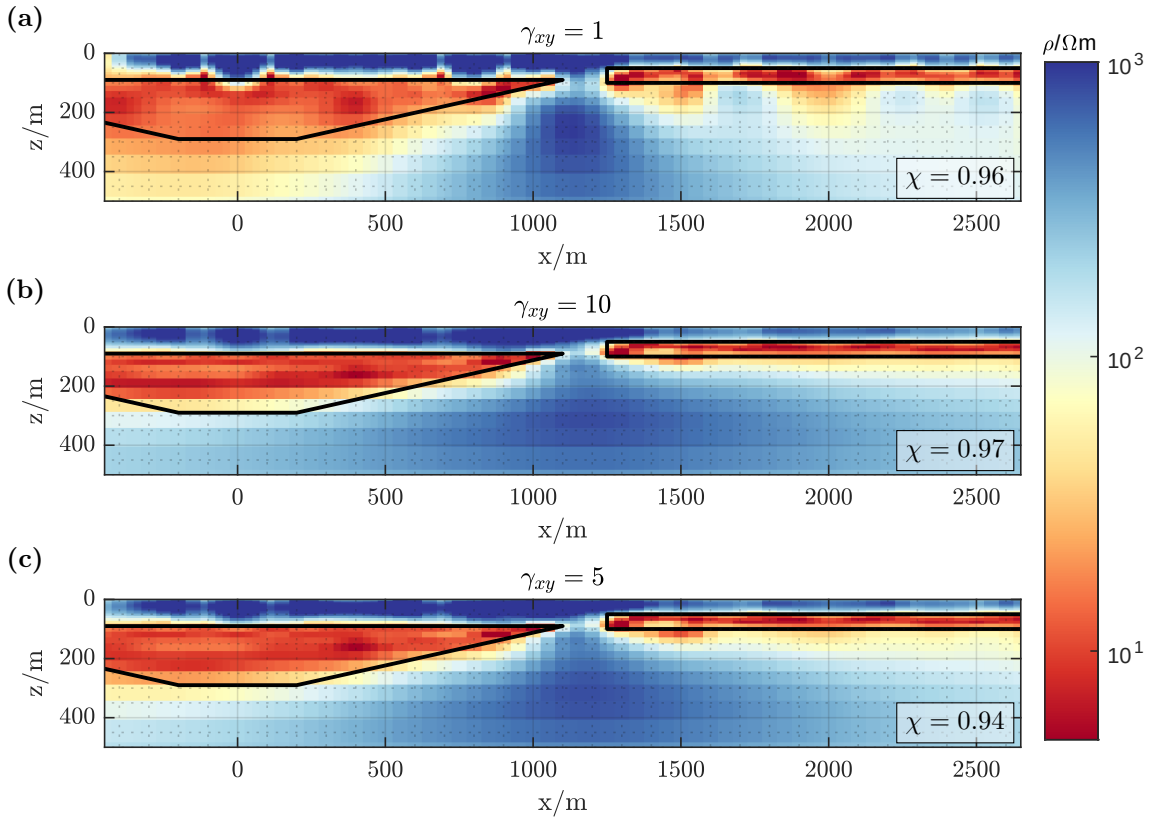

Figure 8.16.: Comparison of different horizontal smoothing parameter for the 3D TEM inversion of the simulated data for an impact crater. The data misfit is presented in the lower right corner of each model. **(a)** Horizontal smoothness weighting parameter of 1. The inversion converged at iteration 11. **(b)** Horizontal smoothness weighting parameter of 10. The inversion converged at iteration 9. **(c)** Horizontal smoothness weighting parameter of 5. The inversion converged at iteration 9.

can be clearly identified by an indentation of the upper boundary of the conductive anomaly (Figure 8.16a). Further, the anomaly appears to be thicker and the thin layer is not represented with a constant thickness. Is the smoothing too high ($\gamma_{xy} = 10$), the lower boundary of the cylindrical, tapered anomaly is underestimated. Otherwise the model is greatly improved. Therefore, a trade-off is necessary, which represents the dimensions of the anomalies in the modelled slice well and is suitable for grid and setup. The final smoothness weighting is presented in Figure 8.16c ($\gamma_{xy} = 5$). This trade-off slightly shows the distortions due to the setup, but represents the boundaries of the anomalies decently. The smoothness parameterw are highly dependent on each cell dimensions. A smaller cell requires a smaller smoothness weighting parameter, as the model covariance matrices contains scaled differences. Therefore, it was necessary to use slightly different values for the inversion grid inverting the full fixed-loop setup ($\gamma_{xy} = 2.5$).

8.4.5. Depth of Investigation

The cumulative sensitivities can be used as another measure of depth of investigation. Christiansen and Auken (2012) proposed them as a global estimation for the depth of investigation as they are considering the number of data points and their data error. Furthermore, they are not based on the assumption of a homogeneous halfspace, such as

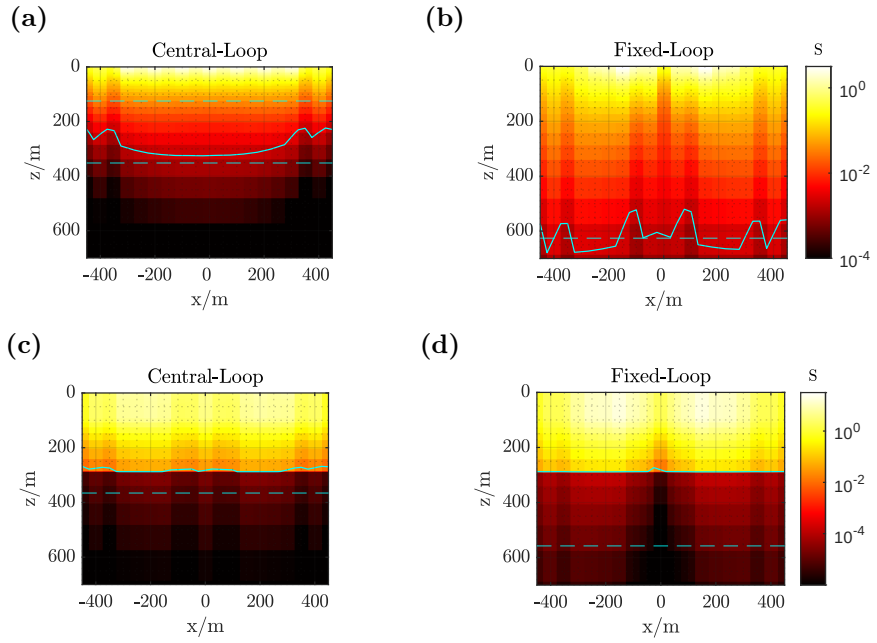

Figure 8.17.: Cumulative sensitivity of a central-loop and a fixed-loop setup for a **(a)** and **(b)** 100 Ωm halfspace and **(c)** and **(d)** a layered halfspace as present in the centre of a large conductive anomaly. Note the different axis ranges of the colour bars. The DOI estimates corresponding to 50 % of the DOI from Spies (1989) for each transmitter size are indicated by the dashed horizontal cyan lines, while those from Christiansen and Auken (2012) are the solid lines. The transmitters are located at x = ±(0,100,200,300,400) for the central-loop setup. The transmitter at x = 0 m has an edge length of 100 m, while the other 6 transmitters have an edge length of 50 m. The fixed-loop setup with a transmitter (200 × 200 m^2) at x = =0 m and receivers at x = ±(0,50,150,200,300,400).

the diffusion depth or the estimate suggested by Spies (1989). The estimation is based on the Jacobian matrix of the model and can easily be derived from the coverage (Equation 8.20), by calculating the cumulative sums in each cell from the lowest cell to the surface. A threshold is set, above which the model is trustworthy, which relies on the experience of the user. Figure 8.17 shows the cumulative coverage S of the vertical components of the induced voltages for a 100 Ωm homogeneous halfspace and the layered halfspace present at x = 0 m of the realistic impact crater model (Figure 8.11). The DOI is estimated using a 50 % of the definition given by Spies (1989). The two plots compare the segments of the central-loop and fixed-loop setups. The central-loop setup has a 100 × 100 m^2 transmitter in the centre, flanked by three smaller 50 × 50 m^2 transmitters at 100 m intervals on either side. The fixed-loop setup consists of a 200 × 200 m^2 transmitter in the centre and receivers with offsets between 50 m and 400 m. A threshold value of 1.5×10^{-3} is chosen for the field data. The columns of the model without surface receivers show a significantly lower cumulative sensitivity. The same isoline is shown for the layered halfspace (Figure 8.17c and d). It can be seen that the TEM method is sensitive to conductive structures but not to the underlying halfspace. The cumulative coverage of the fixed-loop TEM setup is slightly higher below the conductor than that of the central-loop setup. However, the sensitivity based DOI is exactly at the lower boundary of the conductor in both cases.

8.4.6. Multi-Component Inversion

With all parameters and the grid determined, only a suitable starting model has to be chosen. However, the choice depends on the user. The 1D Occam inversions resulted in comparable models relatively independent of the starting model. However, the 3D inversions showed very scattered results for homogeneous halfspaces of 10 Ωm and 500 Ωm, which resemble the resistivities of the anomalies and the background. Therefore, an average of the late-time apparent resistivities for all central-loop transients was calculated. This averages were 91 Ωm and 80 Ωm for the central-loop and 205 Ωm for the fixed-loop simulations. All subsequent inversions use a homogeneous starting model with a resistivity of 91 Ωm, as it converged faster than a more resistive starting model.
Individual and joint inversion for all setups and components were performed using the synthetic crater model depicted in Figure 8.11. For the inversion the error model presented in Section 8.4.2 was used. As shown in Section 8.3, horizontal components inside the transmitter loop are very sensitive to the topography (cf. Figure 8.10), as well as incorrect receiver placement (Seidel, 2019; Yogeshwar and Tezkan, 2017). Therefore, horizontal components are only included outside each transmitter.

The inversion models of all setups and components yield to comparable results (Figure 8.18a). The conductive anomalies are clearly detected, however, the strengths and weaknesses of each setup are visible. The inversion model of the central-loop setup has the best resolution for the upper boundaries of the conductive anomalies and the resistive material above. Its weaknesses lay within the larger depths which are not well resolved and driven by the regularization. The 1D DOI approximation also indicates that the lower boundary is not resolved. The fixed-loop setup shows a better recovery for larger depths, even if the DOI is exactly at the boundary of the conductive layer. Nevertheless, it has been shown that this is an expected behaviour for the DOI underneath a thick conductor (Section 8.4.5). The inversion using both strong horizontal and vertical component indicates improved resolution compared to the inversion of just the vertical component. It shows a more homogeneous top resistive layer, higher resolution in the depth, visible especially below the thin resistive layer, and a slightly increased DOI. The data misfit of the central-loop setup is relative constant along the profile (Figure 8.18a, lowest panel). However, the data misfit of the fixed-loop setups shows an increased misfit in the centre of the profile. This is the area where large multi-dimensional effects are expected (cf. Figure 8.12). The fixed-loop setups is more sensitive to the multi-dimensionality due to the offset between the transmitter and receiver and the larger transmitter size. Therefore, I contribute the increased misfit to the off-profile changes in the conductivity distributions.
The normalized coverages are confirming the observations from studying the inversion models (Figure 8.18b). Here, the coverage is normalized to the maximum value of all coverage matrices. Again the pattern related to the receiver positions is visible. A normalized sensitivity value of 10^{-4} seems to match the DOI estimation best. The coverage of the central-loop setup shows the lowest values at the location of the large conductive anomaly, where the pattern is also the most heterogeneous. The fixed-loop setups show higher values in larger depths and indicate higher coverages for the anomaly representing the interior of the impact crater.

In terms of computations resources, the fixed-loop TEM method is significantly more efficient (Table 8.1). The inversion of two components is using a parallelised transmitter

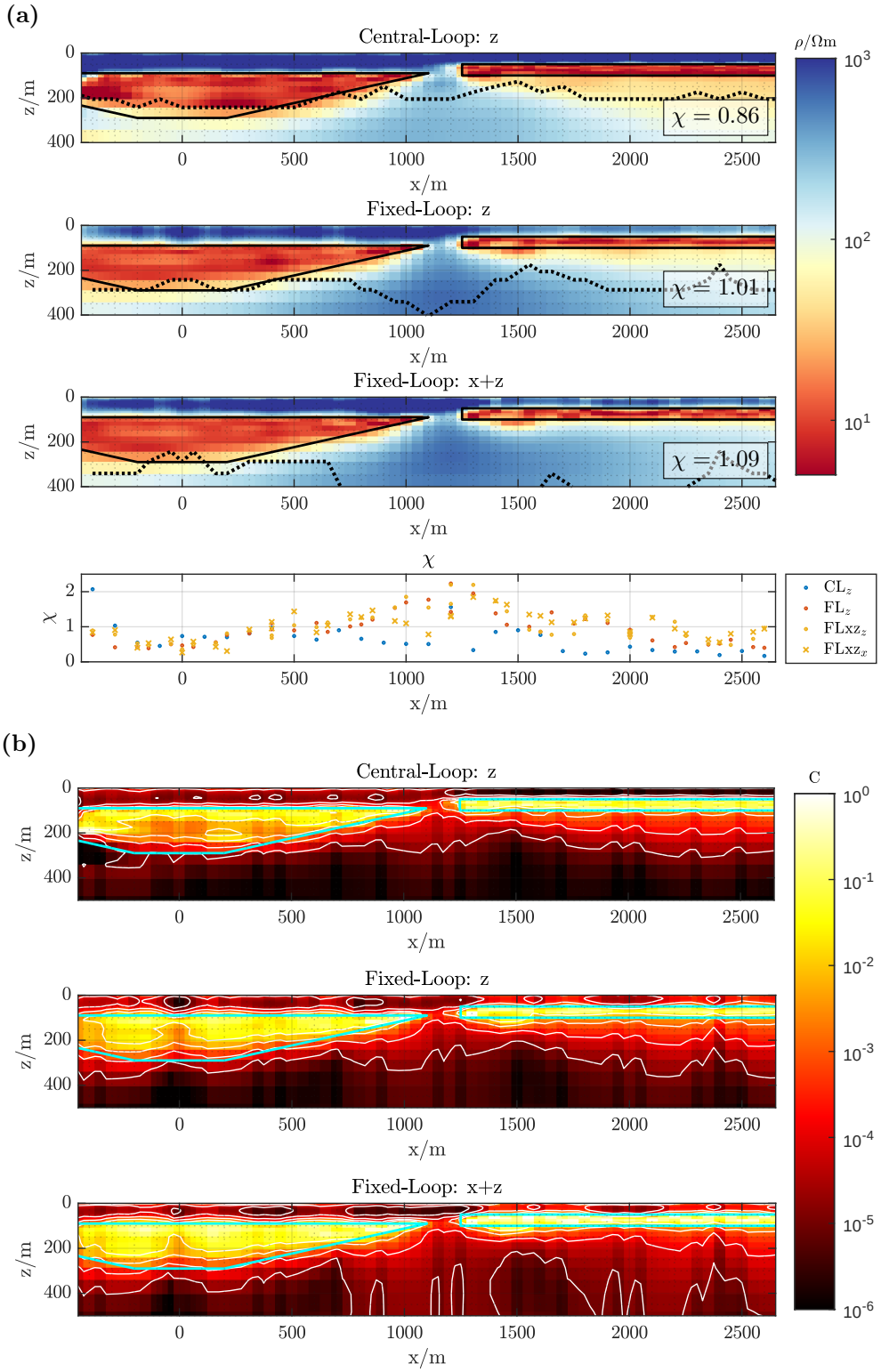

Figure 8.18.: 3D TEM inversion models and corresponding coverages for different TEM setups of a synthetic impact crater model. Modelled conductive anomalies are outlined by a solid line. The upper panel of **(a)** and **(b)** shows the results of the central-loop setup and the results of the Fixed-loop setup are shown in the two panels blow. **(a)** show the resistivities with the 1D DOI estimation (Christensen, 2014) and the data fit. **(b)** Normalized Sensitivities (normed to the highest coverage value of all three matrices) with contours representing the values 10^{-2}, 10^{-3}, 10^{-4} and 10^{-5}.

Table 8.1.: Computational Resources used for the 3D TEM inversion of central-loop and fixed-loop TEM data, without down-weighting of early times for the central-loop data.

	Central-Loop	**Fixed-Loop z**	**Fixed-Loop x+z**
Data Points	807	1056	2015
Processes	39	4	8
Cal. Time/h	25.75	6.75	12.15
Max. Memory/GB	878	125	250

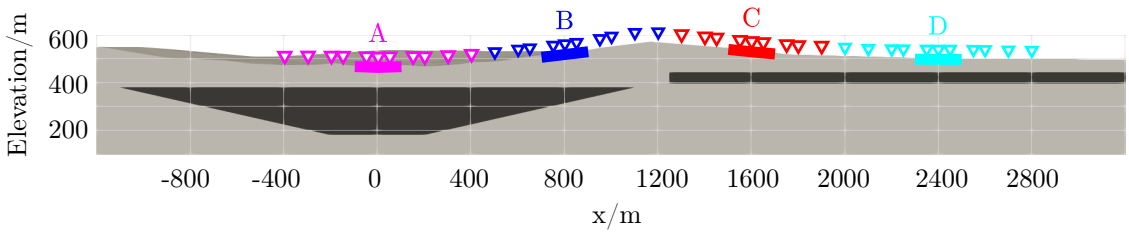

Figure 8.19.: xz-slice of a 3D model of a simple impact crater with with topography from the Roter Kamm Impact Crater. The background has a resistivity of 500 Ωm and the anomalies 10 Ωm. The fixed-loop survey setup is shown at the surface. The thick lines indicate the transmitters, the downward pointing triangles the receivers. Topography data: NASA JPL (2022).

group for each transmitter and component. Thus, it needs twice the amount of processes, which corresponds well with the amount of cores needed. The run time and the memory was also almost twice of what an inversion of just the vertical component needed. If the resources needed just to invert the vertical component is compared to the resources needed to invert the central-loop data (no down-weighting of early times), it becomes clear how much more efficient the fixed-loop setup is. The central-loop inversion needed almost 10 times the amount of cores, 3.8 times the calculation time and 7 time the memory, although the amount of data points was 23.6 % less.
This study shows that smaller central-loop transmitters are better in resolving the shallow subsurface. However, a fixed-loop setup using a larger transmitter and at least one additional horizontal component is almost equally good in shallow depths and resolves deeper structures much better. The needed resources for a 3D TEM inversion, also favour the use of a fixed-loop setup.

8.4.7. Topography

As a last test before inverting the TEM data, the influence of the topography on the inversion result must be considered. Therefore, a model including the same anomalies as before is used and the topography of the survey area is added (Figure 8.19). Only the fixed-loop data is modelled including the topography, as it is more sensitive to topography for the receivers with an offset to the transmitter position (Section 8.3). The setup is the same as used in the field survey. The inversion presented used not only the induced horizontal and vertical component, but also the full receiver arrays in both perpendicular directions with a slightly lower smoothness weighting parameter. The inversion model shows a good agreement with the synthetic model for the outer parts of the profile (Figure 8.20a). However, in the centre of the profile, where the crater rim is located, both anomalies show a deviation from the initial model and appear to bend downwards. The inversion also shows a higher data misfit in this area (Figure 8.20c), even higher than

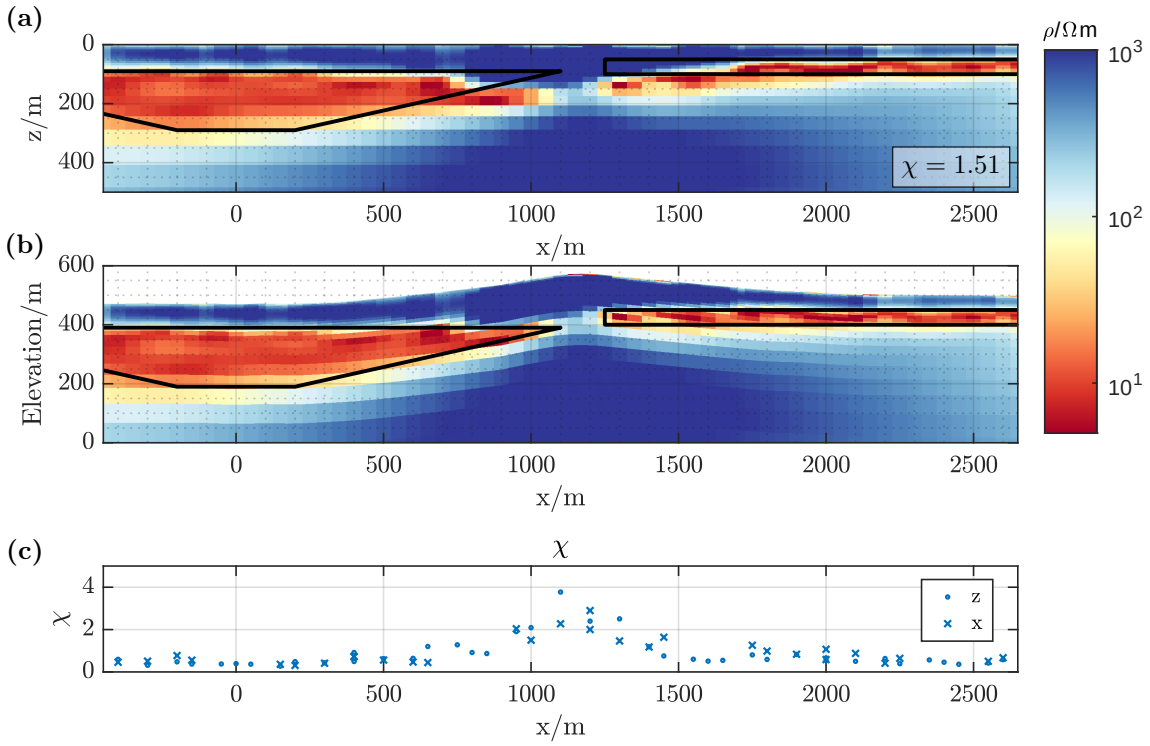

Figure 8.20.: 3D TEM inversion model of a synthetic fixed-loop TEM data of an impact crater model with topography. Modelled conductive anomalies are outlined by a solid line. **(a)** 2D xz-slice of the inversion model at iteration 13 ($\chi = 1.51$). **(b)** The same 2D xz-slice of the inversion model plotted with shifted grid cells in z-direction to simulate the topography. **(c)** Data misfit χ along the profile for both x- and z-components. Topography data: NASA JPL (2022).

observed previously (cf. Figure 8.17a). This lead to the decision to allow a higher target misfit of 1.5 for the field data, to accommodate for neglecting the topography.
The deviation of the anomalies seems to show an inverse behaviour to the topography. In an attempt to improve the presentation of the inversion models and simplify the interpretation the model was plotted shifting the vertical direction of the model grid onto the elevation level used for the modelling (Figure 8.20b). This modified presentation of the inversion model seems to represent the modelled anomalies more accurately. However, this modified presentation has to be used cautiously to avoid wrong interpretation, as it does not replace an inversion where the topography is incorporated.

8.5. Summary

Two three-dimensional TEM algorithms have been used in this thesis. The Python toolbox custEM for its flexibility in modelling arbitrary shaped bodies and incorporating topography. And the inversion algorithm TEM3Dinv, which has been successfully used for the inversion of central-loop data by Blanco-Arrué (2024).
The TEM data from the Roter Kamm impact crater show clear signs of multi-dimensionality, as demonstrated by synthetic studies of a realistic impact crater model using custEM. This confirms the need for a multi-dimensional inversion. Based on the synthetic data generated with custEM, extensive inversion studies were carried out to evaluate different

inversion grids, time stepping parameters and smoothness weighting parameters to find optimal settings for the inversion of profile data using a 3D inversion.
However, TEM3Dinv can not include topography. Therefore, studies with simple and real topography were carried out. The comparison of transient data modelled with homogeneous halfspaces with and without topography showed that the horizontal component may be more affected, while the vertical component seems to be more robust. The central-loop data even appear to be unaffected by topography. The effects of topography are confined to the exact area where the topography changes are observed. This could be observed by inverting the data without topography. The model only showed deviations in the shapes of the anomalies at the exact location of strong topographic changes. This can be very helpful in interpreting the field data.

CHAPTER 9

3D TEM Inversion of Field Data and Geological Interpretation

This chapter presents the 3D inversion results of the measured TEM data of the Roter Kamm impact crater. The same inversion grid, parameters and homogeneous initial model are used as described in Chapter 8. Inversions of both fixed-loop and single-loop TEM data-sets were performed to investigate the individual inversion behaviours. This is important for a final inversion including all TEM data. The fixed-loop TEM data-set inversions were inverted using a 3 % error floor. However, the single-loop data require a more advanced error model as TEM3Dinv does not take into account the dimensions of the receiver. The noise level is 1.7×10^{-11} V/Am^2 for the large fixed loop transmitter and 2.7×10^{-10} V/Am^2 for the small transmitter loop. Which scales with the size of the transmitter loop.

All inversion models were compared to determine the different survey designs and setups. The single loop inversion shows that a point receiver inversion is not a good approximation. Nevertheless, the models seem reasonable considering that the large conductive anomalies are similar to the fixed-loop TEM inversion model. A final inversion of all TEM data along both profiles should provide a comprehensive model of the interior of the Roter Kamm impact crater. This model could combine the resolution characteristics of both TME setups, the good shallow resolution of the single-loop data set and the better depth resolution of the fixed-loop data set. The TEM inversion models along Profile 1 are then compared with the 2D AMT inversion model, which is superior in depth resolution but inferior in horizontal resolution due to the low sounding density.

Finally, the geophysical inversion models are discussed and validated using all available information on the Roter Kamm impact crater and general knowledge of simple impact craters.

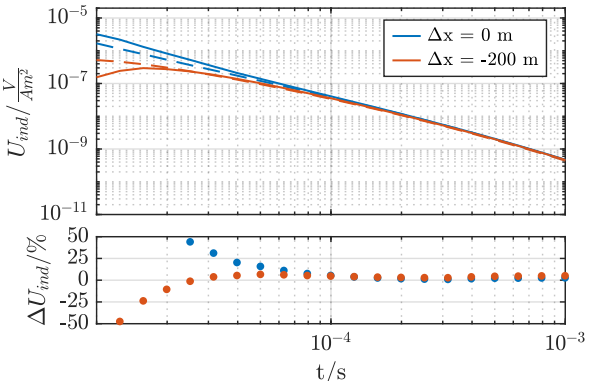

Figure 9.1: Comparison of the influence of a linear ramp with a length of 320 μs using EMUPLUS (dashed lines) and TEM3Dinv (solid lines) with a homogeneous halfspace of 1000 Ωm. The simulated data of the central loop ($\Delta x = 0$ m) and an offset receiver ($\Delta x = -200$ m) are shown.

9.1. Individual 3D Inversion of the TEM Field Data-Sets

To investigate the behaviour of each individual TEM data-set during inversion, both data-sets are first inverted individually using TEM3Dinv. The individual inversions help to identify potential data inversion issues that need to be addressed before a joint inversion of both data-sets can be performed, with particular attention paid to the strengths and weaknesses of each data-set and the different components of the fixed-loop data-set in order to determine an optimal survey setup for future TEM surveys. The aim of this section is not to describe the resistivity distribution, but rather the practical aspects of field data inversion.

9.1.1. 3D Inversion of the Fixed-Loop TEM Data

The inversion of the fixed-loop TEM data-set aims to provide a higher depth resolution than the single-loop data-set. A disadvantage is the lower resolution at shallow depth due to the low sampling rate of the receiver and the slow switching of the transmitter current. In addition, the lateral dimensions of conductive anomalies are expected to be better estimated by including a horizontal component in the TEM inversion. Two inversion models are presented here, one using only profile data and neglecting the perpendicular transects, and one using the full fixed-loop TEM arrays of each transmitter loop.
The influence of the transmitter ramp on the fixed-loop TEM data is shown to be significant. Therefore, prior to any inversion, the accurate modelling of the transmitter waveform must be validated for the chosen grid and inversion parameters.

Influence of the Ramp

The transmitter used for fixed-loop TEM measurements has a very slow, almost linear current decay with a length of 320 μs (Section 4.4.1). EMUPLUS and TEM3Dinv use different approaches to simulate the current waveform. EMUPLUS uses a convolution between the time derivative of the waveform and the response of the model. TEM3Dinv includes it in the source term during the time-stepping process. Both approaches are described and compared by Gao et al. (2023). A comparison between the modelled transient using the same linear ramp and a 1000 Ωm halfspace shows a large discrepancy for early times (Figure 9.1). To include the current ramp in the source term during time

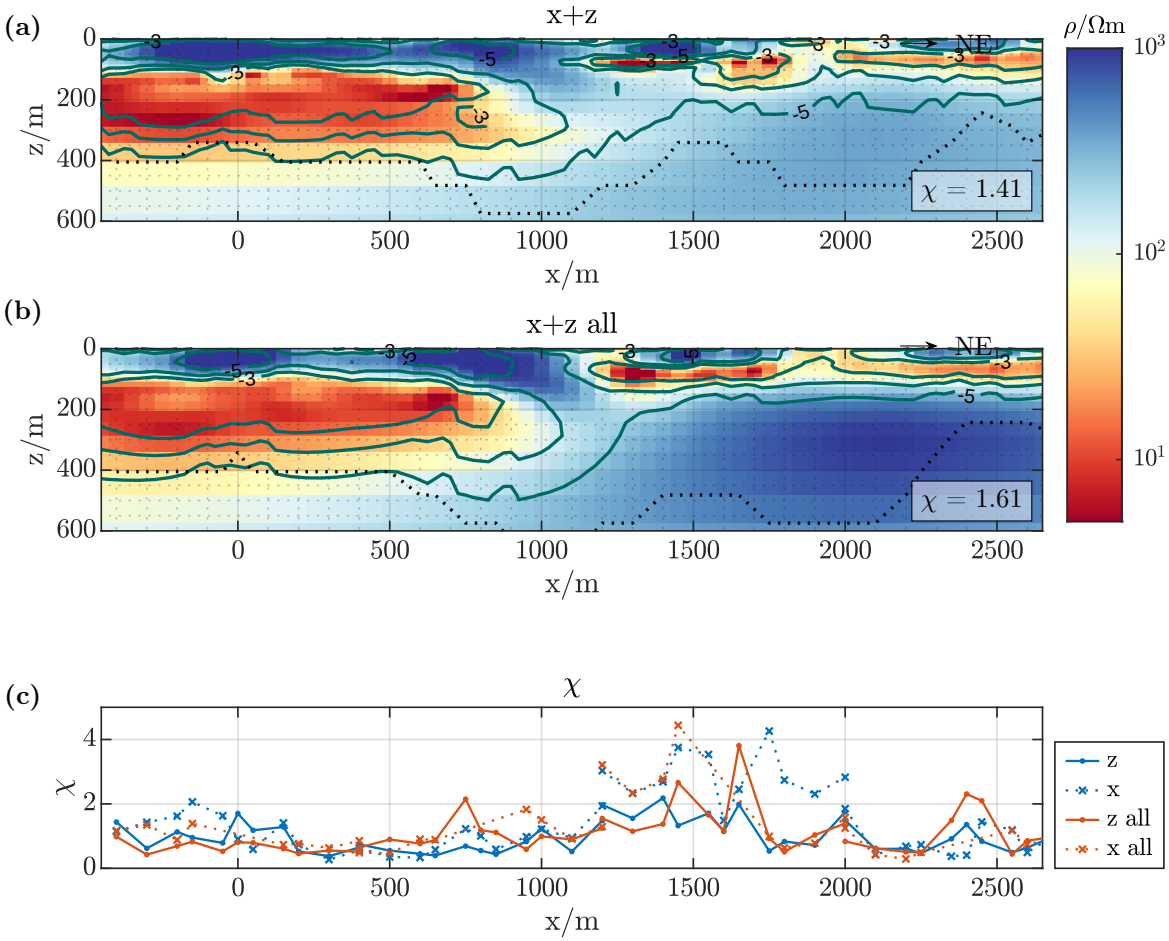

Figure 9.2.: 3D fixed-loop TEM inversion model using vertical and horizontal components along profile 1. The DOI is shown as a black dotted line and the sensitivities are shown in a dark blue-green colour. **(a)** Inversion of the x and z components. **(b)** Inversion of the x and z components of the full data set. **(c)** Data misfit χ value for all measured components.

stepping requires a very fine discretisation of time (Gao et al., 2023). Different starting times and initial step lengths were tested, but only a small improvement was achieved. The additional computational cost is immense, so all data points measured earlier than $t = 5 \times 10^{-5}$ s were excluded from the inversion. Although this sounds like a significant reduction in data, it only reduces the number of data points per transient by five. The discrepancy between the modelled responses decreases with resistivity, but as high resistivities are expected at shallow depths inside the impact crater, only a very resistive halfspace compares best with the real field data.

Inversion Models

Several inversion runs were performed using the fixed-loop data-set. As shown in the previous chapter, it is optimal to invert the vertical and horizontal components parallel to the profile simultaneously to achieve the best resolution. Often data are sampled along single profiles rather than on a 2D grid, similar to the situation presented in this thesis. However, here four vertical transects were included in the survey. Their influence on the inversion model can be seen (Figures 9.2a and b). The inversion model using the full

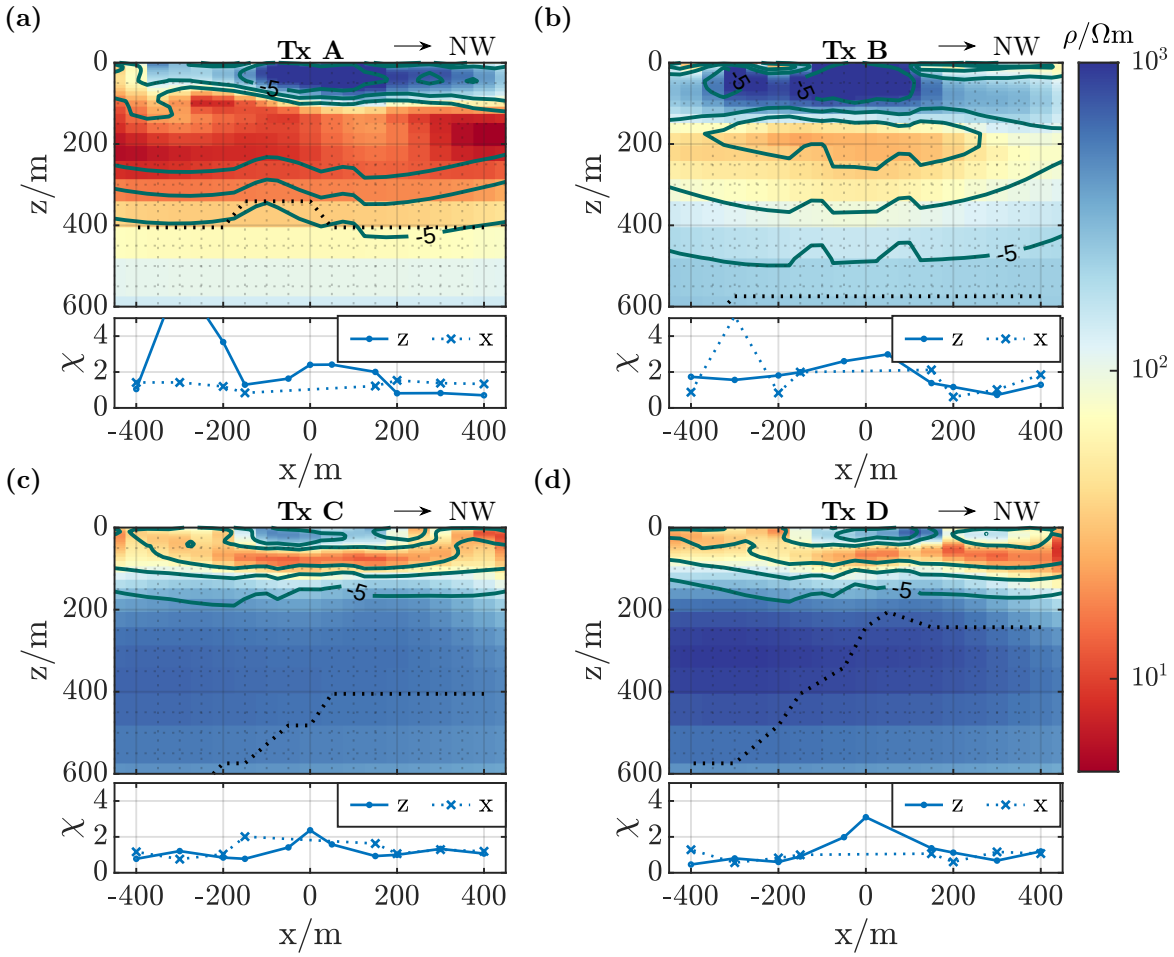

Figure 9.3.: 3D fixed-loop TEM model of the perpendicular transects. The χ value of the modelled data is 1.61. The DOI is shown as a dashed black line and the sensitivities are shown in a dark blue-green colour. The lower panels show the data fit of each transient. **(a)** x = 0 m **(b)** x = 800 m **(c)** x = 1600 m **(d)** x = 2400 m

layout appears smoother and less scattered in the north-eastern part of Profile 1 outside the impact crater. In addition, a dip below Transmitter A is visible in the inversion model using only the data along the profile. The additional data seems to increase the resolution of the resistivity below the conductive layer outside the Roter Kamm impact crater.
The perpendicular transects of Transmitters C and D show no strong variations within the 800 m profile length (Figure 9.3). However, the lack of resolution for receivers with an offset greater than 200 m. This is a direct consequence of the survey setup. Along the profile this effect can also be seen at both ends of the profile. It is less pronounced there because the data quality is slightly better and there is more early time data, especially compared to the perpendicular transects for Transmitters C and D. The transect for Transmitter B shows a weak conductive zone just in the centre, which appears almost symmetrical. This transmitter is placed close to the edge of the large conductive anomaly. Transmitter A is placed in the centre of the anomaly. This section shows that there may be some asymmetry in the interior of the crater, but due to the lack of resolution in the outer parts of the profile, only the single-loop data along Profile 2 can clearly show any structures in this area. The DOI shows that the conductive anomalies are well resolved.

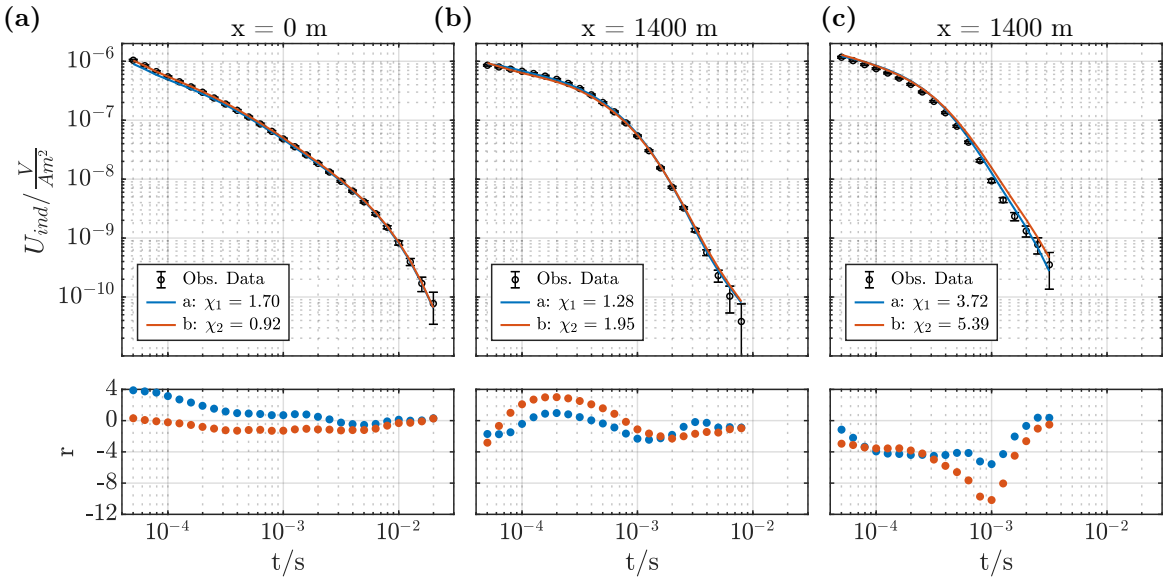

Figure 9.4.: Measured and modelled data from the 3D TEM inversions of the fixed-loop data. The upper panels show the data and the lower panels show the error-weighted residuals. The χ values of each transient are shown in the legend. The inversion of only the data along the profile is shown in blue, the inversion using the full layout is shown in orange. **(a)** Central-loop sounding in the centre of the Roter Kamm impact crater (x = 0 m) **(b)** and **(c)** Vertical and horizontal transients from an offset receiver of Transmitter C on the outer slope of the impact crater.

As discussed in the previous section, the DOI based on the cumulated sensitivities coincides with the lower boundary of a thick conductive anomaly. The normalised coverages with a value of 10^{-5} best match the DOI below the large conductive anomaly within the Roter Kamm impact crater.

The measured data is fitted quite well and the χ value does not vary significantly along the profile and transects (Figures 9.2c and 9.3). There are some slight increases in the centre of each transmitter for the inversion of the full survey layout. Both inversion models have a higher data misfit for Transmitter C. Synthetic studies showed that the strong multi-dimensional and topographic effects are expected here (Section 8.3). As this is a 3D inversion, the topography is most likely the cause of this discrepancy. As an example, the measured and modelled data are shown in figures 9.4b and c. The vertical data could be better fitted than the horizontal data. In particular, the model including all data has a large error-weighted residual at $t \approx 10^{-3}$s, but the residual is high for all times. Inside the crater the data are well fitted (see Figure 6.12) with neither model being superior.

9.1.2. 3D Inversion of the Single-Loop TEM Data

The single-loop data-set is the only data-set sampled over the full length of both profiles. Therefore it contains information that cannot be obtained otherwise. However, TEM3Dinv does not have a solution for the extended receiver loops implemented. 1D studies have shown significant discrepancies for a point and extended receiver (Section 6.1.3). The discrepancy increases with the size of the receiver and the conductivity of the subsurface. Therefore, the large single loops cannot be approximated with a point receiver, especially outside the Roter Kamm impact crater. Initial inversions proved this

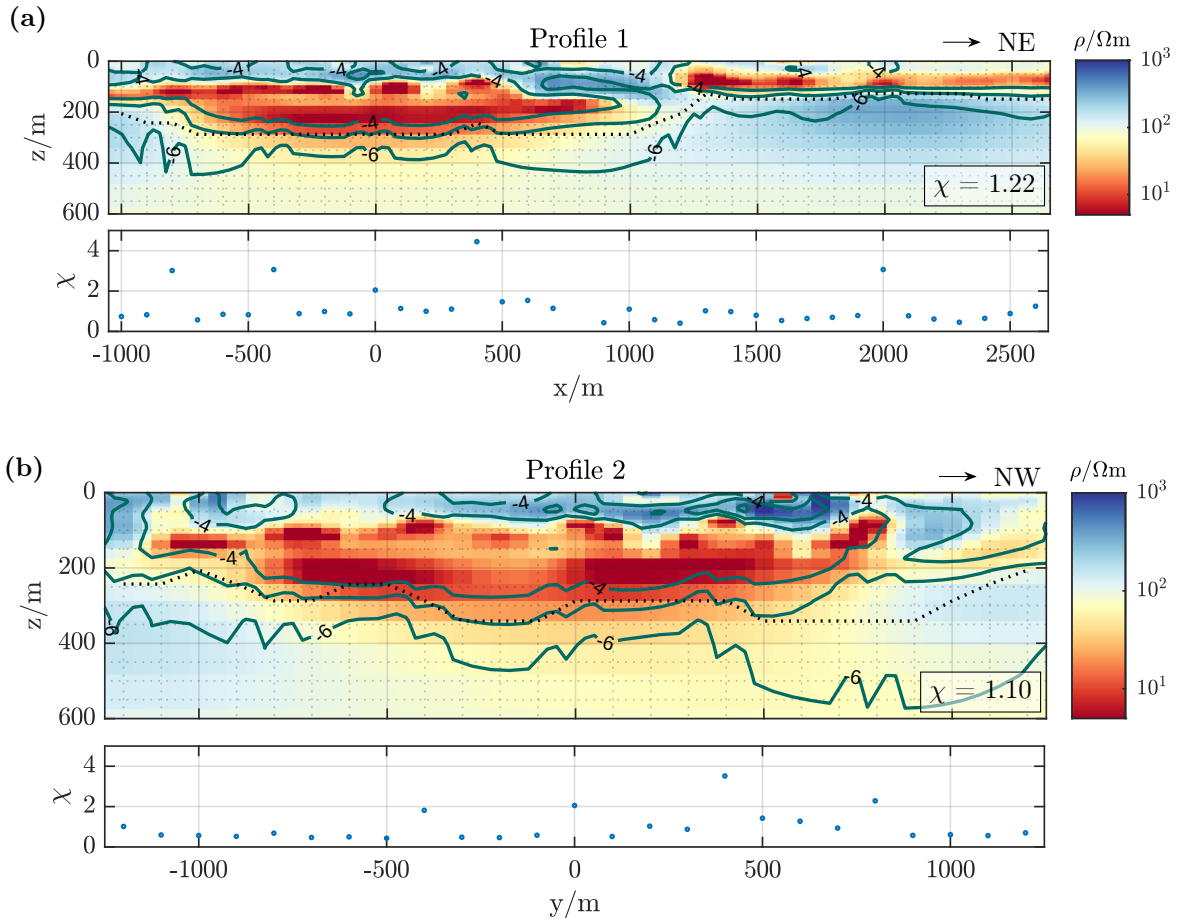

Figure 9.5.: 3D single-loop TEM inversion models along Profiles 1 and 2. The DOI is shown as a dashed black line and the normalised coverages are shown in a dark blue-green colour. The χ values are shown in the lower panels. The large single loops correspond to the higher χ values. **(a)** Profile 1 **(b)** Profile 2.

and showed how badly the wrong receiver approximation affected the data. It was decided to exclude all data for times smaller than $t = 5 \times 10^{-4}$ s from these transients, as only the late time information is valuable for the inversion. Nevertheless, all data points for times smaller than $t = 1 \times 10^{-3}$s were down-weighted by a logarithmically decreasing error of 20 %. This is consistent with the observations made in Section 6.1.3. The smaller single loops are less affected by this and therefore more reliable. The first decade of the transients of the small single loops are down-weighted with a logarithmically decreasing relative error of 10 %. A general error floor of 3.5 % was applied to the inversion.
The 3D inversions of both profiles, show a large conductor inside the Roter Kamm impact crater (Figure 9.5). The lateral extent of this conductor is similar in both profile directions. Both profiles show that the upper boundary of the conductor seemingly varies along the profile and an internal structure can be identified inside the body. However, I would like to point out the different loop sizes used in the same pattern along both profiles, which seems to correlate with the variations. On the other hand, the data fits of the transients measured with the large transmitter are significantly higher (Figure 9.6). Thus, the model is less reliable at those locations. It cannot be determined whether these structures are reliable or not. Profile 1 shows a conductive layer outside the Roter Kamm impact crater. The resistivities in both profiles below the conductive bodies are rather

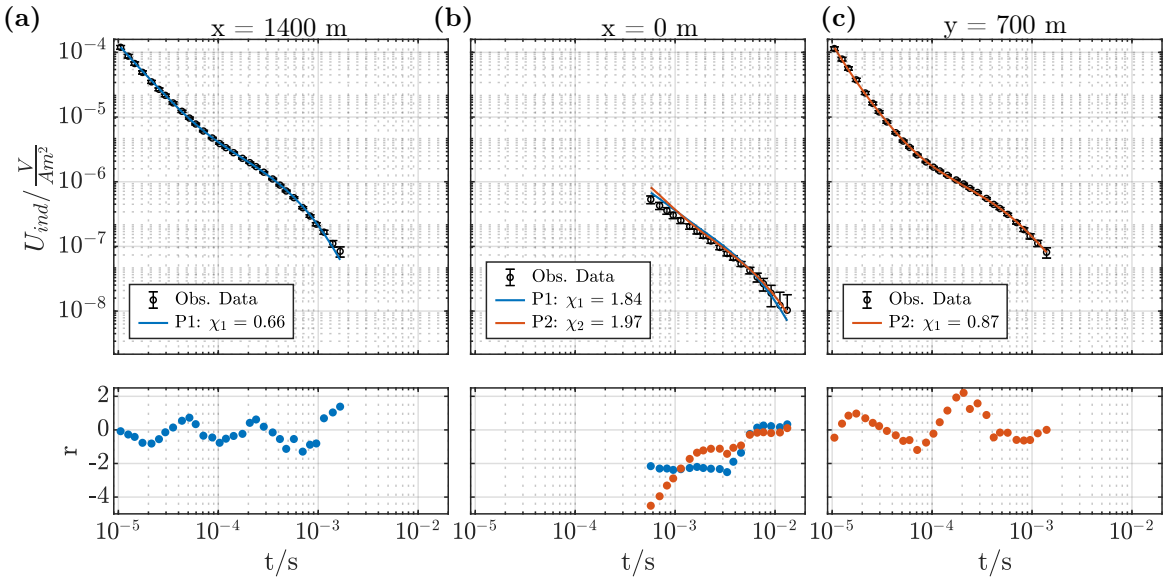

Figure 9.6.: Measured and modelled data from the 3D TEM inversions of the single-loop data. The upper panels show the data and the lower panels show the error-weighted residuals. The χ values of each transient are shown in the legend. The inversion of profile 1 is shown in blue, profile 2 in orange. **(a)** Loop outside the Roter Kamm impact crater (x = 1400 m) **(b)** Loop in the centre of the impact crater (x = 0 m) **(c)** Loop on the inner slope of the impact crater on Profile 2 (y = 700 m).

low and not well resolved. The large loops are only used for the depth information, as their shallow information is very limited because no down-weighting could compensate for the effect of the incorrect receiver size approximation. Therefore, an inversion using the correct receiver size would significantly improve the quality of the model in all depth ranges. The single-loop data alone cannot provide a conclusive interpretation of the Roter Kamm impact crater. However, there is great potential for improvement using the real receiver dimensions.

9.2. 3D Inversion of all TEM Data

Finally, a 3D inversion of all TEM data can be carried out. In theory, an inversion along each profile using all available TEM data should lead to the best model by exploiting the different resolutions of each data-set and component. However, this is questionable due to the incorrect approximation of the receiver loop dimensions. Wherever possible, the large single loops were excluded from the data-set . This was not possible in the south-western segment of Profile 1 and everywhere except the central part of Profile 2. The same error models as described above were used as the convergence rates of all inversions were similar (Figure 9.7). The initial χ value of the single-loop data was lower due to the higher relative errors for early times and the fewer total data points. Therefore, the number of iterations was slightly lower. The data is not weighted in any way other than by the error models, although the investigation shows that the fixed-loop data is more suitable for the inversion algorithm.

Both models converged significantly slower than any of the models presented previously (Figure 9.7). In particular, the inversion of profile 1, which contains the most data,

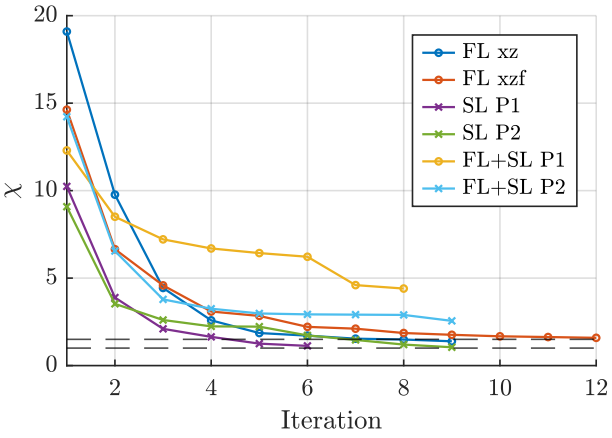

Figure 9.7: Misfit development with each iteration for all inversion models. They are labelled based on their method and the components used: FL for fixed-loop TEM and SL for single-loop TEM.

converged very slowly. Both models show the same general structure as the individual inversions of single and fixed-loop data (Figure 9.8). The inversion of Profile 2 shows the expected combination of shallow features from the single-loop data and the better depth resolution of the fixed-loop data in the centre of the profile (Figure 9.8b). The data misfit is highest in the centre of the profile, where the data density is highest. Nevertheless, this model is an improvement over the single-loop inversion. As discussed, the single-loop data are not modelled optimally by the 3D inversion algorithm, but the effects of receiver misfit are less severe inside the impact crater than outside the impact structure. Therefore, this model is reliable in terms of the general shape and dimensions of the anomaly.
The inversion of the TEM data along Profile 1 does not show as much of the positive aspects of combining the two data sets (Figure 9.8a). The single loops are less well fitted outside the impact crater due to lower resistivities at shallow depths. This is indicated by the high data misfit in the north-eastern part of Profile 1. Furthermore, the data is not well modelled in the area of the impact crater rim (500 m $<$ x $<$ 1300 m). While both individual inversions show a continuous layer outside the impact crater, the structure appears scattered in the combined inversion. The conductive anomaly within the Roter Kamm impact crater shows less sharp transitions to the resistive material in which it is embedded. In particular, the south-western part of the profile is not well defined, but depth resolution also appears to be lacking. It should be noted that the inversion did not converge to a low χ value.

To identify where the data are not well fitted by the inversion model along Profile 1, the error-weighted residuals of all data points can be calculated and plotted along the profile for both data sets and components (Figure 9.9). It can be seen that the fixed-loop data are not fitted as well as the single-loop data. The strongest differences are observed at the receiver arrays of Transmitter A and C in both induced voltage components (Figure 9.9b and c). Interestingly, the overall χ values of the transients corresponding to Transmitter A are low (Figure9.8a), but only the late time could be modelled well. All observations indicate that the data are only well modelled where the data sets do not overlap in the measured time ranges.

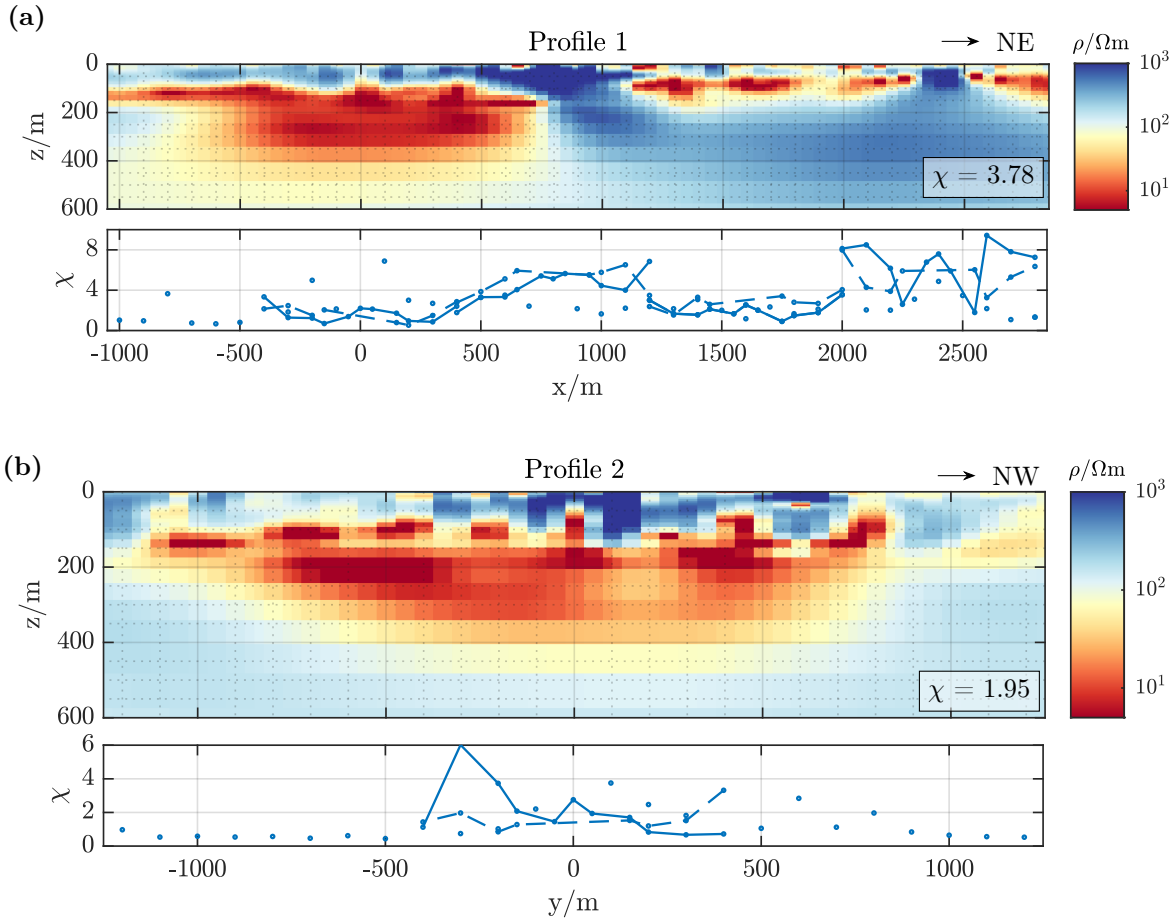

Figure 9.8.: 3D TEM inversion models of all TEM data along Profiles 1 and 2. The χ values are shown in the lower panels. The large single-loops coincide with the higher χ values. **(a)** Profile 1 **(b)** Profile 2.

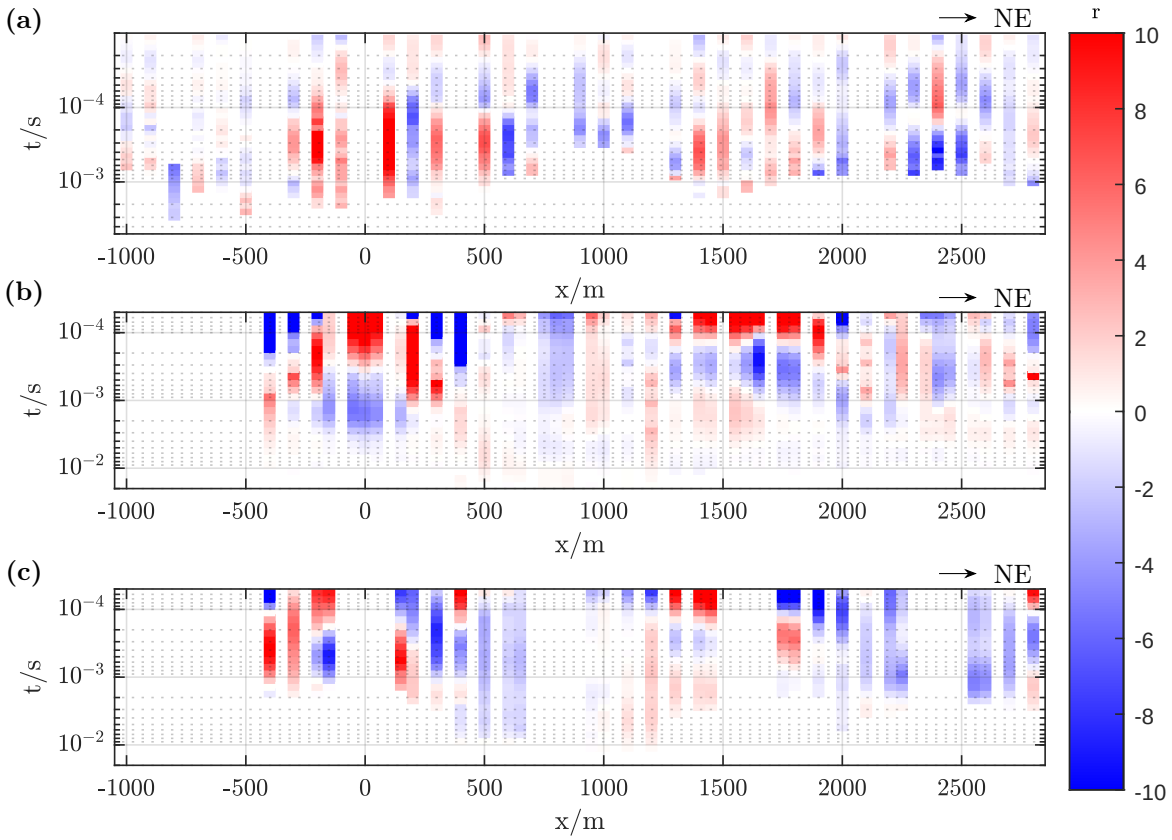

Figure 9.9.: Error weighted residuals of the 3D TEM inversion of single- and fixed-loop data. **(a)** Single-loop data **(b)** Vertical component of the fixed-loop data **(c)** Horizontal component of the fixed-loop data.

9.3. Integration of AMT and TEM Inversion Models

A comprehensive interpretation of the conductivity models requires an integration of all methods applied to the Roter Kamm impact crater. Thus, all final inversion models of TEM and AMT data-sets have to be compared (Figure 9.10). The vertical resistivity profiles at the centre of the Roter Kamm impact crater (x = 0 m) extracted from the 2D AMT and 3D fixed-loop TEM inversions are compared with the combined 1D inversion of both data-sets (Figure 9.10a). The similarities are remarkable and confirm the results of both methods. All three inversions show the same four layered subsurface in the upper 600 m. The surface layer has a resistivity of 80 Ωm and a thickness of 25 m, followed by a 1000-Ωm-layer (thickness: 85 m), a 10-Ωm layer (thickness: 230 m) and a 1000-Ωm halfspace below. The equivalent models show that the upper boundary and the resistivity of the third conductive layer are well resolved, while the lower boundary can only be resolved to an accuracy of ± 30 m. As the TEM and AMT methods are sensitive to conductivity, the resolution of high resistivities is not accurate. The first layer cannot be resolved well, simply because of instrumental limitations such as the sampling frequency of the receiver units.

Both inversion models along Profile 1 show a conductive anomaly shaped like a convex lens in a resistive surounding (Figure 9.10b). The contours shown are the 30 Ωm isolines and correspond well to the layering in the 1D inversion model of the AMT and TEM data. This lens is located centrally within the impact crater. Both methods show the north-eastern lateral boundary of the conductive anomaly along Profile 1 in similar locations. The small difference is probably due to the different horizontal density of the receiver locations and different regularisations. The south-eastern boundary of the conductive lens is not shown in the fixed-loop TEM model, but is shown in the single-loop inversion model at a slightly more south-westerly location. The horizontal dimension of the lens is about 1400 m to 1500 m. The shape of the anomaly is not perfectly symmetric, the slope of the lower boundary is steeper in the south- and northwestern part of the Roter Kamm impact crater (Figures 9.10b and 9.5b). However, while the TEM models resolve the horizontal extent of the conductor better due to much higher data density, the AMT method has a higher depth resolution and can therefore resolve the subsurface beneath the conductive lens. The resistivity beneath the conductive lens appears to increase gradually with depth, revealing resistivities higher than 1000 Ωm. Profile 2 shows a very similar extension of the conductive lens in the vertical direction, but about 300 - 400 m wider.
Outside of the impact structure a conductive layer can be detected, extending from the crater rim in north-eastern direction in a depth of around 50 m. This layer has a similar, but slightly lower resistivity, than the conductive lens inside the crater rims. At the rim location no conductive anomaly can be imaged and the models show just a resistive subsurface.

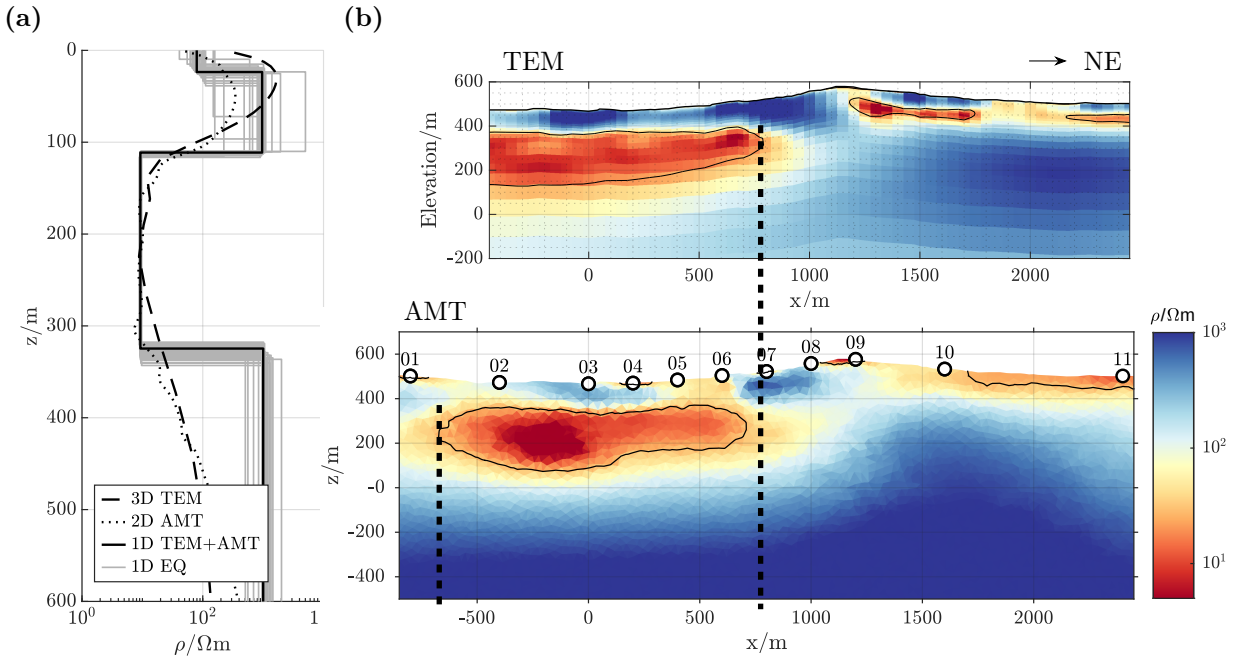

Figure 9.10.: Summary of TEM and AMT inversion results along Profile 1. **(a)** Combined 1D inversion of the AMT and TEM soundings compared with the vertical resistivity profile of the 3D TEM inversion model using the x- and z-components of the fixed-loop data and the 2D AMT inversion model in the centre of the Roter Kamm impact crater. **(b)** The fixed-loop TEM inversion models plotted including the true topography and AMT are shown on the right, with the horizontal dimensions of the anomaly within the crater marked. Topography data: NASA JPL (2022).

9.4. Geological Interpretation

The conductivity models can be used to determine the geological structure of the Roter Kamm impact crater. The thickness of the sedimentary cover can be determined and locations suitable for scientific drilling can be identified by locating areas of maximum sediment accumulation. Conductivity can also indicate water content. A low resistivity can be caused by a water saturated, porous medium, while high resistivities can indicate compact, solid rock. Furthermore, EM studies can be used to identify zones of higher fracturing and it is possible to distinguish between brecciated material and the bedrock (e.g., Pilkington and Grieve, 1992).

9.4.1. Sediment Cover

Four layers can be distinguished in the upper part of the Roter Kamm impact crater, with the conductive anomaly being the most prominent feature. The lower boundary of the conductor can be associated with the interface between the sedimentary cover and the brecciated rock that covers the true surface of an impact structure (Fudali, 1973). The sedimentary cover inside the crater structure is thus about (340 ± 30) m thick. This value is in the same range as previous gravity studies (Brandt et al., 1998; Fudali, 1973). As observed in the field and by previous scientists (e.g., Dietz, 1965; Fudali, 1973; Reimold and Miller, 1989), the rim of the Roter Kamm impact crater is not covered by sediments,

which explains the absence of any conductive anomaly at the crater rims. The resistivity variations in the sediments can be attributed to different moisture contents; the higher the conductivity, the higher the moisture content (Archie, 1942). The conductive lens marks a zone of particularly high moisture content or water accumulation, while the upper two layers are relatively dry. The uppermost layer is probably more conductive due to moisture, originating from the nightly fog and occasional rain events observed during the field survey. The similar resistivities of the conductive lens and the layer outside the crater suggest that the material composition could be similar. Thus aeolian sediments seem more likely and would be consistent with the assumptions of Miller (2010). The shape of the surface of the brecciated zone is asymmetric. Studies show that impact structures with an impact direction of 30° and greater have a circular horizontal shape, but may have asymmetric cross sections that correlate with the impact direction (Elbeshausen and Wünnemann, 2011), similar to what can be seen along Profile 2. Miller (2010) suggest a northwesterly impact based on the breccia apron, the cataclasite veins found in the rim and the different horizontal dimensions. The northwest-southeast diameter is approximately 200 m longer than the northeast-southwest diameter. The profiles presented here have approximately the same orientations (Profile 1: Northeast-Southwest, Profile 2: Northwest-Southeast) and similar observations were made in the lateral extent of the conductive body.

The sedimentary cover in the northeastern direction of the Roter Kamm impact crater is approximately 100 m thick. It has a maximum resistivity at the lowest topographic elevation, which can be attributed to a higher moisture and/or clay content. Several smaller clay pans are located along a transect between this zone of the profile and the Aurus clay pan (Figure 4.1). A single-loop TEM survey was carried out on one of these, which revealed a sediment accumulation of (60 ±5) m, with low resistivities down to 5 Ωm (Appendix B.3), similar to that found in the Aurus clay pan (Nienhaus et al., 2023c).

9.4.2. True shape of the impact structure

The upper boundary of the brecciated zone inside the rims could be revealed by the TEM and AMT measurements. However, only the AMT soundings provide a large enough DOI to map the true shape of the impact structure. Previous resistivity models have shown higher resistivities in brecciated and fractured rocks (Pilkington and Grieve, 1992). Unfortunately, the AMT data presented in this thesis do not show a clear layering beneath the large conductive anomaly within the Roter Kamm impact crater. There may be several reasons for this. On the one hand, the data quality is compromised by the high electrode contact resistance and the short time series inside the impact crater. On the other hand, the resolution of resistive structures below a conductor is very low. It is also possible that there is no large resistivity contrast between the brecciated zone and the fractured and undisturbed bedrock.

9.5. Summary

All TEM data were successfully inverted using the 3D TEM inversion algorithm TEM3Dinv. A 3D inversion using horizontal and vertical induced voltage components is presented,

showing a low data misfit. The inversion of the fixed-loop data showed only minor differences between the inversion using only the fixed-loop data along Profile 1 and one using the whole data set. They resolve the identified conductive anomalies well. Compared to the single-loop inversion models, the fixed-loop inversion models have better depth penetration and a smoother overall appearance. Unfortunately, the neglected extension of the receiver is clearly visible due to the higher data misfit for large single loops. Althougn, a significant time range of transients measured with the large loop was removed. The inversions along both profiles show a strong heterogeneity of the large conductive anomaly within the Roter Kamm impact crater. Whether this is reasonable or not cannot be determined. The inversions of both data-sets combined along Profiles 1 and 2 show that a survey combining fixed and central or single loops can be beneficial to the results. The inversion showed the potential of combining the resolution depth scales well. However, the single-loop data sets require accurate modelling of the receiver.

All TEM inversion models agree with the location and size of the conductive anomalies inside and outside the Roter Kamm impact crater. A comparison with the 2D AMT model shows a striking similarity. Comparison of the vertical resistivity curves from a combined 1D inversion of the AMT and fixed-loop TEM data in the centre of the impact crater with those extracted from their multi-dimensional inversion showed impressive agreement. Based on the thickness of the conductive layer determined in the 1D inversion, contour lines were included in the multi-dimensional inversion of the AMT and fixed-loop data sets. This showed that the cross-sections of the conductive anomaly also agree well in size and depth. Minor differences can be attributed to data errors and different spatial resolutions.

The conductive anomaly can be interpreted as an accumulation of water in porous aeolian sediments covered by dry sediments. The sediment cover reaches a thickness of (340 ± 30) m within the Roter Kamm impact crater. There are no structures visible beneath the sediment cover. Outside the crater the sedimentary cover has a fairly constant thickness of 100 m. The composition may be similar to that inside the crater. However, higher clay contents are possible at the lowest elevation.

CHAPTER 10

Conclusion and Outlook

The Roter Kamm impact crater in southern Namibia was investigated using the TEM and AMT methods, with a particular emphasis on a multi-component fixed-loop TEM configuration. The geophysical information regarding the Roter Kamm impact crater is limited, and to the best of my knowledge, no geophysical inversion model has been proposed. The objective of this study is to determine the thickness of the sediments covering the impact structure, and to evaluate the potential for obtaining a deep climate archive at a later stage of the Collaborative Research Center CRC 1211. The climate archive could be used to study the evolution of the Namib Desert in the near absence of water. A comparison of the Namib Desert's evolution with the findings from the hyper-arid Atacama Desert in Chile, obtained through deep drilling, is a potential direction for future research (Wennrich et al., 2024).

In early 2022, a fixed-loop and single-loop TEM survey was conducted in the southern Namib Desert to study the Aurus clay pan and the Roter Kamm impact crater. The survey at the impact crater was complemented by additional AMT soundings.The main efforts were carried out along a transect crossing the entire impact structure and extending into the surrounding plain.This profile was further extended a few single-loop soundings along the trail between the Roter Kamm impact crater and the Aurus Mountains. The fixed- and single-loop TEM, along with the AMT data, were sampled along this profile, both inside and in close proximity to the impact crater. Additionally, data along a second profile was collected, which is perpendicular to the focus profile and intersects with it in the approximate center of the impact structure. This profile is exclusively located within its boundaries.

The single-loop data and the vertical components of the fixed-loop data were inverted using a 1D inversion algorithm. However, the algorithm can only model point receivers, yet the extended size of the receivers significantly impacts the recorded induced voltages. The discrepancy between point and extended receivers increases with loop size and conductivity of the subsurface, resulting in an adapted error model for early times and a lower resolution for shallow depths. To maximize the potential of the data, it is recommended

that in future studies, that extended receivers be modelled. Furthermore, the utilization of small loop sizes is inadequate in resolving the depth dimensions of the conductive layer. This layer exhibits a substantial resistivity contrast compared to the surrounding media. A 2D section of all 1D inversion models along each profile reveals inconsistencies in the models in the areas of the crater rim, indicating the multi-dimensionality of the subsurface. The vertical components of the fixed-loop TEM data yield reasonable models for the transmitters located in the center of the Roter Kamm impact crater and on the plain outside. However, the data from transmitters located on the inside and outside slope of the crater rim did not converge or show consistent results. The fixed-loop TEM setup is more prone to distortion by multi-dimensionality due to the source-receiver distance. Consequently, a multi-dimensional inversion is crucial to ensure the reliability of the results.

To address these challenges, a comprehensive study was conducted involving 3D forward modelling and inversion studies. These studies aimed to understand the effects of topography and multi-dimensionality on the results. Two 3D time-domain algorithms, custEM for the forward and TEM3Dinv for the inverse modelling, were employed in the study. The results of the tests indicate that both the horizontal and vertical components of the offset data are influenced by topography and multi-dimensionality. The central-loop data demonstrated minimal distortion from topography and exhibited reduced distortion from multi-dimensionality when compared to the fixed-loop data. Utilizing a simplified model of an impact crater, based on the two-dimensional AMT and one-dimensional TEM models, optimal inversion and time-stepping parameters were determined to obtain a reasonable two-dimensional slice of the three-dimensional model. Subsequent resolution studies demonstrated that incorporating an additional horizontal component, enhances the resolution of the model, validating the importance of including this additional component. A comparison between the inversion and sensitivity models of the simulated central- and fixed-loop data indicated that the central-loop data exhibited superior resolution of shallow and the fixed-loop data exhibited superior resolution of larger depths. This outcome is attributed to the distinct time ranges measured by these setups and the used transmitter size. The findings of this study imply that an optimal TEM survey setup should consist of different transmitter sizes. The manual labour involved can be minimized by choosing a fixed-loop TEM setup using large transmitters, which can be complemented by sparse small central-loop soundings for better resolution in shallow depths. Another advantage of this measurement configuration is a severe decrease in computational resources needed for inversion due to the decreased transmitter number.

In the final chapter of this thesis, all gathered experience from the modelling and inverse study were applied to invert all TEM field data. The fixed-loop data set, incorporating all receiver arrays, was successfully inverted using both components excited by the loop-source transmitter. This inversion exhibited a strong agreement with the inversion limited to the data along the profile. The coverages demonstrated a satisfactory resolution for both conductive anomalies revealed. In contrast, the inversion of the single-loop data posed significant challenges due to the absence of consideration for receiver dimensions in the 3D inversion algorithm. To address this challenge, an adapted error model was employed, drawing insights from the 1D modelling study presented in Chapter 6. However, this approach comes with the drawback of reduced resolution in shallow depths, which

limits the potential for enhancing shallow depth resolution through this configuration. Despite these limitations, the models exhibit comparable fundamental characteristics to those of the fixed-loop data inversion. The validity of the models, particularly the representation of small-scale heterogeneities, remains questionable without accounting for the influence of receiver dimensions. A final inversion of all data along both TEM profiles demonstrates a definitive enhancement of the model for Profile 2. Profile 2 just contains an overlap between both data sets in the central part of the impact structure, which is considerably smaller than the data overlap along the main focus profile. The data misfit of the inversion along this profile converged only slowly, and the modelled and measured data shows significant discrepancies between in the time ranges of the data overlap. In contrast, the time ranges that do not overlap exhibit minimal deviation. A comparison of the fixed-loop TEM inversion model and the 3D AMT inversion model demonstrated remarkable agreement. Overall, all three data sets of the Roter Kamm impact crater exhibit significant similarities and are in agreement with respect to the dimensions of the conductive anomalies detected.

Within the Roter Kamm crater, a substantial conductive body, interpreted as water-saturated sediments, is present. This body exhibits a horizontal dimension ranging from 1400 to 1500 meters and a thickness of 220 meters. It features a flat, horizontal upper boundary at a depth of 110 meters and a convex lower boundary, thereby exhibiting a striking resemblance to the expected shape of an impact crater.

This thesis emphasizes the benefits of employing a survey design that integrates a multi-component fixed-loop TEM setup, which ensures optimal depth and lateral resolution, with a central-loop setup utilizing smaller transmitters. This combination enables the acquisition of a substantial vertical resolution across various depth scales. Additionally, this approach reduces the computational resources necessary for three-dimensional inversions. This is essential for incorporating horizontal components, which exhibit heightened sensitivity to lateral boundaries compared to vertical components. However, this thesis stresses the significance of accurately modelling receiver dimensions, as substantial modelling errors can compromise model quality by losing information. The TEM inversion models were validated using an AMT data set, demonstrating the capabilities of the TEM methods for larger target depths by using larger transmitter sizes. Additionally, this thesis presents the first comprehensive geophysical model of the sedimentary cover at the Roter Kamm impact crater, which is not based on any a-priori information.

Bibliography

AEMR, 2007. TEM-FAST 48 (MANUAL): Version 7.3.

Amestoy, P. R., Duff, I. S., L'Excellent, J., Koster, J., 2001. A fully asynchronous multifrontal solver using distributed dynamic scheduling. SIAM Journal on Matrix Analysis and Applications 23 (1), 15–41. https://doi.org/10.1137/S0895479899358194

Archie, G., 1942. The electrical resistivity log as an aid in determining some reservoir characteristics. Transactions of American Institute of Mining Metallurgical Engineers 146, 54–62. https://doi.org/10.2118/942054-G

Auken, E., Christiansen, A. V., Jacobsen, L. H., Sørensen, K. I., 2008. A resolution study of buried valleys using laterally constrained inversion of TEM data. Journal of Applied Geophysics 65 (1), 10–20. https://doi.org/10.1016/j.jappgeo.2008.03.003

Auken, E., Foged, N., Larsen, J. J., Lassen, K. V. T., Maurya, P. K., Søren Møller Dath, Eiskjær, T. T., 2019. tTEM — A towed transient electromagnetic system for detailed 3D imaging of the top 70 m of the subsurface. Geophysics 84 (1), E13–E22. https://doi.org/10.1190/geo2018-0355.1

Avdeev, D. B., 2005. Three-dimensional electromagnetic modelling and inversion from theory to application. Surveys in Geophysics 26 (6), 767–799. https://doi.org/10.1007/s10712-005-1836-x

Bahr, K., 1988. Interpretation of the magnetotelluric impedance tensor: Regional induction and local telluric distortion. Journal of Geophysics 62 (1), 119–127. https://journal.geophysicsjournal.com/jofg/article/view/129

Bahr, K., 1991. Geological noise in magnetotelluric data: A classification of distortion types. Physics of the Earth and Planetary Interiors 66 (1), 24–38. https://doi.org/10.1016/0031-9201(91)90101-M

Blanco-Arrué, B., 2024. Multidimensional transient electromagnetic data for the exploration of clay pans in the Atacama Desert, Chile. PhD Thesis, University of Cologne, Cologne.

Blanco-Arrué, B., Yogeshwar, P., Tezkan, B., Mörbe, W., Díaz, D., Farah, B., Buske, S., Ninnemann, L., Domagala, J. P., Diederich-Leicher, J. L., Gebhardt, A. C., Wennrich, V., 2022. Exploration of sedimentary deposits in the Atacama Desert, Chile, using integrated geophysical techniques. Journal of South American Earth Sciences 115, 103746. https://doi.org/10.1016/j.jsames.2022.103746

Börner, R., 2010. Numerical modelling in geo-electromagnetics: Advances and challenges. Surveys in Geophysics 31 (2), 225–245. https://doi.org/10.1007/s10712-009-9087-x

Börner, R., Ernst, O. G., Güttel, S., 2015. Three-dimensional transient electromagnetic modelling using Rational Krylov methods. Geophysical Journal International 202 (3), 2025–2043. https://doi.org/10.1093/gji/ggv224

Brandt, D., Reimold, W. U., Franzsen, A. J., Koeberl, C., Wendorff, L., 1998. Geophysical profile of the Roter Kamm impact crater, Namibia. Meteoritics & Planetary Science 33 (3), 447–453. https://doi.org/10.1111/j.1945-5100.1998.tb01649.x

Chave, A. D., Jones, A. G., 2012. The magnetotelluric method: Theory and practice. Cambridge University Press, Cambridge.

Christensen, N. B., 2014. Sensitivity functions of transient electromagnetic methods. Geophysics 79 (4), E167–E182. https://doi.org/10.1190/geo2013-0364.1

Christiansen, A. V., Auken, E., 2012. A global measure for depth of investigation. Geophysics 77 (4), WB171–WB177. https://doi.org/10.1190/geo2011-0393.1

Christiansen, A. V., Auken, E., Sørensen, K. I., 2006. The transient electromagnetic method. In: Kirsch, R. (Ed.), Groundwater geophysics. Springer, Berlin and Heidelberg, pp. 179–225.

Cohen, A. S., 2012. Scientific drilling and biological evolution in ancient lakes: Lessons learned and recommendations for the future. Hydrobiologia 682 (1), 3–25. https://doi.org/10.1007/s10750-010-0546-7

Commer, M., Newman, G. A., 2004. A parallel finite–difference approach for 3D transient electromagnetic modeling with galvanic sources. Geophysics 69 (5), 1192–1202. https://doi.org/10.1190/1.1801936

Constable, C. G., Constable, S. C., 2023. A grand spectrum of the geomagnetic field. Physics of the Earth and Planetary Interiors 344, 107090. https://doi.org/10.1016/j.pepi.2023.107090

Constable, S. C., Parker, R. L., Constable, C. G., 1987. Occam's inversion: A practical algorithm for generating smooth models from electromagnetic sounding data. Geophysics 52 (3), 289–300. https://doi.org/10.1190/1.1442303

Cox, L. H., Wilson, G. A., Zhdanov, M. S., 2012. 3D inversion of airborne electromagnetic data. Geophysics 77 (4), WB59–WB69. https://doi.org/10.1190/geo2011-0370.1

Danielsen, J., Auken, E., Jørgensen, F., Søndergaard, V., Sørensen, K. I., 2003. The application of the transient electromagnetic method in hydrogeophysical surveys. Journal of Applied Geophysics 53, 181–198. https://doi.org/10.1016/j.jappgeo.2003.08.004

Dence, M. R., 1972. The nature and significance of terrestrial impact structures. In: Gill, J. E., Goodwin, A. M., Wynne-Edwards, H. R. (Eds.), Proceedings of the 24th International Geological Congress. pp. 77–89.

Dentith, M. C., Mudge, S. T., 2014. Geophysics for the mineral exploration geoscientist. Cambridge University Press, Cambridge.

Diederich, J. L., Wennrich, V., Bao, R., Büttner, C., Bolten, A., Brill, D., Buske, S., Campos, E., Fernández-Galego, E., Gödickmeier, P., Ninnemann, L., Reyers, M., Ritter, B., Ritterbach, L., Rolf, C., Scheidt, S., Dunai, T. J., Melles, M., 2020. A 68 ka precipitation record from the hyperarid core of the Atacama Desert in northern Chile. Global and Planetary Change 184, 103054. https://doi.org/10.1016/j.gloplacha.2019.103054

Dietz, R. S., 1965. Roter Kamm, Southwest Africa: Probable meteorite crater. Meteoritics 2 (4), 311–314. https://doi.org/10.1111/j.1945-5100.1965.tb01438.x

Druskin, V. L., Knizhnerman, L. A., 1988. Spectral differential-difference method for numeric solution of three-dimensional nonstationary problems of electric prospecting. Earth Physics 1 (8).

Druskin, V. L., Knizhnerman, L. A., 1994. Spectral approach to solving three-dimensional Maxwell's diffusion equations int the time and frequency domain. Radio Science 29 (4), 937–953. https://doi.org/10.1029/94RS00747

Dunai, T. J., Melles, M., Quandt, D., Knief, C., Amelung, W., 2020. Whitepaper: Earth – Evolution at the dry limit. Global and Planetary Change 193, 103275. https://doi.org/10.1016/j.gloplacha.2020.103275

Earth Impact Database, 2011. http://www.unb.ca/passc/ImpactDatabase/ (Accessed at 13.08.2024)

Elbeshausen, D., Wünnemann, K., 2011. The effect of target topography and impact angle on crater formation - Insight from 3D numerical modelling. 42nd Lunar and Planetary Science Conference.

EMIT, 2018. USER GUIDE for the SMARTem24 and DigiAtlantis Systems.

ESRI, 2022. World Imagery. https://server.arcgisonline.com/ArcGIS/rest/services/World_Imagery/MapServer/tile/{z}/{y}/{x} (Accessed at 09.11.2024)

Fitterman, D. V., 2014. Mapping saltwater intrusion in the Biscayne Aquifer, Miami-Dade County, Florida using transient electromagnetic sounding. Journal of Environmental and Engineering Geophysics 19 (1), 33–43. https://doi.org/10.2113/JEEG19.1.33

Fudali, R. F., 1973. Roter Kamm: Evidence for an impact origin. Meteoritics 8 (3), 245–257. https://doi.org/10.1111/j.1945-5100.1973.tb01253.x

Gao, J., Liu, X., Zhu, W., Smirnov, M. Y., Rasmussen, T. M., Huang, L., Li, J., Fang, G., 2023. Three-Dimensional Transient Electromagnetic Forward Modeling for Simulating Arbitrary Source Waveform Using Convolution Approach. IEEE Transactions on Geoscience and Remote Sensing 61, 1–13. https://doi.org/10.1109/TGRS.2023.3286977

Geonics, 02.11.2024. GEOPHYSICAL INSTRUMENTATION FOR EXPLORATION & THE ENVIRONMENT. https://geonics.com/pdfs/downloads/catalogue.pdf

Goldman, M., Gilad, D., Ronen, A., Melloul, A., 1991. Mapping of seawater intrusion into the coastal aquifer of Israel by the time domain electromagnetic method. Geoexploration 28 (2), 153–174. https://doi.org/10.1016/0016-7142(91)90046-F

Goldman, M., Tabarovsky, L., Rabinovich, M., 1994. On the Influence of 3-D structures in the interpretation of transient electromagnetic sounding data. Geophysics 59 (6), 889–901. https://doi.org/10.1190/1.1443648

Grant, J. A., 1999. Evaluating the evolution of process specific degradation signatures around impact craters. International Journal of Impact Engineering 23 (1, Part 1), 331–340. https://doi.org/10.1016/S0734-743X(99)00084-6

Grant, J. A., Koeberl, C., Reimold, W. U., Schultz, P. H., 1997. Gradation of the Roter Kamm impact crater, Namibia. Journal of Geophysical Research: Planets 102 (E7), 16327–16338. https://doi.org/10.1029/97JE01315

Grieve, R. A., 1993. Recent studies at the Roter Kamm impact crater. Meteoritics 28 (2), 160. https://doi.org/10.1111/j.1945-5100.1993.tb00754.x

Haber, E., Oldenburg, D. W., Shekhtman, R., 2007. Inversion of time domain three-dimensional electromagnetic data. Geophysical Journal International 171 (2), 550–564. https://doi.org/10.1111/j.1365-246X.2007.03365.x

Han, B., Li, Y., Li, G., 2018. 3D forward modeling of magnetotelluric fields in general anisotropic media and its numerical implementation in Julia. Geophysics 83 (4), F29–F40. https://doi.org/10.1190/geo2017-0515.1

Hansen, P. C., O'Leary, D. P., 1993. The use of the L-curve in the regularization of discrete ill-posed problems. SIAM Journal on Scientific Computing 14 (6), 1487–1503. https://doi.org/10.1137/0914086

Hanstein, T., Eilenz, H., Strack, K., 1986. Einige Aspekte der Aufbereitung von LOTEM Daten. In: Haak, V., Homilius, J. (Eds.), Protokoll über das 11. Kolloquium für Elektromagnetische Tiefenforschung. https://gfzpublic.gfz-potsdam.de/rest/items/item_5013724_2/component/file_5013725/content

Haroon, A., Adrian, J., Bergers, R., Gurk, M., Tezkan, B., Mammadov, A. L., Novruzov, A. G., 2015. Joint inversion of long–offset and central–loop transient electromagnetic data: Application to a mud volcano exploration in Perekishkul, Azerbaijan. Geophysical Prospecting 63 (2), 478–494. https://doi.org/10.1111/1365-2478.12157

Heagy, L. J., Cockett, R., Kang, S., Rosenkjaer, G. K., Oldenburg, D. W., 2017. A framework for simulation and inversion in electromagnetics. Computers & Geosciences 107, 1–19. https://doi.org/10.1016/j.cageo.2017.06.018

Hecht, L., Reimold, W. U., Sherlock, S., Tagle, R., Koeberl, C., Schmitt, R., 2008. New impact–melt rock from the Roter Kamm impact structure, Namibia: Further constraints on impact age, melt rock chemistry, and projectile composition. Meteoritics & Planetary Science 43 (7), 1201–1218. https://doi.org/10.1111/j.1945-5100.2008.tb01123.x

Hermeline, F., Layouni, S., Omnes, P., 2008. A finite volume method for the approximation of Maxwell's equations in two space dimensions on arbitrary meshes. Journal of Computational Physics 227 (22), 9365–9388. https://doi.org/10.1016/j.jcp.2008.05.013

Hördt, A., Druskin, V. L., Knizhnerman, L. A., Strack, K., 1992. Interpretation of 3-D effects in long–offset transient electromagnetic (LOTEM) soundings in the Münsterland area/Germany. Geophysics 57 (9), 1127–1137. https://doi.org/10.1190/1.1443327

Hördt, A., Müller, M., 2000. Understanding LOTEM data from mountainous terrain. Geophysics 65 (4), 1113–1123. https://doi.org/10.1190/1.1444804

Jahandari, H., Ansari, S., Farquharson, C. G., 2017. Comparison between staggered grid finite–volume and edge–based finite–element modelling of geophysical electromagnetic data on unstructured grids. Journal of Applied Geophysics 138, 185–197. https://doi.org/10.1016/j.jappgeo.2017.01.016

Jørgensen, F., Sandersen, P. B. E., Auken, E., 2003. Imaging buried Quaternary valleys using the transient electromagnetic method. Journal of Applied Geophysics 53 (4), 199–213. https://doi.org/10.1016/j.jappgeo.2003.08.016

Jupp, D. L. B., Vozoff, K., 1975. Stable iterative methods for the inversion of geophysical data. Geophysical Journal of the Royal Astronomical Society 42 (3), 957–976. https://doi.org/10.1111/j.1365-246X.1975.tb06461.x

Kaufman, A. A., Keller, G. V., 1983. Frequency and transient soundings. Vol. 16 of Methods in geochemistry and geophysics. Elsevier, Amsterdam.

Key, K., 2016. MARE2DEM: A 2-D inversion code for controlled-source electromagnetic and magnetotelluric data. Geophysical Journal International 207 (1), 571–588. https://doi.org/10.1093/gji/ggw290

Kirkegaard, C., Foged, N., Auken, E., Christiansen, A. V., Sørensen, K. I., 2012. On the value of including x-component data in 1D modeling of electromagnetic data from helicopterborne time domain systems in horizontally layered environments. Journal of Applied Geophysics 84, 61–69. https://doi.org/10.1016/j.jappgeo.2012.06.006

Klose, R., Schmidt, G., Ritter, O., Dawes, G., 2011. What is SPAM four for? In: Börner, R., Schwalenberg, K. (Eds.), Protokoll über das 24. Schmucker-Weidelt-Kolloquium für Elektromagnetische Tiefenforschung. Deutsche Geophysikalische Gesellschaft e. V., Potsdam, pp. 127–134. https://gfzpublic.gfz-potsdam.de/rest/items/item_65327_1/component/file_65325/content

KMS Technologies, 2019. KMS-820 Data Acquisition Unit. https://kmstechnologies.com/KMS_820.html

Knödel, K., Krummel, H., Lange, G., 2005. Handbuch zur Erkundung des Untergrundes von Deponien und Altlasten : Band 3: Geophysik. Springer Berlin / Heidelberg, Berlin, Heidelberg, GERMANY. http://ebookcentral.proquest.com/lib/ubkoeln/detail.action?docID=323731

Koeberl, C., 1994. African meteorite impact craters: Characteristics and geological importance. Journal of African Earth Sciences 18 (4), 263–295. https://doi.org/10.1016/0899-5362(94)90068-X

Larsen, J. J., Pedersen, S. S., Foged, N., Auken, E., 2021. Suppression of very low frequency radio noise in transient electromagnetic data with semi-tapered gates. Geoscientific Instrumentation, Methods and Data Systems 10 (1), 81–90. https://doi.org/10.5194/gi-10-81-2021

Levenberg, K., 1944. A method for the solution of certain non-linear problems in least squares. Quarterly of Applied Mathematics 2 (2), 164–168. https://doi.org/10.1090/qam/10666

Ley-Cooper, A. Y., Macnae, J. C., Viezzoli, A., 2010. Breaks in lithology: Interpretation problems when handling 2D structures with a 1D approximation. Geophysics 75 (4), WA179–WA188. https://doi.org/10.1190/1.3483101

Liu, Y., Yogeshwar, P., Hu, X., Peng, R., Tezkan, B., Mörbe, W., Li, J., 2020. Effects of electrical anisotropy on long-offset transient electromagnetic data. Geophysical Journal International 222 (2), 1074–1089. https://doi.org/10.1093/gji/ggaa213

Liu, Y., Yogeshwar, P., Peng, R., Hu, X., Han, B., Blanco-Arrué, B., 2024. Three-dimensional inversion of time-domain electromagnetic data using various loop source configurations. IEEE Transactions on Geoscience and Remote Sensing 62, 1–15. https://doi.org/10.1109/TGRS.2024.3383288

Logg, A., Mardal, K., Wells, G. (Eds.), 2012. Automated solution of differential equations by the finite element method: The FEniCS Book. Vol. 84 of Lecture Notes in Computational Science and Engineering. Springer Berlin Heidelberg, Berlin, Heidelberg.

Lu, X., Farquharson, C. G., 2020. 3D finite-volume time-domain modeling of geophysical electromagnetic data on unstructured grids using potentials. Geophysics 85 (6), E221–E240. https://doi.org/10.1190/geo2020-0088.1

Lu, X., Farquharson, C. G., Miehé, J., Harrison, G., 2021. 3D electromagnetic modeling of graphitic faults in the Athabasca Basin using a finite-volume time-domain approach with unstructured grids. Geophysics 86 (6), B349–B367. https://doi.org/10.1190/geo2020-0657.1

Marquardt, D. W., 1963. An algorithm for least-squares estimation of nonlinear parameters. Journal of the Society for Industrial and Applied Mathematics 11 (2), 431–441. http://www.jstor.org/stable/2098941 (Accessed at 23.10.2024)

Martin, R., 2009. Development and application of 2D and 3D transient electromagnetic inverse solutions based on adjoint Green functions: A feasibility study for the spatial reconstruction of conductivity distributions by means of sensitivities.

Maurya, P. K., Christensen, F. E., Kass, M. A., Pedersen, J. B., Frederiksen, R. R., Foged, N., Christiansen, A. V., Auken, E., 2022. Technical note: Efficient imaging of hydrological units below lakes and fjords with a floating, transient electromagnetic (FloaTEM) system. Hydrology and Earth System Sciences 26 (11), 2813–2827. https://doi.org/10.5194/hess-26-2813-2022

Meju, M. A., 1994. Geophysical data analysis: Understanding inverse problem theory and practice. Course Note Series. Society of Exploration Geophysicists.

Melles, M., Brigham-Grette, J., Minyuk, P., Koeberl, C., Andreev, A., Cook, T., Fedorov, G., Gebhardt, C., Haltia-Hovi, E., Kukkonen, M., Nowaczyk, N., Shwamborn, G., Wennrich, V., 2011. The Lake El'gygytgyn Scientific Drilling Project Conquering Arctic Challenges through Continental Drilling. Scientific Drilling (11, March 2011). https://doi.org/10.2204/iodp.sd.11.03.2011

Menke, W., 2018. Geophysical data analysis: discrete inverse theory. Academic Press and Candice Janco.

Miller, R. M., 2010. Roter Kamm impact crater of Namibia: New data on rim structure, target rock geochemistry, ejecta, and meteorite trajectory. In: Gibson, R. L., Reimold, W. U. (Eds.), Large meteorite impacts and planetary evolution IV. Special paper / The Geological Society of America. Geological Society of America, Boulder, Colo.

Mörbe, W., 2020. Deep controlled source electromagnetics for mineral exploration: A multidimensional validation study in time and frequency domain. Dissertation, University of Cologne, Cologne.

Mulder, W. A., Wirianto, M., Slob, E. C., 2008. Time-domain modeling of electromagnetic diffusion with a frequency-domain code. Geophysics 73 (1), F1–F8. https://doi.org/10.1190/1.2799093

Munkholm, M. S., Auken, E., 1996. Electromagnetic noise contamination on transient electromagnetic soundings in culturally disturbed environments. Journal of Environmental and Engineering Geophysics 1 (2), 119–127. https://doi.org/10.4133/JEEG1.2.119

Nabighian, M. N., 1979. Quasi–static transient response of a conducting half–space—An approximate representation. Geophysics 44 (10), 1700–1705. https://doi.org/10.1190/1.1440931

Nabighian, M. N., Macnae, J. C., 1988. Time domain electromagnetic prospecting methods. In: Nabighian, M. N. (Ed.), Electromagnetic methods in applied geophysics. Investigations in Geophysics. Society of Exploration Geophysicists, pp. 427–520.

NASA JPL, 2022. NASADEM Merged DEM Global 1 arc second V001 [Data Set]. NASA EOSDIS Land Processes DAAC. https://doi.org/10.5067/MEaSUREs/NASADEM/NASADEM_HGT.001

Nedelec, J. C., 1980. Mixed finite elements in $\mathbb{R}^3$. Numerische Mathematik 35 (3), 315–341. https://doi.org/10.1007/BF01396415

Newman, G. A., Anderson, W. L., Hohmann, G. W., 1987. Interpretation of transient electromagnetic soundings over three-dimensional structures for the central-loop configuration. Geophysical Journal International 89 (3), 889–914. https://doi.org/10.1111/j.1365-246X.1987.tb05200.x

Nienhaus, H., Yogeshwar, P., Melles, M., 2023a. Transient electromagnetic data of the Aurus clay pan, Namibia [Data Set]. CRC1211 Database (CRC1211DB). https://doi.org/10.5880/CRC1211DB.62

Nienhaus, H., Yogeshwar, P., Mörbe, W., Melles, M., 2023b. Transient electromagnetic data of the Roter Kamm crater, Namibia. [Data Set]. CRC1211 Database (CRC1211DB). https://www.crc1211db.uni-koeln.de/search/view.php?dataID=793. (Accessed at 12.01.2025)

Nienhaus, H., Yogeshwar, P., Mörbe, W., Tezkan, B., Büttner, C., Legler, M., Buske, S., Lushetile, B., Wennrich, V., Melles, M., 2023c. Geophysical and geological exploration of the Aurus clay pan as an archive of the long-term climatic and environmental history of the Namib Desert. Global and Planetary Change 230, 104259. https://doi.org/10.1016/j.gloplacha.2023.104259

Nocedal, J., Wright, S. J., 1999. Numerical optimization, second edition Edition. Springer series in operations research and financial engineering. Springer, New York, NY.

Oldenburg, D. W., Haber, E., Shekhtman, R., 2013. Three dimensional inversion of multisource time domain electromagnetic data. Geophysics 78 (1), E47–E57. https://doi.org/10.1190/geo2012-0131.1

Peng, R., Han, B., Liu, Y., Hu, X., 2021. EM3DANI: A Julia package for fully anisotropic 3D forward modeling of electromagnetic data. Geophysics 86 (5), F49–F60. https://doi.org/10.1190/geo2020-0489.1

Petry, H., 1987. Transient Elektromagnetische Tiefensondierung - Modellrechnungen und Inversion. Diploma Thesis, University of Cologne, Köln.

Pilkington, M., Grieve, R. A., 1992. The geophysical signature of terrestrial impact craters. Reviews of Geophysics 30 (2), 161–181. https://doi.org/10.1029/92RG00192

QGIS Development Team, 2022. QGIS Geographic Information System. https://www.qgis.org

Rätz, S., 2000. Ein dreidimensionales Finite Elemente Programm zur Simulation elektromagnetischer Oberflächen- und Bohrlochverfahren. PhD Thesis, University of Cologne, Cologne.

Reimold, W. U., Miller, R., 1989. The Roter Kamm Impact Crater, SWA/Namibia. In: Proceedings of the Lunar and Planetary Science Conference. Cambridge/Houston, pp. 711–732.

Reimold, W. U., Reid, A. M., Jakes, P., Zolensky, M., Miller, R. (Eds.), 1992. A magnetic survey across the Roter Kamm impact crater, Namibia. Vol. 23 of Abstracts of the Lunar and Planetary Science Conference.

Ritter, B., Wennrich, V., Medialdea, A., Brill, D., King, G., Schneiderwind, S., Niemann, K., Fernández-Galego, E., Diederich, J. L., Rolf, C., Bao, R., Melles, M., Dunai, T. J., 2019. Climatic fluctuations in the hyperarid core of the Atacama Desert during the past 215 ka. Scientific reports 9 (1), 5270. https://doi.org/10.1038/s41598-019-41743-8

Ritter, O., Junge, A., Dawes, G. J., 1998. New equipment and processing for magnetotelluric remote reference observations. Geophysical Journal International 132 (3), 535–548. https://doi.org/10.1046/j.1365-246X.1998.00440.x

Rochlitz, R., Becken, M., Günther, T., 2023. Three-dimensional inversion of semi-airborne electromagnetic data with a second-order finite-element forward solver. Geophysical Journal International 234 (1), 528–545. https://doi.org/10.1093/gji/ggad056

Rochlitz, R., Seidel, M., Börner, R., 2021. Evaluation of three approaches for simulating 3-D time-domain electromagnetic data. Geophysical Journal International 227 (3), 1980–1995. https://doi.org/10.1093/gji/ggab302

Rochlitz, R., Skibbe, N., Günther, T., 2019. custEM: Customizable finite-element simulation of complex controlled-source electromagnetic data. Geophysics 84 (2), F17–F33. https://doi.org/10.1190/geo2018-0208.1

Rodi, W., Mackie, R. L., 2001. Nonlinear conjugate gradients algorithm for 2-D magnetotelluric inversion. Geophysics 66 (1), 174–187. https://doi.org/10.1190/1.1444893

Rücker, C., Günther, T., Wagner, F. M., 2017. pyGIMLi: An open-source library for modelling and inversion in geophysics. Computers & Geosciences 109, 106–123. https://doi.org/10.1016/j.cageo.2017.07.011

Ruiz-Aguilar, D., Tezkan, B., Arango-Galván, C., 2018. Exploration of the aquifer of San Felipe Geothermal Area (Mexico) by spatially constrained inversion of transient electromagnetic data. Journal of Environmental and Engineering Geophysics 23 (2), 197–209. https://doi.org/10.2113/JEEG23.2.197

SanFilipo, W. A., Eaton, P. A., Hohmann, G. W., 1985. The effect of a conductive half–space on the transient electromagnetic response of a three–dimensional body. Geophysics 50 (7), 1144–1162. https://doi.org/10.1190/1.1441988

Scholl, C., 2005. The influence of multidimensional structures on the interpretation of LOTEM data with one-dimensional models and the application to data from Israel. Ph.D. thesis, University of Cologne, Cologne.

Seidel, M., 2019. A 3D time domain CSEM forward modeling code using custEM and FEniCS. PhD Thesis, University of Cologne, Cologne.

Seidel, M., Tezkan, B., 2017. 1D Cole-Cole inversion of TEM transients influenced by induced polarization. Journal of Applied Geophysics 138, 220–232. https://doi.org/10.1016/j.jappgeo.2017.01.011

Sen, M. K., Stoffa, P. L., 2013. Global optimization methods in geophysical inversion, 2nd Edition. Cambridge University Press, Cambridge.

Si, H., 2015. TetGen, a Delaunay-Based quality tetrahedral mesh generator. ACM Transactions on Mathematical Software 41 (2), 1–36. https://doi.org/10.1145/2629697

Simpson, F., Bahr, K., 2005. Practical magnetotellurics. Cambridge University Press.

Smith, R. S., Keating, P. B., 1996. The usefulness of multicomponent, time–domain airborne electromagnetic measurements. Geophysics 61 (1), 74–81. https://doi.org/10.1190/1.1443958

Spies, B. R., 1989. Depth of investigation in electromagnetic sounding methods. Geophysics 54 (7), 872–888. https://doi.org/10.1190/1.1442716

Spies, B. R., Eggers, D. E., 1986. The use and misuse of apparent resistivity in electromagnetic methods. Geophysics 51 (7), 1462–1471. https://doi.org/10.1190/1.1442194

Spies, B. R., Frischknecht, F. C., 1988. Electromagnetic sounding. In: Nabighian, M. N. (Ed.), Electromagnetic methods in applied geophysics. Investigations in Geophysics. Society of Exploration Geophysicists, pp. 285–426.

Sternberg, B. K., Washburne, J. C., Pellerin, L., 1988. Correction for the static shift in magnetotellurics using transient electromagnetic soundings. Geophysics 53 (11), 1459–1468. https://doi.org/10.1190/1.1442426

Swift, C. M., 1967. A magnetotelluric investigation of an electrical conductivity anomaly in the southwestern United States. Ph.D. thesis, MIT, Massachusetts.

Telford, W. M., Geldart, L. P., Sheriff, R. E., 1990. Applied geophysics, 2nd Edition. Press Syndicate of the University of Cambridge.

Thomas, R. J., Macey, P. H., Spencer, C., Dhansay, T., Diener, J. F., Lambert, C. W., Frei, D., Nguno, A., 2016. The Sperrgebiet Domain, Aurus Mountains, SW Namibia: A ∼2020–850Ma window within the Pan-African Gariep Orogen. Precambrian Research 286, 35–58. https://doi.org/10.1016/j.precamres.2016.09.023

Tikhonov, A. N., Arsenin, V. Y., 1977. Solutions of ill-posed problems. V. H. Winston & Sons, Washington, D.C.: John Wiley & Sons, New York.

Um, E. S., Harris, J. M., Alumbaugh, D. L., 2010. 3D time-domain simulation of electromagnetic diffusion phenomena: A finite-element electric-field approach. Geophysics 75 (4), F115–F126. https://doi.org/10.1190/1.3473694

Vignoli, G., Fiandaca, G., Christiansen, A. V., Kirkegaard, C., Auken, E., 2015. Sharp spatially constrained inversion with applications to transient electromagnetic data. Geophysical Prospecting 63 (1), 243–255. https://doi.org/10.1111/1365-2478.12185

Vozoff, K., 1988. The magnetotelluric method. In: Nabighian, M. N. (Ed.), Electromagnetic methods in applied geophysics. Investigations in Geophysics. Society of Exploration Geophysicists, pp. 641–712.

Ward, S. H., 1997. Resistivity and induced polarization methods. In: Ward, S. H. (Ed.), Geotechnical and environmental geophysics. Investigations in Geophysics. Society of Exploration Geophysicists, Tulsa, Okla., pp. 147–189.

Ward, S. H., Hohmann, G. W., 1988. Electromagnetic theory for geophysical applications. In: Nabighian, M. N. (Ed.), Electromagnetic methods in applied geophysics. Investigations in Geophysics. Society of Exploration Geophysicists, pp. 131–311.

Weidelt, P., 1986. Einführung in die elektromagnetische Tiefenforschung: Lecture Technische Universität Braunschweig.

Wennrich, V., Böhm, C., Brill, D., Carballeira, R., Hoffmeister, D., Jaeschke, A., Kerber, F., Maldonado, A., May, S. M., Olivares, L., Opitz, S., Rethemeyer, J., Reyers, M., Ritter, B., Schween, J. H., Sevinç, F., Steiner, J., Walber-Hellmann, K., Melles, M., 2024. Late Pleistocene to modern precipitation changes at the Paranal clay pan, central Atacama Desert. Global and Planetary Change 233, 104349. https://doi.org/10.1016/j.gloplacha.2023.104349

Xiao, L., Fiandaca, G., Maurya, P. K., Christiansen, A. V., 2023. 3D inversion of an integrated ground-based and waterborne transient electromagnetic survey. Geophysics 88 (5), B221–B231. https://doi.org/10.1190/geo2022-0318.1

Xiao, L., Fiandaca, G., Zhang, B., Auken, E., Christiansen, A. V., 2022. Fast 2.5D and 3D inversion of transient electromagnetic surveys using the octree-based finite-element method. Geophysics 87 (4), E267–E277. https://doi.org/10.1190/geo2021-0402.1

Yang, D., Fournier, D., Kang, S., Oldenburg, D. W., 2019. Deep mineral exploration using multi-scale electromagnetic geophysics: the Lalor massive sulphide deposit case study. Canadian Journal of Earth Sciences 56 (5), 544–555. https://doi.org/10.1139/cjes-2018-0069

Yee, K., 1966. Numerical solution of initial boundary value problems involving maxwell's equations in isotropic media. IEEE Transactions on Antennas and Propagation 14 (3), 302–307. https://doi.org/10.1109/TAP.1966.1138693

Yogeshwar, P., 2014. A resistivity-depth model of the central Azarq basin area, Jordan: 2D forward and inverse modeling of time domain electromagnetic data. PhD Thesis, University of Cologne, Cologne.

Yogeshwar, P., Tezkan, B., 2017. Two-dimensional basement modeling of central loop transient electromagnetic data from the central Azraq basin area, Jordan. Journal of Applied Geophysics 136, 198–210. https://doi.org/10.1016/j.jappgeo.2016.11.001

Zeng, S., Hu, X., Li, J., Farquharson, C. G., Wood, P. C., Lu, X., Peng, R., 2019. Effects of full transmitting-current waveforms on transient electromagnetics: Insights from modeling the Albany graphite deposit. Geophysics 84 (4), E255–E268. https://doi.org/10.1190/geo2018-0573.1

Zhang, B., Engebretsen, K. W., Fiandaca, G., Cai, H., Auken, E., 2021. 3D inversion of time-domain electromagnetic data using finite elements and a triple mesh formulation. Geophysics 86 (3), E257–E267. https://doi.org/10.1190/geo2020-0079.1

Zhdanov, M. S., 2002. Geophysical Inverse Theory and Regularization Problems. Vol. 36 of Methods in geochemistry and geophysics. Elsevier.

Zonge, 2000. ZT-30 ZeroTEM TRANSMITTER MANUAL. http://www.zonge.com/legacy/PDF_TxManuals/Zt-30_man.pdf (Accessed at 02.11.2024)

Zonge, 2013. TEM / 3 Magnetic Antenna: Single Channel Magnetic Field Antenna. http://www.zonge.com/legacy/PDF_Equipment/Tem-3.pdf

Zonge, K. L., Hughes, L. J., 1985. Effect of electrode contact resistance on electric field measurements. In: SEG Technical Program Expanded Abstracts. SEG, pp. 231–234.

APPENDIX A

Field Data from the Roter Kamm impact crater

Here, the additional figures and tables are presented, giving further information about the field survey and the TEM and AMT data.

A.1. Single-Loop TEM Data

Table A.1.: Coordinates of single-loop sounding locations along Profile 1. Additionally, the corresponding profile meter and the transmitter size are given.

Name	Longitude	Latitude	x/m	Tx/m
P1-01	16.281628 E	-27.772267 N	-1000	50
P1-02	16.282325 E	-27.771611 N	-900	50
P1-03	16.283023 E	-27.770955 N	-800	50 / 100
P1-04	16.283720 E	-27.770300 N	-700	50
P1-05	16.284417 E	-27.769644 N	-600	50
P1-06	16.285114 E	-27.768988 N	-500	50
P1-07	16.285811 E	-27.768332 N	-400	50 / 100
P1-08	16.286509 E	-27.767676 N	-300	50
P1-09	16.287206 E	-27.767021 N	-200	50
P1-10	16.287903 E	-27.766365 N	-100	50
P1-11	16.288600 E	-27.765709 N	0	50 / 100
P1-12	16.289297 E	-27.765053 N	100	50
P1-13	16.289994 E	-27.764397 N	200	50
P1-14	16.290692 E	-27.763742 N	300	50
P1-15	16.291389 E	-27.763086 N	400	50 / 100
P1-16	16.292086 E	-27.762430 N	500	50
P1-17	16.292783 E	-27.761774 N	600	50
P1-18	16.293480 E	-27.761118 N	700	50
P1-19	16.294177 E	-27.760463 N	800	50
P1-20	16.295571 E	-27.759151 N	1000	50

Continuation of coordinates.

Name	**Longitude**	**Latitude**	**x/m**	**Tx/m**
P1-21	16.296268 E	-27.758495 N	1100	50
P1-22	16.296965 E	-27.757839 N	1200	50 / 100
P1-23	16.297663 E	-27.757183 N	1300	50
P1-24	16.298360 E	-27.756528 N	1400	50
P1-25	16.299057 E	-27.755872 N	1500	50
P1-26	16.299754 E	-27.755216 N	1600	50
P1-27	16.300451 E	-27.754560 N	1700	50
P1-28	16.301148 E	-27.753904 N	1800	50
P1-29	16.301845 E	-27.753248 N	1900	50
P1-30	16.302542 E	-27.752592 N	2000	100
P1-31	16.303239 E	-27.751937 N	2100	50
P1-32	16.303936 E	-27.751281 N	2200	50
P1-33	16.304633 E	-27.750625 N	2300	50
P1-34	16.305330 E	-27.749969 N	2400	50
P1-35	16.306027 E	-27.749313 N	2500	50
P1-36	16.306724 E	-27.748657 N	2600	50
P1-37	16.307420 E	-27.748001 N	2700	50
P1-38	16.308117 E	-27.747345 N	2800	50

Table A.2.: Coordinates of single-loop sounding locations along Profile 2. Additionally, the corresponding profile meter and the transmitter size are given.

Name	Longitude	Latitude	y/m	Tx /m
P2-01	16.297448 E	-27.773150 N	-1200	100
P2-02	16.296710 E	-27.772530 N	-1100	50
P2-03	16.296320 E	-27.771644 N	-1000	50
P2-04	16.295601 E	-27.771000 N	-900	50
P2-05	16.294498 E	-27.770670 N	-800	100
P2-06	16.293761 E	-27.770050 N	-700	50
P2-07	16.293024 E	-27.769430 N	-600	50
P2-08	16.292286 E	-27.768810 N	-500	50
P2-09	16.291549 E	-27.768190 N	-400	100
P2-10	16.290812 E	-27.767569 N	-300	50
P2-11	16.290075 E	-27.766949 N	-200	50
P2-12	16.289337 E	-27.766329 N	-100	50
P2-13	16.288600 E	-27.765709 N	0	100
P2-14	16.287863 E	-27.765089 N	100	50
P2-15	16.287126 E	-27.764469 N	200	50
P2-16	16.286388 E	-27.763849 N	300	50
P2-17	16.285651 E	-27.763228 N	400	100
P2-18	16.284914 E	-27.762608 N	500	50
P2-19	16.284177 E	-27.761988 N	600	50
P2-20	16.283440 E	-27.761368 N	700	50
P2-21	16.282702 E	-27.760748 N	800	100
P2-22	16.281965 E	-27.760128 N	900	50
P2-23	16.281228 E	-27.759507 N	1000	50
P2-24	16.280491 E	-27.758887 N	1100	50
P2-25	16.279754 E	-27.758267 N	1200	50

Table A.3.: Coordinates of single-loop sounding locations along the regional profile. Additionally, the corresponding profile meter and the transmitter size are given.

Name	Longitude	Latitude	x/m	Tx /m
Reg 01	16.2997123 E	-27.7375603 N	3000	50
Reg 02	16.3021553 E	-27.7337415 N	3500	50
Reg 03	16.3050629 E	-27.7299587 N	4000	50
Reg 04	16.3073860 E	-27.7261648 N	4500	50
Reg 05	16.3100044 E	-27.7222708 N	5000	50
Reg 06	16.3128887 E	-27.7185564 N	5500	50
Reg 07	16.3154053 E	-27.7144401 N	6000	50
Reg 08	16.3199196 E	-27.7061344 N	7000	50
Reg 09	16.3241102 E	-27.6978561 N	8000	50
Reg 10	16.3290150 E	-27.6900828 N	9000	50
Reg 11	16.3341557 E	-27.6824244 N	10000	50
Reg 12	16.3397766 E	-27.6734936 N	11000	50

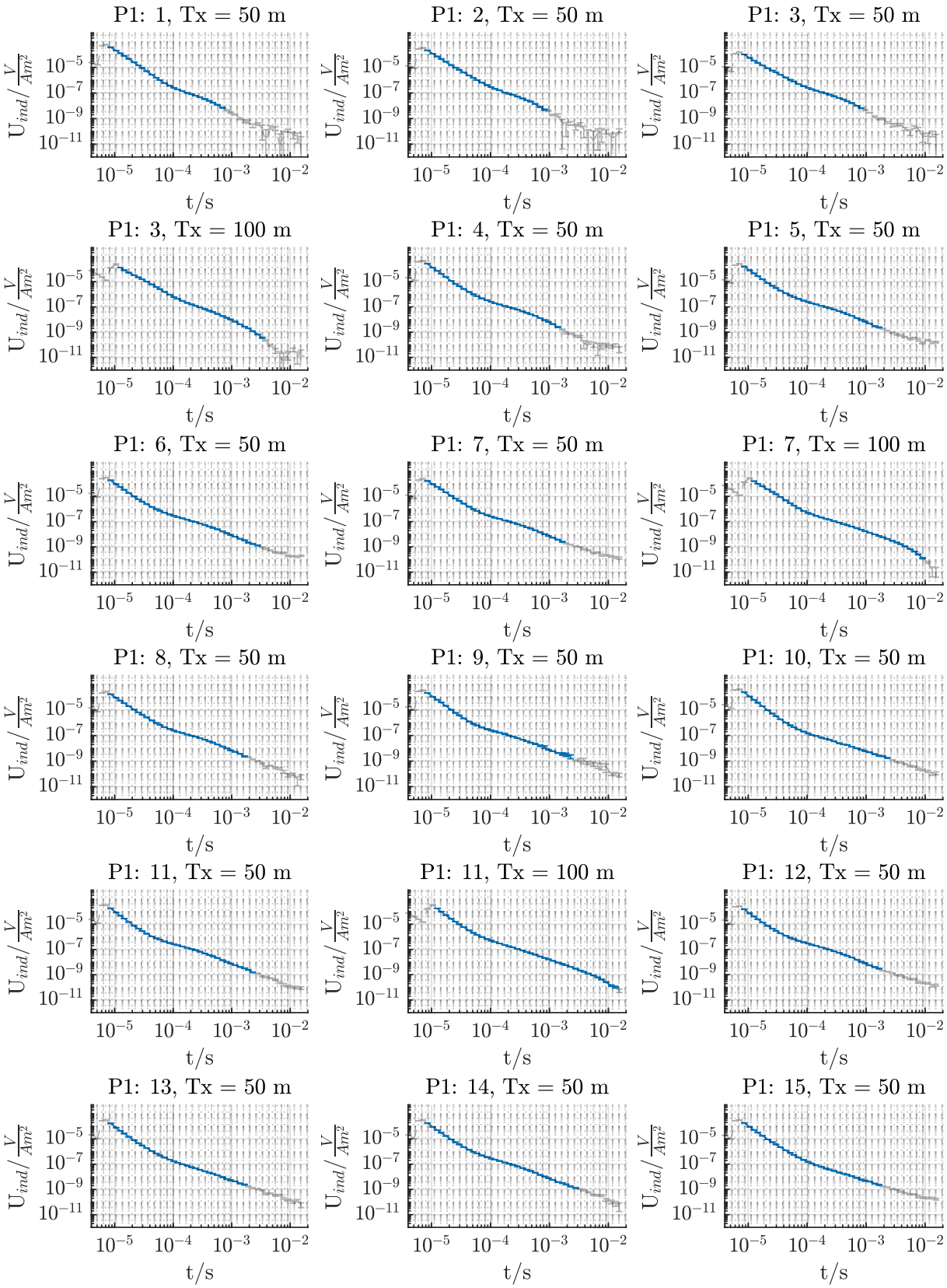

Figure A.1.: Single-loop data along Profile 1. The whole transient is indicated in light gray and the transient inside the resolution boundaries of the TEM-FAST 48 in blue.

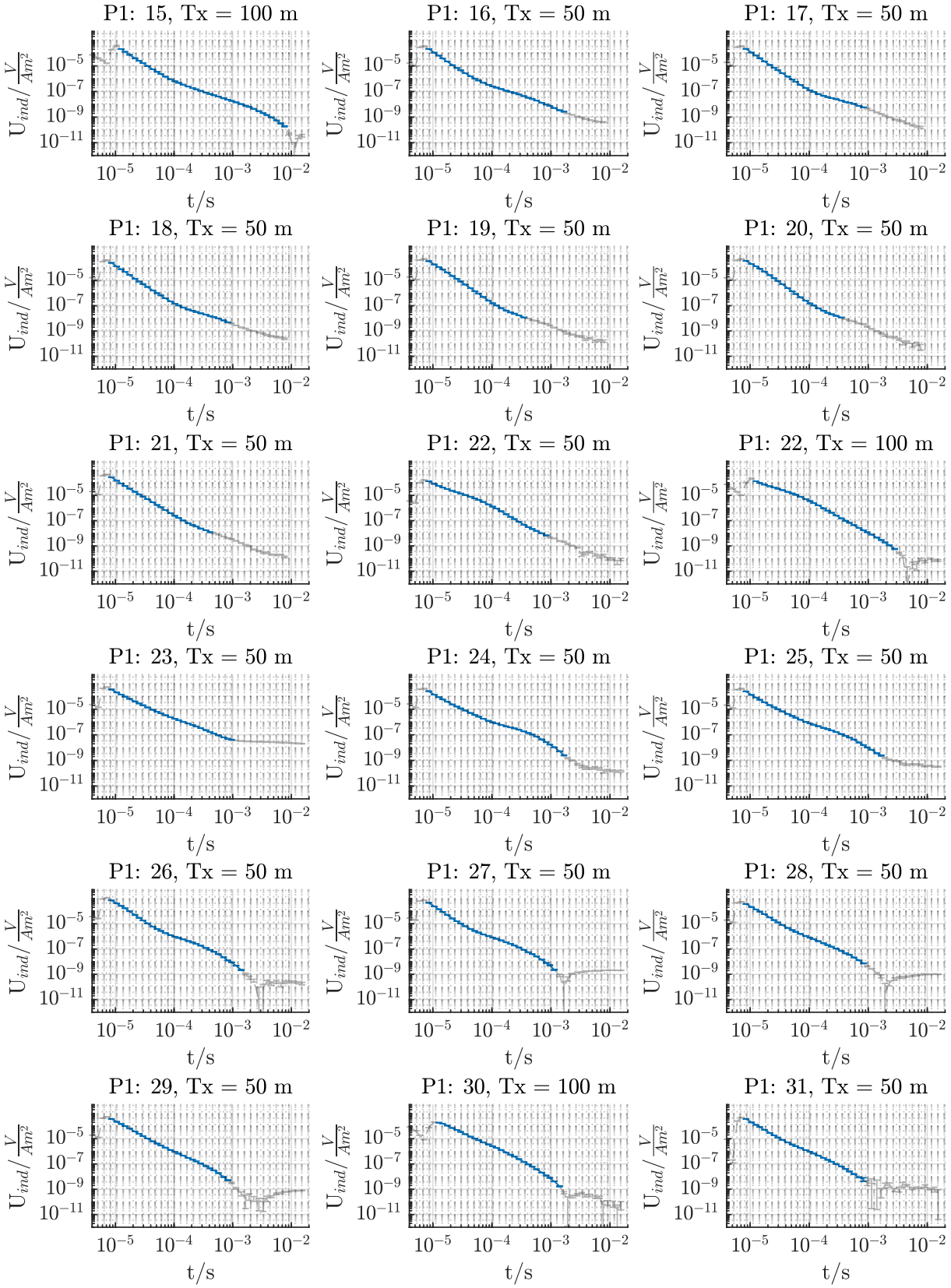

Figure A.1.: Single-loop data along Profile 1. (cont.)

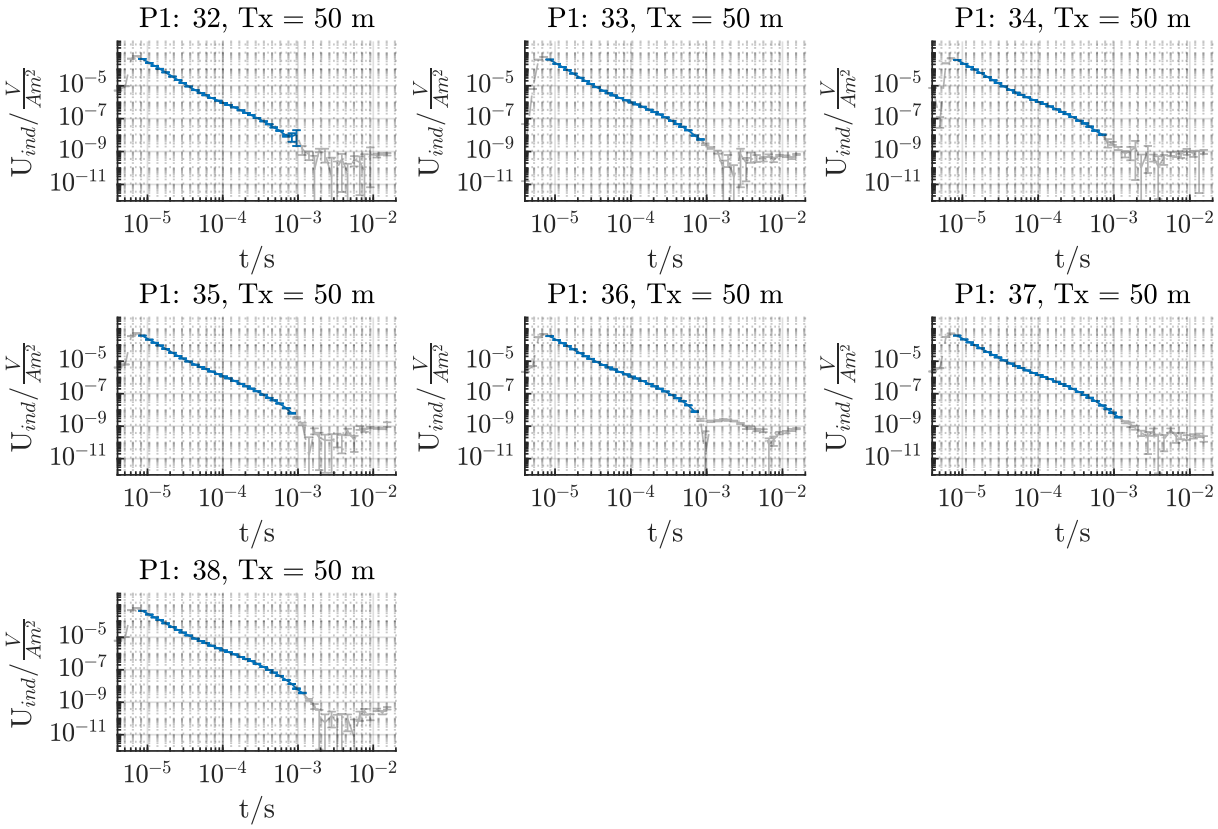

Figure A.1.: Single-loop data along Profile 1. (cont.)

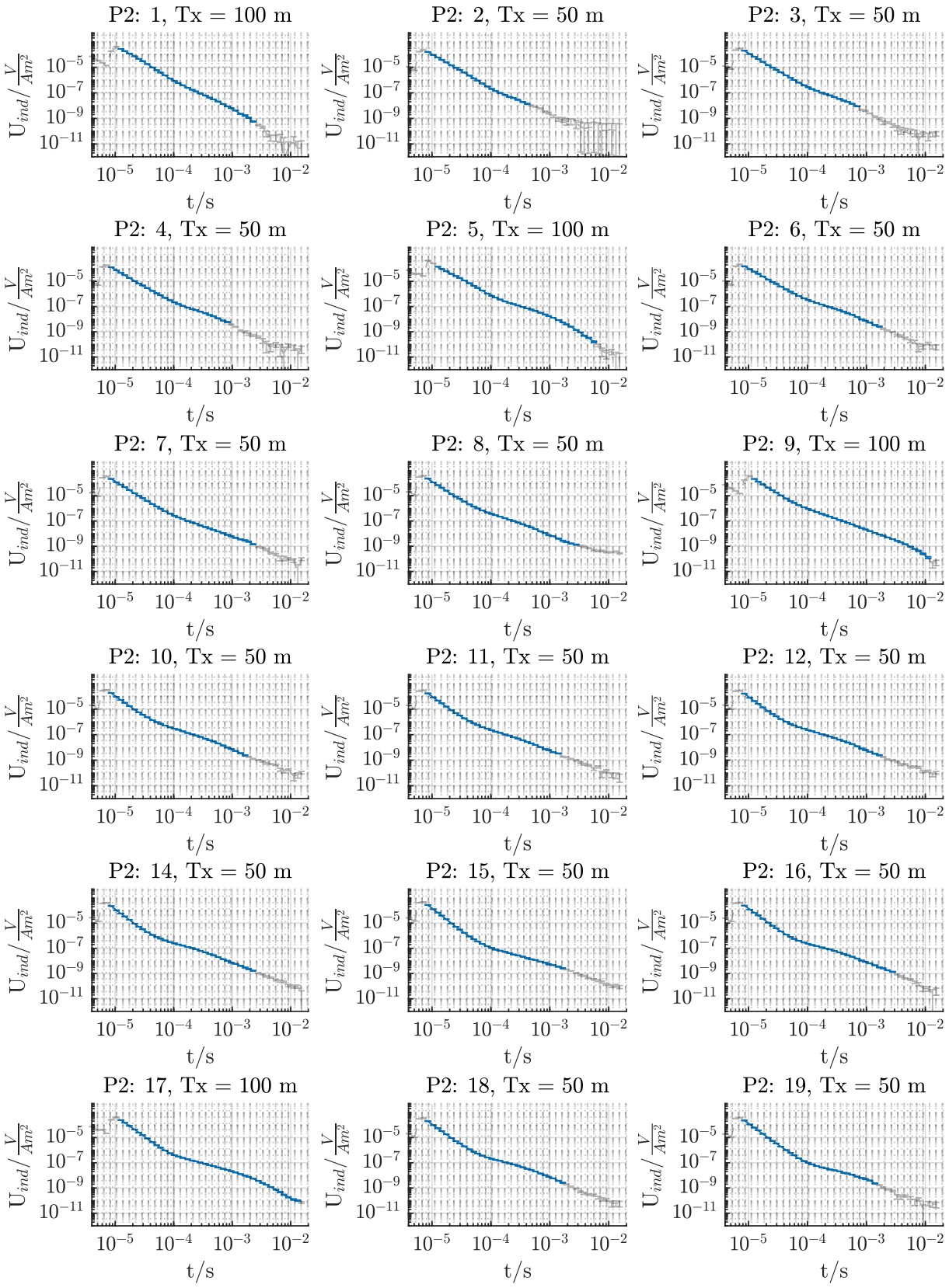

Figure A.2.: Single-loop data along Profile 2. The whole transient is indicated in light gray and the transient inside the resolution boundaries of the TEM-FAST 48 in blue.

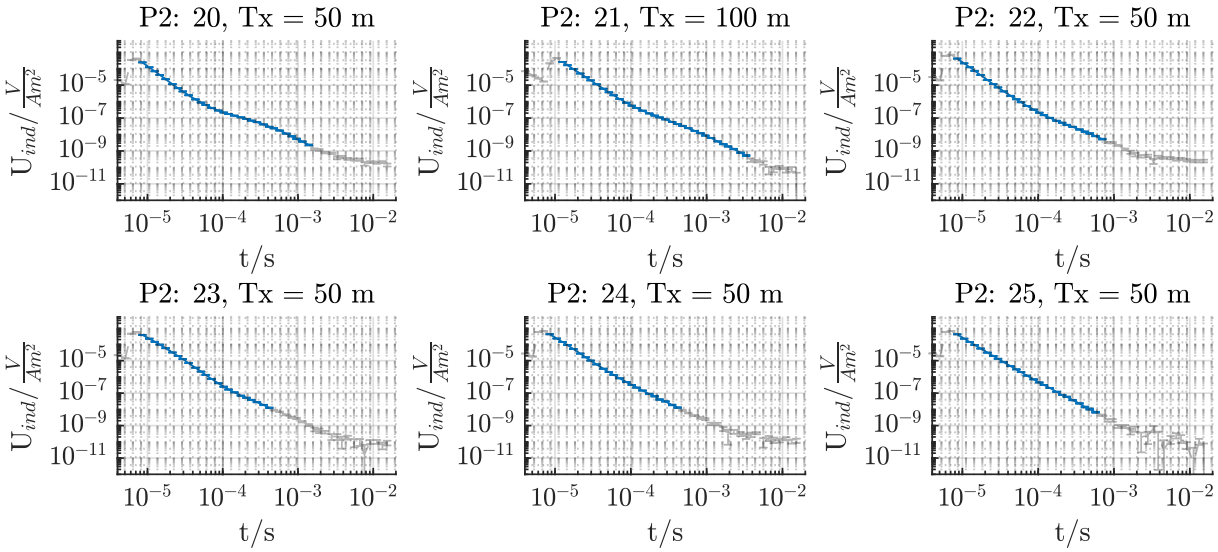

Figure A.2.: Single-loop data along Profile 2. (cont.)

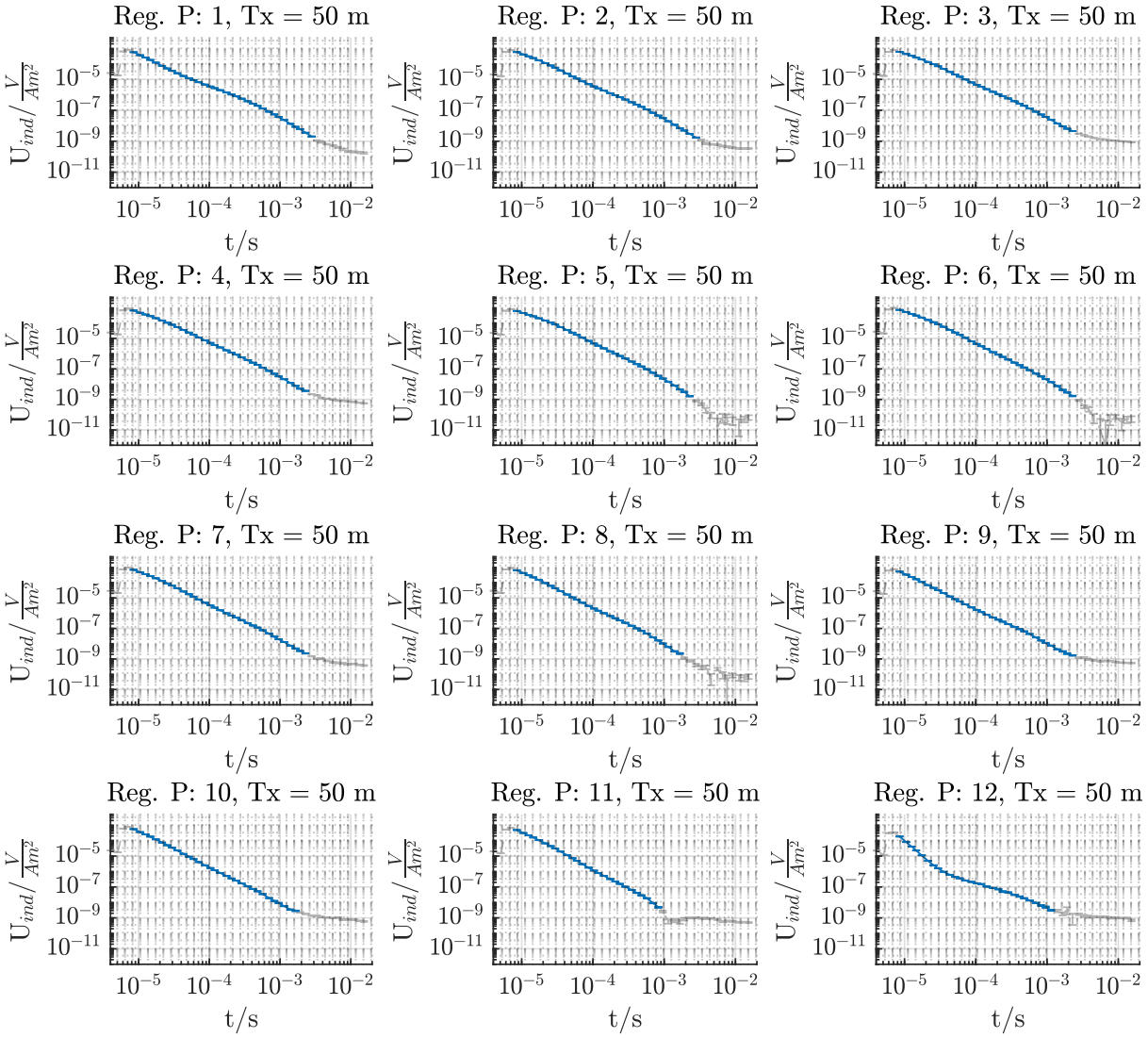

Figure A.3.: Single-loop data along the regional profile. The whole transient is indicated in light gray and the transient inside the resolution boundaries of the TEM-FAST 48 in blue.

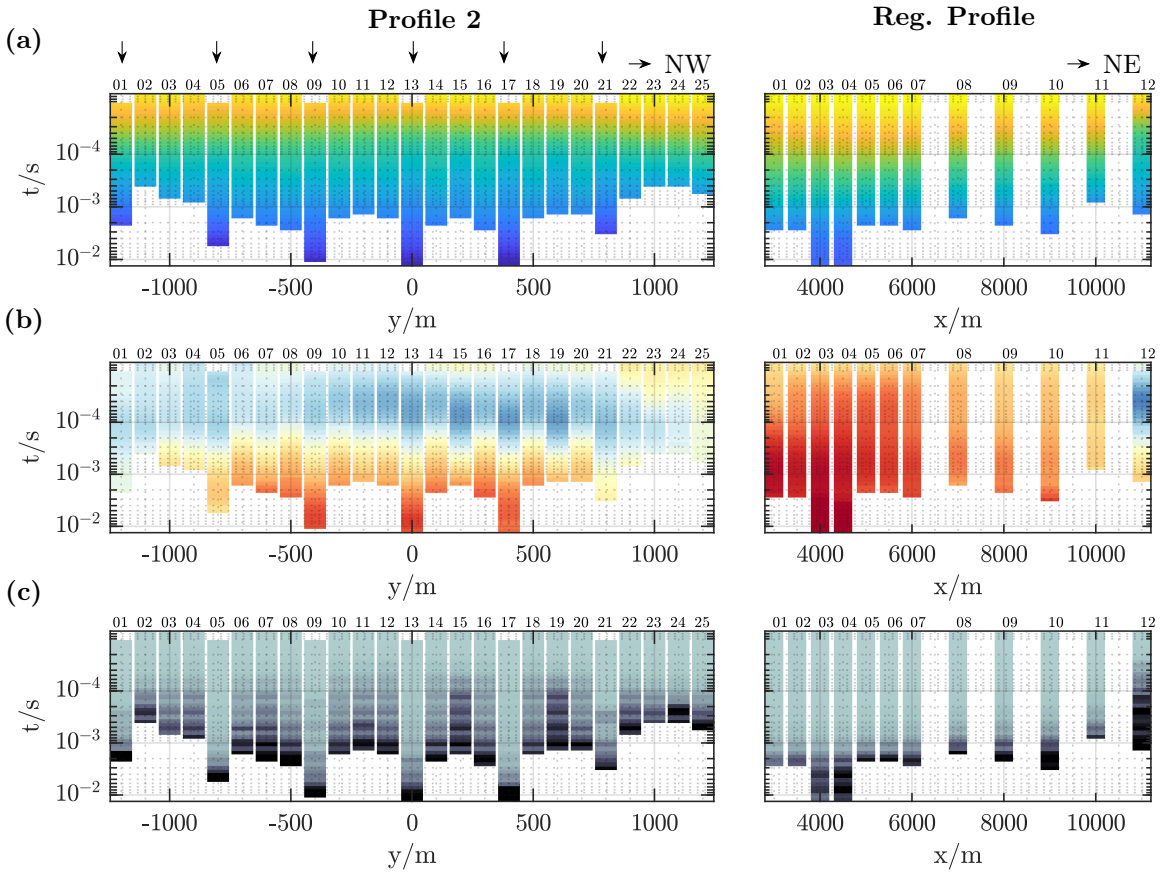

Figure A.4.: Single-loop TEM data along Profile 2 and the regional profile.. All data is normalized to a transmitter area of 100×100 m^2 for comparison. The x-axis denotes the position along Profile 2 or the regional Profile with the center of the crater being the reference (y = x = 0 m). The y-axis indicates the time after initiating the current turn-off. (a) Induced voltage, (b) late-time apparent resistivity and (c) relative error of the induced voltage. As the late-time apparent resistivity is a transformation of the data, it only differs from the induced voltage error by a factor of 2/3. The location of the large loops are indicated by the downward pointing arrows at the top.

A.2. Fixed-Loop TEM Data

Table A.4.: Coordinates of the transmitter and receiver locations of fixed-loop A. Additionally, the profile positions are presented.

Name	Longitude	Latitude	x/m	y/m
Transmitter A	16.288600	-27.765709	0	0
01	16.285811 E	-27.768332 N	-400	0
02	16.286509 E	-27.767676 N	-300	0
03	16.287206 E	-27.767021 N	-200	0
04	16.287554 E	-27.766693 N	-150	0
05	16.288252 E	-27.766037 N	-50	0
06	16.288600 E	-27.765709 N	0	0
07	16.288949 E	-27.765381 N	50	0
08	16.289646 E	-27.764725 N	150	0
09	16.289994 E	-27.764397 N	200	0
10	16.290692 E	-27.763742 N	300	0
11	16.291389 E	-27.763086 N	400	0
12	16.285651 E	-27.763228 N	0	-400
13	16.286388 E	-27.763849 N	0	-300
14	16.287126 E	-27.764469 N	0	-200
15	16.287494 E	-27.764779 N	0	-150
16	16.288231 E	-27.765399 N	0	-50
17	16.288969 E	-27.766019 N	0	50
18	16.289706 E	-27.766639 N	0	150
19	16.290075 E	-27.766949 N	0	200
20	16.290812 E	-27.767569 N	0	300
21	16.291549 E	-27.768190 N	0	400

Table A.5.: Coordinates of the transmitter and receiver locations of fixed-loop B. Additionally, the profile positions are presented.

Name	**Longitude**	**Latitude**	**x/m**	**y/m**
Transmitter B	16.294177	-27.760463	800	0
1	16.291389 E	-27.763086 N	400	0
2	16.292086 E	-27.762430 N	500	0
3	16.292783 E	-27.761774 N	600	0
4	16.293131 E	-27.761446 N	650	0
5	16.293829 E	-27.760790 N	750	0
6	16.294177 E	-27.760463 N	800	0
7	16.294526 E	-27.760135 N	850	0
8	16.295223 E	-27.759479 N	950	0
9	16.295571 E	-27.759151 N	1000	0
10	16.296268 E	-27.758495 N	1100	0
11	16.296965 E	-27.757839 N	1200	0
12	16.291228 E	-27.757982 N	800	-400
13	16.291965 E	-27.758602 N	800	-300
14	16.292703 E	-27.759222 N	800	-200
15	16.293071 E	-27.759532 N	800	-150
16	16.293809 E	-27.760152 N	800	-50
17	16.294546 E	-27.760773 N	800	50
18	16.295283 E	-27.761393 N	800	150
19	16.295652 E	-27.761703 N	800	200
20	16.296389 E	-27.762323 N	800	300
21	16.297126 E	-27.762943 N	800	400

Table A.6.: Coordinates of the transmitter and receiver locations of fixed-loop C. Additionally, the profile positions are presented.

Name	**Longitude**	**Latitude**	**x/m**	**y/m**
Transmitter C	16.299754	-27.755216	1600	0
1	16.296965 E	-27.757839 N	1200	0
2	16.297663 E	-27.757183 N	1300	0
3	16.298360 E	-27.756528 N	1400	0
4	16.298708 E	-27.756200 N	1450	0
5	16.299405 E	-27.755544 N	1550	0
6	16.299754 E	-27.755216 N	1600	0
7	16.300102 E	-27.754888 N	1650	0
8	16.300799 E	-27.754232 N	1750	0
9	16.301148 E	-27.753904 N	1800	0
10	16.301845 E	-27.753248 N	1900	0
11	16.302542 E	-27.752592 N	2000	0
12	16.296805 E	-27.752735 N	1600	-400
13	16.297542 E	-27.753356 N	1600	-300
14	16.298279 E	-27.753976 N	1600	-200
15	16.298648 E	-27.754286 N	1600	-150
16	16.299385 E	-27.754906 N	1600	-50
17	16.300122 E	-27.755526 N	1600	50
18	16.300859 E	-27.756146 N	1600	150
19	16.301228 E	-27.756456 N	1600	200
20	16.301965 E	-27.757076 N	1600	300
21	16.302703 E	-27.757696 N	1600	400

Table A.7.: Coordinates of the transmitter and receiver locations of fixed-loop D. Additionally, the profile positions are presented.

Name	**Longitude**	**Latitude**	**x/m**	**y/m**
Transmitter D	16.299754	-27.755216	2400	0
1	16.296965 E	-27.757839 N	2000	0
2	16.297663 E	-27.757183 N	2100	0
3	16.298360 E	-27.756528 N	2200	0
4	16.298708 E	-27.756200 N	2250	0
5	16.299405 E	-27.755544 N	2350	0
6	16.299754 E	-27.755216 N	2400	0
7	16.300102 E	-27.754888 N	2450	0
8	16.300799 E	-27.754232 N	2550	0
9	16.301148 E	-27.753904 N	2600	0
10	16.301845 E	-27.753248 N	2700	0
11	16.302542 E	-27.752592 N	2800	0
12	16.296805 E	-27.752735 N	2400	-400
13	16.297542 E	-27.753356 N	2400	-300
14	16.298279 E	-27.753976 N	2400	-200
15	16.298648 E	-27.754286 N	2400	-150
16	16.299385 E	-27.754906 N	2400	-50
17	16.300122 E	-27.755526 N	2400	50
18	16.300859 E	-27.756146 N	2400	150
19	16.301228 E	-27.756456 N	2400	200
20	16.301965 E	-27.757076 N	2400	300
21	16.302703 E	-27.757696 N	2400	400

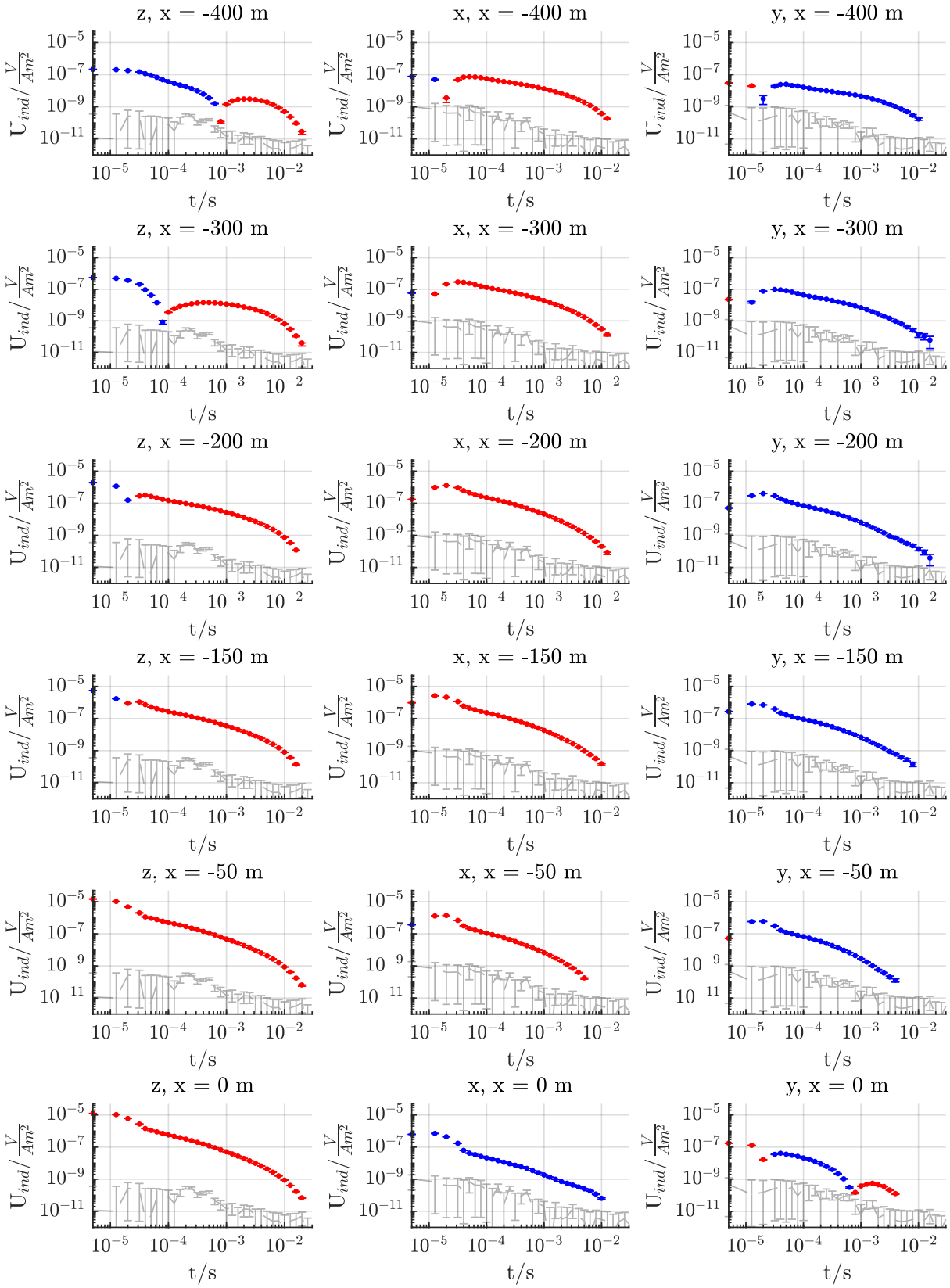

Figure A.5.: Fixed-loop data of transmitter A along profile 1. Positive induced voltage values are indicated in red and negative in blue. The measured noise level is shown in light gray. Each column represents one component and each row the components at a certain offset.

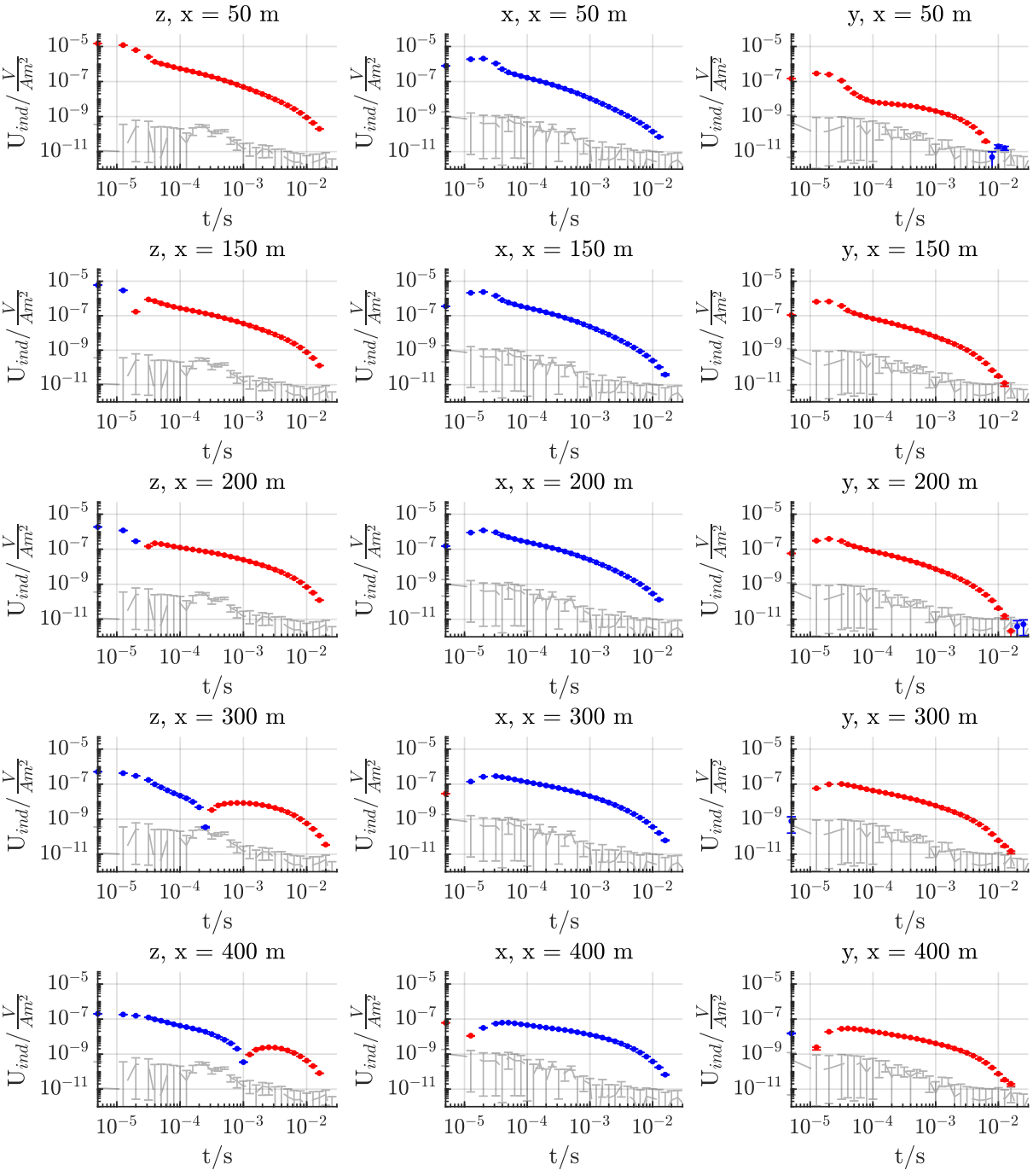

Figure A.5.: Fixed-loop data of transmitter A along profile 1. (cont.)

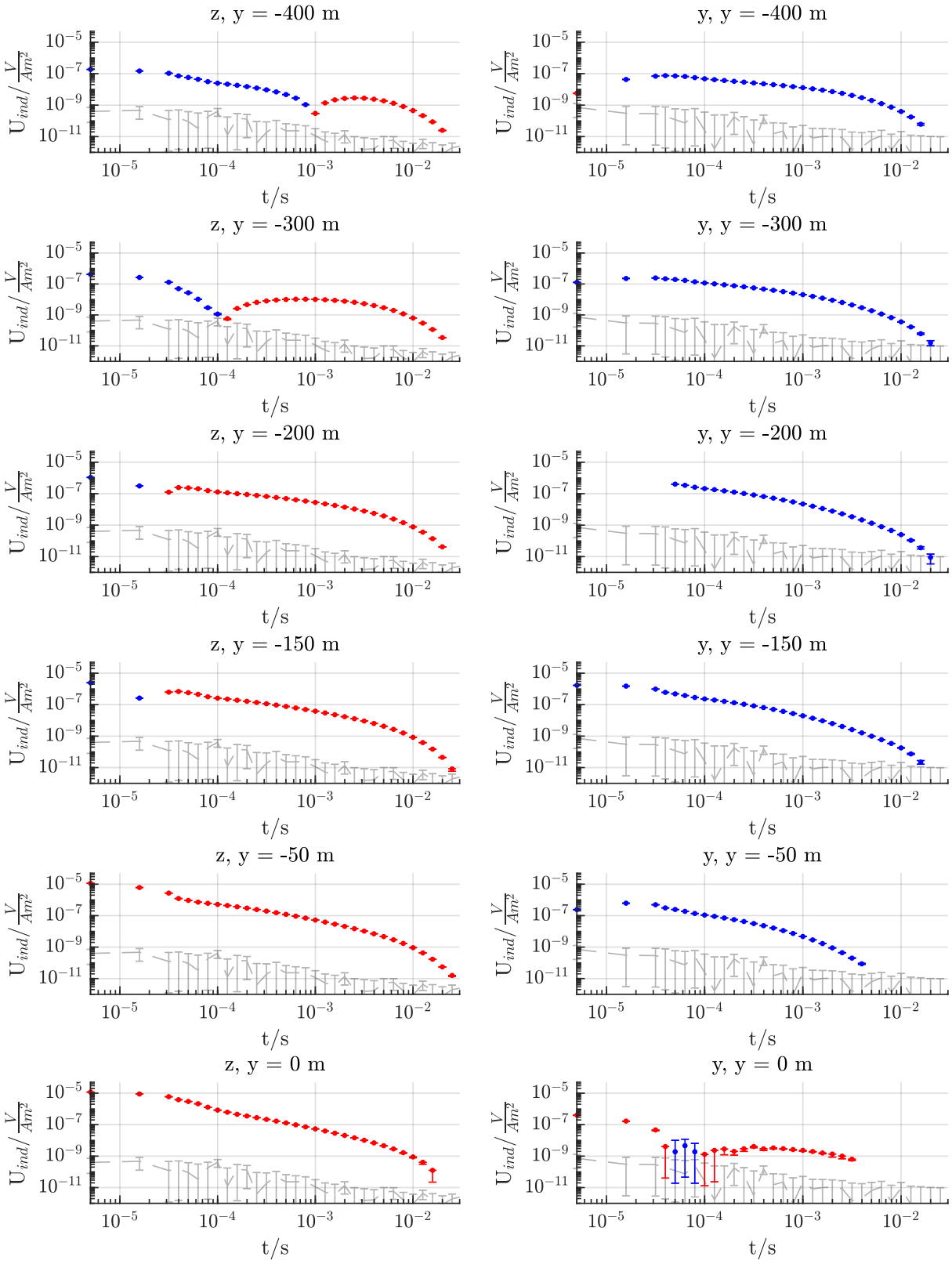

Figure A.6.: Fixed-loop data of transmitter A perpendicular to profile 1. Positive induced voltage values are indicated in red and negative in blue. The measured noise level is shown in light gray. Each column represents one component and each row the components at a certain offset.

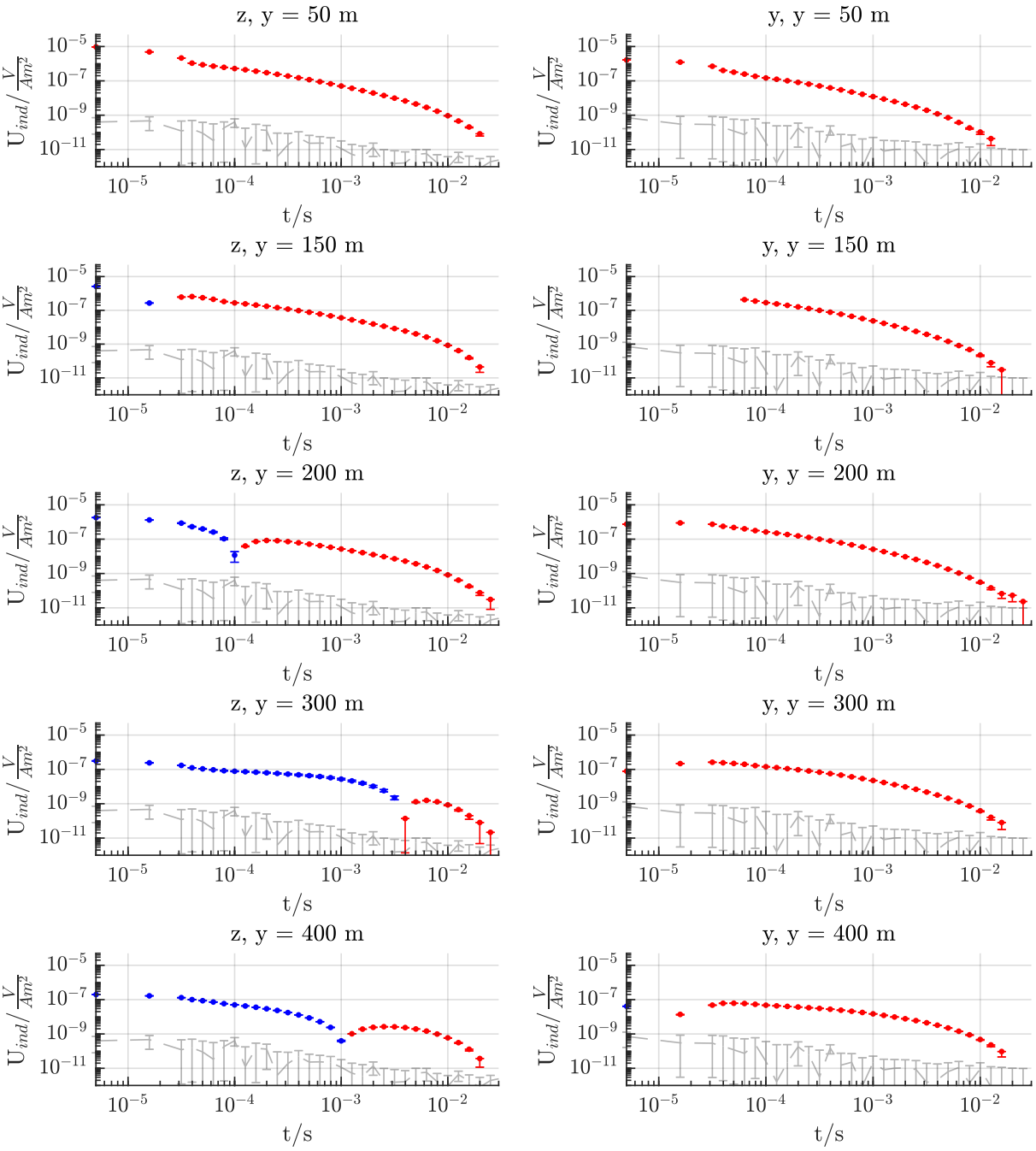

Figure A.6.: Fixed-loop data of transmitter A perpendicular to profile 1. (cont.)

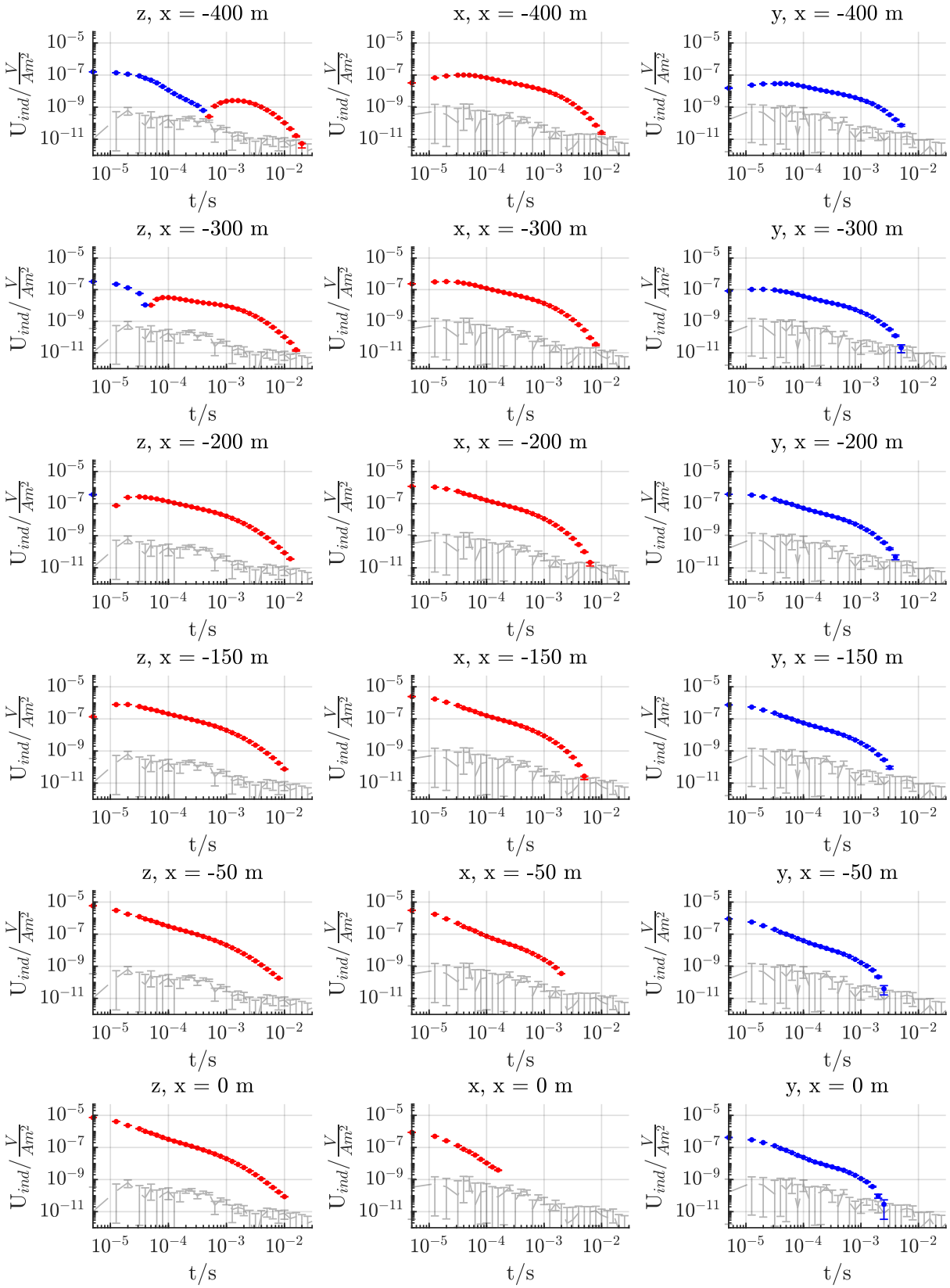

Figure A.7.: Fixed-loop data of transmitter B along profile 1. Positive induced voltage values are indicated in red and negative in blue. The measured noise level is shown in light gray. Each column represents one component and each row the components at a certain offset.

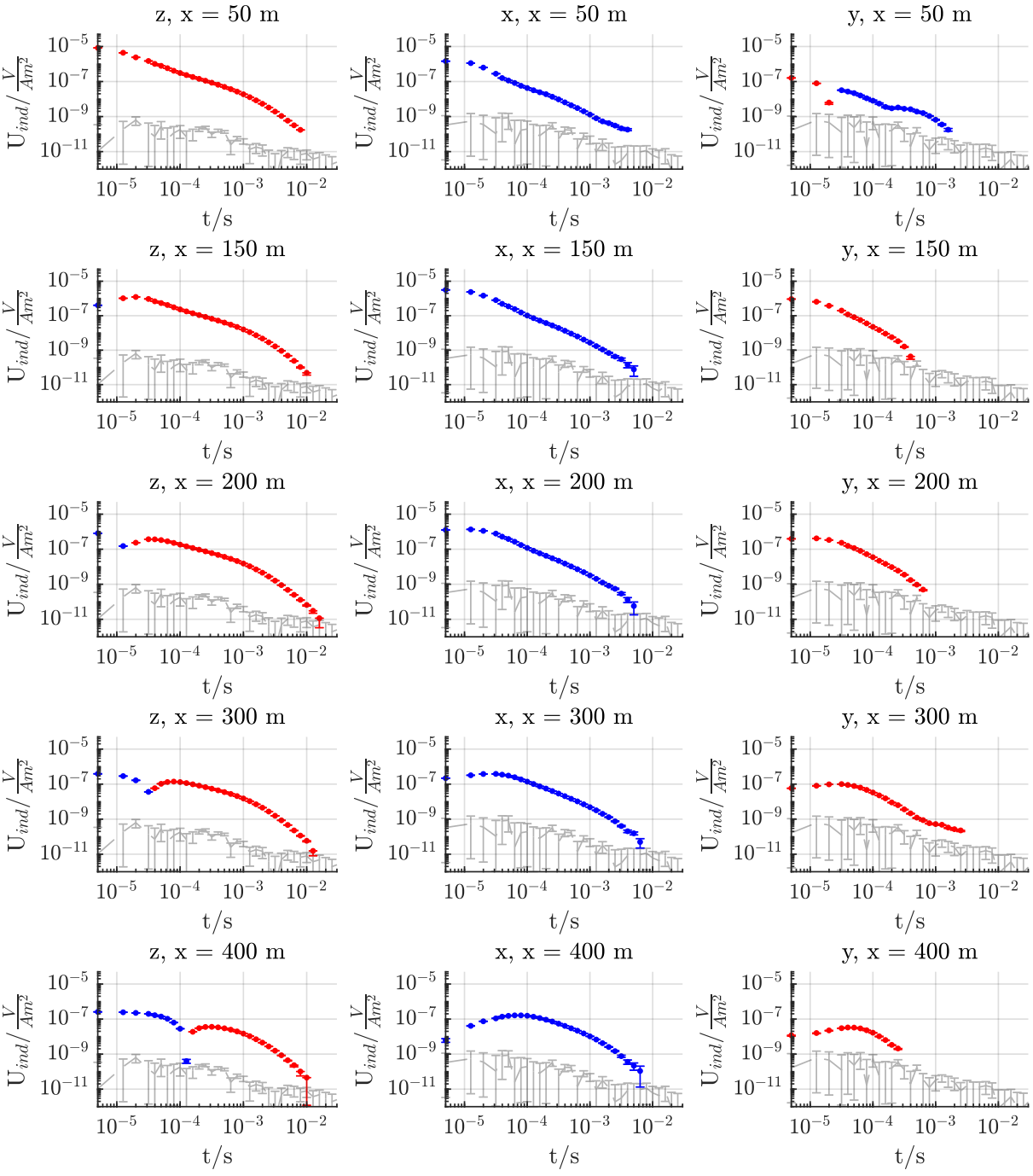

Figure A.7.: Fixed-loop data of transmitter B along profile 1. (cont.)

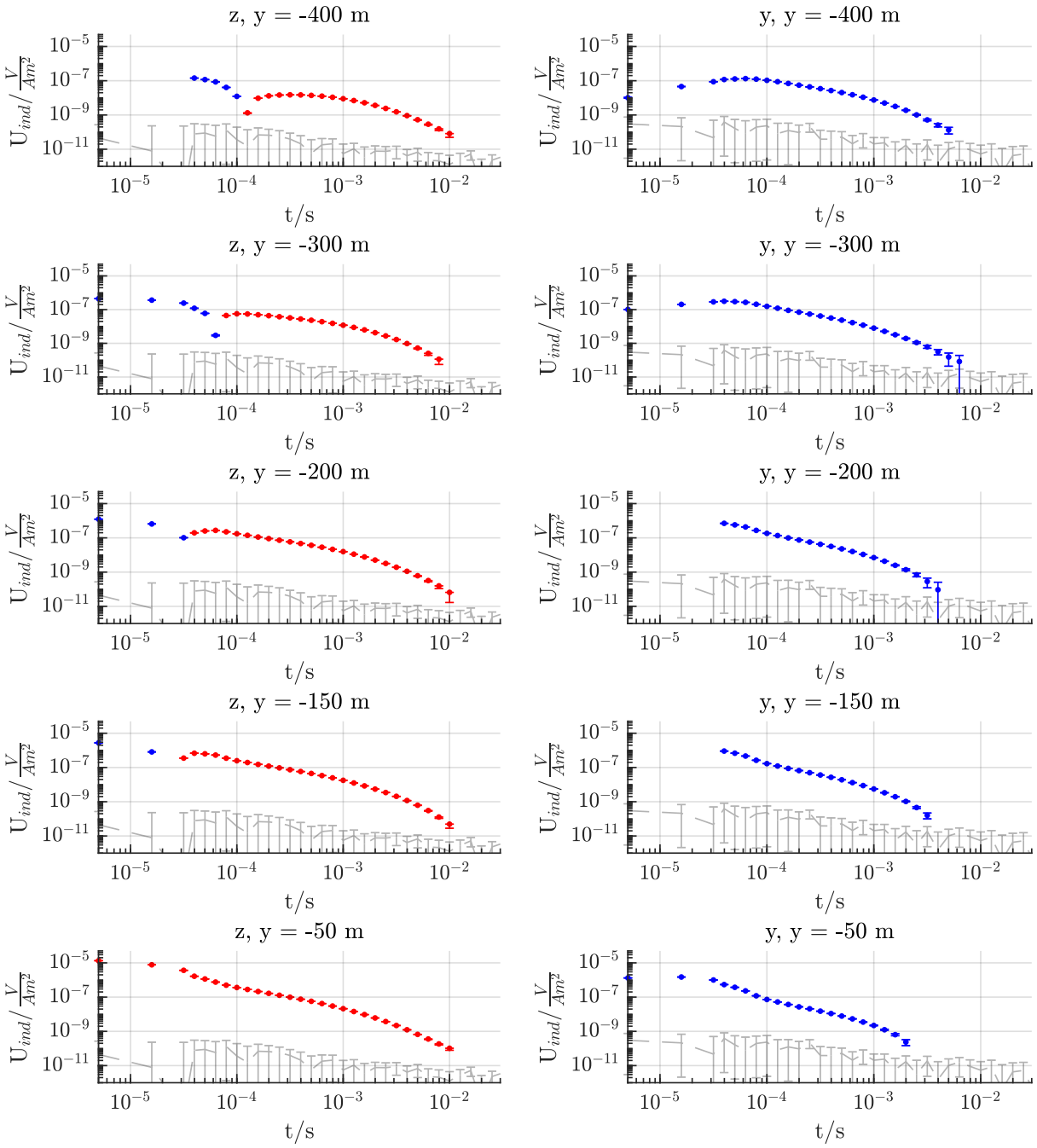

Figure A.8.: Fixed-loop data of transmitter B perpendicular to profile 1. Positive induced voltage values are indicated in red and negative in blue. The measured noise level is shown in light gray. Each column represents one component and each row the components at a certain offset.

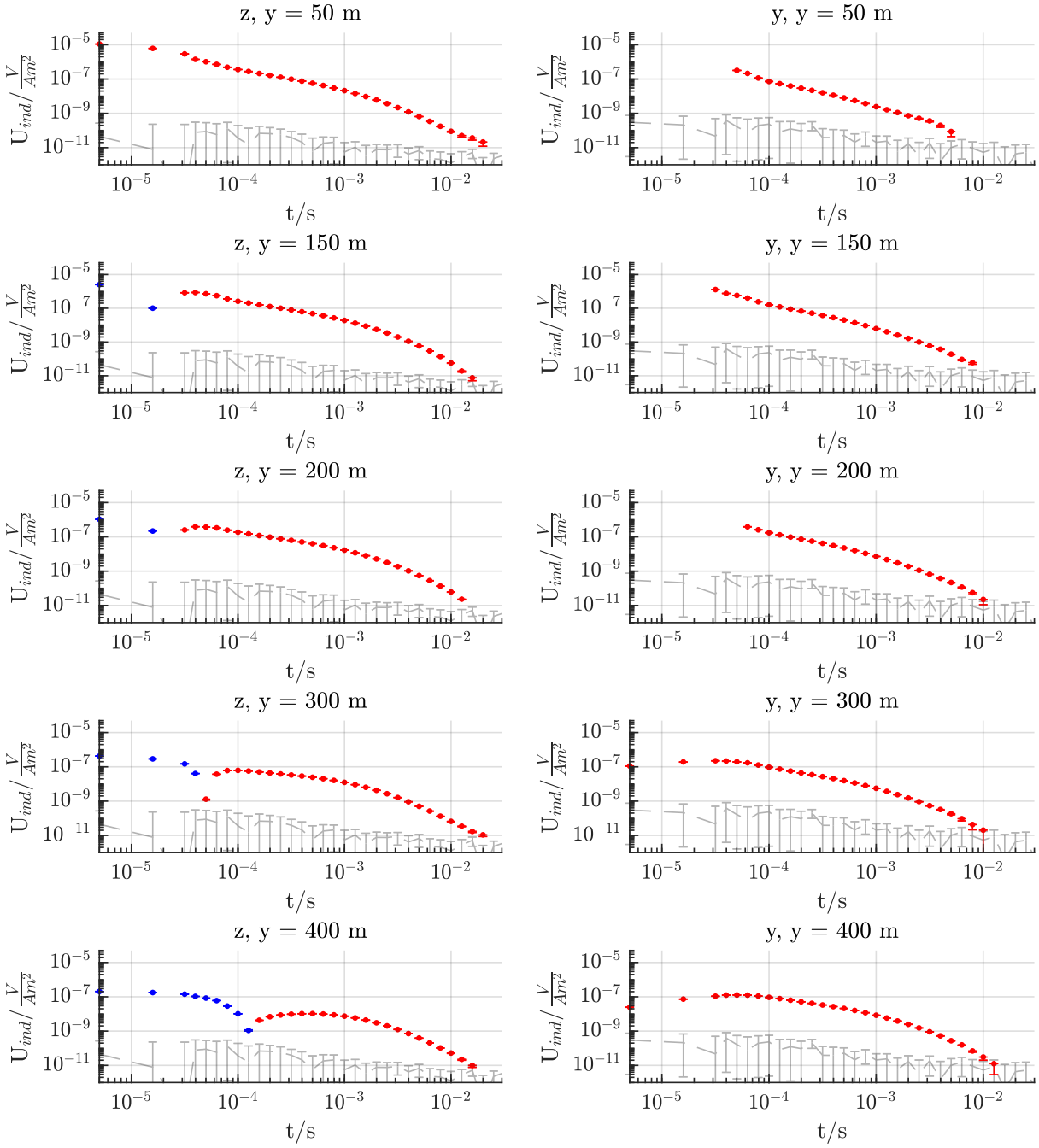

Figure A.8.: Fixed-loop data of transmitter B perpendicular to profile 1. (cont.)

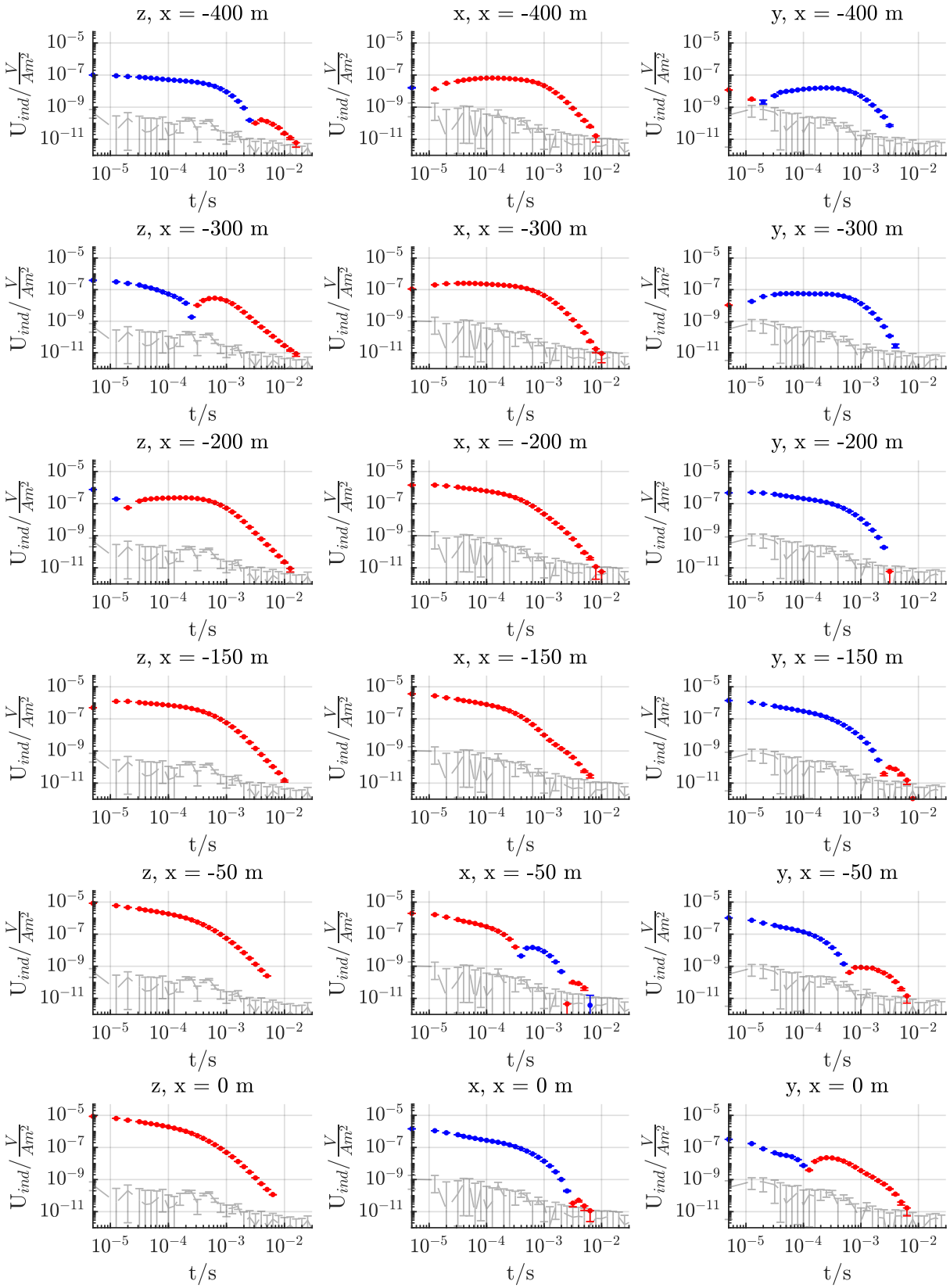

Figure A.9.: Fixed-loop data of transmitter C along profile 1. Positive induced voltage values are indicated in red and negative in blue. The measured noise level is shown in light gray. Each column represents one component and each row the components at a certain offset.

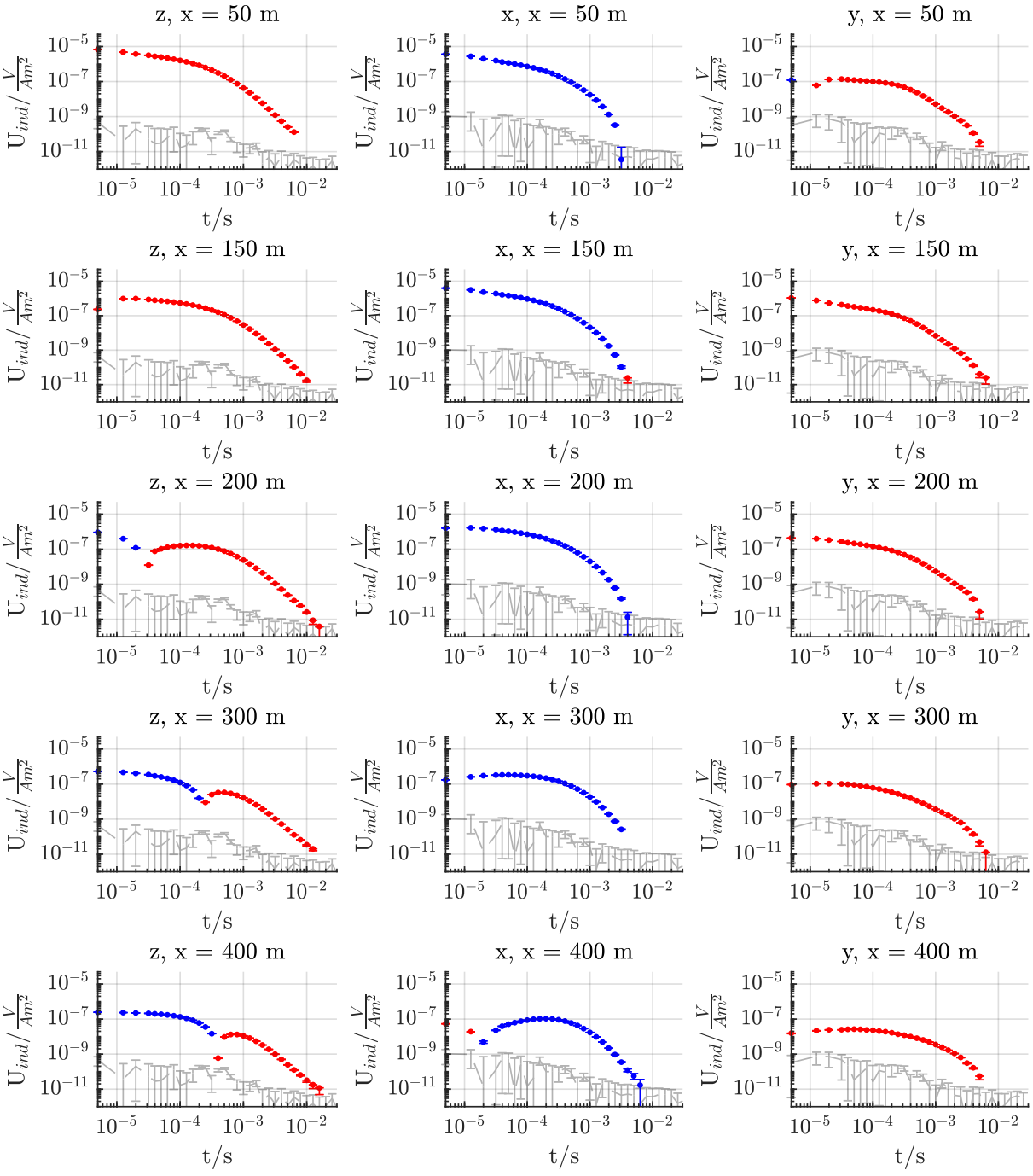

Figure A.9.: Fixed-loop data of transmitter C along profile 1. (cont.)

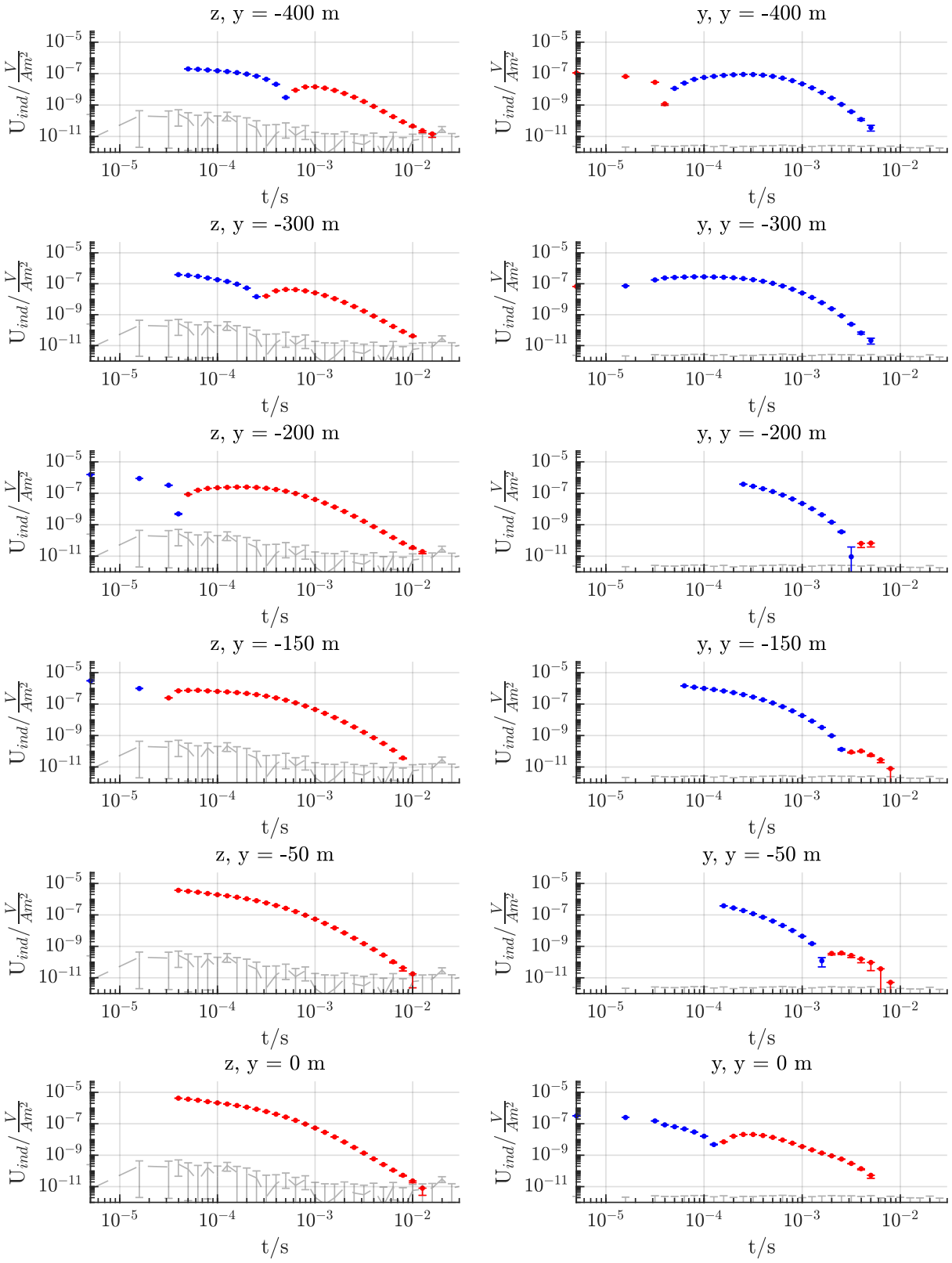

Figure A.10.: Fixed-loop data of transmitter C perpendicular to profile 1. Positive induced voltage values are indicated in red and negative in blue. The measured noise level is shown in light gray. Each column represents one component and each row the components at a certain offset.

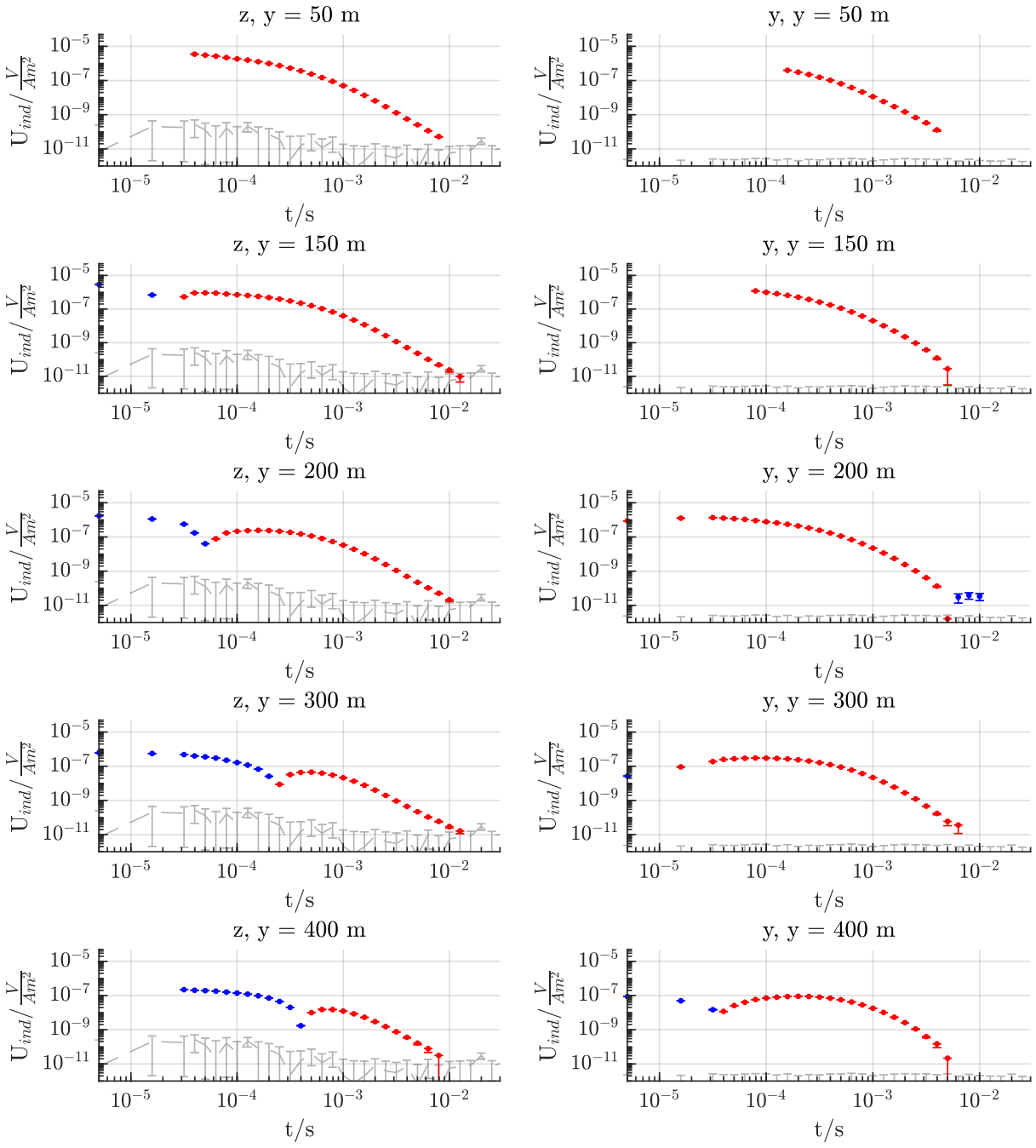

Figure A.10.: Fixed-loop data of transmitter C perpendicular to profile 1. (cont.)

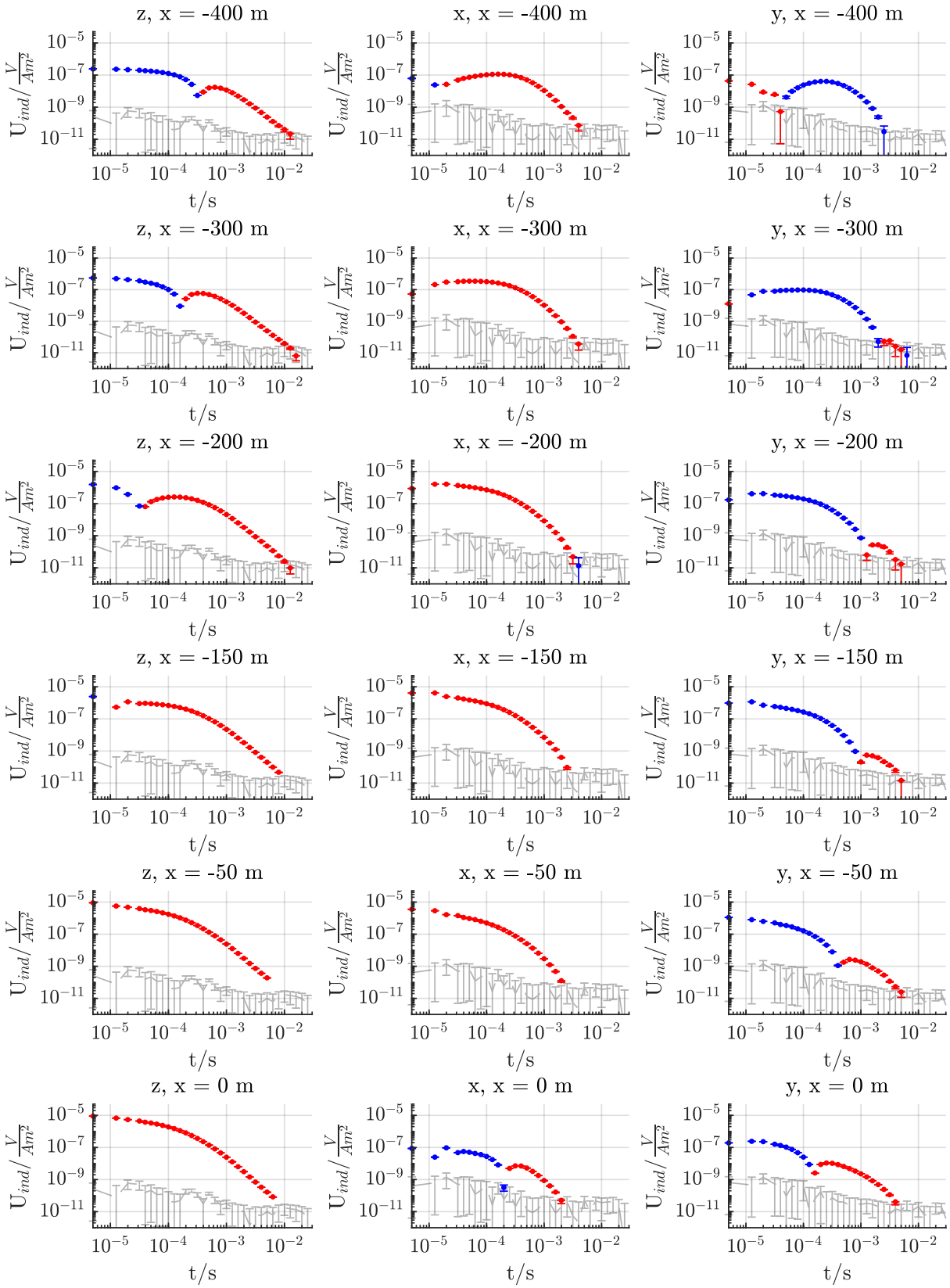

Figure A.11.: Fixed-loop data of transmitter D along profile 1. Positive induced voltage values are indicated in red and negative in blue. The measured noise level is shown in light gray. Each column represents one component and each row the components at a certain offset.

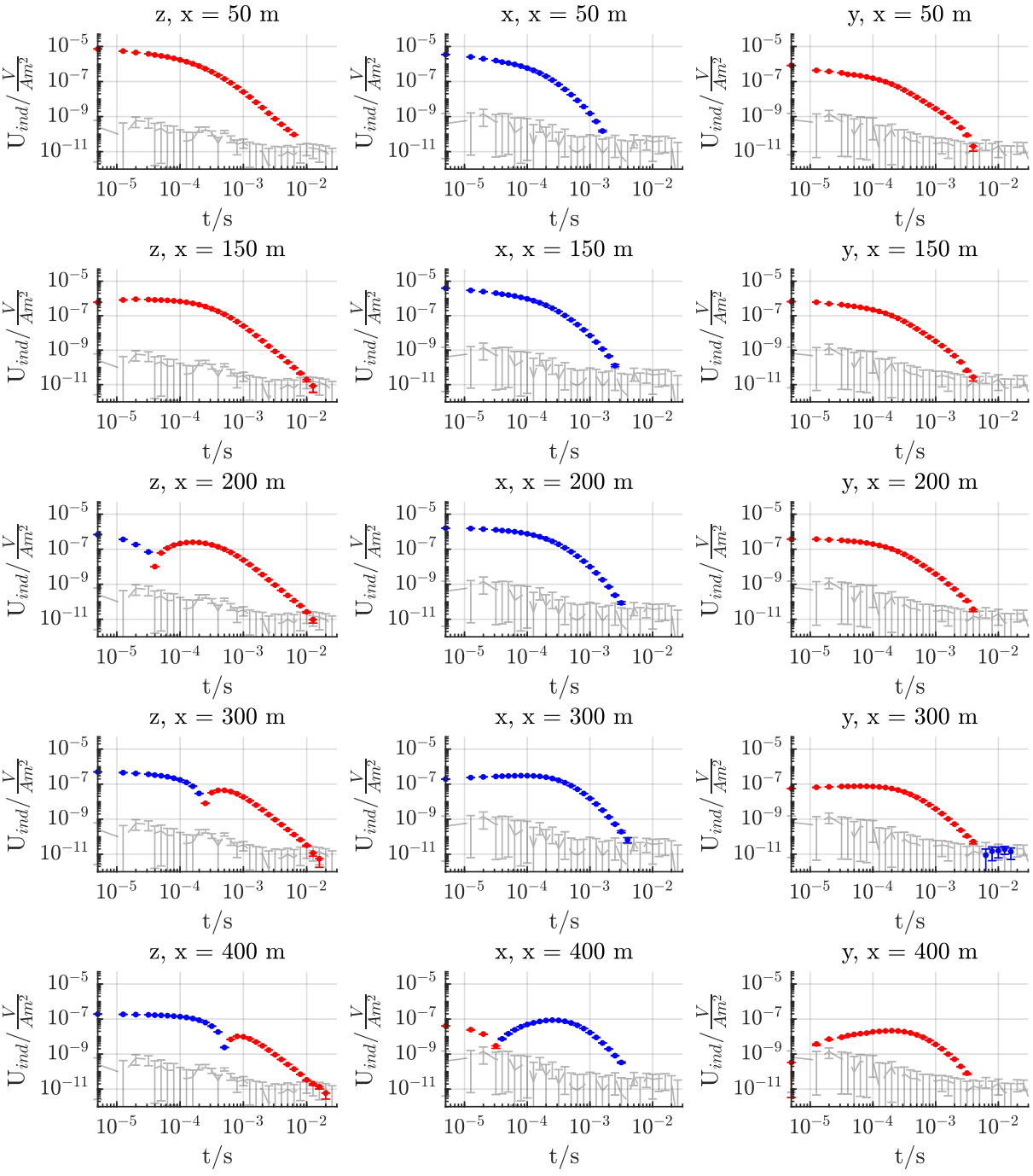

Figure A.11.: Fixed-loop data of transmitter D along profile 1. (cont.)

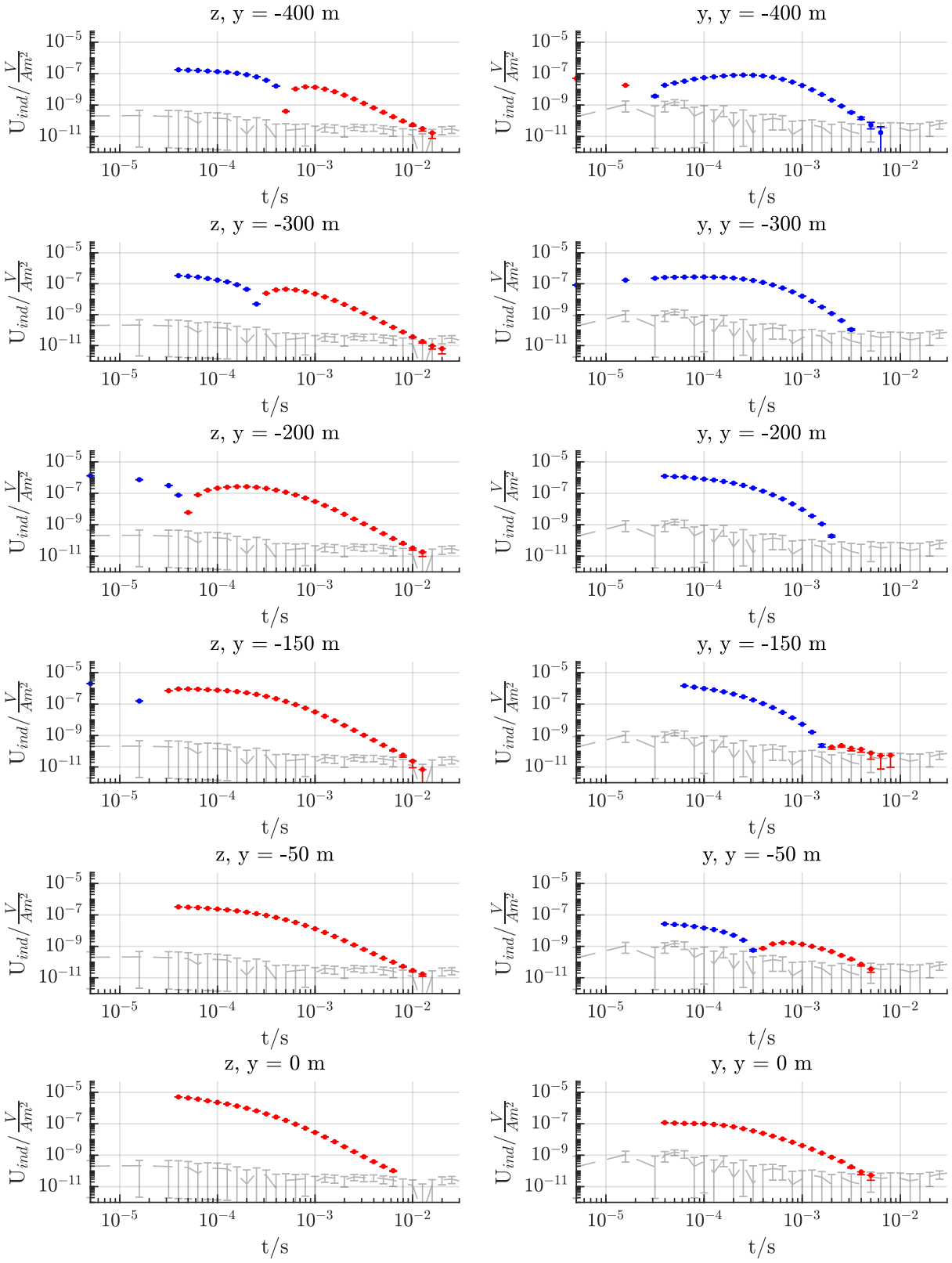

Figure A.12.: Fixed-loop data of transmitter D perpendicular to profile 1. Positive induced voltage values are indicated in red and negative in blue. The measured noise level is shown in light gray. Each column represents one component and each row the components at a certain offset.

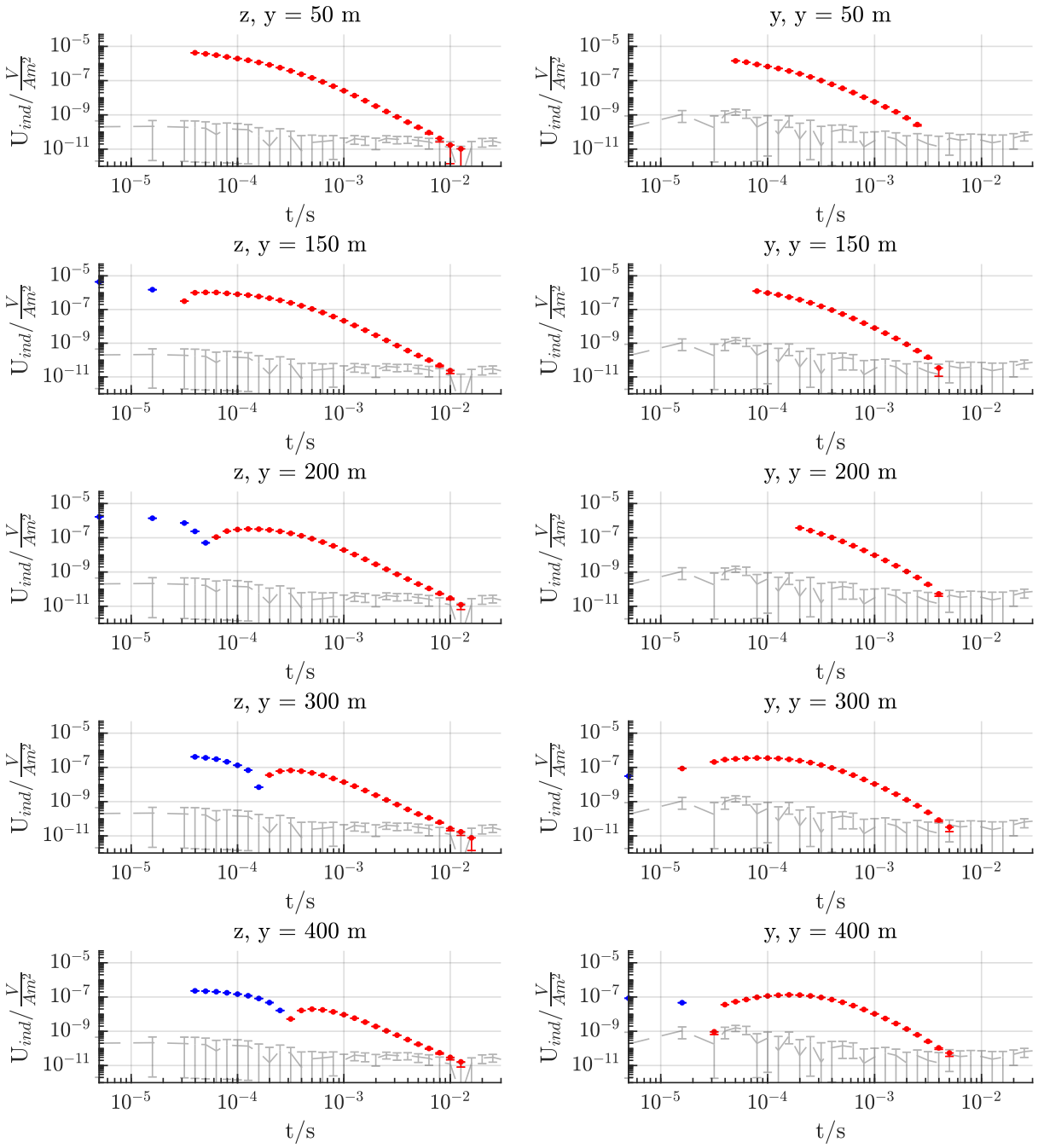

Figure A.12.: Fixed-loop data of transmitter D perpendicular to profile 1. (cont.)

A.3. AMT Data

Table A.8.: Coordinates, Recording Times and Electrode Contact Resistances of the AMT soundings.

Name	Longitude	Latitude	Recording Length/min		Electrode Contact Resistance/kΩ			
			sf = 500 Hz	sf = 25 kHz	Ex (pos)	Ex (neg)	Ey (pos)	Ey (neg)
1	16.283023 E	-27.770955 N	20	12	26.7	38.4	78.5	21.8
2	16.285811 E	-27.768332 N	20	10	9	2.1	14.7	14.8
3	16.288600 E	-27.765709 N	20	10	6.9	1.2	2.4	6.6
4	16.289994 E	-27.764397 N	20	10	x	x	x	x
5	16.291389 E	-27.763086 N	20	10	x	x	x	x
6	16.292783 E	-27.761774 N	20	10	12.2	21	22.4	33.2
7	16.294177 E	-27.760463 N	20	10	7.9	2.7	5.5	4
8	16.295519 E	-27.759308 N	20	5	2.7	2.2	6.3	7.3
9	16.296965 E	-27.757839 N	180	170	1.8	1.2	5.2	5.4
10	16.299754 E	-27.755216 N	20	10	0.6	0.2	7.8	2
11	16.305330 E	-27.749969 N	20	10	x	x	x	x
12	16.299712 E	-27.737560 N	20	9	48.4	7.8	12.1	6.5
13	16.310004 E	-27.722271 N	20	10	5.1	1.7	38.4	3.6
14	16.319920 E	-27.706134 N	20	10	4.1	17.1	2.7	10.4
15	16.329015 E	-27.690083 N	20	10	1.8	5.2	4.8	4.8
16	16.339777 E	-27.673494 N	20	10	19.7	11.4	3.2	9.1
100	16.207800 E	-27.658009 N	20	7.5	1.1	1.4	1.8	1.2

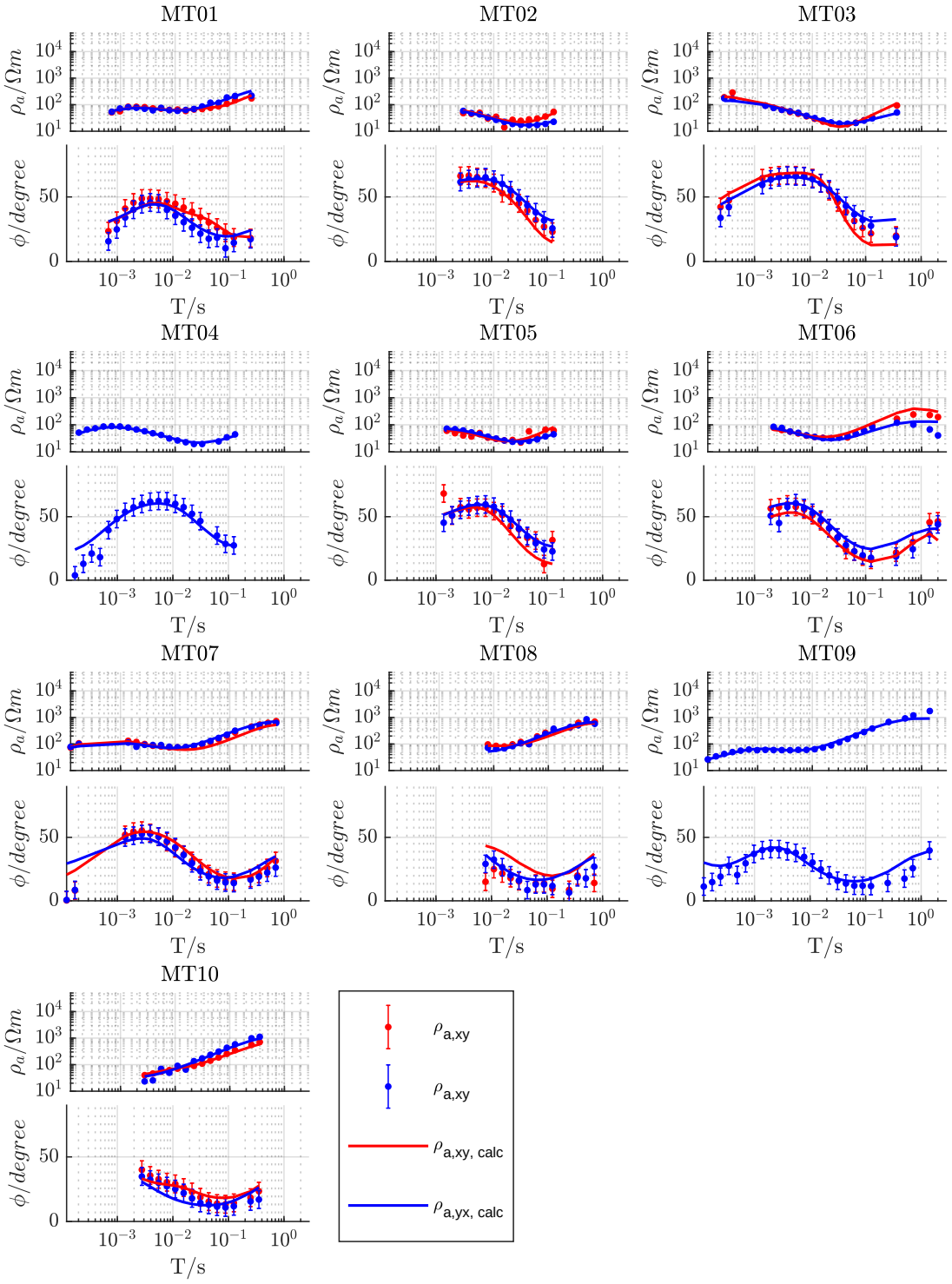

Figure A.13.: AMT transfer functions and modelled data by 2D inversion for Profile 1.

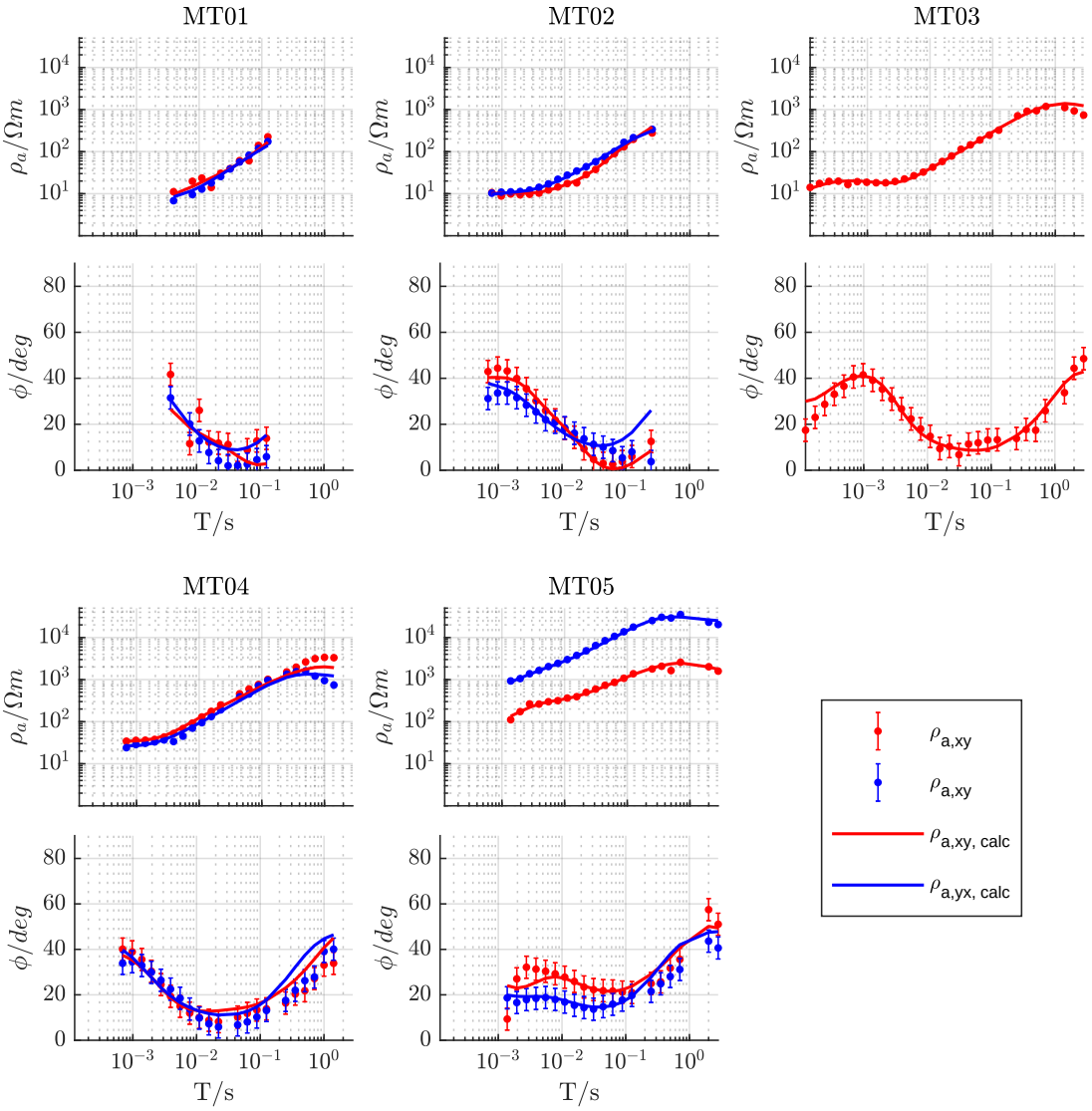

Figure A.14.: AMT transfer functions and modelled data by 2D inversion for the regional profile.

APPENDIX B

1D TEM Inversion

Here, all 1D inversion models of the single-loop data of the Roter Kamm impact crater is shown.

B.1. Profile 1

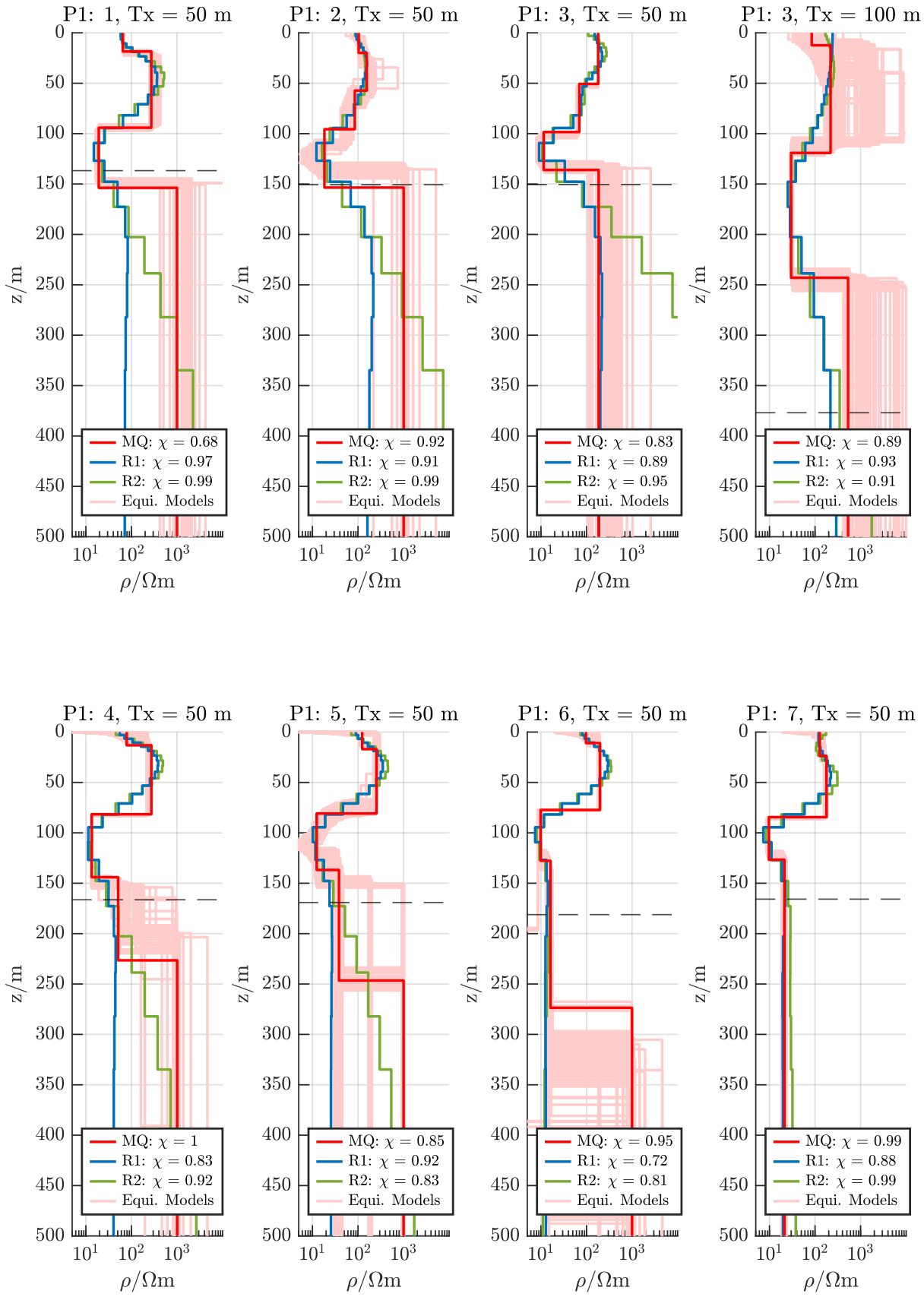

Figure B.1.: 1D inversion models along profile 1. The Marquardt-Levenberg models are indicated in red, the equivalent models in light red, the Occam R1 and R2 models in blue and green. The χ-values are shown in the legend.

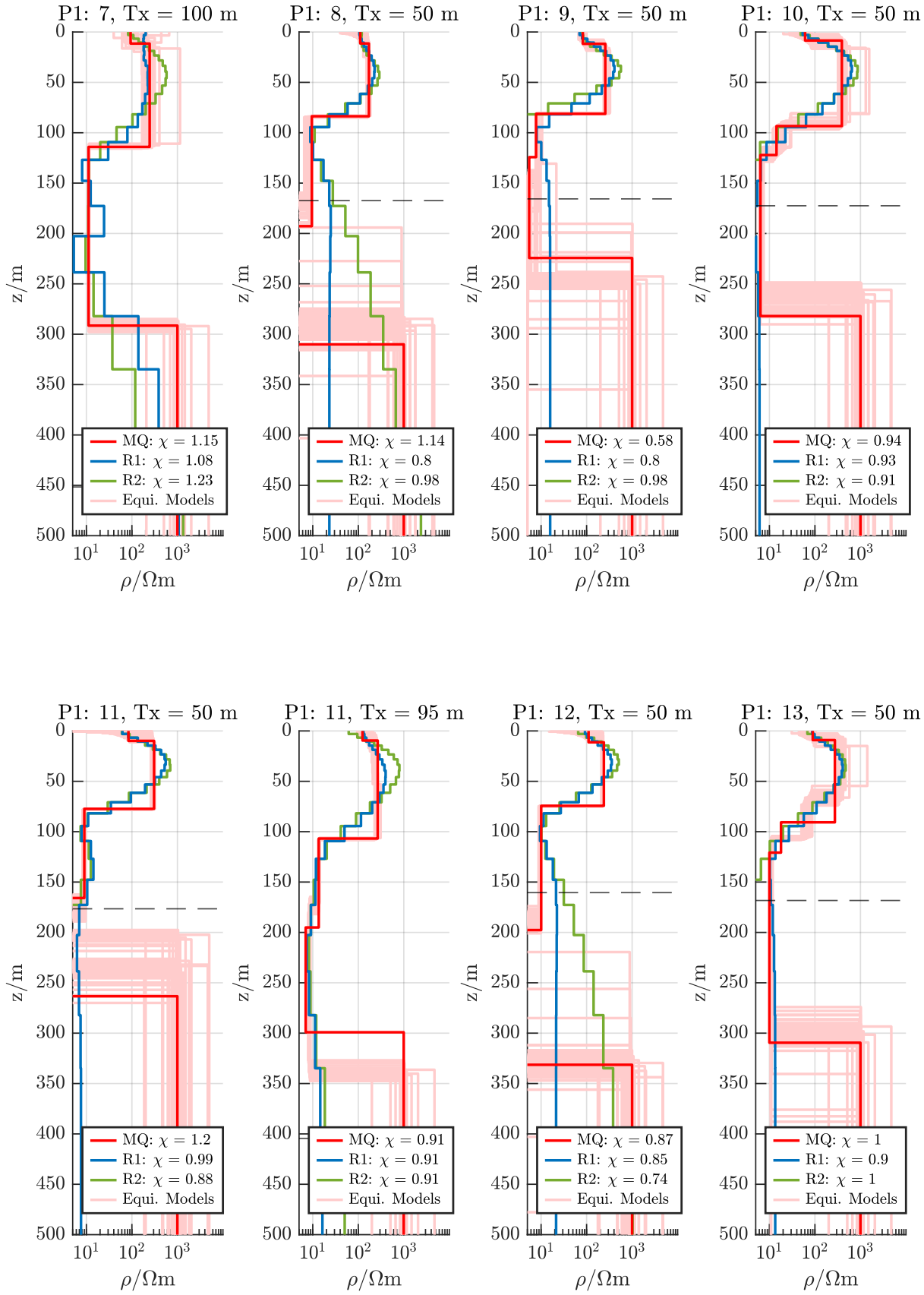

Figure B.1.: 1D inversion models along profile 1. (cont.)

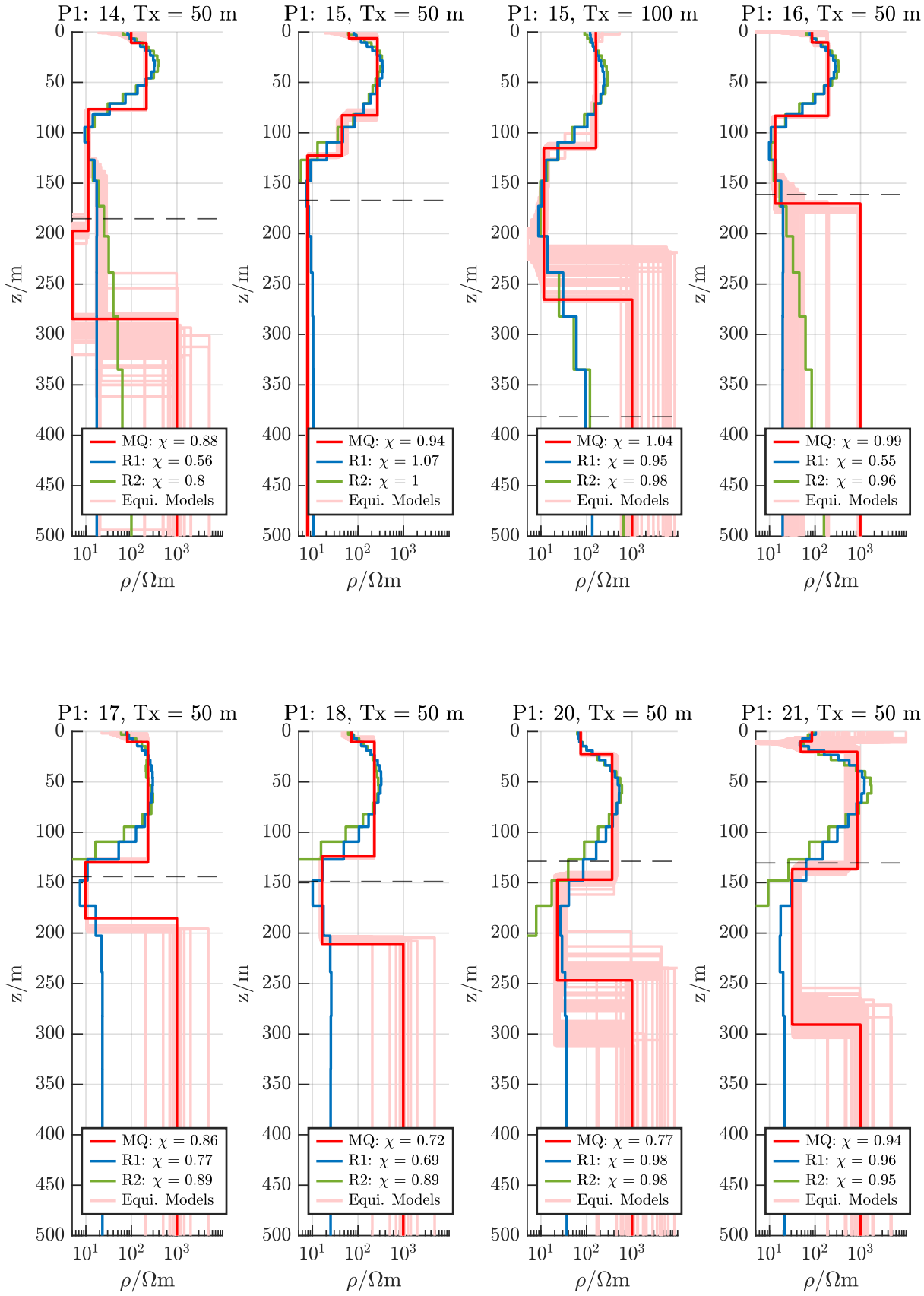

Figure B.1.: 1D inversion models along profile 1. (cont.)

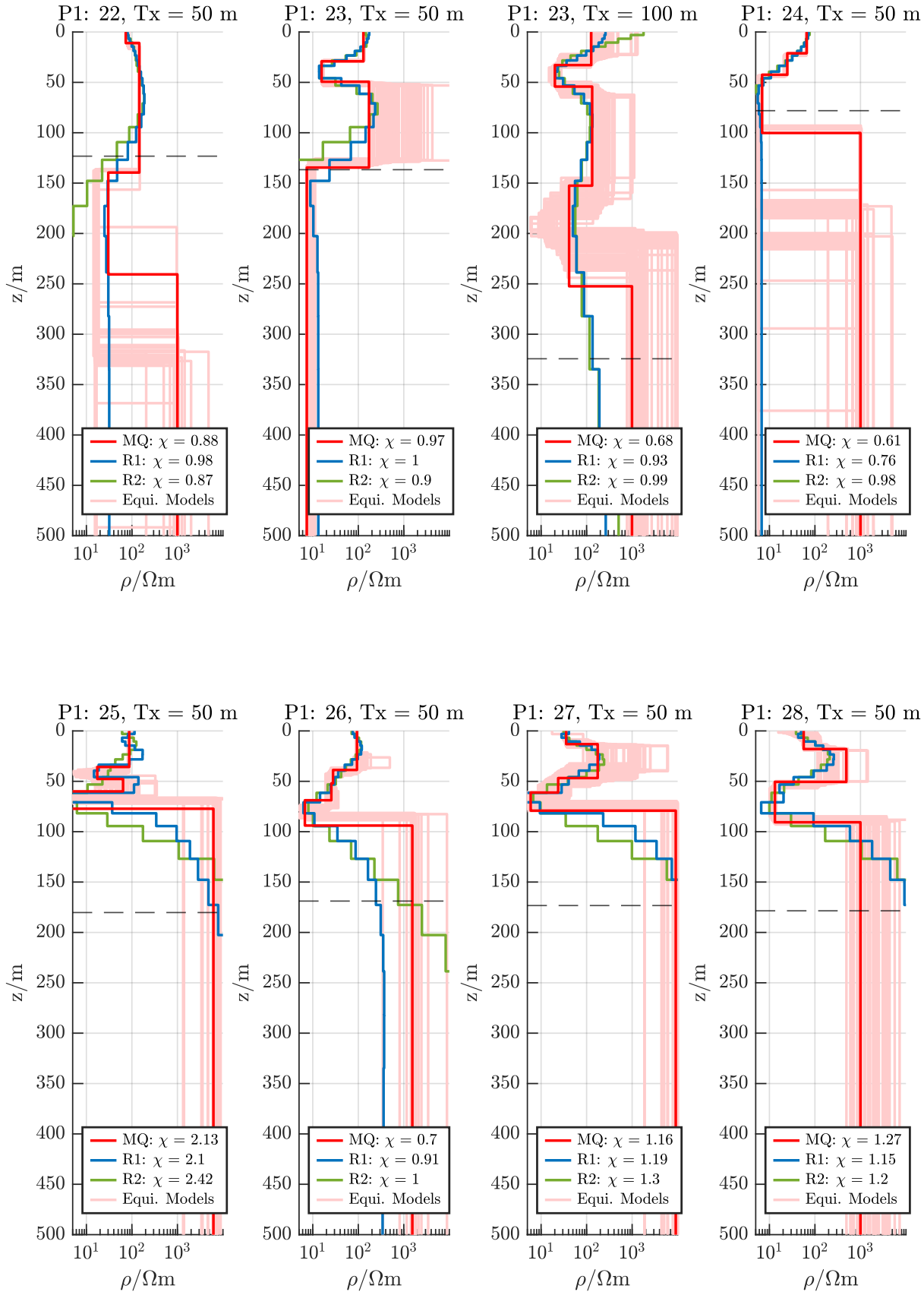

Figure B.1.: 1D inversion models along profile 1. (cont.)

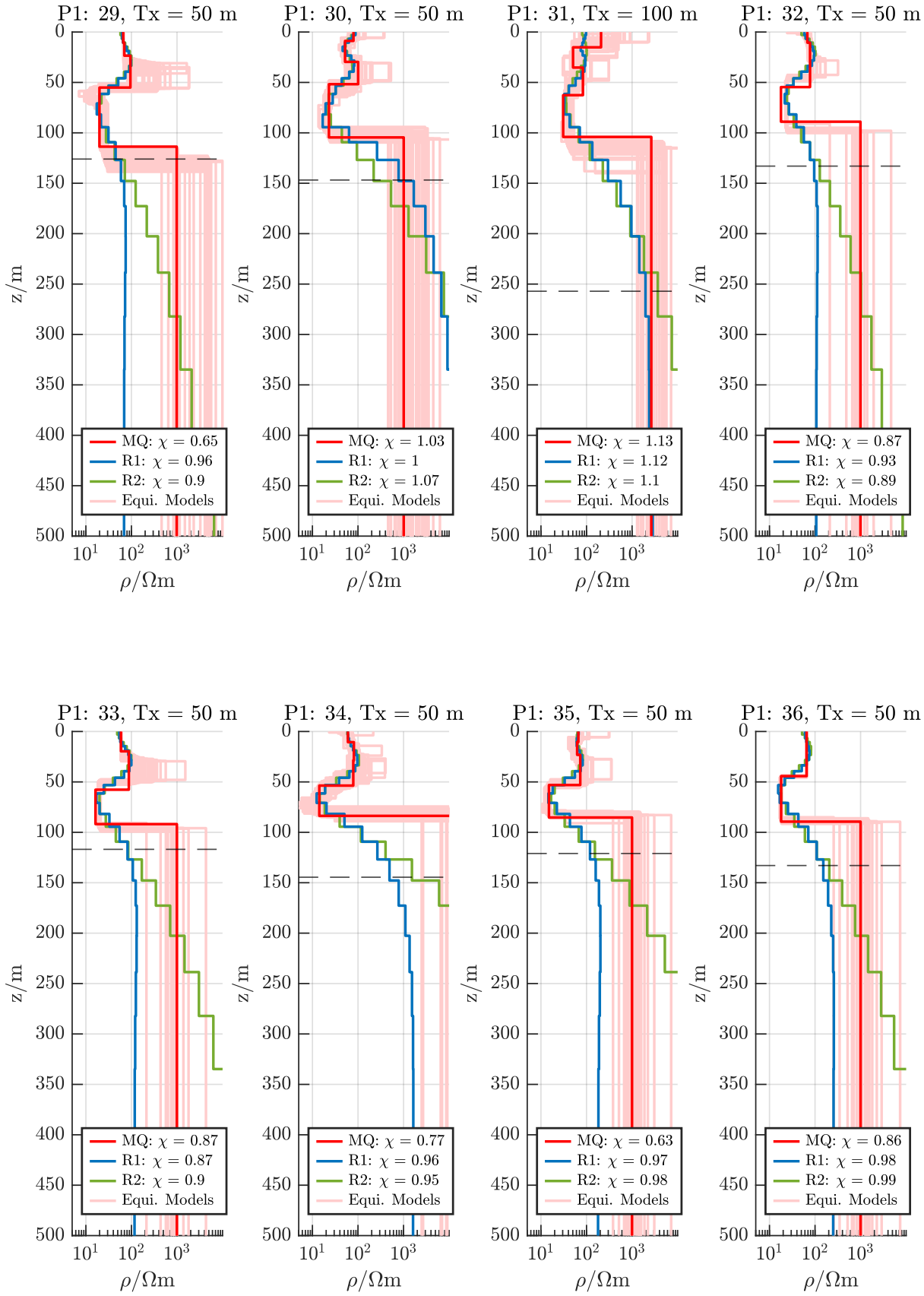

Figure B.1.: 1D inversion models along profile 1. (cont.)

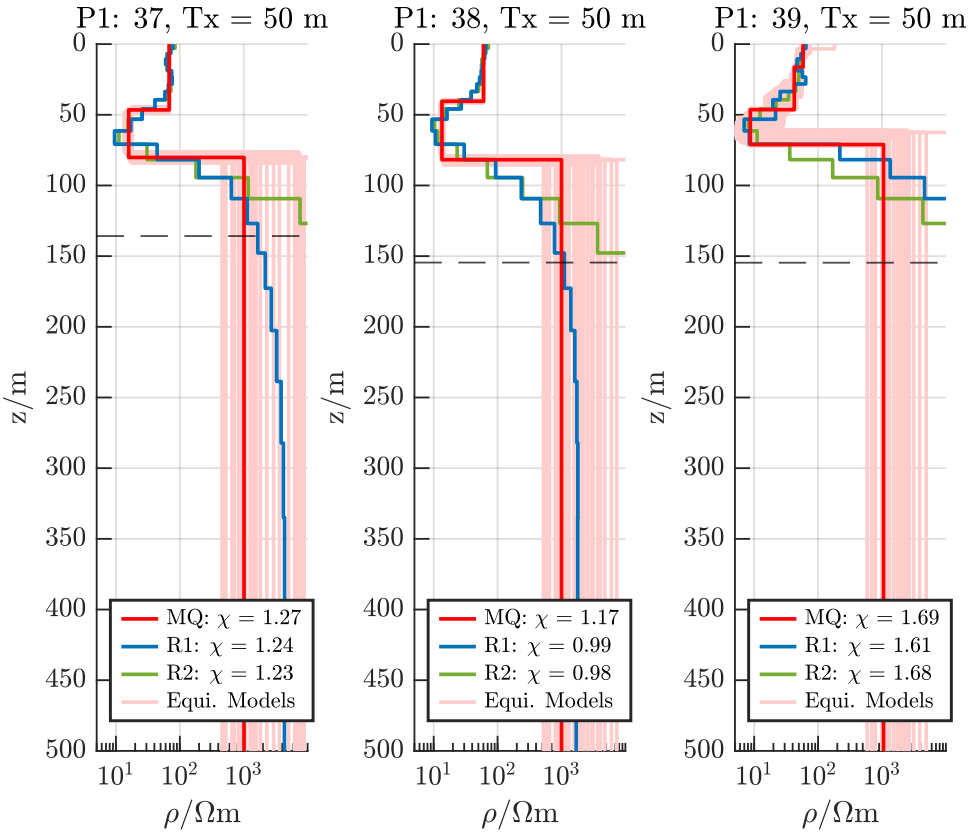

Figure B.1.: 1D inversion models along profile 1. (cont.)

B.2. Profile 2

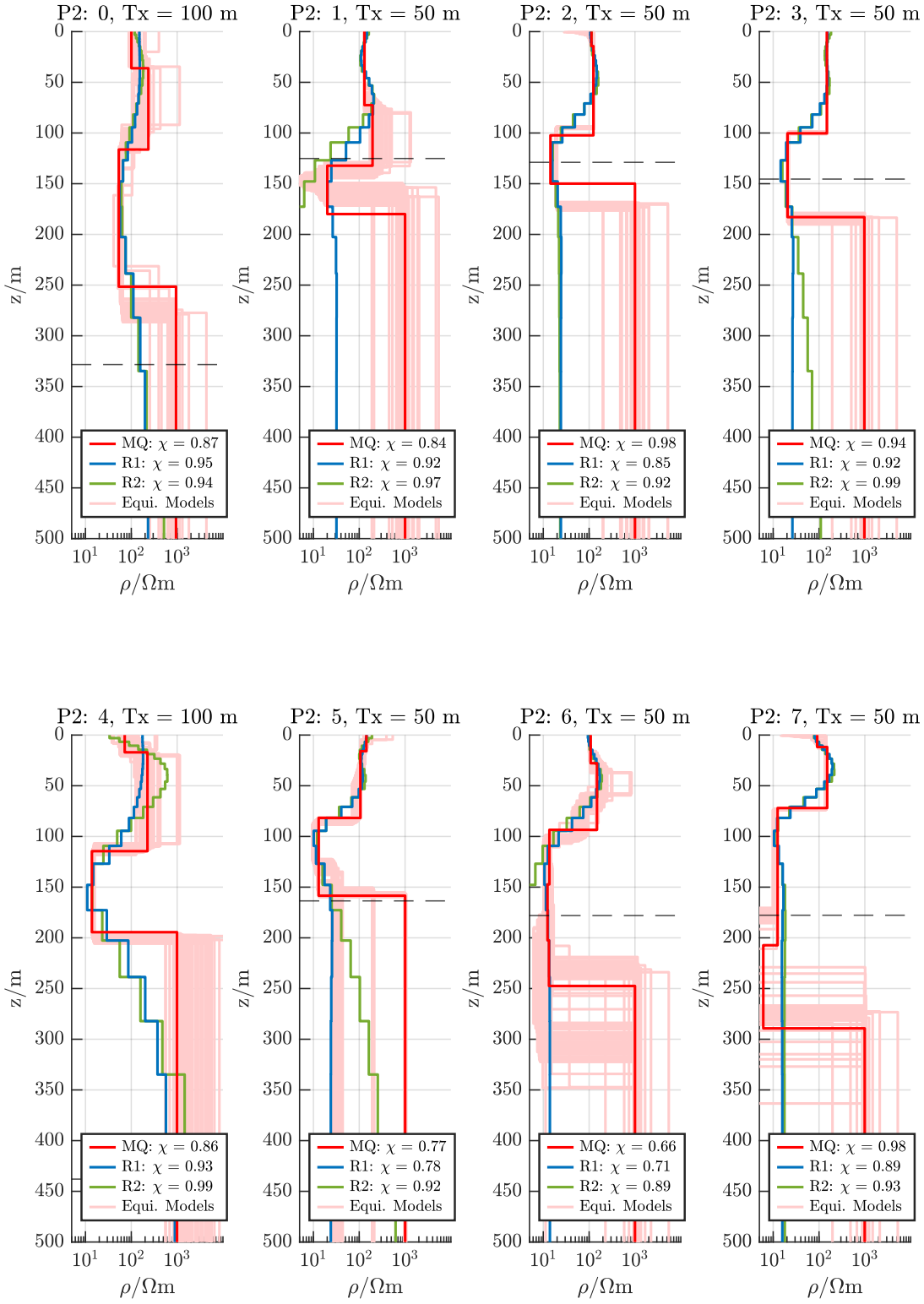

Figure B.2.: 1D inversion models along profile 2. The Marquardt-Levenberg models are indicated in red, the equivalent models in light red, the Occam R1 and R2 models in blue and green. The χ-values are shown in the legend.

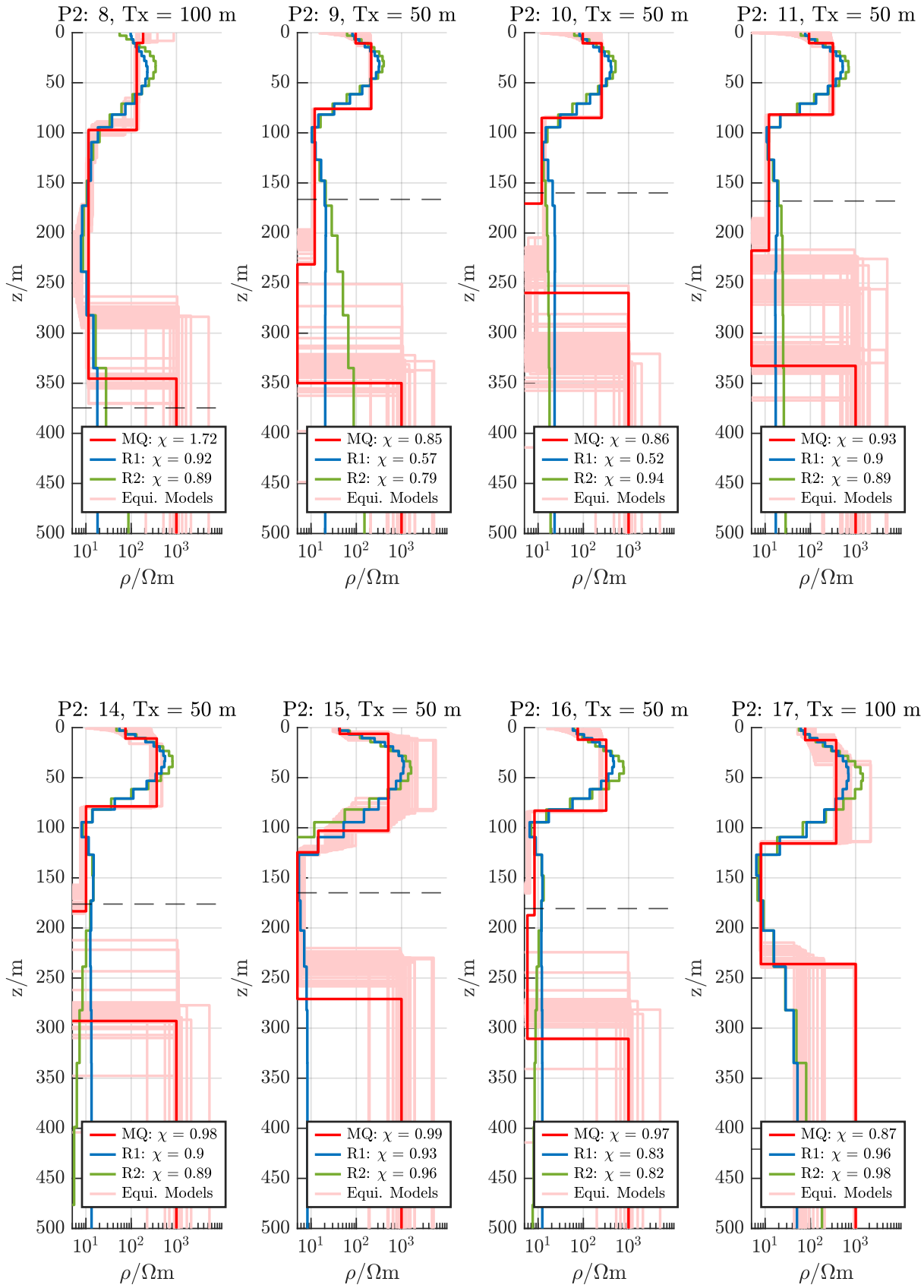

Figure B.2.: 1D inversion models along profile 2. (cont.)

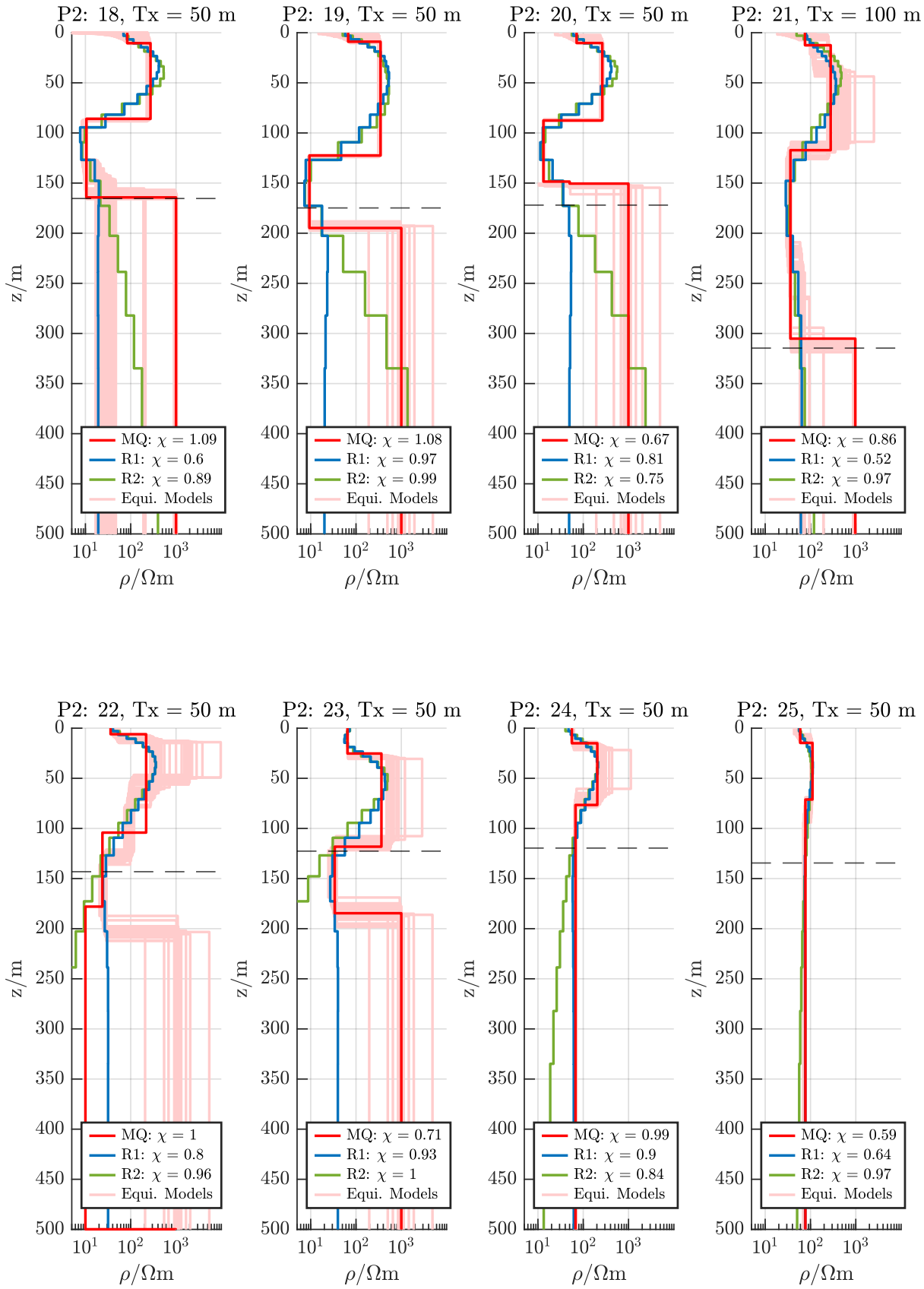

Figure B.2.: 1D inversion models along profile 2. (cont.)

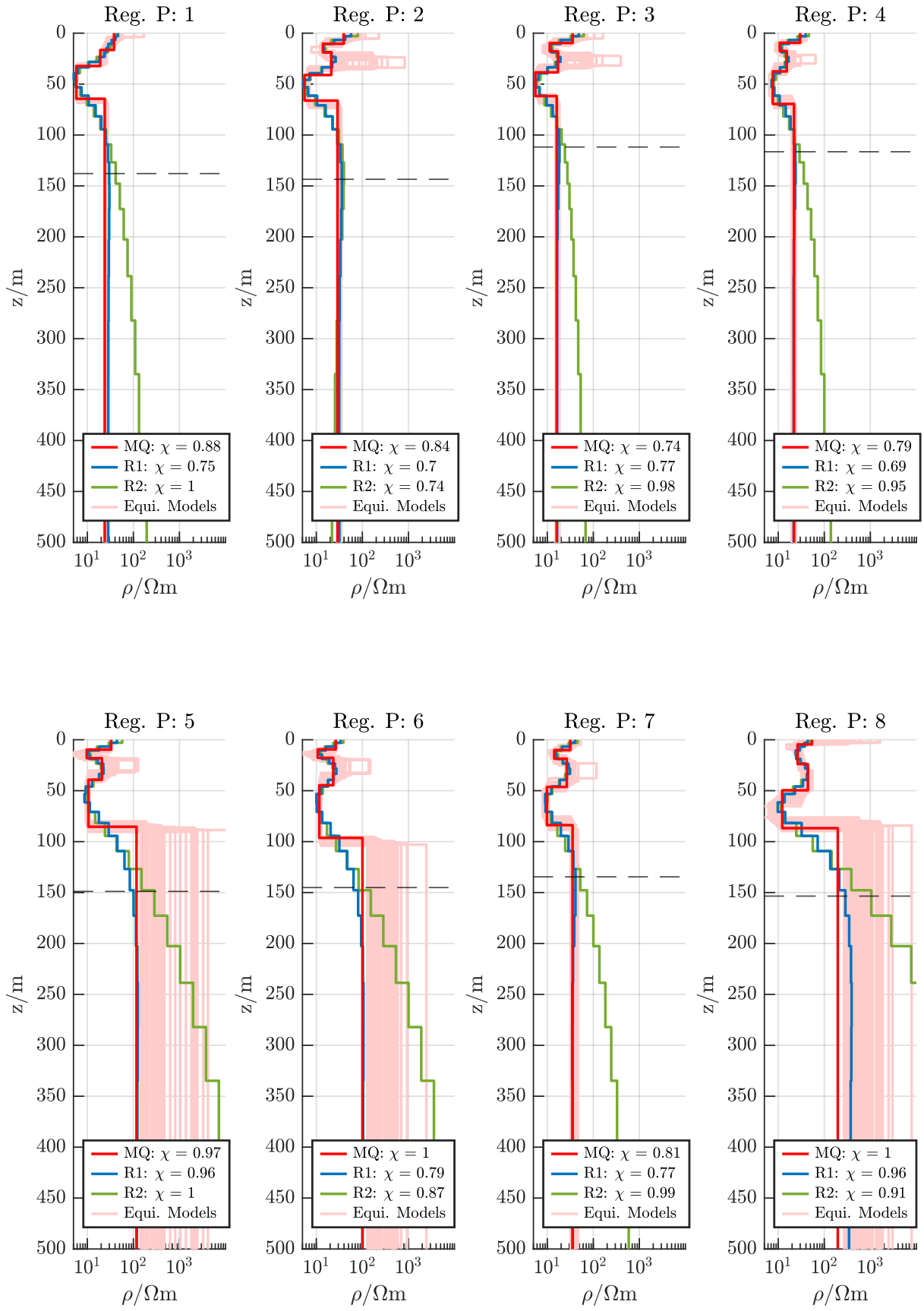

Figure B.3.: 1D inversion models along the regional profile. The Marquardt-Levenberg models are indicated in red, the equivalent models in light red, the Occam R1 and R2 models in blue and green. The χ-values are shown in the legend.

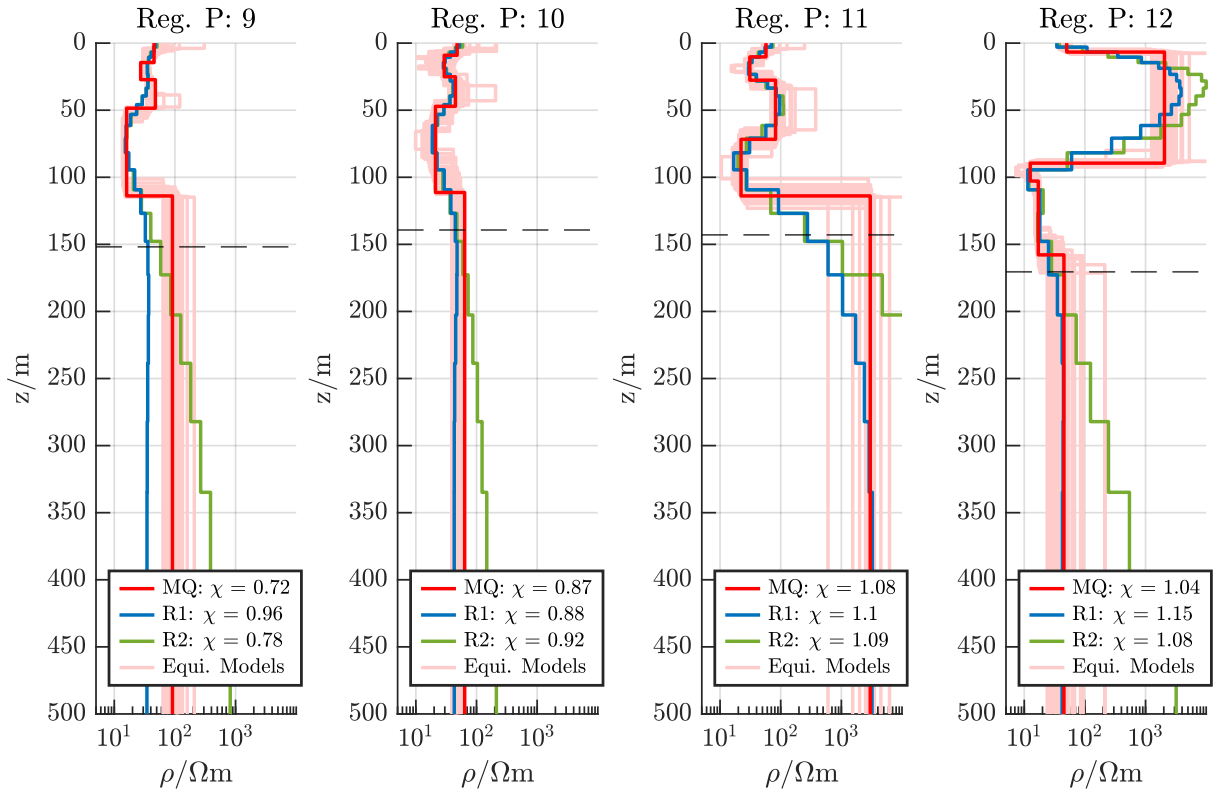

Figure B.3.: 1D inversion models along the regional profile. (cont.)

B.3. Single-Loop TEM Sounding of Clay Pan

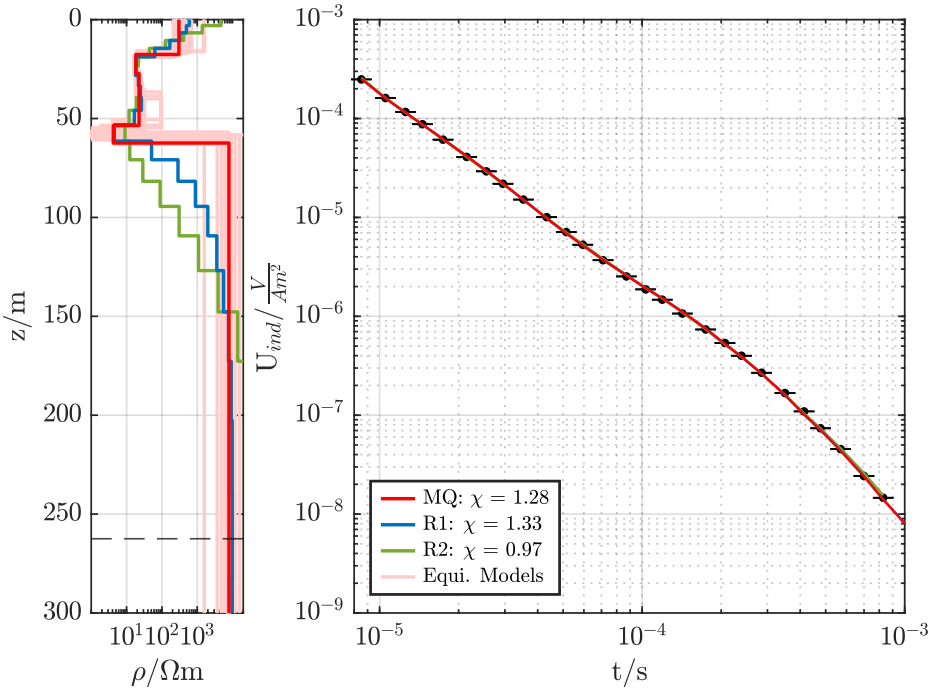

Figure B.4.: 1D inversion models and data fit for a small clay pan between the Aurus clay pan and the Roter Kamm impact crater.

APPENDIX C

Aurus Clay Pan

This Appendix presents the single-loop soundings, their coordinates and 1D inversions of the Aurus clay pan. All inversion were carried out using a 3 % relative error. A summary of the results can be found in Nienhaus et al. (2023c).

Table C.1.: Coordinates of single-loop sounding locations at the Aurus clay pan along Profile 1. Additionally, the corresponding profile meter and the transmitter size are given.

Name	Longitude	Latitude	x/m	Tx/m
P1-01	16.213986	-27.667336	-1200	50
P1-02	16.213470	-27.666558	-1100	50
P1-03	16.212955	-27.665781	-1000	50
P1-04	16.212439	-27.665004	-900	50
P1-05	16.211924	-27.664227	-800	50
P1-06	16.211408	-27.663450	-700	50
P1-07	16.210893	-27.662672	-600	50
P1-08	16.210377	-27.661895	-500	50
P1-09	16.209862	-27.661118	-400	50
P1-10	16.209346	-27.660341	-300	50
P1-11	16.208831	-27.659563	-200	50
P1-12	16.208316	-27.658786	-100	50
P1-13	16.207800	-27.658009	0	50
P1-14	16.207285	-27.657232	100	50
P1-15	16.206769	-27.656455	200	50
P1-16	16.206254	-27.655677	300	50
P1-17	16.205738	-27.654900	400	50
P1-18	16.205223	-27.654123	500	50
P1-19	16.204708	-27.653346	600	50
P1-20	16.204192	-27.652568	700	50
P1-21	16.203677	-27.651791	800	50
P1-22	16.203162	-27.651014	900	50
P1-23	16.202646	-27.650237	1000	50

Continuation of coordinates.

Name	Longitude	Latitude	x/m	Tx/m
P1-24	16.202131	-27.649459	1100	50
P1-25	16.201616	-27.648682	1200	50
P1-26	16.200585	-27.647128	1300	50
P1-27	16.199554	-27.645573	1400	50

Table C.2.: Coordinates of single-loop sounding locations at the Aurus clay pan along Profile 2. Additionally, the corresponding profile meter and the transmitter size are given.

Name	Longitude	Latitude	y/m	Tx/m
P2-01	16.200817	-27.661680	-800	50
P2-02	16.201690	-27.661221	-700	50
P2-03	16.202563	-27.660763	-600	50
P2-04	16.203436	-27.660304	-500	50
P2-05	16.204308	-27.659845	-400	50
P2-06	16.205181	-27.659386	-300	50
P2-07	16.206054	-27.658927	-200	50
P2-08	16.206927	-27.658468	-100	50
P2-09	16.207800	-27.658009	0	50
P2-10	16.208673	-27.657550	100	50
P2-11	16.209546	-27.657091	200	50
P2-12	16.210419	-27.656632	300	50
P2-13	16.211292	-27.656173	400	50
P2-14	16.212164	-27.655714	500	50
P2-15	16.213037	-27.655255	600	50
P2-16	16.213910	-27.654796	700	50
P2-17	16.214783	-27.654337	800	50
P2-18	16.215656	-27.653878	900	50
P2-19	16.216529	-27.653419	1000	50
P2-20	16.217401	-27.652960	1100	50
P2-21	16.218274	-27.652501	1200	50
P2-22	16.219147	-27.652042	1300	50

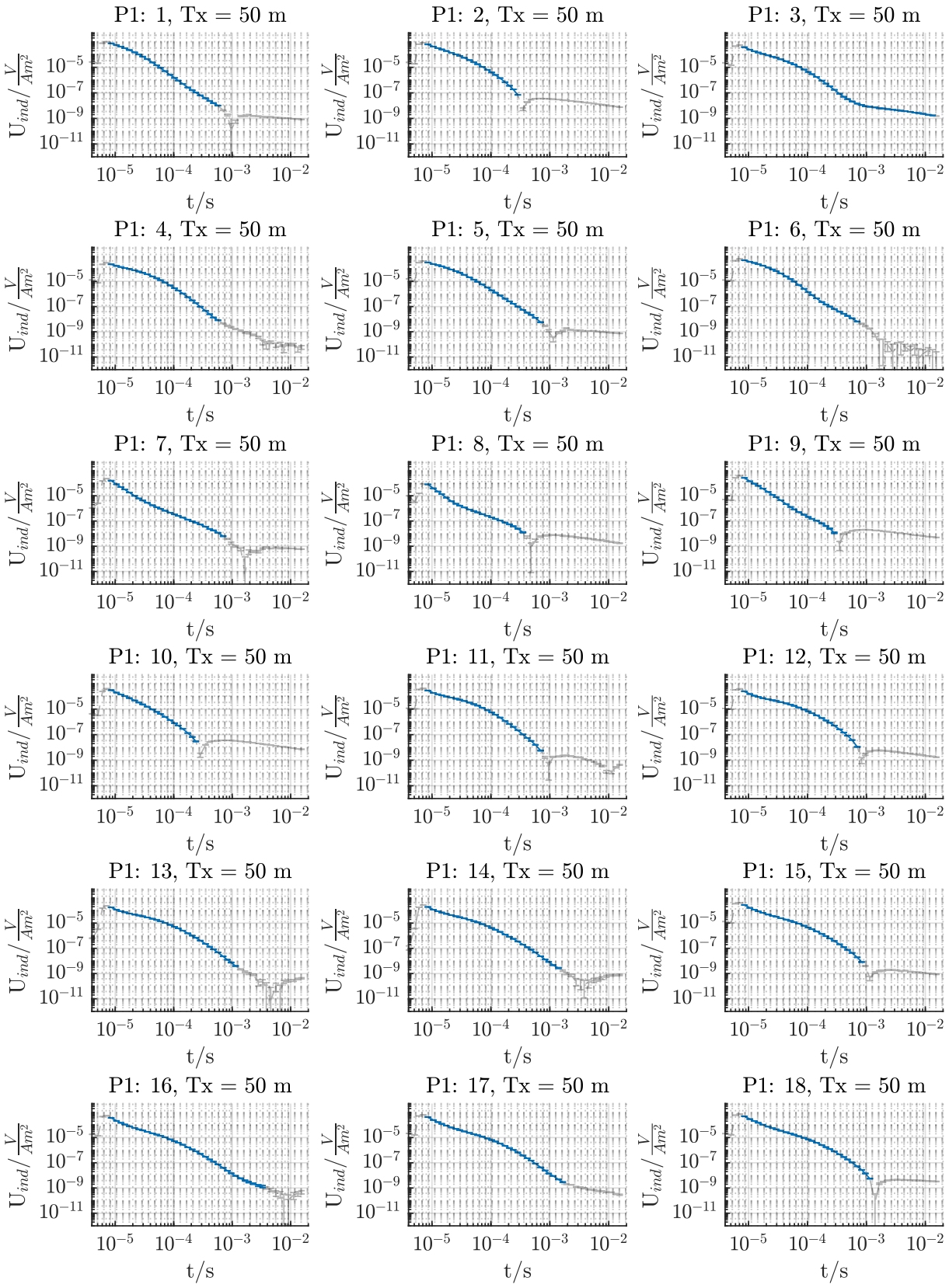

Figure C.1.: Single-loop data of the Aurus clay pan along Profile 1. The whole transient is indicated in light gray and the transient inside the resolution boundaries of the TEM-FAST 48 in blue.

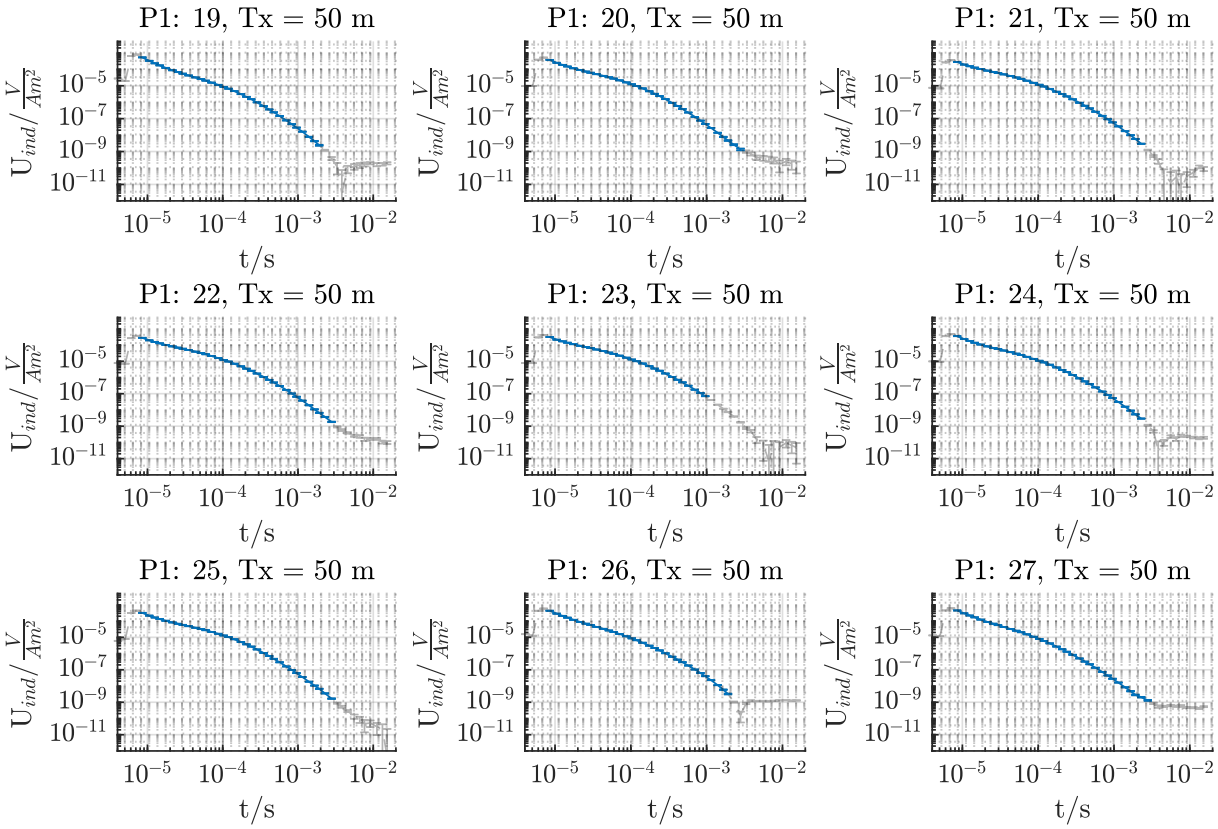

Figure C.1.: Single-loop data of the Aurus clay pan along Profile 1. (cont.)

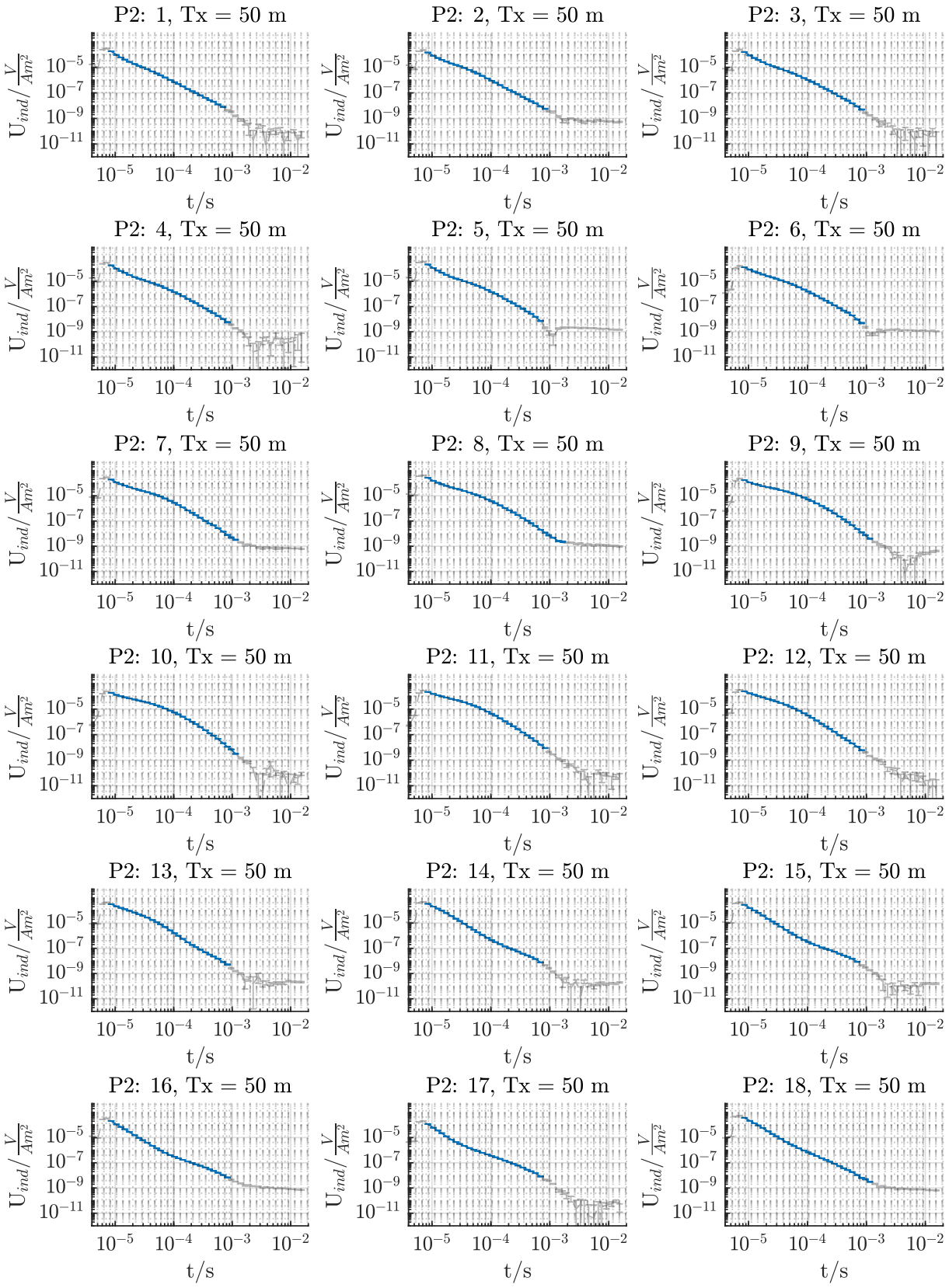

Figure C.2.: Single-loop data of the Aurus clay pan along Profile 2. The whole transient is indicated in light gray and the transient inside the resolution boundaries of the TEM-FAST 48 in blue.

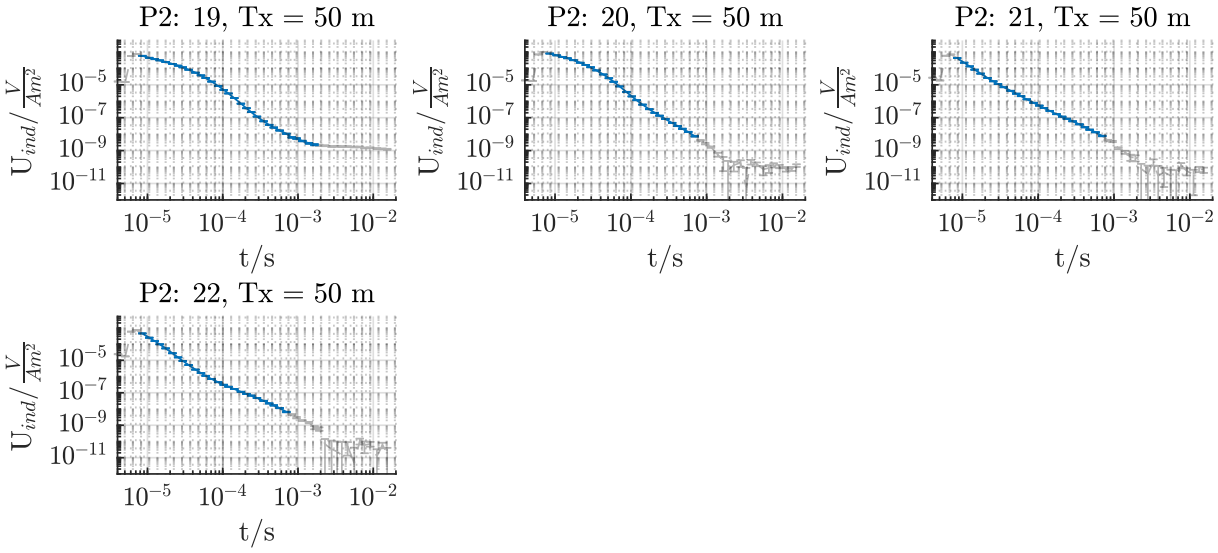

Figure C.2.: Single-loop data of the Aurus clay pan along Profile 2. (cont.)

C.1. 1D Inversion Results

C.1.1. Profile 1

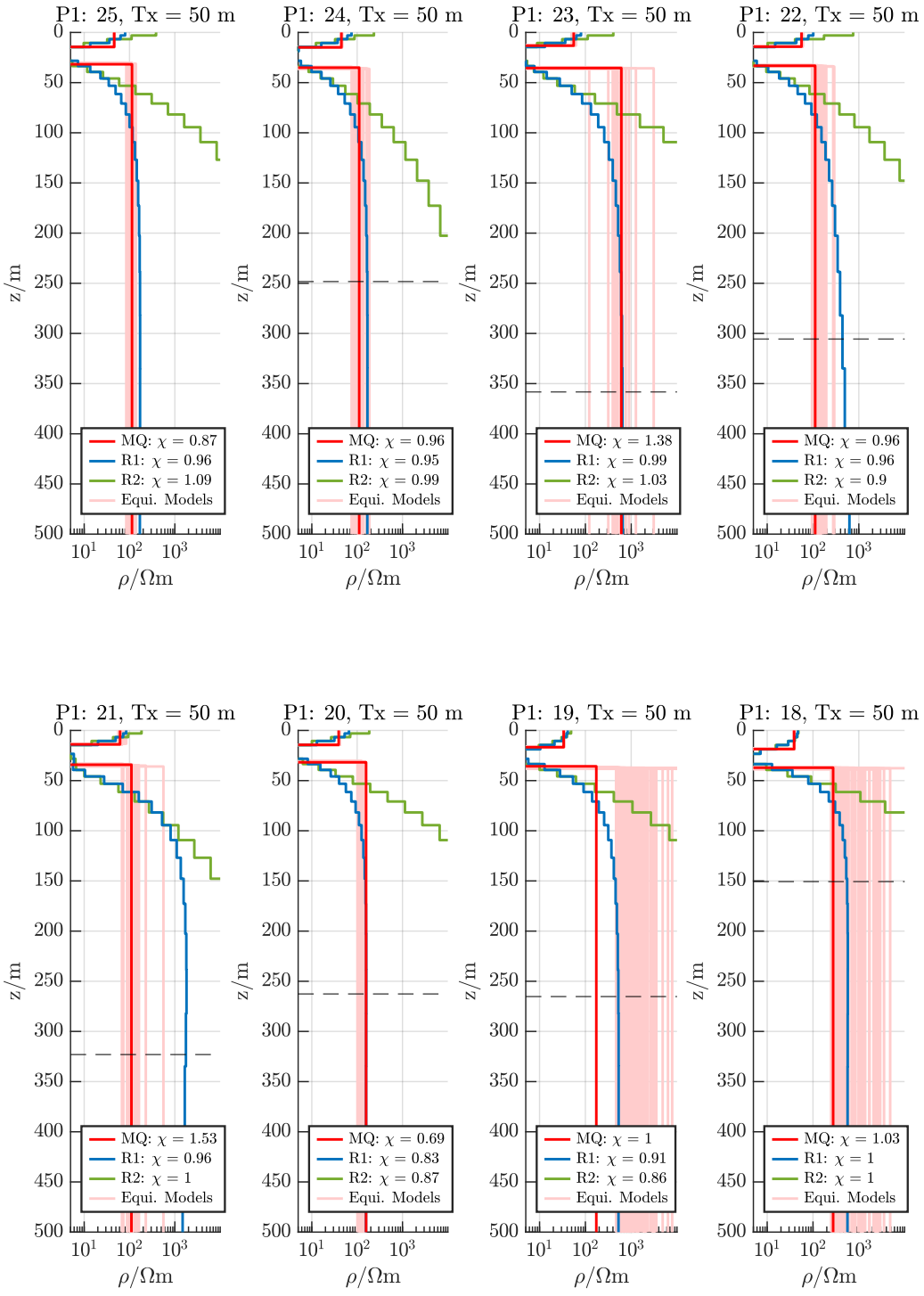

Figure C.3.: 1D inversion models of the Aurus clay pan along profile 1. The Marquardt-Levenberg models are indicated in red, the equivalent models in light red, the Occam R1 and R2 models in blue and green. The χ-values are shown in the legend.

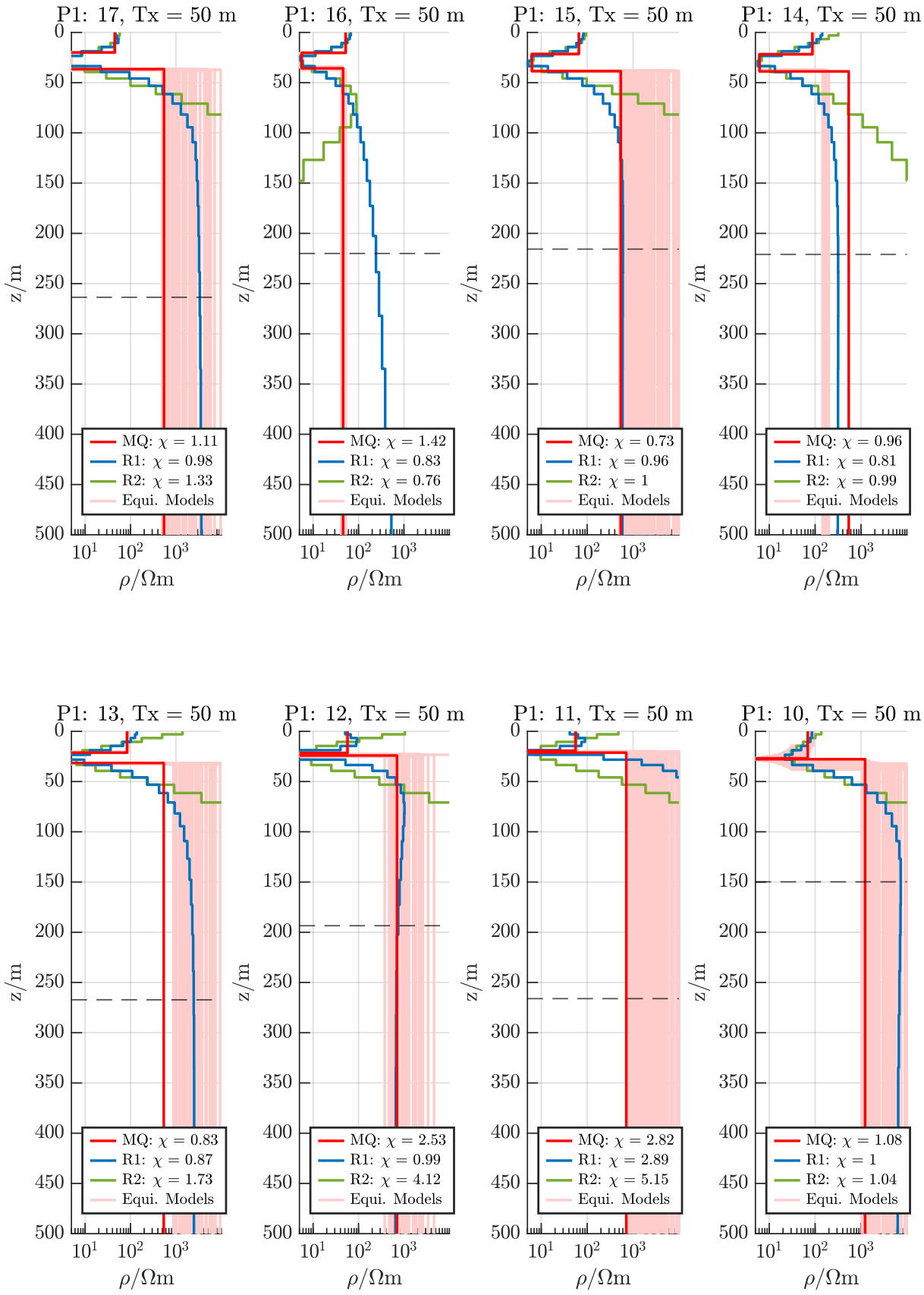

Figure C.3.: 1D inversion models of the Aurus clay pan along profile 1. (cont.)

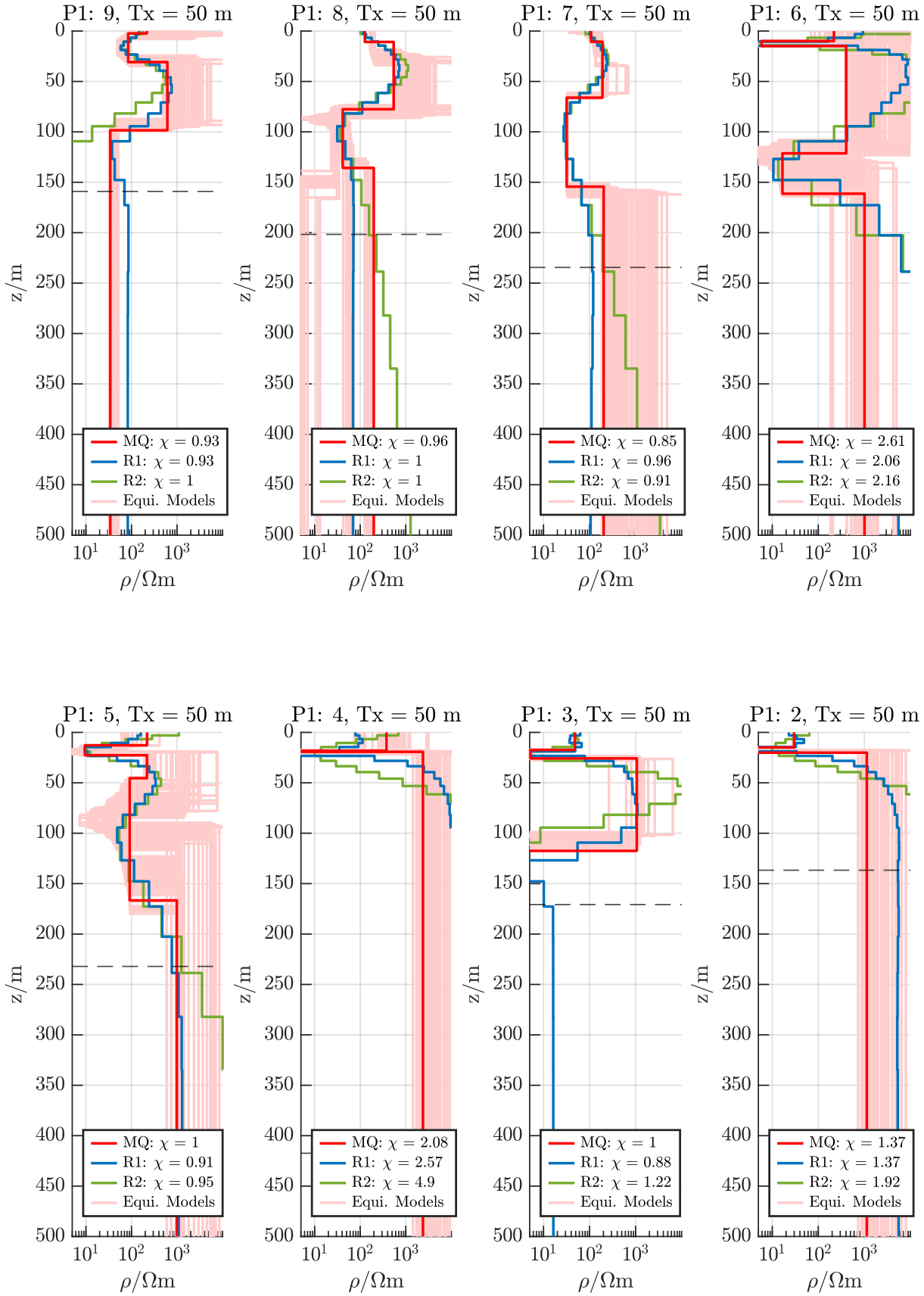

Figure C.3.: 1D inversion models of the Aurus clay pan along profile 1. (cont.)

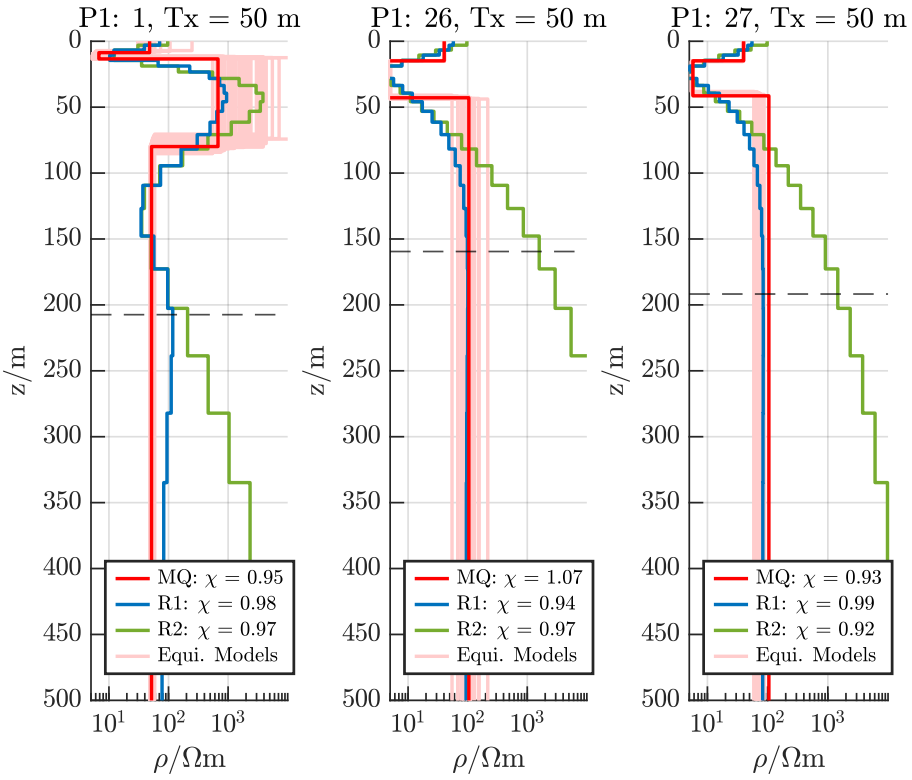

Figure C.3.: 1D inversion models of the Aurus clay pan along profile 1. (cont.)

C.1.2. Profile 2

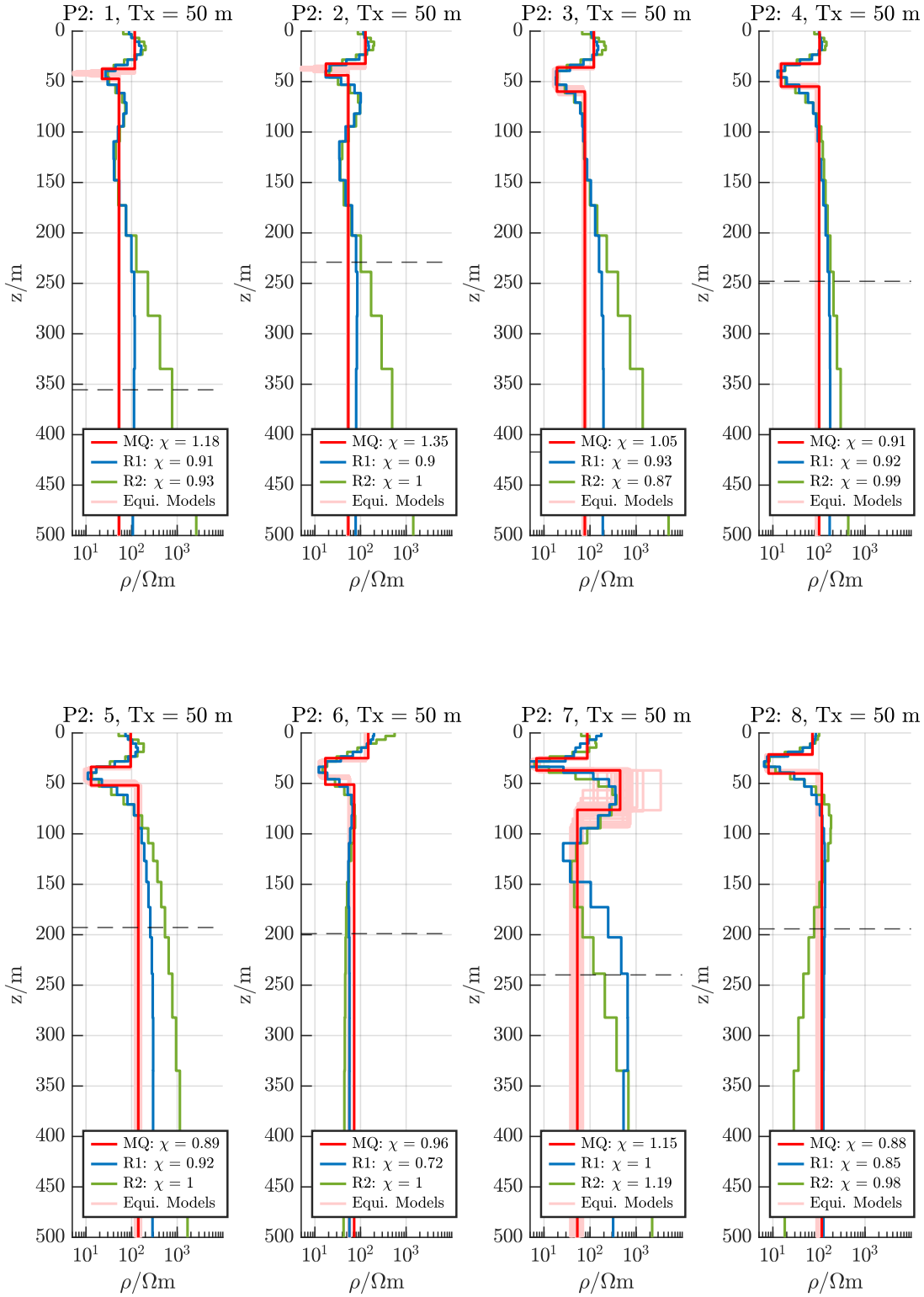

Figure C.4.: 1D inversion models of the Aurus clay pan along profile 2. The Marquardt-Levenberg models are indicated in red, the equivalent models in light red, the Occam R1 and R2 models in blue and green. The χ-values are shown in the legend.

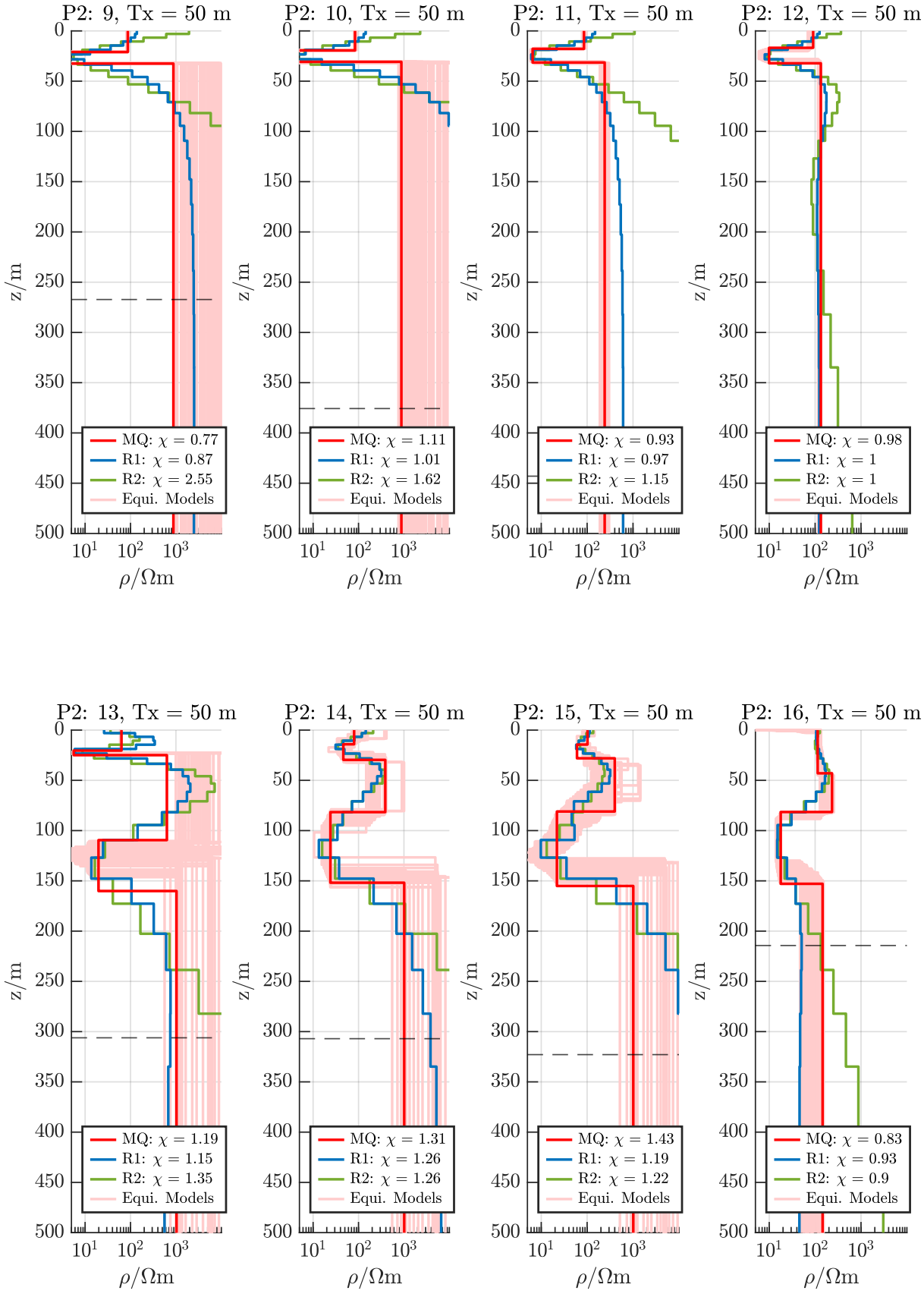

Figure C.4.: 1D inversion models of the Aurus clay pan along profile 2. (cont.)

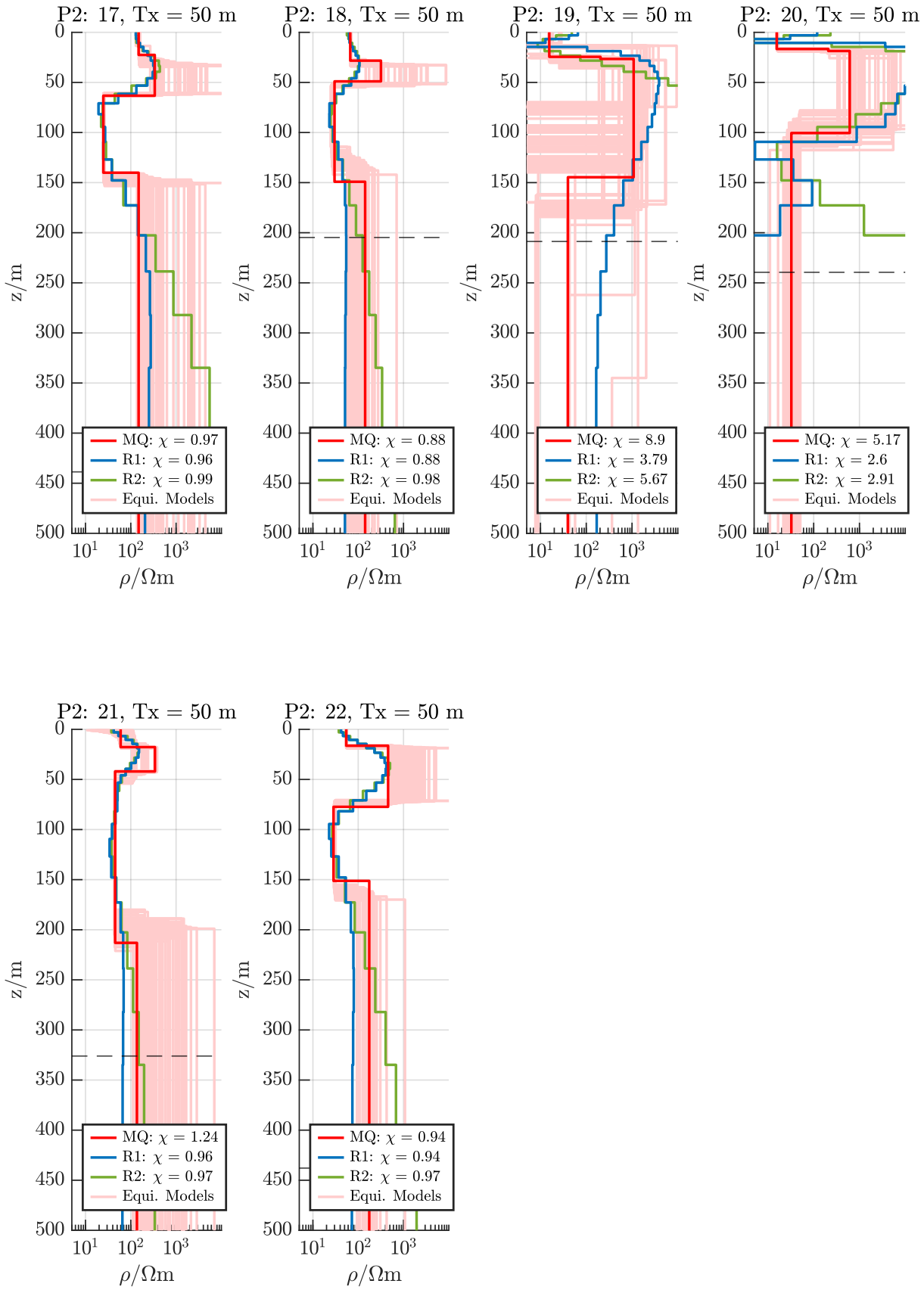

Figure C.4.: 1D inversion models of the Aurus clay pan along profile 2. (cont.)

Acknowledgements

I would like to express my gratitude to:

- Prof. Dr. Bülent Tezkan and Dr. Pritam Yogeshwar for supervising this work and their guidance and support in the last years
- Prof. Dr. Andreas Hördt for appraising this thesis
- Dr. Wiebke Mörbe for being a source of peace and reason in difficult times and for sharing your knowledge about data processing and AMT
- Prof. Dr. Martin Melles for his support and all explanations about geology
- Stefan Schöttle for the useful discussions and providing a more theoretical perspective
- Dr. Yajun Liu and his colleagues providing the 3D TEM algorithm and Yajun for answering all my questions and adapting the algorithm
- Martin, Pritam, Wiebke, Till, Bufelo, Andries, Christoph, Michelle and the other scientist and students from the Geological Survey of Namibia and the University of Namibia for their participation in the field work, as well as Andreas Busse for his support organising the logistics
- Rainer Bergers and Andreas Busse for their technical support
- Dr. Wiebke Mörbe, Stefan Schöttle, Sophia Schiebel and Andrej Jakubowski for proof-reading this thesis
- The rest of the AGEO working group for creating a welcoming and friendly working atmosphere, especially Wiebke, Stefan, Shiva and Barbara
- the RRZK for the possibility to use CHEOPS
- The German Research Foundation (DFG) has funded this work in the framework of the CRC 1211 (project number: 268236062)
- the Geophysical Intrument Pool Potsdam (GIPP) for providing the MT equipment (grant: 202127)
- the Federal Institute for Geosciences and Natural Resources (BGR) for providing the TEMFAST 48 device
- Andrej and my father, Dirk, for being my biggest supporters in life

Erklärung zur Dissertation

Hiermit versichere ich an Eides statt, dass ich die vorliegende Dissertation selbstständig und ohne die Benutzung anderer als der angegebenen Hilfsmittel und Literatur angefertigt habe. Alle Stellen, die wörtlich oder sinngemäß aus veröffentlichten und nicht veröffentlichten Werken dem Wortlaut oder dem Sinn nach entnommen wurden, sind als solche kenntlich gemacht. Ich versichere an Eides statt, dass diese Dissertation noch keiner anderen Fakultät oder Universität zur Prüfung vorgelegen hat; dass sie - abgesehen von unten angegebenen Teilpublikationen und eingebundenen Artikeln und Manuskripten - noch nicht veröffentlicht worden ist sowie, dass ich eine Veröffentlichung der Dissertation vor Abschluss der Promotion nicht ohne Genehmigung des Promotionsausschusses vornehmen werde. Die Bestimmungen dieser Ordnung sind mir bekannt. Darüber hinaus erkläre ich hiermit, dass ich die Ordnung zur Sicherung guter wissenschaftlicher Praxis und zum Umgang mit wissenschaftlichem Fehlverhalten der Universität zu Köln gelesen und sie bei der Durchführung der Dissertation zugrundeliegenden Arbeiten und der schriftlich verfassten Dissertation beachtet habe und verpflichte mich hiermit, die dort genannten Vorgaben bei allen wissenschaftlichen Tätigkeiten zu beachten und umzusetzen. Ich versichere, dass die eingereichte elektronische Fassung der eingereichten Druckfassung vollständig entspricht.

Köln, Januar 2025

Teilpublikation:
Nienhaus, H., Yogeshwar, P., Mörbe, W., Tezkan, B., Büttner, C., Legler, M., Buske, S., Lushetile, B., Wennrich, V., and Melles, M. (2023). Geophysical and geological exploration of the Aurus clay pan as an archive of the long-term climatic and environmental history of the Namib Desert. *Global and Planetary Change*, 230:104259.
Anteile: Manuskript und Korrekturen, Prozessieren und Invertieren aller electromangetischer Daten, Visualisierung, Interpretation und Diskussion aller geophysikalischer Modelle.